STUDY ON THE MULTI-SCALE STRUCTURE AND INTERFACIAL PROPERTIES OF PLANT FIBER REINFORCED COMPOSITES

QIAN LI

PhD

The Hong Kong Polytechnic University

This programme is jointly offered by

The Hong Kong Polytechnic University and

Tongji University

2019

The Hong Kong Polytechnic University

Department of Mechanical Engineering

Tongji University

School of Aerospace Engineering and Applied Mechanics

Study on the Multi-Scale Structure and Interfacial Properties of Plant Fiber Reinforced Composites

Qian LI

A Thesis Submitted in Partial Fulfillment of the Requirements

for the Degree of Doctor of Philosophy

November 2018

CERTIFICATE OF ORIGINALITY

I hereby declare that this thesis is my own work and that, to the best of my knowledge and belief, it reproduces no material previously published or written, nor material that has been accepted for the award of any other degree or diploma, except where due acknowledgment has been made in the text.

_____ (Signature)

LI Qian (Name of student)

ABSTRACT

Plant fibers used as reinforcing materials for green composites have become a common concern among scholars in recent years. However, cellulose, the main chemical composition of plant fibers, contains a large number of hydroxyl groups which leads to poor interfacial properties of plant fibers with hydrophobic polymeric matrices, thus low mechanical properties of plant-fiber-reinforced composites (*PFRCs*). To promote the mechanical performances of *PFRCs* and extend their large-scale industrial applications, it is highly desirable to comprehensively quantify the interfacial properties of *PFRCs* in the multi-scale by considering the distinct multi-layer microstructure of plant fibers. To serve the task of interfacial design of *PFRCs*, a series of experimental techniques (nanoindentation and nano-scale dynamic mechanical analysis (*nano-DMA*), single fiber pull-out measurement and acoustic emission (*AE*) characterization) and analysis methods (multiple interfaces modelling and *ABAQUS* simulation) have been systematically developed, based on the multi-layer structure of *PFRCs*.

In this *Ph.D.* study, experimental investigations were firstly conducted to facilitate understanding of the multi-layer structure of plant fibers. Elastic modulus and

hardness of the epoxy matrix and cell wall layers of sisal fibers (a typical plant fiber) along with interfacial mechanical properties in the sisal-fiber-reinforced composites (*SFRCs*) were measured from the nanoindentation technique. Single-step and multi-step nanoindentation methods were respectively employed on the multi-layer interfaces of *SFRCs* to present their distinct mechanical properties upon compressive loading. Specifically, this study measured the transition zones of the multi-layer interfaces regarding modulus and hardness and the interfacial failure loads, which consequently facilitated quantitative analysis of fracture mechanisms for *SFRCs* with a multi-layer and multi-scale structure. Fatigue performance of multiple interfaces in *SFRCs* in the nano-scale was evaluated with *nano-DMA* technique by using the cyclic loading.

Subsequently, interfacial failure behaviors of *SFRCs* during the single fiber pull-out test were studied experimentally with theoretical analysis and simulation. The residual pull-out strength of the single *SFRCs* was observed to gradually decrease during the test and the corresponding fracture mechanisms were characterized by in-situ *AE* technique. The single *SFRCs* were found to present multiple failure modes at three interfaces, namely interfacial failure between technical fiber and matrix, that between elementary fibers and that between cell walls. Meantime, the failure mechanisms of the interfaces in the single *SFRCs* were described with the help of *AE*. Statistical analysis was employed to evaluate the failure probability of technical fiber, elementary fiber and micro-fibrils pull-out. The embedded fiber length was concluded to play a critical role in determining the failure modes of the single *SFRCs*. To further gain insight in the failure mechanisms of single *SFRCs*, a double-interface model

using the traditional shear lag model and a triple-interface finite element (*FE*) model based on the cohesive zone model (*CZM*), tailored to the unique multi-layer structure of plant fibers, were developed to describe the fiber pull-out behavior with two and three failure stages, respectively. Quantitative comparisons between the numerical predictions from the single-, double- and triple-interface models and the experimental results, using the applied stress as reference, surmised that the single-, double- and triple-interface models need to be comprehensively considered to accurately describe the pull-out behaviors of single *SFRCs*.

With nanoindentation and single fiber pull-out technique, interface failure mechanisms of plant fibers and single *PFRCs* at nanoscopic and microscopic scale were revealed through both experiment and analysis. The effects of hierarchical structure of plant fibers on the interfacial failure behaviors of laminated *PFRCs* in the macro-scale were further investigated using double cantilever beam (*DCB*) experiments. Compared with unidirectional *AFRCs* (especially glass fiber), the *PFRCs* possess higher Mode I interlaminar fracture toughness, which was because the existence of the hierarchical structure of plant fibers and the multiple interfaces of *PFRCs* made the crack propagation path tortuous, further bringing in a more pronounced phenomenon of fiber bridging and fiber entanglement. To model the multi-scale interfacial regions of laminated *PFRCs* and to further simulate their multiple interfacial fracture behaviors, *FE* model was developed in *ABAQUS* with designed *CZM* in the crack front. Good consistency between the numerical simulation and the experiment results verified the efficiency of *CZM* in modelling the multi-layer failure behaviors of laminated *PFRCs*. Using the micromechanics theory and cohesion

model of composite materials, a quantitative relationship among the microstructure characteristic, interlaminar fracture toughness and parameters of the mechanical model was studied based on the design principle of composite structures in this thesis. Conclusively, through experimental investigations, theoretical modelling and numerical simulation, a series of characterization techniques from nanoscopic to macroscopic scale for identifying multiple interfacial failure modes in *PFRCs* were employed in this thesis by considering the hierarchical structural features of plant fibers. The presented thesis provides a solid theoretical foundation, whereby theoretical and numerical analysis can be accurately conducted to achieve the goal of interface design in laminated *PFRCs* with multi-layer and multi-scale structures. Research achievements in this *Ph.D.* study are expected to serve for improving the mechanical performances of *PFRCs*, achieving large-scale applications of *PFRCs* in the fields of aerospace, automotive engineering and civil infrastructures and expanding the theories on multi-scale mechanics of composite materials to some extent.

LIST OF PUBLICATIONS ARISING FROM THIS WORK

Referred Journal Papers

1. **Li Q.**, Li Y.*, Zhou L.M.*. A micromechanical model of interfacial debonding and elementary fiber pull-out for sisal fiber reinforced composites [J]. *Composites Science and Technology*, 2017, 153: 84-94. (SCI, IF=5.160)

2. **Li Q.**, Li Y.*, Zhou L.M.*. Nanoscale evaluation of multi-layer interfacial mechanical properties of sisal fiber reinforced composites by nanoindentation technique [J]. *Composites Science and Technology*, 2017, 152: 211-221. (SCI, IF=5.160)

3. Li Y.*, **Li Q.** High mechanical performance and multi-functionalities of plant-fiber-reinforced composites [J]. *Acta Mechanica Solida Sinica*, 2017, 38(3): 215-243. (Chinese Review, Core Journal)

4. Li Y.*, **Li Q.**, Ma H. The voids formation mechanisms and their effects on the mechanical properties of flax fiber reinforced epoxy composites [J]. *Composites Part A: Applied Science and Manufacturing*, 2015, 72: 40-8. (SCI, IF=4.514)

5. **Li Q.**, Li Y.*, Zhou L.M.*. Quantitative investigations on multi-layer interface debonding behavior for sisal fiber-reinforced composites using acoustic emission and finite element method [J]. *Submitted to Composites Science and Technology*. (SCI, IF=5.160)

6. **Li Q.**, Li Y.*, Ma H., Cai S.M., Huang X.L. Effect of processing temperature on the mechanical properties and failure mechanisms of flax fiber reinforced composites [J]. *Submitted to Composites Part A: Applied Science and Manufacturing*. (SCI, IF=4.514)

7. **Li Q.**, Li Y.*, Zhang Z.S., Zhou L.M.*. Modelling of the multi-layer interfacial debonding and fiber pull-out for sisal fiber reinforced composites [J]. *Submitted to Composites Communications*.

8. Li Y.*, Ma H., Shen Y.O., **Li Q.**, Zheng Z.Y. Effects of resin inside fiber lumen on the mechanical properties of sisal fiber reinforced composites [J]. *Composites Science and Technology*, 2015, 108: 32-40. (SCI, IF=5.160)

Refereed Conference Papers

1. **Li Q.**, Li Y.*, Zhou L.M. The investigations of multi-layer interface failure behavior for sisal fiber reinforced composites via acoustic emission and finite element method [C]. *The 21st International Conference on Composite Materials (ICCM-21)*, 20-25 August 2017, Xi'an, China. (EI, Tsai Best Student Paper)

2. **Li Q.**, Zhou L.M., Li Y.*. Simulation and analysis on multi-layer interfacial debonding and elementary fiber pull out for sisal fiber reinforced composites [C]. *The 1st Conference on Natural Fiber Composite Materials (NFCM1)*, 16-18 December 2016, Guangzhou, China. (Conference Excellent Paper)

3. **Li Q.**, Zhou L.M., Li Y.*. Modelling and analysis on multi-layer interfacial debonding and elementary fiber pull out for sisal fiber reinforced composites [C]. *2016 National Doctoral Student Forum in Aviation Science and Technology*, 25-27 November 2016, Xi'an, China.

4. **Li Q.**, Zhou L.M., Li Y.*. Evaluation of multi-layer interphase of sisal fiber reinforced composites via nanoindentation and theoretical calculation [C]. *The 10th Asian-Australasian Conference on Composite Materials (ACCM-10)*, 16-19 October 2016, Busan, Korea. (EI)

5. **Li Q.**, Li Y., Zhou L.M.*. Experimental characterization of interfacial mechanical properties in sisal fiber reinforced composites by the nanoindentation technique [C]. *International Symposium on Advanced Materials and Structures (ISAMS-2016)*, 2-4 January 2016, Hong Kong, China.

6. **Li Q.**, Li Y., Zhang Z.S., Zhou L.M.*. Modeling and analysis on interfacial debonding and elementary fiber pull out for sisal fiber reinforced composites [C]. *The 2nd China International Congress on Composite Materials (CCCM2)*, 21-23 September 2015, Zhenjiang, China.

7. **Li Q.**, Li Y.*. The investigations of voids effects on the mechanical properties of plant fiber reinforced composites [C]. *The 9th Asian-Australasian Conference on Composite Materials (ACCM-9)*, 15-17 October 2014, Suzhou, China. (EI)

ACKNOWLEDGMENTS

During my study at the Hong Kong Polytechnic University, many teachers inspired me with their vast knowledge, constant guidance, constructive suggestion and useful advice, to whom I want to express my sincere thanks for their kind help.

Firstly, I would like to express my deepest appreciation and special gratitude to my chief supervisor at the Hong Kong Polytechnic University, Prof. Limin Zhou, for his timely offer which admits me to study at PolyU as a joint *Ph.D.* student between the Hong Kong Polytechnic University and Tongji University. I gained a lot during the time spent together with Prof. Zhou. With his extensive knowledge and research experience, he has been providing valuable advice for my *Ph.D.* study. My English writing capabilities and presentation skills have been greatly improved with his guidance. Thanks to his continuous support and thoughtful arrangement, I was able to focus on my study and deepen my research to a large extent in the 18 months at PolyU. What I have learned from him will have a lasting positive influence on my current and further academic life.

In the meanwhile, I want to express my sincere appreciations to Technical staff Mr. Benny Leung for his useful guidance on experimental operations, especially in nanoindentation. I would like to thank Dr. Hardy Lui at Materials Research Centre in The Hong Kong Polytechnic University for his useful help in SEM characterization. And I appreciate that I have adequate access to the experiment and office equipment, journals and books relevant to my research, sufficient office supplies and expertise from both my supervisors and technicians. I appreciate the resources provided to me and will continue to make best use of them.

I would also like to express my thanks to my co-supervisor Prof. Yan Li at Tongji University, for her unreserved guidance and support. Prof. Li encouraged me to join this exchange program and has always tried her best to create valuable opportunities for me to improve my research skill and regulated my academic behavior with her rigorous academic attitude.

During my exchange period at PolyU, I have met and made some great friends in the Department of Mechanical Engineering. Special thanks should be delivered to all the past and present group members for their great help and friendship. We share the joy, frustration and difficulties, work together and grow. They accompanied me to truly integrate into the life of Hong Kong and spend an enjoyable time at PolyU. Thanks to my research fellow Dr. Jingjing Tang, Dr. Xiaoyan Li, Dr. Yuming Chen, Dr. Weiqun Li, Miss Jing Hu and Mr. Qian Wang to bring my colorful life and leave the unforgettable memories. I benefited a lot from their useful advice and timely help.

I would also like to thank The Hong Kong Polytechnic University for its financial support to my *Ph.D.* study.

Finally, I am heartily thankful to my beloved family for their unconditional love and support. Special thanks to my parents and my husband Zhen Zhang, who accompanied me through all the stages of my *Ph.D.* study. They are always the source of my courage to overcome difficulties. My genuine thanks go to them for their forever understanding, encouragement and continuous support.

TABLE OF CONTENTS

ABSTRACT ..... **i**

LIST OF PUBLICATIONS ARISING FROM THIS WORK ..... **v**

ACKNOWLEDGMENTS ..... **ix**

TABLE OF CONTENTS ..... **xii**

NOMENCLATURE ..... **xvii**

LIST OF FIGURES ..... **xxvii**

LIST OF TABLES ..... **xxxviii**

CHAPTER 1 ..... **1**

Introduction **1**

1.1. Research background and motivations 1

1.2. Scope of the thesis 8

CHAPTER 2 ..... **14**

State of the Art of Evaluation of Interfacial Properties: *From AFRCs to PFRCs* **14**

2.1. Introduction 14

2.2. Comparisons of structural characteristics between plant fibers and synthetic fibers 16
2.2.1. Chemical compositions 17
2.2.2. Microstructure 19
2.3. Comparisons of interfacial evaluation between *PFRCs* and *AFRCs* 23
2.3.1. Experimental characterization of the interfacial mechanical properties 24
2.3.2. Theoretical analysis of the interfacial mechanical behaviors--Shear lag model 35
2.3.3. Numerical simulation of the interfacial mechanical behaviors--*CZM* 38
2.4. Comparisons of interfacial behaviors between *PFRCs* and *AFRCs* 42
2.4.1. Interfacial modification 43
2.4.2. Interfacial failure mechanisms 48
2.5. Summary 53
CHAPTER 3 55
Nanoscale Evaluation of Multi-Layer Interfacial Mechanical Properties of *PFRCs* by the Nanoindentation and *Nano-DMA* Technique 55
3.1. Introduction 55
3.2. Materials and experimental procedures 58
3.2.1. Materials and specimen fabrication for nanoindentation and *nano-DMA* measurements 58
3.2.2. Nanoindentation tests and morphology characterization 60
3.2.3. Basis of *nano-DMA* theory and morphology characterization 64

3.3. Evaluation of nano-properties for pure epoxy matrix, cell wall layers and the multi-layer interphase in the *SFRCs* 69

3.4. Interfacial failure mechanisms of *SFRCs* in single-step and multi-step nanoindentation 76

3.5. Interfacial failure mechanisms of *SFRCs* in *nano-DMA* 84

3.6. Summary 93

CHAPTER 4 96

Experimental Investigation on Multi-Layer Interface Debonding Behaviors of Single *PFRC*s in the Pull-Out Test Using *AE* and Statistical Analysis 96

4.1. Introduction 96

4.2. Sisal technical, elementary fibers and micro-fibrils pull-out experiments and characterizations 99

4.3. Single sisal fiber pull-out behaviors of *SFRCs* monitored by *AE* technique 103

4.4. Multi-interface debonding and multi-stage fiber component fracture and pull-out mechanisms of *SFRCs* characterized by *AE* signal analysis 107

4.5. Statistical analysis on the multi-stage fracture performance of *SFRCs* ... 132

4.6. Summary 136

CHAPTER 5 139

A Micromechanical Model of Interfacial Debonding between Technical and Elementary Fibers during the Pull-Out Test of Single *PFRCs* 139

5.1. Introduction 139

5.2. Theoretical analysis of multi-layer interface debonding behaviors for single *PFRCs* 141

5.2.1. Basic governing equations for *PFRCs* 141

5.2.2. Process 1: Debonding between the technical fiber and epoxy matrix 144

5.2.3. Process 2: Debonding between the elementary fibers.....147

5.3. Evaluations of interfacial parameters and maximum debond stresses of *SFRCs* 150

5.4. Comparisons of the applied stresses on sisal technical fiber between experiment and theory 154

5.5. Double-stage fracture mechanisms of *SFRCs* 158

5.6. Summary.....161

CHAPTER 6.....163

An *FE* Model of Multi-Layer Interface Debonding Behaviors for Single *PFRCs* during the Pull-Out Test.....163

6.1. Introduction 163

6.2. Numerical analysis of multi-layer interface debonding behaviors for single *SFRCs* 165

6.3. Effects of the interfacial parameters on the interfacial failure behaviors of *SFRCs* 188

6.4. Comparisons of the applied stresses on sisal technical fiber with multi-layer interface between experimental test and numerical simulation.....192

6.5. Multi-stage fracture mechanisms of *SFRCs* 195

6.6. Summary.....198

CHAPTER 7.....201

An *FE* Model of Multi-Layer Interlaminar Fracture Behaviors for Laminated *PFRCs* during the *DCB* Test 201

7.1. Introduction 201

7.2. *DCB* experiments for laminated *SFRCs* 203

7.3. Numerical simulation of multi-layer interlaminar fracture behaviors for laminated *SFRCs* 209

7.4. Effects of the interfacial parameters on the interlaminar failure behaviors of *SFRCs* 227

7.5. Comparisons between experimental and numerical results on Mode I interlaminar fracture of laminated *SFRCs* with multi-layer interface 230

7.6. Multi-stage interlaminar fracture mechanisms of *SFRCs* 237

7.7. Summary 247

CHAPTER 8 251

Conclusions and Recommendations for Future Research 251

8.1. Concluding remarks 251

8.2. Problematic issues and recommendations for future research 259

APPENDICES 263

BIBILIOGRAPHY 271

NOMENCLATURE

Acronyms and Initialisms

AE	Acoustic emission
AFM	Atomic Force Microscopy
AFRC(s)	Synthetic fiber reinforced composite(s)
ASTM	American society for testing materials
BC	Boundary condition
CFRC(s)	Carbon fiber reinforced composite(s)
CNC(s)	Cellulose nanocrystal(s)
CNT(s)	Carbon nanotube(s)
CSM	Continuous stiffness measurement
CZM	Cohesive zone model
DCB	Double cantilever beam
DOF	Degrees of freedom
EMD	Empirical mode decomposition
ENF	End Notched Flexure
FE	Finite element

FFRC(s)	Flax fiber reinforced composite(s)
FFT	Fast Fourier transform
GFRC(s)	Glass fiber reinforced composite(s)
HHT	Hilbert-Huang transform
IFSS	Interfacial shear strength
IF-FM	Interfaces between technical or elementary fiber and matrix
IF-ELE	Interfaces between elementary fibers
IF-CW	Interfaces between cell wall layers
IF-IL	Interfaces between interlaminar layer
InEFs	Inner elementary fibers
ILFT	Interlaminar fracture toughness
ILSS	Interlaminar shear strength
IMF(s)	Intrinsic mode function(s)
Nano-DMA	Nano-scale dynamic mechanical analysis
NFRC(s)	Natural fiber reinforced composite(s)
OM	Optical Microscopy
OutEFs	Outer elementary fibers
PFRC(s)	Plant-fiber-reinforced composite(s)
PLA	Polylactide
PTFE	Polytetrafluoroethylene
SEM	Scanning Electronic Microscopy

SFRC(s)	Sisal fiber reinforced composite(s)
3D	Three-dimensional
VARI	Vacuum assistant resin infusion
VCCT	Virtual crack closure technique
WED	Wave energy attenuation
WOI	Work of indentation

Symbols

F	Maximum load before fiber debonding
d	Diameter of the fiber
l	Embedded length of the fiber
C	Circumference of the fiber
E_r	Reduced modulus of related indent regions
E_I	Indenter modulus
ν_I	Poisson's ratio of indenter
E_S	Elastic modulus of each indent region
ν_S	Poisson's ratio of each indent region
H	Hardness of each indent region
A_C	Contact area between the indenter tip and sample at the maximum indentation load

P_{max}	Maximum indentation load
W_t	Total work
W_{el}	Reversible (elastic) work
W_{pl}	Irreversible (plastic) work
E'	Storage modulus or dynamic stiffness
E''	Loss modulus or damping
$P(t)$	Cyclic load
P_{mean}	Mean load
P_{OL}	Oscillation load amplitude
ω	Oscillation frequency
P	Applied force
h_C	Contact depth
ϕ	Face angle of the indenter head
m	Mass of the tip and shaft
K_I	Stiffness of the indenter
K_S	Stiffness of the sample
C_I	Damping coefficients of the indenter
C_S	Damping coefficients of the sample
F_0	Load amplitude
$x(t)$	Position of the tip as a function of time

X	Displacement amplitude
φ	Phase lag between the applied force and the tip displacement.
K_S'	Storage stiffness
K_S''	Loss stiffness
$Y(t)$	An original signal to conduct *EMD*
m_{ij}	Average of the maxima and minima envelopes
h_{ij}	Proto-Intrinsic Mode Function
c_i	i^{th} intrinsic mode function
r_i	i^{th} residue function
S_i^T	i^{th} *IMF* of the *AE* signals generated from specimens under a process of T ($T = 11,\ 21,\ 22,\ 31,\ 32\ or\ 33$)
R_k	Energy ratio of each *IMF*
$E(c_k)$	Equivalent energy of each *IMF*
R_{1-3}	Summation of energy ratios of first three *IMFs*
$R_{Residual}$	Summation of energy ratios of residual *IMFs*
a_1	Radius of a technical fiber

b	Radius of matrix
a_2	Radius of inner elementary fibers
a_3	Radius of cell walls
z	Axial directions of the fiber
r	Radial directions of the fiber
L	Total embedded length of the technical fiber
σ	Tensile stress
E	Young's modulus
ν	Poisson's ratio
$i = m, f_1, f_2$	m, matrix
$j = m, f_1$	f_1, *OutEFs*
	f_2, *InEFs*
$\sigma_{f1}, \sigma_{f2}, \sigma_m$	Internal stresses
τ_{i1}, τ_{i2}	Interfacial shear stresses
η	Volume ratio of the elementary fiber to the technical fiber
γ	Volume ratio of the technical fiber to the matrix
σ_{lf1}	Crack tip debond stress acting at the critical point ($z = l_{f1}$)
σ_{lf2}	Debond stress at the crack tip ($z = l_{f2}$)

$\sigma_f{}^z(z)$, $\sigma_m{}^z(z)$	Axial normal stress of fiber or matrix
$\tau_{i1}{}^{rz}(z)$, $\tau_{i2}{}^{rz}(z)$	Axial shear stresses of two interfaces
μ_1, μ_2	Constant friction coefficient
q_{01}, q_{02}	Residual clamping stress caused by matrix shrinkage and the difference in thermal contraction or expansion between the constituents during fabrication
$q_{a1}(z)$, $q_{a2}(z)$	Radial stress arising from the Poisson contraction of fibers subject to tension
$q_{R1}(z)$	Additional radial stress due to the asperity mismatch between the technical fiber and matrix
$q_{R2}(z)$	Additional radial stress due to the asperity mismatch between the *OutEFs* and *InEFs*
q_1^*, q_2^*	Radial stresses for Process 1
q_1^{**}, q_2^{**}	Radial stresses for Process 2
α_{f1}	Thermal expansion coefficients of the technical fiber
α_m	Thermal expansion coefficients of the matrix

ΔT	Temperature change
U_{t1}, U_{t2}	Total elastic strain energy
U_f	Elastic strain energies of fiber
U_m	Elastic strain energies of matrix
U_{f1}, U_{f2}	Elastic strain energies of *OutEFs* or *InEFs*
${\sigma_{d1}}^p$, ${\sigma_{d2}}^p$	Partial debonding stress during Process 1 or Process 2
σ_{fr}	Frictional pull-out stress
s	Fiber sliding distance
d_{max}	Maximum amplitude
$d_i(z)$	Interfacial amplitude function
$\delta_i(z)$	Asperities mismatch function
$v_i(z)$	Relative displacements
B_{n1}	Fourier series coefficient for Process 1
B_{n2}	Fourier series coefficient for Process 2
$\boldsymbol{\tau}$	Nominal stress vector of the cohesive element
$\boldsymbol{K}$	Elastic constitutive nominal stiffness matrix
K_{nn}	Stiffness in the normal direction
K_{ss}	Stiffness in the first shear direction

K_{tt}	Stiffness in the second shear direction
τ_n, τ_s, τ_t	Traction stresses in the normal, the first and second shear directions
ε_n, ε_s, ε_t	Strains in the normal, the first and second shear directions
δ_n, δ_s, δ_t	Separations in normal, the first shear and second shear directions
T_0	Constitutive thickness
G^C	Total mixed fracture energy
a_0	Pre-crack length
Δa	Delamination propagation length
m, n	Superposition parameters
G_1	Critical strain energy release rate
l_{cb}	Characteristic length of bilinear cohesive law
l_{ctr}	Characteristic length of the process zone for the trilinear cohesive law
l_{pztr}^{ss}	Length of process zone under steady-state propagation for the trilinear cohesive law
t_{lam}	Block thickness (thickness of plies stacking in the same orientation)

LIST OF FIGURES

Figure 1.1 Trend and forecast in the market value of *NFRCs* from the year 2005 to 2020 [9, 10]. 3

Figure 2.1 Chemical structure of cellulose [23]. 19

Figure 2.2 Comparisons of the surface structure of (a) sisal fiber and (b) carbon fiber and the cross section of (c) sisal fiber and (d) glass fiber [43, 44]. 20

Figure 2.3 (a) Diagram for structure of a single plant fiber, (b) multi-scale structure of sisal fiber [48] and (c) multi-layer cell structure of flax fiber. 21

Figure 2.4 A typical pull-out stress-displacement curve for single *AFRCs*. 38

Figure 2.5 Fractography of sisal fibers after tensile failure: (a) overall morphology, (b) and (c) details of delamination within the cell walls and between cells [48]. 51

Figure 2.6 Initiation and development of fracture in an elementary flax fiber: (a) and (b) crack initiation in the primary cell wall, (c) separation between the primary and secondary cell walls, (d) the secondary cell wall deformation and the micro-fibrils bridging in S2 layer, (e) extended plastic deformation

of the fibrils in the secondary cell wall and (f) the fiber before complete failure [153]. 51

Figure 2.7 *SEM* images of Phormium fiber reinforced composites after tensile test: (a) cell-cell debonding and (b) the micro-fibrils pulled-out and resin pulled-out from the lumens of thin-walled cells [155]..... 52

Figure 2.8 *SEM* morphologies of *FFRCs* after Charpy impact tests: (a) pulled out deformed fibers and fiber bundle and (b) splitting of a technical fiber followed by fracture of the elementary fibers [25]. 52

Figure 2.9 Multi-layer and multi-scale interfacial damage micrographs of *PFRCs* ((a)-(c) multi-layer damage of elementary fiber and (b) micro-fibril pull-out) [32, 33]. 53

Figure 3.1 *SEM* photographs of the surface modification of the sisal fiber (a) before and (b) after pretreatment..... 60

Figure 3.2 Schematic of the process of fiber impregnated. 60

Figure 3.3 (a) Specimen configuration for nanoindentation test and (b) schematic illustration of nanoindentation position. 61

Figure 3.4 Schematic of three types of interfaces for the *SFRCs*. 63

Figure 3.5 Schematic of typical loading function used in the (a) single-step, (b) multi-step and (c) cyclic nanoindentation and (d) plastic and elastic work calculated from load-depth curve of nanoindentation test. 64

Figure 3.6 Schematics of (a) the nanoscale fatigue test and (b) the loading cycle by the *CSM* technique. 66

Figure 3.7 Schematic of (a) the nanoindentor-sample system and (b) the dynamic nanoindentation model. 67

Figure 3.8 Elastic modulus and hardness measured at different indentation depths for (a) epoxy matrix and (b) S2 layer of the sisal fiber. 70

Figure 3.9 Load-depth curves obtained from different points. 72

Figure 3.10 (a) Distributions of intents on the epoxy matrix and a sisal elementary fiber of the *SFRC*, (b) *AFM* image of a typical indent, cartography of (c) reduced elastic modulus and (d) hardness for the *SFRC*. 73

Figure 3.11 Distributions of (a) reduced elastic modulus and (b) hardness of the *SFRC* regarding indent positions. 76

Figure 3.12 Comparison of relationships in terms of (a) W_{pl}/W_t *vs*. indentation loads and (b) W_{pl}/W_t *vs*. H/E_r for the three interfaces obtained from single-step nanoindentations. 78

Figure 3.13 Comparison of (a) load-depth curves and relationships in terms of (b) W_{pl}/W_t vs. indentation loads for the three interfaces obtained from multi-step nanoindentations. 80

Figure 3.14 W_{pl}/W_t over cycle times obtained with indent forces of (a) 600, (b) 2000, (c) 4400 and (d) 6200 μN for the three interfaces. 83

Figure 3.15 *SEM* photographs of cracks on the three interfaces: (a) *IF-FM*, (b) *IF-ELE* and (c) *IF-CW* for *SFRCs* subject to the cyclic indentation loads. 84

Figure 3.16 Storage modulus as a function of the oscillation frequencies on three types of interfaces for the *SFRCs* in different oscillation loads: (a) 500, (b) 1000 and (c) 1500 μN 88

Figure 3.17 $Tan\ \delta$ as a function of the oscillation frequencies on three types of interfaces for the *SFRCs* in different oscillation loads: (a) 500, (b) 1000 and (c) 1500 μN 88

Figure 3.18 Storage modulus as a function of the number of cycles on three types of interfaces for the *SFRCs* in different oscillation loads: (a) 500, (b) 1000 and (c) 1500 μN 90

Figure 3.19 $Tan\ \delta$ as a function of the number of cycles on three types of interfaces for the *SFRCs* in different oscillation loads: (a) 500, (b) 1000 and (c) 1500 μN 91

Figure 3.20 Storage modulus as a function of the number of cycles on three types of interfaces for the *SFRCs* in different oscillation frequencies: (a) 180, (b) 220 and (c) 260 Hz 92

Figure 3.21 $Tan\ \delta$ as a function of the number of cycles on three types of interfaces for the *SFRCs* in different oscillation frequencies: (a) 180, (b) 220 and (c) 260 Hz 93

Figure 4.1 Measurement on the diameter of single sisal fiber. 101

Figure 4.2 Specimen preparation for single sisal fiber pull-out measurements..... 101

Figure 4.3 (a) Schematic illustration of the principle and mechanism and (b) experimental setup of *AE* in the single sisal fiber pull-out measurement. 102

Figure 4.4 The applied stress-displacement curves for the single sisal fiber pull-out with (a) single-, (b) double- and (c) triple-stage pull-out and fracture. 103

Figure 4.5 *SEM* photographs of pulled-out sisal fibers after single fiber pull-out tests: (a) technical fiber, (b) elementary fibers and (c) micro-fibrils pull-out.104

Figure 4.6 The *AE* response about energy versus time for the single sisal fiber pull-out with (a) single-stage debonding, (b) double- and (c) triple-stage debonding, fracture and pull-out. 106

Figure 4.7 Flowchart of *EMD*. 111

Figure 4.8 Time presentations of the original *AE* signal and its first two *IMFs* captured from multiple interfaces debonding during single sisal fiber pull-out process: *IF-FM* debonding (Process 1) in (a) single-stage, (b) double-stage and (c) triple-stage, *IF-ELE* debonding (Process 2) in (d) double-stage and (e) triple-stage, and *IF-CW* debonding (Process 3) in (f) triple-stage...114

Figure 4.9 Time presentations of the original *AE* signal and its first two *IMFs* captured from the fiber component multi-stage fracture or pull-out during single sisal fiber pull-out process: (a) *TF* pull-out (Process 1) in single-stage, *ELE* fracture (Process 1) in (b) double-stage and (c) triple-stage, (d) *ELE* pull-out (Process 2) in double-stage, (e) *CW* fracture (Process 2) in triple-stage, and (f) *CW* pull-out (Process 3) in triple-stage.....115

Figure 4.10 *HHT* spectra of the *AE* signals captured from the multiple interfaces debonding during the single sisal fiber pull-out process: *IF-FM* debonding (Process 1) in (a) single-stage (refer to Figure 4.8 (a)), (b) double-stage (refer to Figure 4.8 (b)) and (c) triple-stage (refer to Figure 4.8 (c)), *IF-ELE* debonding (Process 2) in (d) double-stage (refer to Figure 4.8 (d)) and (e) triple-stage (refer to Figure 4.8 (e)), and *IF-CW* debonding (Process 3) in (f) triple-stage (refer to Figure 4.8 (f)). 118

Figure 4.11 *HHT* spectra of the *AE* signals captured from the fiber components multi-stage fracture or pull-out during single sisal fiber pull-out process: (a) *TF* pull-out (Process 1) in single-stage (refer to Figure 4.9 (a)), *ELE* fracture (Process 1) in (b) double-stage (refer to Figure 4.9 (b)) and (c) triple-stage (refer to Figure 4.9 (c)), (d) *ELE* pull-out (Process 2) in double-stage (refer to Figure 4.9 (d)), (e) *CW* fracture (Process 2) in triple-stage (refer to Figure 4.9 (e)), and (f) *CW* pull-out (Process 3) in triple-stage (refer to Figure 4.9 (f)). 122

Figure 4.12 Marginal spectra of the *AE* signals captured from the multiple interfaces debonding during the single sisal fiber pull-out process. 129

Figure 4.13 Marginal spectra of the *AE* signals captured from the fiber components multi-stage fracture or pull-out during the single sisal fiber pull-out process..... 129

Figure 4.14 (a) Distribution of the number of occurrences of multi-stage debonding of the *SFRCs* and (b) corresponding Weibull distribution..... 134

Figure 4.15 Distribution of the interfacial strength of different interfaces with occurrences of multi-stage debonding of the *SFRCs*. 135

Figure 5.1 Schematic of the double-interface model describing pull-out behaviors of *PFRCs*: (a) original stage, (b)-(c) Process 1 and (d)-(g) Process 2. 143

Figure 5.2 (a) Distribution of diameters of the sisal fibers and (b) corresponding Weibull distribution. 151

Figure 5.3 Simulated rough interface with d_{max} of 0.1 μm. 153

Figure 5.4 Maximum debond stress of *SFRCs* with different embedded fiber lengths during (a) Process 1 and (b) Process 2. 154

Figure 5.5 Applied stress-displacement curves in the single fiber pull-out behaviors of single *SFRCs* obtained from (a) experiment and (b) theory. 155

Figure 5.6 *SEM* photographs of pulled-out sisal fibers after single sisal fiber pull-out tests: (a) elementary fiber debonding and (b) elementary fiber pull-out ($L = 0.332\ mm$). 157

Figure 5.7 Applied stress-displacement curves obtained from experiment, single- and double-interface model in a typical case $L = 0.332\ mm$ 158

Figure 5.8 Distributions of (a) and (b) axial fiber stress, (c) and (d) axial matrix stress and (e) and (f) interfacial shear stress in the single fiber pull-out behaviors of single *SFRCs* ((a), (c) and (e) for Process 1 and (b), (d) and (f) for Process 2).....160

Figure 6.1 Schematic of the triple-interface model describing single-stage debond behavior of *PFRCs*: (a) original process, (b) *IF-FM* interfacial debond process and (c) pull-out process. 167

Figure 6.2 Schematic of the triple-interface model describing double-stage debond behavior of *PFRCs*: (a) original process, (b) *IF-FM* interfacial debond process, (c) partial elementary fibers fracture process, (d) *IF-ELE* interfacial debond process and (e) pull-out process. 168

Figure 6.3 Schematic of the triple-interface model describing triple-stage debond behavior of *PFRCs*: (a) original process, (b) *IF-FM* interfacial debond process, (c) partial elementary fibers fracture process, (d) *IF-ELE*

interfacial debond process, (e) partial cell wall micro-fibrils fracture process, (f)-(g) *IF-CW* interfacial debond process and (h)-(i) pull-out process..... 169

Figure 6.4 The full view of *FE* model with multi-layer interfaces for the single sisal fiber pull-out. 170

Figure 6.5 One quarter *3D* discretized *FE* model with mesh for the single sisal fiber pull-out with multi-layer interfaces (fine mesh around the interface).. 172

Figure 6.6 Schematic illustration of typical bilinear traction-separation cohesive law for modeling cohesive failure and its damage evolution. 181

Figure 6.7 Load and boundary conditions of fiber and matrix for the *FE* model of the single sisal fiber pull-out with multi-layer interfaces. 184

Figure 6.8 Interaction and constraint conditions of multi-layer interfaces (i.e., *IF-FM*, *IF-ELE* and *IF-CW*) for the *FE* model of the single sisal fiber pull-out. 184

Figure 6.9 Schematic of typical stress-displacement behavior during single sisal fiber pull-out process with multi-stage debonding and fiber fracture and pull-out. 187

Figure 6.10 Flowchart of the proposed *FE* model for solving the multi-stage debonding and fracture process. 188

Figure 6.11 Applied stress-displacement curves obtained from numerical simulation and experimental test for the multi-stage pull-out of single *SFRCs* with various embedded fiber length: (a) single-stage ($L = 0.187\ mm$), (b) double-stage ($L = 0.347\ mm$) and (c) triple-stage ($L = 0.440\ mm$).... 192

Figure 6.12 Stress distributions on sisal fibers and multi-layer interfaces in triple-interface *FE* model describing multi-stage debond, fracture and pull-out behaviors of single *SFRCs*: (a) the *IF-FM* interface debonding, (b) the outer single technical fiber *TF* breakage, (c) the *IF-ELE* interface debonding, (d) the P/S1 layer of cell wall for the inner elementary fiber *ELE* breakage, (e) the *IF-CW* interface debonding and (f) pulling-out. 196

Figure 7.1 Sewing fabrication method of unidirectional sisal fiber fabrics. 204

Figure 7.2 Schematic illustration of *VARI* technique for preparing the laminated *SFRCs* and *GFRCs*. 206

Figure 7.3 Experimental setup of *VARI* for the unidirectional sisal fiber reinforced composite laminate. 207

Figure 7.4 Schematic presentation of *DCB* specimen geometry and dimensions and the full view of *FE* model with multi-layer interfaces for simulating the interlaminar fracture of laminated *SFRCs*. 210

Figure 7.5 Schematic of the multiple interface model describing multi-stage Mode I interlaminar fracture behaviors of *PFRCs*: (a) original status, (b) *IF-IL* cracking, (c) elementary fibers breaking, (d) *IF-ELE* cracking, (e) cell walls breaking, (f) *IF-CW* cracking and (g) micro-fibrils pulling-out. .211

Figure 7.6 *3D* discretized *FE* model with mesh for the Mode I interlaminar fracture of laminated *SFRCs* with multi-layer interfaces (fine mesh at the cracking zone). 214

Figure 7.7 R-curve in experiment for unidirectional laminated *SFRCs* and *GFRCs*. 217

Figure 7.8 Schematic illustration of typical resultant trilinear traction-separation cohesive law (superposition of two bilinear cohesive laws) for modeling cohesive failure and its damage evolution. 218

Figure 7.9 Load and boundary conditions of whole laminate for the *FE* model of the Mode I interlaminar fracture in *DCB* test specimen of *SFRCs* with multi-layer interfaces. 223

Figure 7.10 Interaction and constraint conditions of multi-layer interfaces (i.e., *IF-IL*, *IF-ELE* and *IF-CW*) for the *FE* model of the Mode I interlaminar fracture in *DCB* test specimen of *SFRCs*. 223

Figure 7.11 Schematic showing of typical R-curve behavior during multi-stage interlaminar cracking process of unidirectional *SFRCs* laminate. 226

Figure 7.12 Schematic of typical force-displacement response behavior during multi-stage interlaminar cracking process of unidirectional *SFRCs* laminate.226

Figure 7.13 Flowchart of the proposed *FE* model for solving the multi-stage interlaminar cracking process. 227

Figure 7.14 Comparison of the force-displacement response between the experimental results and the numerical results for the *DCB* test specimen of composite laminates (i.e., *SFRCs* and *GFRCs*). 232

Figure 7.15 Comparison of R-curves (measured fracture toughness values of the composite versus crack length) between the experimental results and the *FE* analysis results for the *DCB* test specimen of composite laminates (i.e., *SFRCs* and *GFRCs*). 235

Figure 7.16 Comparison of change in crack length against opening displacement between the experimental and *FE* analysis results for the *DCB* test specimen of *SFRCs*.....236

Figure 7.17 Stress distributions on sisal fiber layers and multi-layer interfaces in triple-interface *FE* model describing multi-stage cracking and fracture behaviors of laminated *SFRCs*: (a) the *IF-IL* interface cracking, (b) the elementary fiber layer *ELE* breakage, (c) the *IF-ELE* interface cracking, (d) the P/S1 layer of cell wall for the inner elementary fiber breakage and (e) the *IF-CW* interface cracking. 238

Figure 7.18 (a) and (c) Macroscopic and (b) and (d) *SEM* photographs of laminated *SFRCs* ((a) and (b)) and *GFRCs* ((c) and (d)). 241

LIST OF TABLES

Table 2.1 Comparisons of the chemical composition in plant fibers [17-21]..... 18

Table 2.2 Comparisons on the mechanical properties between plant fibers and glass fibers [5, 52]..... 23

Table 4.1 Evolution of energy ratios of *IMF* components decomposed from the *AE* signals from the multiple interfaces under different debonding processes during the single fiber pull-out test of the *SFRCs* (unit: %). 131

Table 4.2 Variation of energy ratios of *IMF* components decomposed from the *AE* signals from the fiber component multi-stage fracture under different fracture processes during the single fiber pull-out test of the *SFRCs* (unit: %)..... 132

Table 4.3 Weibull distribution statistical parameters for the occurrence of multi-stage debonding of the *SFRCs*. 134

Table 5.1 Material properties and geometric factors used in the model..... 152

Table 6.1 Material constants and geometric parameters for sisal fibers and their composites used in the *FE* model. 191

Table 7.1 Material constants and geometric parameters for sisal fibers and their composites used in the *FE* model. 229

CHAPTER 1

Introduction

1.1. Research background and motivations

The applications of composite materials have gained ground for aerospace, automotive and construction industries thanks to their high specific strength and modulus, excellent fatigue resistance and outstanding designability **[1, 2]**. High-performance composite materials usually refer to the composites using the continuous fiber as reinforcing material to obtain excellent mechanical properties **[1]**. Predominately, the usage of high-performance composite materials (i.e., carbon or glass fiber reinforced composites (*CFRCs* or *GFRCs*)) in aerospace structures increase rapidly. For instance, Boeing has adopted the composites airframe from 11 % in B777 airliner to 50 % in B787 Dreamliner while Airbus as the earlier composites adopter also has improved the composites content in A350 to 52 % **[3, 4]**. However, the production of these synthetic fibers consumes large amount of natural

resources and energy and these high-performance synthetic fiber reinforced composites (*AFRCs*) cause a lot of waste after their service period. Conclusively, the synthetic fibers have serious shortcomings including non-renewability, non-recyclability, difficult degradation, abrasion to equipment, health risk to workers when inhaled and excessive energy consumption and environment pollution arising from manufacturing process **[5]**. As a potential alternative of *AFRCs*, green composites as the next generation of sustainable composite materials have come into the global spotlight to address the public concerns of environmental pollution and climate change and rapid developing industry and expanding population. These disadvantages have been effectively exploited with the appearance of green composites.

Natural fibers as one representative green eco-material have attracted a lot of attention among scholars and engineers **[5-7]**. Compared with those traditional synthetic fibers, natural fibers are abundant in natural environment, lower in price, lighter in weight and lower in energy consumption for manufacturing. Besides, natural fibers possess excellent properties regarding heat isolation, sound insulation, shock absorption, noise reduction and biodegradability **[5]**. Natural fibers are traditionally used to make ropes, upholstery, fishing nets and fancy articles such as purses, wall hangings, table mats, etc. **[8]**. The annual growing usage of most natural fibers seems to be the good solution for the increasing energy and resources crisis so far. The degradability property makes natural fiber as an environment-friendly material, which has obvious significance for packaging industry and solving the white pollution caused by plastics. Natural fibers with better heat insulation, sound absorption and shock absorption compared to synthetic fibers are paving a new path to manufacturing industry (e.g., leisure chair

and tennis or badminton rackets). Therefore, new industrial applications of natural fibers as reinforcement in fiber reinforced composites have raised great concerns among scholars from various countries and entrepreneurs in recent years **[7]**. As shown in **Figure 1.1**, there is a rising trend in the market value of natural fiber reinforced composites (*NFRCs*) in the past fourteen years and will continue to increase in the near future. Meantime, researches on green composite materials are also increasing due to the needs of social development.

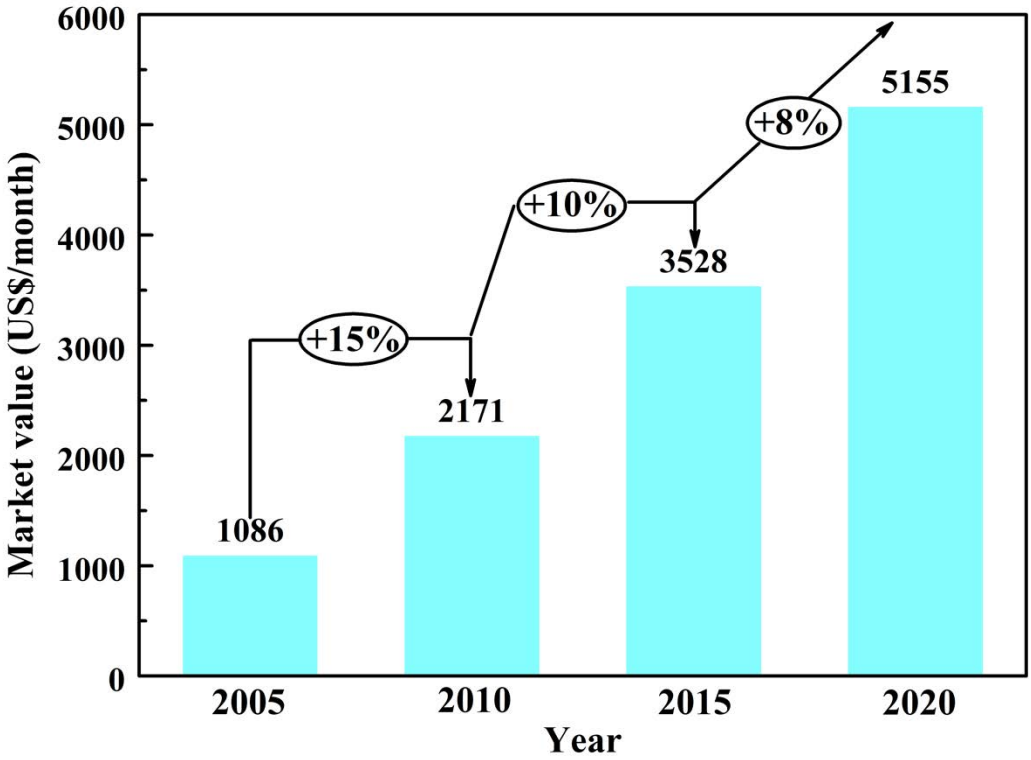

Figure 1.1 Trend and forecast in the market value of *NFRCs* from the year 2005 to 2020 **[9, 10]**.

To date, plant fibers, derived from natural resources, are the most widely used natural fibers and possess wide application prospects in civil and automotive industries due to their numerous advantages **[11-13]**. With the increasing energy and resources crisis

all over the world, using plant fibers as reinforcement to replace synthetic fibers in making fiber-reinforced composites in some applications has raised great interests and attentions in recent years. For example, non-disposable or difficult disposable *GFRCs* could be substituted by plant-fiber-reinforced composites (*PFRCs*) in some application fields including civil engineering, automotive or building interiors and transportation industry **[10]**. Eco-composite is a new term tailed to *PFRCs*, thanks to their economic advantages over *AFRCs*. Due to the increasing environmental consciousness and demands of legislative authorities, the manufacture, use and removal of traditional composites, which are usually made of glass, carbon or aramid fibers, are considered critically. The prices of plant fibers are much lower than those of synthetic fibers. For example, the price of sisal fibers is only a half of that of glass fibers and one-thousandth of that of carbon fibers **[14]**. Apart from the environment and economic concerns, interesting mechanical and physical properties, including the low density, excellent thermal insulation, sound absorption and shock absorption, are other reasons for using plant fibers as reinforcements in making fiber reinforced composites. To conclude that, *PFRCs* can be considered as an ideal choice for the design of composite structural products and become the promising alternatives to traditional *AFRCs* during the fabrication of products **[15]**.

However, two major obstacles of the characteristics have severely limited the applications of these eco-composites.

Composite materials are heterogeneous materials and generally composed of reinforcement (i.e. fiber), matrix (i.e. polymer) and interfacial phase. The interfaces

are not only the bridge for the load transfer between the fiber and matrix, but also a key factor affecting the physical and chemical properties of composites. Experience has demonstrated that the mechanical performance of composite materials is largely dependent on their interfacial properties, which indicates the decisive role of the interfaces in the design of composite structures **[16]**.

Study on the chemical compositions of plant fibers has already revealed that the major content of these fibers is cellulose **[17-21]**. Cellulose is a kind of hydrophilic glucan polymer consisting of a linear chain of 1, 4-β-bonded anhydroglucose unit (hydroxyl groups), which leads to the strong hydrophilic properties of plant fibers **[22, 23]**. In particular, when manufacturing composites with hydrophilic plant fibers and hydrophobic epoxy resin, weak interfacial bonding occurred between the fiber and resin, thus low mechanical properties of *PFRCs* are formed due to the poor impregnation of the polymeric resin to plant fibers and poor moisture absorption resistance of plant fibers. The relatively low mechanical properties hinder the large-scale industrial applications of *PFRCs*, the fields of automotive interiors, building interiors, transportation and other non-load-bearing pieces. Therefore, modifying fiber surfaces for improving the interfacial bonding properties between plant fibers and polymeric matrices of *PFRCs* have great significance to the promotion of mechanical properties of such composites and the purpose of extending the use of these fibers to structural applications in various fields. While, the current research only focuses on improving the interface between plant fibers and matrix, ignoring the analysis of multi-layer interfacial failure mechanism of plant fibers.

Meantime, it is widely accepted that the properties and failure mechanisms of composite materials not only depend on the macroscopic properties of their component materials, but also on the microstructure characteristics. Compared with traditional synthetic fibers (carbon and glass fibers), plant fibers possess distinct microstructural characteristics, such as rough surfaces, porous morphology, non-uniform diameters and multi-layer structure **[6, 24]**. The unique hierarchical structure of plant fibers definitely leads to different interfacial bonding and fracture behaviors, complex failure mechanisms and unique mechanical and physical properties for *PFRCs*. As a consequence, *PFRCs* possess a multi-scale structure with the minimum scale at nano size, which makes them different from *AFRCs* (e.g., *GFRCs* or *CFRCs*). Several researchers have performed impact and fatigue experiments on *PFRCs* and found that the presence of the multi-layer interfaces can effectively improve the abilities of energy absorption and dissipation of *PFRCs* compared to *AFRCs* **[25, 26]**. While, more attention is paid to the macroscopic failure behavior of PFRCs, but not comprehensively evaluate the interfacial properties of *PFRCs* from a multi-scale perspective. In order to further reveal the interfacial failure mechanisms of *PFRCs*, it is necessary to understand the influence of the multi-layer and multi-scale structure of *PFRCs* on their interfacial properties and failure modes by combining theoretical modelling with experimental characterization.

However, current studies are mainly focused on the experimental exploration with various modifications of plant fibers to investigate the interfacial adhesion of *PFRCs* **[27-29]**. As previous description, the interface plays a predominant role on the load transfer between the fiber and matrix. Good interfacial bonding is important for taking

advantages of the mechanical properties of both the reinforcing fibers and matrix **[30, 31]**. The interfacial and mechanical properties of *PFRCs* have been reported to be improved through surface modification. Currently, the surface treatment is only designed to modify the interface between the fiber and matrix but neglects the existence of the multi-layer and multi-scale structure of plant fibers, that is, not considering the interfaces existing within the plant fiber itself. However, through experimental observation, the interfacial failures of *PFRCs* feature phenomenal multi-layer and multi-scale modes **[32, 33]**. It is therefore worth analyzing and discussing the limitation of the reported modification methods arising from ignoring the hierarchical structure of plant fibers. Study on the multi-stage failure mechanisms of *PFRCs*, by considering the multi-layer and multi-scale structure of plant fibers, is expected to play a key role in improving the mechanical properties of *PFRCs* through the interface design which is of vital importance to obtain high-performance *PFRCs* by integrating the process of design and manufacturing.

To conclude, previous works regarding modification of *PFRCs* have been dedicated to improving the interface bonding between plant fibers and matrix and investigating the macro-failure behaviors of *PFRCs* but ignore the distinct hierarchical structure of plant fibers. In this study, the multi-layer structure of plant fibers, the differences of the mechanical performances among the multiple interfaces in *PFRCs* at the nanoscopic perspective and the multi-layer interfacial failure process are comprehensively quantified. On this basis, a quantitative evaluation of the effects of the multi-layer and multi-scale structure of plant fibers, which is distinct from that of synthetic fibers, on the interfacial properties and failure mechanisms of *PFRCs*, is

proposed in this thesis using meso-mechanical methods, featuring a multi-scale analysis with experimental, theoretical and numerical studies. The objectives of this thesis are to

- Measure the multi-interfacial mechanical performances of *PFRCs* and analyze the interfacial failure process;
- Develop a new multi-interface theoretical model for *PFRCs* by considering the distinct multi-layer characteristics of plant fibers;
- Identify the multi-layer and multi-scale failure modes of plant fibers and reveal the damage mechanisms of *PFRCs* by performing the experimental characterization and finite element (*FE*) simulation;
- Put forward suitable theory and experimental research methods for investigating the interfacial behaviors of *PFRCs* in order to provide the basis and guidance on the interface structural design of *PFRCs*, by considering the unique characteristics, and further obtain the high performances of *PFRCs*.

1.2. Scope of the thesis

In this *Ph.D.* thesis, the multi-scale structure and interface properties of *PFRCs* are studied. The differences of the interfacial mechanical properties among the multi-interfaces within *PFRCs* are identified by performing nanoscale experimental characterizations. To facilitate a better comprehending of the influence of the multi-layer and multi-scale structure of plant fibers on the mechanical performances of *PFRCs*, the multi-stage failure modes of *PFRCs* are illustrated by the single fiber pull-

out measurements in conjunction with in-situ acoustic emission (*AE*) technique and statistical analysis method. Subsequently, double-interface theoretical model for *PFRCs* is proposed by considering the distinct characteristics of the multi-layer interfaces within plant fibers. The relevant three-interface *FE* simulation is established to further illustrate the multi-stage fracture performances of *PFRCs* and estimate the stress variation of *PFRCs* during the pull-out process. Thus, the multi-layer and multi-scale damage mechanisms of *PFRCs* are revealed experimentally and theoretically. To obtain more accurate predictions on the macroscopic interfacial properties of *PFRCs*, on the basis of double cantilever beam (*DCB*, Mode I interlaminar fracture toughness (*ILFT*)) experiments, an *FE* model of the *DCB* specimen with multi-layer and multi-scale interfacial regions is constructed by inserting the cohesive zone model (*CZM*) into the crack front. Finally, the relationship between the microstructure of plant fibers and parameters of the *FE* model from the nanoscopic to the macroscopic scale is presented to provide new ideas and evidence for the structural design of *PFRCs* and further contribute to enhancing the mechanical properties of *PFRCs*.

There are 8 chapters in this thesis, which are organized in the order of experimental evaluation, theoretical interpretation and numerical simulation. The research progress in this thesis is listed as follows.

In Chapter 1, a general introduction is given on the objective of this research, including the background, motivation, major outcome or contribution and structure of this thesis.

A detailed literature review on the recent development for the evaluation of interfacial properties of *AFRCs* and *PFRCs* is presented in Chapter 2. The importance of fiber-matrix interface is described firstly. The chemical compositions, microstructure and mechanical properties of plant fibers different from those of synthetic fibers are introduced. Subsequently, researches on building the interfacial theoretical model of *PFRCs* and *AFRCs* are reviewed and discussed together with a review of the existing interfacial characterization techniques. The latest research progress in improving the interfacial mechanical properties of *PFRCs* by using fiber surface modifications is reviewed. The limitative effects of the reported improvement methods caused by ignoring the hierarchical structure of plant fibers are then discussed. Furthermore, the recent advances on the effects of the multi-layer and multi-scale structure of *PFRCs* on their interfacial performance and failure mechanisms are reviewed and analyzed, facilitating the understanding of the significance and the research objective of this dissertation.

The multi-interfacial mechanical performances of *PFRCs* from a nanoscopic point of view are the focus of Chapter 3. Elastic modulus and hardness of the epoxy matrix, the cell wall layers of sisal fibers (a typical plant fiber) and their interfaces are measured by applying the nanoindentation technique to quantitatively characterize the unique structural characteristics of plant fibers and evaluate the nanoscopic mechanical properties of sisal-fiber-reinforced composites (*SFRCs*). Single-step and multi-step nanoindentation methods are respectively employed on the multi-layer interfaces of *SFRCs* to present their distinct mechanical properties with regards to modulus and hardness, energy dissipation, crack initiation and propagation upon compressive loading. Specifically, the transition zones of the multi-layer interfaces

and the interfacial failure loads are determined, which consequently facilitates a quantitative analysis of fracture mechanisms for *SFRCs* with a multi-layer and multi-scale structure. The dynamic mechanical behaviors of the multiple interfaces within *SFRCs* are examined by the nanoscale dynamic mechanical analysis (*nano-DMA*) technique. The evaluation of nano-fatigue properties of the multiple interfaces within *SFRCs* is achieved by using the cyclic loading with varying applied indentation loads and frequencies. The fatigue behaviors and interfacial failure properties of each interface within *SFRCs* are studied by monitoring the changes of storage modulus.

In Chapter 4, the interfacial failure behaviors of *SFRCs* are firstly studied experimentally at the mesoscopic perspective. The single sisal fiber pull-out test is used to measure the interfacial shear strength (*IFSS*) of the different interfaces of *SFRCs*, whereby distinct failure behaviors of the distinct interfaces are observed. To further identify the occurrence of multi-interface failure behavior, in-situ *AE* technique is applied during the single sisal fiber pull-out experiment. The probability of technical fiber failure, elementary fiber failure and micro-fibrils pull-out is evaluated through the statistical analysis. The relevant embedded fiber lengths leading to the multi-stage debond and pull-out behaviors for the single *SFRCs* are indicated with the aid of the *Weibull* statistical method.

To further illustrate the phenomenon of single *SFRCs* during the pull-out process in Chapter 4, a double-interface theoretical model using the traditional shear lag model and a triple-interface *FE* model utilizing the *CZM*, tailored to the unique multi-layer interface structure of plant fibers, are respectively proposed and developed in

Chapters 5 and 6, by simultaneously considering the important role of interfacial asperity on the fiber pull-out behavior. The fiber pull-out behavior and the interfacial adhesion status of single *SFRCs* are described to interpret the multi-stage fracture phenomenon of *SFRCs*. The hierarchical structure characteristics of plant fibers are fully considered, from the views of structural design and manufacturing of composites, to achieve a more accurate quantitative theoretical prediction of the multiple interfacial failure behaviors and damage modes of single *SFRCs*. The validity and accuracy of the double- and triple-interface model proposed in these two chapters are then both examined through a quantitative comparison with an existing single-interface model, by using the experimental applied stress as reference.

Chapter 7 introduces a numerical model for *PFRCs* subject to the *DCB* experiment through considering their multi-layer structure to investigate the effects of the hierarchical structure on the macroscopic mechanical and interfacial properties (i.e. *ILFT*) and failure behaviors of laminated *PFRCs*. Relying on the micro-mechanics of composite materials, the *CZM*, developed in Chapter 6, is inserted into the crack front of the *FE* model. The geometric model with the multi-layer and multi-scale interfacial regions is developed to describe the multiple interface fracture behaviors of the laminated *PFRCs*. The relationship between the microstructure characteristic, interfacial properties and mechanical properties is built based on the design principle of composite structures, for enhancing the practical applications of laminated *PFRCs* in large-scale industrial fields.

Finally, Chapter 8 serves as the general discussions and the conclusions of the thesis. Proposals, recommendations and suggestions on the future research are also put forward, relying on the fundamental research findings obtained in this thesis, for achieving the large-scale real applications of *PFRCs* in the engineering fields (i.e., aviation, railway transportation, automotive engineering, civil infrastructures, etc.).

CHAPTER 2

State of the Art of Evaluation of Interfacial Properties: *From AFRCs to PFRCs*

2.1. Introduction

Composite materials are widely used materials and have showed their competitive advantages in the national economy and national defense construction. Fiber, matrix and interface are the three major components of a composite. Due to the presence of the interface, the composites possess many unique properties compared with isotropic materials. Once the fiber and the matrix of a composite are chosen, the characteristics of the interface region and further the final properties of the composite are determined. Consequently, perhaps the fiber-matrix interface is the most critical yet least understood component of the composite material, which is even treated as the heart of the composite.

The important role that the fiber-matrix interface plays has been recognized in the mid-1960s in the case that advanced composites started to be used as structural materials **[34]**. Since then, the subject of interface has become a vital research interest on composite materials. Previous researches indicated that the interfacial layer is a transition zone of two phases with a certain thickness, which exists the chemical bonding effect. Earlier studies also have reported that macromolecular chains proliferation, morphology of the interfacial phase, physical and chemical compositions and intermolecular forces have a significant impact on the mechanical performance of the interface region **[35, 36]**.

Generally speaking, the fiber-matrix interface is the weakest part of the composite material and this is mainly due to the poor interaction at the interface. Thus, interface failure is a common failure mode observed in the fiber reinforced composites, which potentially results in catastrophic failure of the composites. This issue has drawn a great deal of attentions from researchers to develop effective and accurate experimental characterization techniques for evaluating the interfacial properties of composites. Many sophisticated techniques are currently available to characterize the interface region. Theoretical modelling and numerical simulation are the other two main tools to provide guidance on the structural design of the interface of a composite. To better understand and predict the interfacial mechanical behaviors of the composites, many factors that govern the characteristics of composites involving fibrous materials need to be clearly illustrated in advance and the effects of these factors on the final interfacial properties of the composites also need to be demonstrated.

In this regard, this chapter will firstly comparably analyze the structural characteristics (i.e. chemical composition and microstructure) of plant fibers and synthetic fibers. Then the assessment methods on the interfacial properties of *PFRCs* and *AFRCs*, including experimental characterization, theoretical modelling and numerical simulation are reviewed. Finally, interfacial modification and interfacial failure mechanisms of *PFRCs* and *AFRCs* are comparably discussed at the final part of this chapter.

2.2. Comparisons of structural characteristics between plant fibers and synthetic fibers

Plant fibers, as environment-friendly materials, have been thrust into the global spotlight with the concerns of energy crisis and environmental pollution and billion tons of plant fibers are produced every year throughout the world. Plant fibers also possess such advantages as short in renewal time, abundance in source, cheapness in price, low in energy consumption. Besides, they are natural materials with excellent thermal insulation, sound absorption and shock absorption. Plant fibers have become promising alternatives to traditional synthetic fibers in making fiber-reinforced composites, owing to their interesting mechanical and physical properties.

The processing methods to extract plant fibers, include retting followed by scrapping and decorticators **[8, 37]**. It has been reported that the mechanical process yields about 2-4 % fiber with good quality while the retting process yields a large quantity of poor

quality fibers. After extraction, the fibers are washed thoroughly in plenty of clean water to remove the surplus wastes, such as chlorophyll, leaf juices and adhesive solids **[38]**. In macro-scale, plant fibers are extracted from the stems or leaves of plants, which can be divided into six categories based on different extracted positions, namely seed fibers (i.e. cotton and coir fiber), bast fibers (i.e. ramie, hemp, kenaf, jute and flax), leaf fibers (i.e. sisal and pineapple fiber), wood fibers (i.e. soft and hard wood), straw fiber (i.e. corn, rice and wheat) and grass fiber (i.e. bagasse and bamboo). To better understand and predict the interfacial mechanical behaviors of *PFRCs*, differences on the structural characteristics (i.e. chemical composition and microstructure) between plant fibers and synthetic fibers arising from different sources are comparably introduced in what follows.

2.2.1. Chemical compositions

Carbon fibers are made from the graphite, one of allotropic forms of carbon, while glass fibers are consisting of SiO_2 and a host of other metallic oxides. Compared with traditional synthetic fibers, the distinct chemical compositions of plant fibers have been reported by several groups of researchers. Plant fibers are mainly composed of cellulose, lignin, hemicellulose, pectins, waxes and other mineral components **[21]**. However, large variations in chemical compositions of plant fibers are caused by their different sources, age and measurement methods, etc. The chemical compositions of various plant fibers are plotted in **Table 2.1**, which all show that the main composition of plant fibers is cellulose **[17-21]**. Cellulose is one kind of polysaccharides, a hydrophilic glucan polymer, composed of D-anhydroglucose with the repeating units of 1, 4-β-glycosidic bonds (**Figure 2.1**), and the degree of polymerization is around

10,000 **[22, 23]**. Each repeating unit contains three hydroxyl groups, which lead to a strong hydrophilic property, weak water absorption resistance properties and poor interfacial performance between plant fibers and the hydrophobic matrix in *PFRCs*, due to the poor impregnation of the polymeric resin to plant fibers **[39]**. Hemicellulose, which constitutes the second large carbohydrates of plant cell wall, is a group of polysaccharides consisting of a combination of 5- and 6- carbon sugars and the amount is relatively lower than cellulose in the plant fibers. Lignin has a more complex three-dimensional structure polymerized by the disorder phenylpropane monomeric units that substituted by hydroxyl and methoxyl groups **[23]**. Plant fibers, e.g., sisal fibers, are actually a bundle of hollow sub-fibers. Their cell walls are reinforced with spirally oriented cellulose in a hemi-cellulose and lignin matrix. Therefore, the cell walls possess a composite structure of lignocellulosic material reinforced by helical microfibrillar bands of cellulose. The composition of the external surface of each cell wall is a layer of ligneous material and waxy substances, which bonds the cell to its adjacent neighbours.

Table 2.1 Comparisons of the chemical composition in plant fibers **[17-21]**.

Fiber	Cellulose / %	Hemi-cellulose / %	Lignin / %	Pectin / %	Wax / %
Coir	36.0-43.0	0.15-0.25	41.0-45.0	3.0-4.0	/
Ramie	68.6-76.2	13.1-16.7	0.6-0.7	1.9	0.3
Hemp	70.2-74.4	17.9-22.4	3.7-5.7	0.9	0.8
Kenaf	31.0-39.0	15.0-19.0	21.5	/	/
Jute	61.0-71.5	13.6-20.4	12.0-13.0	0.4	0.5
Flax	71.0	18.6-20.6	2.2	2.3	1.7
Sisal	64.0-73.0	10.0-14.2	6.0-10.0	8.0	2.0
Bamboo	77.6	4.0-8.0	13.1	/	/

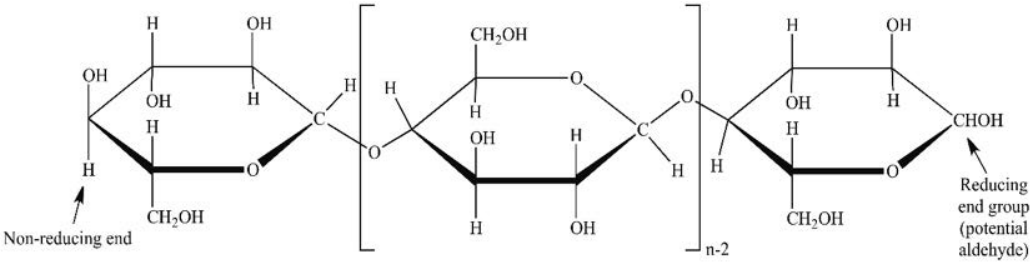

Figure 2.1 Chemical structure of cellulose **[23]**.

2.2.2. Microstructure

The microstructure of a material dictates its macroscopic properties. The microstructures of plant fibers are different from those of synthetic fibers because of their naturally growing characteristics. Accordingly, the mechanical properties and fracture mechanisms of plant fibers are different from those of synthetic fibers, such as carbon and glass fibers. Therefore, to provide a sound basis for practical applications of plant fibers, it is necessary to have an in-depth understanding of the relationships between the microstructure of plant fibers and the mechanical properties.

The length of plant fibers varies from between 1.0 to 1.5 m and its diameter is in the range between 100 and 300 μm **[40]**. Plant fibers possess the rough surface (**Figure 2.2** (a)), non-uniform diameter and porous structure (**Figure 2.2** (c)), while the cross-section of the synthetic fibers are regular and usually solid round (**Figure 2.2** (d)) **[41]**. In addition, the length of plant fibers is limited due to their naturally growing characteristics and twisting is normally applied to fabricate the continuous natural fiber yarns, whereas the synthetic fibers are usually untwisted continuous filaments (**Figure 2.2** (b)) **[42]**. It should be noted that the twisting might lead to the poor impregnation of the resin inside the yarns of plant fibers.

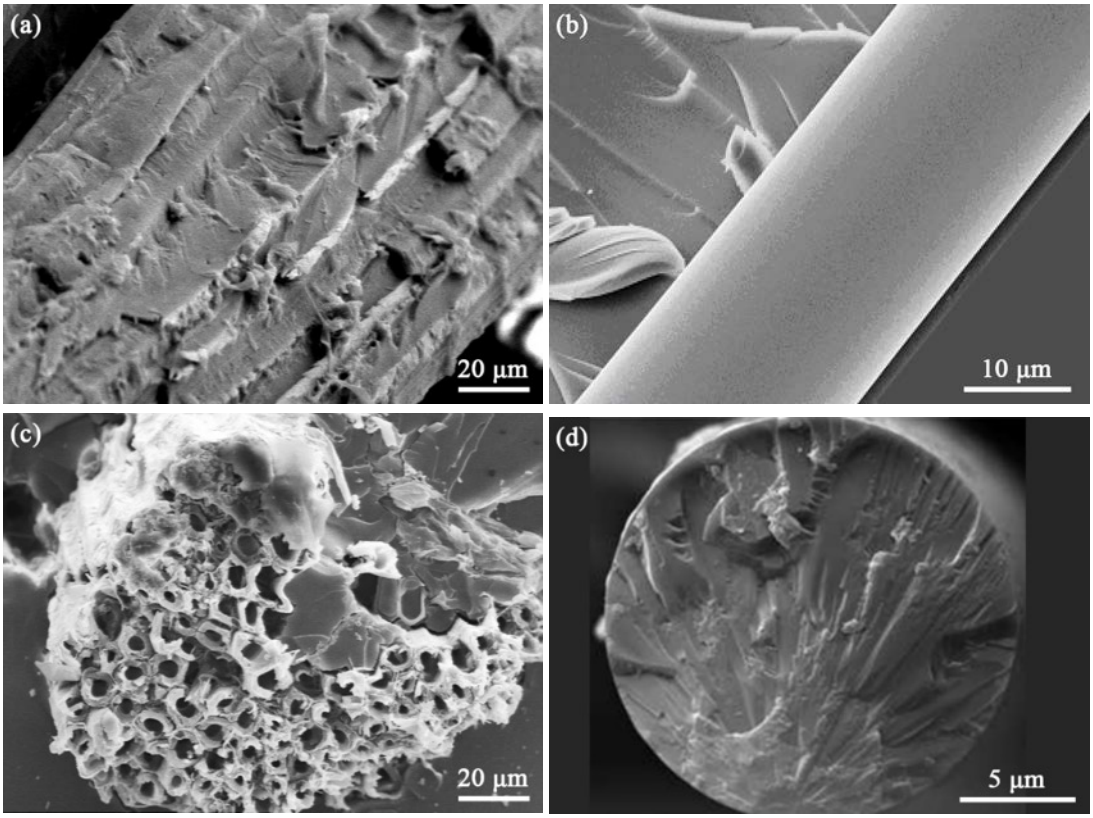

Figure 2.2 Comparisons of the surface structure of (a) sisal fiber and (b) carbon fiber and the cross section of (c) sisal fiber and (d) glass fiber **[43, 44]**.

Previous researches have demonstrated plant fibers possess the distinct multi-layer, multi-scale and porous structure relative to synthetic fibers **[24, 32, 45, 46]** . Stamboulis et al. **[47]** pointed out that the plant fiber itself is a kind of composites consisting of a primary cell wall and three secondary cell walls. Consequently, plant fibers could be depicted as a composite structure from the macroscopic scale to nanoscopic scale. As shown in **Figure 2.3**, single plant fiber, called technical fiber, is usually constitutive of 30-100 elementary fibers glued together by pectin (CML, Compound Middle Lamellae). Each elementary fiber contains two types of cell walls, named as the outer primary (P) and the inner secondary. P layer is formed by protoplasts secretion during the growth process of the cell, which is made up of pectins.

The inner secondary cell wall can be considered as a series of helically cellular micro-fibrils reinforced lignin and hemicellulose composite, which is separated as S1, S2 and S3 layers owing to their various thickness and structure. To note that the thickest middle layer S2 determines the mechanical properties of plant fibers. The microfibrillar angle is defined as the angle between the fiber axis and the micro-fibrils. A hole located in the central of the elementary fiber is called lumen. Therefore, the hierarchical organization leads to multi-interphase regions of the plant fiber with different morphological characterizations.

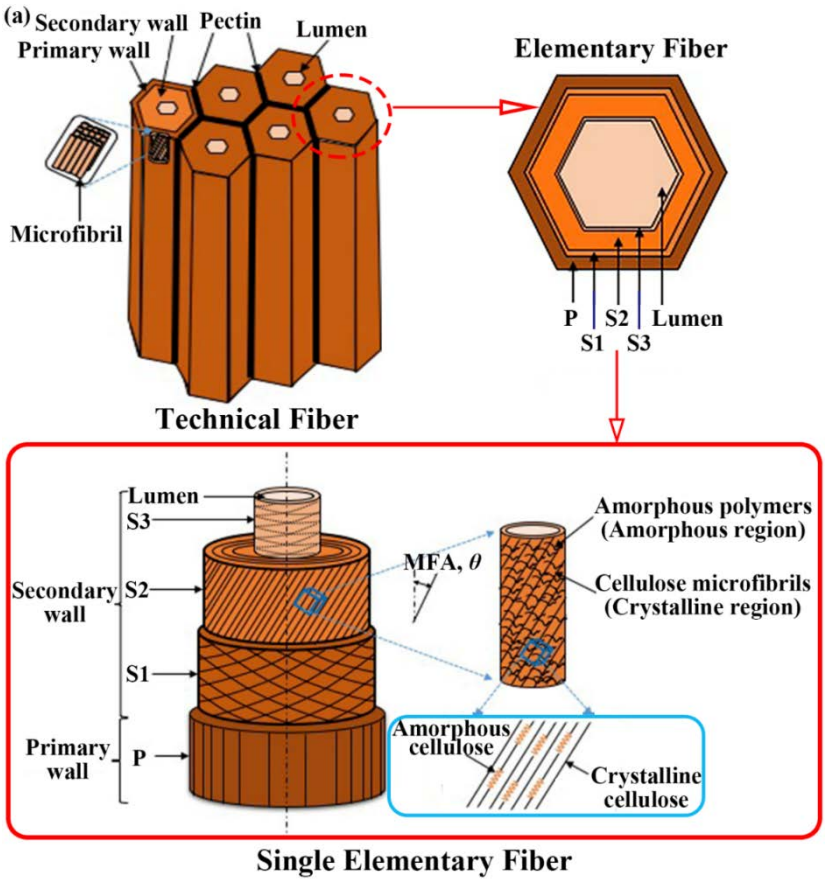

Figure 2.3 (a) Diagram for structure of a single plant fiber, (b) multi-scale structure of sisal fiber **[48]** and (c) multi-layer cell structure of flax fiber.

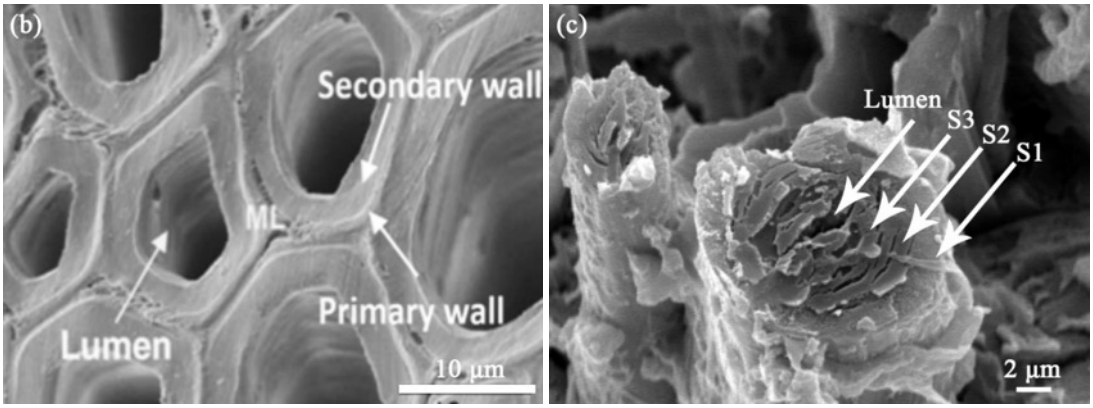

Figure 2.3 (continued).

Generally, the strength and stiffness of plant fibers depend on the cellulose content and the spiral angle, which refers to the angle between the bands of micro-fibrils in the inner secondary cell wall and the fiber axis. Thus, the mechanical properties of plant fibers largely depend on the extracted positions **[49, 50]**, chemical composition **[51]**, microstructure **[45]**, lumen size **[32]**, and so on. **Table 2.2** presents the different mechanical properties of various plant fibers as reported by different researchers **[5, 52]**. The obvious dispersion exists not only for different plant fibers but also for the same kind of plant fibers. Gassan et al. **[20]** investigated that the effects of chemical composition and microstructure on the mechanical performance of plant fibers by building a microstructure model. The mechanical properties of plant fibers were found to improve with the increase of the content of cellulose.

Table 2.2 Comparisons on the mechanical properties between plant fibers and glass fibers **[5, 52]**.

Properties	Fibers					
	Ramie	Hemp	Jute	Flax	Sisal	Glass
Density/ $g \cdot cm^{-3}$	1.50	1.48	1.3-1.45	1.20	1.33-1.45	2.5
Tensile strength / *MPa*	400-938	270-900	270-800	800-2000	511-700	2000-3500
Young's modulus / *GPa*	44-128	20-70	10-30	60-80	3-98	73
Specific strength/ $MPa \cdot g^{-1} \cdot cm^{-3}$	267-626	183-610	208-550	667-1667	352-526	800-1400
Specific modulus/ $GPa \cdot g^{-1} \cdot cm^{-3}$	30-86	14-48	8-21	50-67	2-74	30
Elongation at break / %	3.6-3.8	1.6	1.5-1.8	1.4-1.5	2.0-2.5	2.5

Sisal fibers and flax fibers had been considered as the excellent reinforcement material over other plant fibers. With lower density and higher mechanical strength owing to the higher cellulose content, these two materials have specific properties closed to those of E-glass fibers, which make them a prospective reinforcing material (**Table 2.2**) for real application. With the growing energy and resource crisis in the worldwide and the growing awareness of environmental protection, the biodegradable plant fibers are expected to replace synthetic fibers and become an ideal environment-friendly and sustainable material to achieve the current urgent task.

2.3. Comparisons of interfacial evaluation between *PFRCs* and *AFRCs*

The interface of the composites is the main factor affecting the mechanical behaviors of the final products. Accurate analysis of the interfacial performance is important but difficult to achieve for the research on the interface in the composites. A great number

of assessment methods, including experimental characterization technique, theoretical model and numerical simulation, have been proposed to determine the interfacial performances of the traditional composites, typified by *CFRCs* and *GFRCs*. Meantime, different interfacial assessment techniques from macro-scale to nano-scale for *AFRCs* have been employed to investigate the interfacial behaviors of *PFRCs*. Previous investigations on *PFRCs* also have been fully reviewed, which provided an impetus for this research.

2.3.1. Experimental characterization of the interfacial mechanical properties

Various experimental characterization techniques have been introduced to evaluate the interfacial strength of *PFRCs* and *AFRCs* from the macroscopic to nanoscopic point of view.

Generally, in the macro-scale, an important failure mode in the composite laminates is the interlaminar failure or delamination. Interlaminar shear strength (*ILSS*) and *ILFT* are two main interfacial parameters adopted to evaluate the interfacial bonding properties of composite materials in the macro-scale. In detail, *ILSS* can be characterized by the macroscopic mechanical methods, including short beam shear test, compression shear test and transverse or 45° off-axis tensile test **[53-55]**. *ILFT* is another mechanical property, which is synergistically determined by the properties of the fiber, matrix and interfaces. *DCB* test and End Notched Flexure (*ENF*) test can be used to obtain the Mode I and Mode II *ILFT* of the composite materials, respectively. Sela et al. **[56]** provided a review in the subject of *ILFT* of polymeric composite materials, discussing the relation between the structural performance and the damage

tolerance. Comprehensive *ILFT* data was found to be necessary for evaluating the interlaminar properties for different composite systems. Sham et al. **[57]** successfully employed the above-mentioned interlaminar measurement techniques to characterize the interlaminar fracture properties of glass fabric reinforced composites, including the *ILSS* and Mode I and Mode II *ILFT*. Meanwhile, Zhang et al. **[52]** found that the *ILSS* and *ILFT* of unidirectional flax and glass fiber reinforced phenolic polymeric matrix hybrid composites were even higher than those of *GFRCs* due to the excellent performance of the hybrid interface. Wong et al. **[58]** added hyperbranched polymers into flax fiber reinforced *PLA* composites and found the *ILFT* was significantly influenced due to better wetting of the fibers by the matrix. Li et al. **[59]** assessed the effects of carbon nanotubes (*CNTs*) coating on the interfacial properties of *FFRCs* by performing *DCB* and short beam shear tests. The results showed the maximum enhancements for *ILSS* and Mode I *ILFT* were 20 and 31 $\%$, respectively, by introducing 1 $wt.\%$ of multi-walled *CNTs* onto the surfaces of flax fibers. Ravandi et al. **[60]** experimentally studied and revealed that stitching with flax yarn can improve the Mode I *ILFT* of flax fiber reinforced epoxy composite laminates by at least 10 $\%$ at the lowest stitch fiber areal fraction.

In recent years, researchers in the international composites fields have been paying more attention to the effect of the meso- and micro-structure of composites on their macroscopic properties. It is widely accepted that the effective way for solving the interfacial problems of composite materials should employ both the microscopic measurement and characterization techniques along with the meso-mechanical analysis to study the damage mechanisms and failure modes of composite materials.

The *IFSS* is one of the most important parameters to characterize the composite interfacial properties in the meso- and micro-scale. Various micromechanical techniques have been developed to characterize and evaluate the interfacial behaviors of *PFRCs* and *AFRCs* in researchers' previous efforts, including single fiber pull-out **[61]**, push-out **[62]**, fragment testing **[63]** and micro-droplet testing **[64]**. Herrera-Franco et al. **[65]** compared the performance of different experimental micro-mechanic characterization methods with regards to evaluate the *IFSS* and concluded that single fiber pull-out test was the most popular method used for years to determine the interfacial debond stresses. Single fiber pull-out test was firstly proposed by Broutman in the 1960s **[66, 67]**, which can provide the accurate information about the interface parameters, including critical fiber length, fiber pull energy, interfacial friction coefficient, interfacial adhesion and interfacial failure energy. Single fiber pull-out test can also be adopted to evaluate the effects of different surface treatment methods on the mechanical properties of the composites. The measurement of interfacial bonding condition can quantitatively reflect the surface modification effect. George et al. **[68]** summarized the interfacial characterization methods and concluded the failure mechanisms of *PFRCs* in meso-scale. The enhancement of the interfacial adhesion was found to provide an effective stress transfer between fiber and matrix. During the single fiber pull-out test, if the fiber was pulled-out from the matrix, shear failure modes at the interface occur in the composite material, that is, the interface would occur debonding and fail, otherwise when the *IFSS* was greater than the strength of matrix or fiber, that is, the fiber length embedded into the matrix was larger than the critical length, the matrix or fiber would fail, then there was no interfacial

failure in the composites before the break of the fiber. Khalil **[69]**, Joseph **[70]** and Joffe **[71]** respectively carried out the single fiber pull-out tests to investigate the interfacial performances of various *PFRCs* with different treatments. The results showed that, since the hydrophobic characteristics in matrix were improved by the treatment, the ability of adhesion and interlocked between the fiber and matrix enhanced, which made the *IFSS* increased. From this perspective, the main advantages of pull-out tests are that without considering composite processing variables, *PFRCs* with good performance may be selected before their laborious and material-consuming preparation step.

The calculations of the *IFSS* for *PFRCs* in the single fiber pull-out test are different from those of *AFRCs*. The formula for *AFRCs* can be expressed as

$$\tau = F/(\pi dl) \quad \textbf{(2.1)}$$

where F is the maximum load before fiber debonding, d represents the diameter of the fiber, l denotes the embedded length of the fiber. However, compared with synthetic fibers, the non-circular cross-section and diameter of plant fibers have a large variation along the length direction. To address this issue, Karlsson et al. **[72]**, Valadez-Gonzalez et al. **[73]** and Li et al. **[74]** reported the circumference with lower dispersibility is more suitable for the calculation of *IFSS* instead of the diameter of plant fibers due to the large dispersion in the areas and diameters. The revised formula for the *IFSS* in the single plant fiber pull-out test can be written as follows

$$\tau = F/(Cl) \quad \textbf{(2.2)}$$

Here C is the circumference of the fiber.

The mechanical performance of composite materials strongly depends on the interphase properties and the stress transform at the interface. Without loss of generally, the interphase of fiber reinforced polymer composites is a narrow region, which is difficult to quantitatively characterize due to the nature of nanometer dimension. In general, the width of the interphase between the polymer matrix and the fiber is expected to range from a few micrometers to several hundred nanometers. Therefore, it is of necessity to develop a reliable method to characterize the interfacial properties of the fiber reinforced composites at the nanoscopic level.

Amongst the nanoscopic evaluation methods regarding material interfacial properties, nanoindentation measurement is a suitable, effective and promising technique to characterize the interphase zone and quantitatively evaluate the interfacial mechanical properties for the fiber-reinforced polymer composites **[75-81]**, especially for *PFRCs* with multi-layer and multi-scale interfaces **[82-84]**. Although instrumented nanoindentation testing had been used to characterize the mechanical properties of materials since the 1970s **[77]**, the vast application of the nanoindentation on the polymer composite materials and their constituents occurred until the 1990s **[78]**. Several researchers have attempted to measure the interphase properties in *CFRCs* or *GFRCs* using nanoindentation method **[79-81]**. As representative results, Urena et al. **[79]** employed the nanoindentation method to analyze the interfacial mechanical properties of short *CFRCs* coated with metallic films. They found that the nanoindentation technique can achieve a complete characterization of the interfaces in the composites, which made it possible to measure the interfacial fracture and

friction strengths in the nano-scale. Similarly, Gao et al. **[80]** and Kim et al. **[81]** investigated the interphase nano-scale property in *GFRCs* and the results revealed effective interphase thickness in such composites was less than 1 μm. These pioneering works presented the availability of the nanoindentation technique on characterizing interfacial morphology (thickness of interface zone) and determining interfacial mechanical properties (elastic modulus and hardness) for the composites in the nano-scale. In 1997, nanoindentation was used to study the mechanical properties of cell walls in the wood materials for the first time **[82]**. Subsequently, Bourmaud et al. **[83]** performed nanoindentation tests on flax fibers to study the effect of fiber maturity on their mechanical properties, including Young's modulus and hardness. Li et al. **[85]** studied the physical properties (including fiber size, micro fibril angle and relative degree of crystallinity) and mechanical properties (hardness and elastic modulus) of hemp stalk fibers in the xylem part and hemp fiber cell wall along the height of the stem by using nanoindentation measurements. However, limited studies have been carried out regarding evaluating the interfacial properties of *PFRCs*. Lee et al. **[84]** evaluated the interphase mechanical properties of cellulose fiber reinforced polypropylene composites by applying a continuous stiffness technique in nanoindentation tests. The results revealed interphase property transition between the fiber and matrix and concluded that indent area played a critical role in accurately determining the mechanical properties of the interphase region.

The *nano-DMA* technique has been developed as a dynamic indentation test to improve the current capabilities of nanoindentation method **[86-88]**. Sinusoidal loading, that is treated as quasi-static loading, is repeatedly applied for the *nano-DMA*

test **[86]**. During the test, the indenter of the setup is derived to interact with the sample, and the displacement of the indenter column is continuously recorded. The displacement response is measured at the same frequency as that of the applied oscillating force whereby local properties of the specimen can be obtained. Data from such measurements allows the calculation of material properties such as the storage and loss modulus **[87, 88]**. Previous researches have demonstrated that the storage modulus (also called the dynamic stiffness) is related to the energy stored by the sample during a cycle of loading **[89]**. Any resulting phase lag between the force applied and the displacement is determined by the loss modulus or damping. Overall, the storage and loss moduli decide the stored energy in the elastic portion and the energy dissipated in the form of heat in the viscous portion for viscoelastic solids, respectively.

Nano-DMA technique is an effective method newly developed for the study of the viscoelastic properties of various polymers. Zhang et al. **[90]** and Li et al. **[91]** employed *nano-DMA* to investigate the effects of frequency, particle volume fraction and load amplitudes on the storage and loss moduli of nano-silica-filled and single-walled *CNTs* reinforced epoxy nanocomposites, respectively. Sikdar et al. **[92]** applied both static and dynamic nanoindentation on the clay/polycaprolactam nanocomposites and concluded that addition of organic modifiers in polycaprolactam increased the storage modulus, loss modulus and loss factor of intercalated clay/polycaprolactam nanocomposites in comparison with the pure polymer. Study onto the fiber-matrix interfacial adhesion using the *nano-DMA* technique has been reported in the literature. Gu et al. **[93]** presented a nanomechanical imaging technique for mapping the

dynamic mechanical property around the interphase region in *CFRCs*, and for providing nanoscale information of the interfacial dimension. The experimental results showed that the width and topography of the interphase with a nanoscale resolution can be determined by the storage modulus of the cross section of the composite. The average interphase thicknesses of a T300 carbon fiber/epoxy resin composite and a T700 carbon fiber/bismaleimide resin composite were ascertained as 118 and 163 *nm* , respectively. Furthermore, they further demonstrated that hygroscopic treatment increased the interphase width and caused interface debonding due to a degradation in the interphase region. Meantime, Hayot et al. **[89]** used a dynamic nanoindentation technique to achieve quantifiable measurements of the time-dependent response and the viscoelastic behaviors of cell walls in a single plant fiber at the nano-scale.

Though the results are promising, the above-mentioned studies are mainly focused on the basic mechanical or interfacial properties between the fiber and matrix of the composites, while for *PFRCs*, ignoring the distinct hierarchical structure (i.e., multi-layer and multi-scale) of plant fibers. Thus, relevant research endeavors in extending such a technique to the quantitative evaluation of hierarchical interfacial properties and interfacial failure of *PFRCs* with a multi-layer and multi-scale structure are worthy of further investigation and validation.

Fatigue, also called delayed fracture, implies failure of a material or a structure in a finite time when it is subject to any sustained externally applied cyclic stress. Nanoscale fatigue has rarely been studied in the past due to the limitation of

instruments. *Nano-DMA* technique, capable of providing force cycles of a sinusoidal shape at high frequencies, can be used to measure the fatigue performance of specimen in the nano-scale. The fatigue behaviors of thin films and micro-beams have been studied by monitoring the change in contact stiffness which is sensitive to damage formation **[94]**. Li et al. **[94]** studied the fatigue properties of ultrathin amorphous carbon coatings using the *nano-DMA* technique. The results provided the contact stiffness as a function of the cyclic number for a 20-nm-thick amorphous carbon coating on a silicon substrate, cyclically deformed by an oscillation load with a magnitude of 8 mN and a mean load of 10 mN at a frequency of 45 Hz. The occurrence of fatigue damage was indicated by the abrupt decrease in the contact stiffness at a certain cycle. The nano-fatigue data of the interfaces are of critical importance to the interfacial structural design of the composites.

AE is another promising method to evaluate the interfacial failure behaviors of composites. *AE* describes a rapid release of strain energy (manifested as transient elastic waves) caused by initiation and propagation of a crack. *AE* has been proved its capability of real-time monitoring over the whole material volume and high sensitivity to any process generating sudden stress waves. Notably, characteristics of *AE* signals can be used to 'listen' to the structure and interpret the details of physical processes (e.g., initiation and propagation of cracks) occurring in the monitored structure, but not need to interact with it. To achieve the evaluation of a monitored structure using *AE* signal characteristics, generation mechanisms of *AE* signals and their relationship with the occurrence and severity of structural damage must be firstly understood. The onset and growth of cracks in the material under an external force is a complicated

process. Cracks are initiated and propagated due to shearing force and followed by material damage or fracture, during which *AE* generates with distinct signal characteristics. A great amount of studies has been reported to reveal the crack propagation mechanisms of the macroscopic composite laminates and achieve identification of their relevant failure modes by employing the *AE* method, including matrix cracking, fiber-matrix interfacial debonding, fiber pull-out and breakage. Bourchak et al. **[95]** adopted the *AE* method to monitor the state of *CFRCs* subject to static and fatigue loadings. The good correlation between *AE* energy and structural damage exhibited the efficiency of *AE* technique in identifying cracks. Meantime, it is worthy to note that some studies have successfully demonstrated the possibility of determining the failure modes of green composites using the *AE* technique. Li et al. **[32]** applied *AE* method to characterize the crack propagation mechanisms of the *SFRCs* with resin penetration into fiber lumens. When tensile loading is applied to the *SFRCs*, the matrix cracking firstly occurs with lower *AE* energy, subsequently interfacial debonding between the fiber and matrix, and finally fibers breaking in greater *AE* energy. Results from these studies together demonstrate that it is feasible and efficient to surveil the failure modes and fracture behaviour of *PFRCs* (e.g., matrix cracking, fiber-matrix debonding, fiber pull-out and breakage) according to the *AE* amplitude and energy.

AE is reportedly sensitive to microscopic events presenting in a material **[96]**. Recently, *AE* technique is well known as one of the important nondestructive testing methods for micromechanical test. *AE* can not only be adopted to monitor the fracture behaviors of composite materials, but also to characterize *AE* parameters to identify

the micro-failure sources during the fracture progressing. *AE* method has been widely used to monitor the health conditions of traditional polymer composites, i.e., reinforced with carbon, glass or aramid fibers. For instance, Ageorges et al. **[97, 98]** investigated the debonding process and stress distributions for the carbon fiber-epoxy matrix interface during the single-fiber fragmentation test by using a transverse tensile load with the aid of *AE*. Park et al. **[99-101]** evaluated the interfacial properties and micro-failure modes of *CFRCs* and *GFRCs* in both tensile and compressive fragmentation tests through the analysis of characteristics of *AE* signals. Three distinct *AE* signals were received from fiber break, matrix cracking and interlayer failure in the micro-composite specimens. Narisawa et al. **[102]** carried out an analysis of *AE* on a single aramid fiber reinforced epoxy matrix composite to identify the source of *AE*. The *AE* activity was observed in a narrow range of strain when fiber fracture occurred, whereas in a relatively wide range of strain, debonding occurred at the fiber-matrix interface. The total number of *AE* events had one to one correspondence with the number of broken fibers. They all indicated that *AE* could provide more likely the quantitative information on the interfacial adhesion and micro-failure.

Although an examination of the literature with regards to the application of *AE* to monitor the micromechanical tests of *PFRCs* allows a sounder knowledge of the micro-failure modes, the results are still only focused on the adhesion between the plant fiber and matrix. Park et al. **[103, 104]** evaluated the micro-failure mechanisms of various single plant (ramie, kenaf, jute and hemp) fiber reinforced composites using the combination of micro-droplet test and *AE* technique. The debonding and slipping between plant fibers and matrix were indicated by *AE* signals with different amplitude,

energy and duration. The clarification of micro-failure mechanism of single fiber composites is a very important step towards the understanding of the fracture behaviors of laminated composite. Analysis of *AE* signals is useful for identifying the failure modes of the composites, even though not in a quantitative way. Therefore, along the same line of thinking, *AE* technique can be extended to identify the possible multiple micro-failure behaviors of *PFRCs* caused by the hierarchical structure of plant fibers and to further elucidate the effects of multi-layer and multi-scale structure of *PFRCs* on their interfacial behaviors.

2.3.2. Theoretical analysis of the interfacial mechanical behaviors-- Shear lag model

In the early 1950s, Cox **[105]** proposed the interfacial shear lag model with assumptions that the fibers and matrix were cylindrical and complete isotropic elastic and the interface was perfect bonding. This model was simple, convenient and practical, which could provide the axial stress and shear stress. However, there was no consideration on the effects of material properties on the interfacial load transfer. Based on the Cox's one-dimensional shear lag theory, Fukuda et al. **[106]** and Christoffersen et al. **[107]** introduced the concept of the length of load transfer and the critical aspect ratio and developed a series of new analysis model to provide more realistic predication of interfacial stress transfer. Dinter et al. **[108]** analyzed the stress distribution of complete interfacial debonding and interfacial slipping in SiC composites on the basis of the shear lag theory. Ananth et al. **[109]** and Honda et al. **[110]** applied different shear strength criterions to analyze the process of interfacial debonding for various composites relying on the Cox shear lag model. All the above

studies showed that the Cox shear lag model could preliminarily describe the interfacial debonding process of composite materials and the stress variation in the process, and the theoretical and experimental results were consistent.

As described in section 2.3.1, the single fiber pull-out test was widely used to evaluate the interfacial debonding process of composites in the 1990s. Then, based on the existed shear lag model, researches on the understanding of the interfacial debonding and fiber pull-out behaviors of *AFRCs* have been extensively carried out **[61, 111-119]**. Three interfacial bonding conditions between the fiber and matrix, including fully bonded, partial debonding and complete frictional debonding were comprehensively investigated **[111-113]**. On this basis, stress drop theory was proposed to characterize the instability of interfacial debonding and fiber pull-out. According to the stress drop theory and the stress-displacement curve in the single fiber pull-out experiments, as shown in **Figure 2.4**, the scholars summarized a typical pull-out test of *AFRCs* as follows: 1) The applied stress firstly increased linearly with increasing displacement until the onset of debonding. 2) The fiber slipped with the start of interfacial debonding and the complete debonding stage reached until there accumulated enough cracks, followed by a significant drop in the applied stress due to complete debonding of the interface between fiber and matrix. 3) The load decreased slowly when the fiber overcame the friction and was pulled out from the matrix. Finally, our understanding of the fiber pull-out behaviors of *AFRCs* has been enhanced by a rich body of literature based on theoretical modelling of the fracture of the fiber-matrix interfaces in *CFRCs* and *GFRCs* **[61, 113-119]**. Representatively, Kim and Zhou et al. **[61, 113-117]** presented a theoretical model based on fracture mechanics to describe the interfacial

debonding and fiber pull-out behaviors of *CFRCs* and *GFRCs*, and to determine the interfacial properties (interfacial fracture toughness, interfacial friction coefficient, radial compressive residual stress, etc.), assuming the fibers, matrix and viscoelastic interface layer were isotropic. They provided the solutions for the interfacial fracture toughness, the partial debond stress, the maximum debond stress and the initial frictional pull-out stress in the pull-out process of *CFRCs*. The theoretical results showed that increasing the contact area between the fibers and matrix could improve the chemical and mechanical bonding between the fiber-matrix interface regions and further improve the interface properties, which achieved a good agreement with experimental data. Liu et al. **[118]** developed a fiber sliding model to study the effects of the interfacial roughness and residual clamping stress on the frictional pull-out stress of single *CFRCs*. The calculated results identified that the fiber frictional pull-out stress improved with the increase of the interfacial roughness but declined with the increase of residual clamping stress. Brandstetter et al. **[119]** studied the influence of interface roughness on the frictional properties of the material during the pull-out process of single carbon fiber. The results demonstrated that the theoretical modelling of single fiber pull-out based on the shear lag model can be used to predict the interfacial properties of composites. Kim et al. **[113]** and Yao et al. **[120]** proposed a series of improved interfacial debonding and fiber pull-out models by considering thermal residual stresses and the surface roughness based on traditional shear lag model and the fracture mechanics approach, which were employed on determining the interfacial debond stresses and fiber pull-out stresses of *AFRCs*.

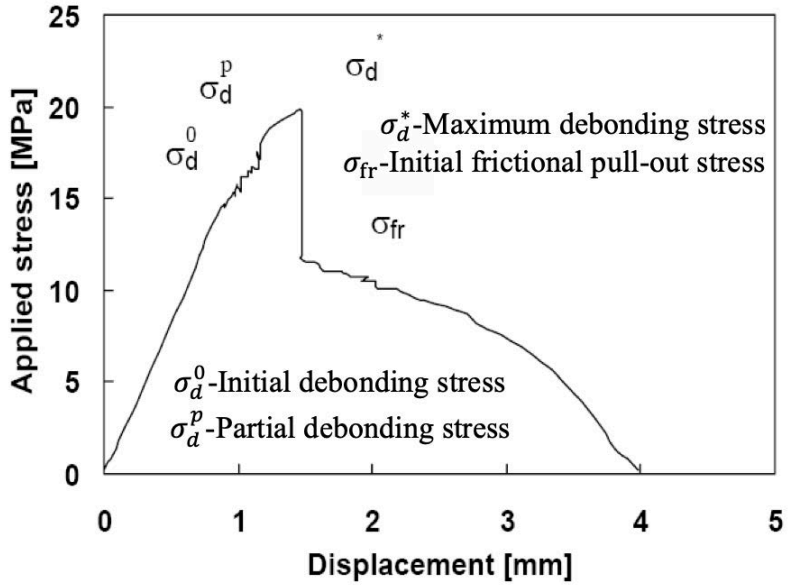

Figure 2.4 A typical pull-out stress-displacement curve for single *AFRCs*.

2.3.3. Numerical simulation of the interfacial mechanical behaviors--*CZM*

CZM is a widely used model technique in the elasto-plastic fracture mechanics. By considering the plastic zone, *CZM* avoids the stress singularity at the tip of the crack, which occurs in the linear elastic fracture mechanics. Consequently, the stress and the fracture energy in the process of crack initiation and propagation can be calculated. Researches demonstrated that the cohesive interface elements are subject to the traction-separation law, including the behaviors of viscoelasticity, cracking, fiber breakage, kinetic failure and cyclic loading failure. *CZM* suggests that there is a tiny cohesive zone at the tip of the crack, where the stress in this zone is a function of the displacement of the crack. *CZM* can be used to describe the mechanical behaviors during the material damage and fracture from the atomic point of view. It also can predict the leading-edge of the crack tip and the loss of energy in the complete

cracking zone, reflecting the effect of the interface in each layer of the composite material on the overall mechanical behaviors in structure.

CZM was first proposed by Barenblatt **[121]** in 1959 with the purpose of describing and explaining the atomic interactions near the tip of the crack for brittle materials. In 1987, Needleman **[122]** employed *CZM* to describe the process of void nucleation from initial debonding through complete decohesion and investigate the condition of debonding within matrix caused by inclusion, after then the *CZM* was introduced into the numerical simulation method. The combination of the *CZM* with the *FE* method was first used in the numerical calculation of fracture process of concrete and later in the fracture research of metals and composites. As representative results, Giessen et al. **[123]** developed a two-dimensional model that combined the normal and tangential tension stress with separating distances in 1995 by using the potential functions. Ortiz et al. **[124]** developed three-dimensional models to simulate the fracture failure.

With demonstrated efficiency of describing cracking behaviors within metals, *CZM* has been extended to model interfacial behaviors for the composites. Researchers firstly built the constitutive relationship of the interface in *CZM* by defining the interfacial bonding stress as a function of interfacial opening displacement and introduced the concept of interfacial fracture energy, that is, the energy released in the cohesive zone to form a new crack surface during the interface cracking. The expansion behavior of the crack tip at the interface of the composites is described through establishing the relationship between the interfacial bonding stress, the opening displacement and the critical fracture energy and regarding the composite

interface as a cohesive force zone with zero thickness. When the cohesive zone begins to be loaded, the interfacial adhesion force increases with the increase of the interfacial delamination. Then the interfacial damage occurs after the interfacial stress reaches the interface strength, while the interfacial adhesion force decreases with the increase of relative displacement between the interface. The interfacial failure propagates until the interface fracture energy reaches the critical value, after which, complete failure of the interface happens, and the cohesive zone expands forward. Therefore, the two main parameters that need to be determined during the use of *CZM* in composites are the interfacial strength and the interface critical fracture energy. Single fiber pull-out and *DCB* tests can be directly used to obtain the values of these two parameters. To identify the accuracy of these two measured parameters and comprehensively evaluate the debonding behavior of fiber-matrix interface, the fiber pull-out behavior and the delamination behavior of interface for *CFRCs* or *GFRCs*, numerical modelling aiming to demonstrate the whole fiber pull-out process or interface delamination process has been reported in a rich body of literature **[113, 125-130]**. Representatively, Kim et al. **[113]** employed the *FE* method to analyze the interfacial stress transfer and stress distribution of the treated and untreated carbon fiber and Kevlar fiber reinforced epoxy composites in the single fiber pull-out tests. The numerical results indicated that the interfacial debonding occurred when the maximum interfacial shear stress reached the interfacial bond strength. Jia et al. **[128]** adopted the *ABAQUS* software to simulate the pull-out process of a single carbon fiber from the polymer matrix by considering the influence of residual thermal stresses. The numerical analysis also proved that the residual thermal stresses had a significant influence on the fiber pull-out process at the stage of frictional sliding after the interfacial debonding. In addition, interfacial

shear strength was found to decrease with the increase in the fiber embedded length. Koyanagi et al. **[130]** implemented the *FE* analysis to calculate the interfacial stress of glass fiber-epoxy interface under a combined stress state in the single-fiber pull-out test. The constant interface failure stresses were found to be independent of the fiber embedded length whereas the apparent interfacial strength relied on the fiber embedded length. Kim et al. **[131]** established the *FE* model in the *ABAQUS* software based on *CZM*, to calculate Mode I *ILFT* of carbon fiber, Kevlar fiber and carbon/Kevlar hybrid reinforced composites and obtained prediction results within deviation of 5 %.

The above-mentioned literatures show that plenty of researches have been performed to develop interfacial theoretical models and numerical simulations of the composites to describe the interfacial mechanisms, especially for those traditional *AFRCs*. Previous studies have demonstrated the interfacial characteristics of *PFRCs* from the experimental point of view, whilst the theoretical calculation is another important method for quantitative evaluation of interfacial properties of *PFRCs*. Existing theoretical researches on *PFRCs* concentrated on the analysis of the interfacial failure between the fiber and matrix and followed the similar modelling methods for *AFRCs*. Li et al. **[74]** evaluated the interfacial properties of sisal fiber reinforced HDPE composites by single fiber pull-out test and calculated inherent interfacial parameters by Gao-Mai-Cotterel model. However, interfacial fracture toughness cannot be calculated due to the unavailable of initial debond stress value and the large scatter of obtained results. Ravandi et al. **[132]** proposed a three-dimensional (*3D*) *FE* model of *DCB* specimen to predict the Mode I *ILFT* and analyzed delamination propagation of

stitched *FFRCs* using cohesive element with nonlinear softening law. The above researches did not mention the multi-layer and multi-scale characteristics of *PFRCs* when analyzing the interfacial failure behaviors. Therefore, it is necessary to combine the exploration of the interface microstructure with the prediction of interfacial mechanical properties and to develop the criterions for *PFRCs* with multi-layer interfacial failure, whereby accurate theoretical model can be proposed for the interface structural design of *PFRCs*.

It is widely accepted that the interface has a great impact on the overall mechanical properties of composites. The shear lag model and *CZM* can be considered as useful tools for the theoretical and numerical analysis of the interfacial behavior of composite materials, respectively. In this thesis, the shear lag model and *CZM* are to be used to describe the multi-layer failure behaviors of *PFRCs*.

2.4. Comparisons of interfacial behaviors between *PFRCs* and *AFRCs*

As analyzed in previous section, plant fibers can be considered as an ideal choice for the design of composite structural products and can gradually replace *AFRCs*. Differences on the structural characteristics between plant fibers and synthetic fibers lead to different interfacial behaviors in their reinforcing composites. Therefore, interface control is a critical aspect to extend the industrial applications of the *PFRCs*. Strong adhesion at the fiber-matrix interface is desirable with respects to obtain good interfacial mechanical properties of the composites. In this backdrop, various

modification of the fiber and matrix can be considered as a versatile option and various modifications of the matrix, fibers or both of the components can be employed to improve both the interfacial properties of *PFRC*s and *AFRCs*. Therefore, interfacial modification and interfacial failure mechanisms of *PFRCs* and *AFRCs* are comparably discussed in this section.

2.4.1. Interfacial modification

Referring to the existing literatures **[133-135]**, the interfacial modification on *AFRCs*, mainly changes the surface roughness of synthetic fibers and the mechanical interlocking function between the fiber and matrix, actually, which is only relying on the physical process. However, the interfacial modification on *PFRCs* not only can change the surface roughness of plant fibers through physical modification, but also could generate hydrophobic and non-polar functional groups and reduce the mutually exclusive effects between the plant fibers and the hydrophobic polymer by chemical modification. Such methods modify plant fibers through heat treatment, physical (alkali) treatment, chemical (coupling agent, peroxide or permanganate) treatment and adding nano-particles (*CNTs* or nano cellulose (*NC*)). The main purpose of the above-mentioned methods is to modify the surface structure of fibers to enhance the bond strength between the fiber and matrix and simultaneously improve the interface compatibility.

Numerous researchers have conducted a series of experiments to compare the effects of different treatment methods on the interfacial properties of *PFRCs*. George et al. **[136]** improved the adhesion between jute yarns and polypropylene matrix by

chemically treating the interface with various reagents like stearic acid, toluene diisocyanate, permanganate and maleic anhydride modified polypropylene (*MAH-PP*) treatments. Scanning Electronic Microscopy (*SEM*) micrographs revealed that the interfacial bonding between the treated jute yarn and the matrix had improved significantly after the chemical treatments. The tensile and flexural properties were found to increase considerably due to the increase of the adhesion between the treated fiber and matrix. However, impact properties of the treated jute yarns composites got reduced slightly owing to enhancing the role of matrix in the stress transfer within the composites. Rong et al. **[27]** employed the heat treatment, alkaline, silane-coupling agent, acetylation and cyanoethylation to modify the surface and internal structure of sisal fibers and subsequently studied the mechanical performance of unidirectional sisal fiber reinforced epoxy composites. Infrared spectroscopy, X-ray diffraction and tensile tests indicated that these treatments would significantly improve the interface bonding between the fiber bundles and matrix, whereby the resin could be easier penetrated into the fiber and hinder the fiber pull-out during the failure process. Bledzki et al. **[137]** compared the variations of *IFSS* of different *PFRCs* after applying different physical and chemical treatments on the plant fibers. The results of single fiber pull-out tests showed that the possible of fiber breakage increased but that of fiber pull-out reduced after the treatment. With the improvement of the interfacial adhesion between the plant fiber and matrix, observed by *SEM* and polarized light optical microscope, the interfacial mechanical performance of the composites was concluded to improve. Juntaro and Pommet et al. **[138-140]** found that the interfacial properties of sisal fiber reinforced *PLA* or cellulose acetate butyrate (*CAB*) composites and hemp reinforced *CAB* composites were improved by adding *NC* onto the surface

of plant fibers with the *IFSS* increased by 21, 46 and 140 %, respectively. Similarly, Lee et al. **[141]** used *NC* to modify sisal fibers and the results showed the *IFSS* between the sisal fiber and poly-L-lactic acid increased by 21 %.

Although the above studies evidenced the interfacial properties and mechanical properties of *PFRCs* could be improved by using physical and chemical treatments on the surface of plant fibers, the limitation of these modification methods has also been reported in literatures. Sydenstricker et al. **[142]** modified the surface of sisal fibers through the treatment with *NaOH* or N-isopropyl-acrylamide solutions. It was found that the interfacial properties improved initially, while the shear strength of the composites began to decrease when the concentrations reached 5 and 3 % respectively. Hu et al. **[143]** observed the surface morphologies of hemp fibers and the fracture surfaces of hemp fiber reinforced polylactic acid (*PLA*) composites by using *SEM* photograph and found that the interface adhesion between the hemp fiber and *PLA* obtained the phenomenal improvement after alkali treatment. The results illustrated that the effect of alkali treatment on the interfacial properties of the composites was weakened with more than 40 % treated fiber volume fraction **[142]**. Paul et al. **[144]** investigated the effect of concentration of *MAH-PP* on the mechanical properties of the banana fiber reinforced polypropylene composites. The results showed that the mechanical properties of the composites depend on the concentration of *MAH-PP* and tensile, flexural and interfacial properties of the composites tend to be stabilized after the addition of *MAH-PP* up to 2 *wt.%*. Therefore, the interfacial and mechanical properties of *PFRCs* increase with treatment concentration up to a

critical level, which is decided by the content of plant fiber, and then remains constant or even declines. Chen et al. **[59, 145]** adopted three methods, including matrix modification, buckypaper interleaving and fiber modification by *CNTs*, to modify the interface of *FFRCs*. The results showed that *IFSS*, Mode I *ILFT*, *ILSS* and impact property of the modified composites were all improved with the *CNTs* content of 1 $wt.\%$. Microscopic observation revealed that the main failure mode of the composites was peeling-off and micro-fibrillation of flax elementary fibers. The generation of friction and the increase of fracture area during micro-fibrillation strengthened the interlaminar interfacial bonding of composite laminates. However, the pull-out experiments on the single flax yarn modified with different *CNTs* contents showed that although the *IFSS* of the modified *FFRCs* was improved, the *IFSS* did not increase significantly or even declined as *CNTs* content was continuously increased. In our research group, Wang et al. **[146]** used *NC* to modify flax yarns and manufactured *FFRCs* with untreated and treated flax yarns. The results showed that, by the modification of *NC*, the *IFSS* of the composites firstly improved and then decreased with the increase of *NC* content. The *IFSS* of the composites modified by 2 $wt.\%$ *NC* reached the highest value, which was increased by 23 $\%$ compared with untreated composites. Zhang et al. **[147]** employed electrophoretic deposition to modify sisal fibers with alkali before *NC* was deposited on their surface. The results showed that *IFSS* between the *NC*-treated sisal fibers and epoxy resin did not show any effect on the *IFSS* values, while the improvement of *IFSS* can make the debonding process into a stable mode and increase the debonding frictional force.

To conclude, treatments on the interface between the fibers and matrix of *PFRCs* was currently analyzed and discussed in most reported literatures. The strengthening effect was often limited to modifying the interactions between the plant fibers and matrix. The above work showed that it was not so effective to use the physical and chemical modifications to significantly improve the interfacial properties of *PFRCs*. As illustrated in section 2.2.2, compared with synthetic fibers, plant fibers possess irregular non-circular cross-section, uniform diameter and the multi-layer structure, which inevitably lead to differences in the interfacial adhesion properties and stress transfer mechanisms between *PFRCs* and *AFRCs*. However, in most research work on the interfacial modification of *PFRCs*, the failure arising from the existence of the multi-layer and multi-scale structure of plant fibers is generally neglected. Although the previous work conducted in our research group (Chen et al. **[59, 145]**, Wang et al. **[146]** and Zhang et al. **[147]**) has already considered the hierarchical structural characteristics of plant fibers and the possible internal interfacial failure occurred in the elementary fibers of plant fibers, the effects of the hierarchical structure and multiple damage sources on the interfacial performances and failure mechanisms of *PFRCs* have not yet been comprehensively taken into account to make the thorough discussion. Therefore, it is necessary to deeply explore the *IFSS*, adhesive properties, stress distributions, debonding criterion, load transfer mechanism and failure process of *PFRCs*, caused by the unique multi-layer interfacial structure features of plant fibers themselves, which are expected to play a key role in improving the interfacial mechanical properties of *PFRCs*.

2.4.2. Interfacial failure mechanisms

Theoretical analysis on the interfacial failure mechanisms of the composites is important but requires some great efforts to achieve. The interfacial failure of traditional *AFRCs* mainly manifest as the interface bond failure, the interface cohesive failure and the mixed failure at the interface according to the different interfacial conditions **[148]**. Compared to traditional synthetic fibers, the multi-layer and multi-scale microstructure of plant fibers leads to complex interfacial damage performance and failure mechanisms of *PFRCs* when subject to external loads.

The improvement of interfacial properties changes the stress transfer mechanisms within the composites under external loads. In macro-scale, various techniques to enhance the interlaminar performance of *PFRCs* bring in different interfacial failure mechanisms. For instance, Li et al. **[149]** studied the effect of fiber surface treatments on the *ILFT* of sisal textile reinforced vinyl ester and epoxy composite using *DCB* and *ENF* tests. With the increase in the applied load, matrix cracking occurred, followed by fiber bridging. When the fiber bridging was fully formed, the bridging fibers started to break or pull-out. The treated *SFRCs* were found to possess higher crack-toughness against delamination and superior *ILSS* than the untreated *SFRCs* due to the improvement of interfacial bonding properties between the sisal fiber and vinyl ester resin. Chen et al. **[145]** utilized *CNTs* buckypaper interleaf in the interface between unidirectional flax fiber layers to improve the *ILFT* of composite laminates. The multi-scale microstructures of flax fibers were concluded to induce new mechanisms for enhancing the interfacial properties of *FFRCs*. Microscopic observation revealed that synergistic effects between the buckypaper and the hierarchical structure of flax

fibers enhanced mechanical interlocking between the flax fiber and matrix, and thus strengthened the interlaminar interfacial bonding of composite laminates. Li et al. **[150]** found Mode I *ILFT* of unidirectional flax fabrics reinforced epoxy laminates, measured from *DCB* tests, increased with the introduction of the chopped flax yarns. With the aid of *SEM*, the toughening mechanism of the laminates was revealed as that the introduction of the chopped yarns resulted in more tortuous in-plane crack propagation paths as well as the "trans-layer" phenomenon and fiber bridging effect between the unidirectional yarns and chopped yarns. The mentioned phenomena combinedly hindered the growth of crack and led to more energy dissipation during the delamination progress. Rong et al. **[151]** found that the delamination resistance of stitched unidirectional sisal fiber reinforced epoxy laminates was improved via expanding the fiber bridging zone, thus greatly enhancing the interlaminar toughness. Distinct from *GFRCs*, laminated *SFRCs* have a rather high tolerance against the damages induced by the stitching process. Zhang et al. **[52]** found that the *ILFT* and *ILSS* of unidirectional flax and glass fiber reinforced phenolic polymeric matrix hybrid composites were even higher than those of *GFRCs* due to the excellent performance of the hybrid interface, which were correlated with the twist flax yarn structure, rough surface of flax fiber and fiber bridging between the flax and glass fiber layers. It was also observed that crack propagation in the *FFRCs* was accompanied by extensive fiber bridging. Ma et al. **[152]** found the *ILFT* of ramie fiber yarn reinforced composites was relatively high due to the extensive fiber bridging observed during the *DCB* test.

Numerous scholars have carried out the macroscopic mechanical experiments (i.e. tensile, impact, etc.) on plant fibers and their composites and reported their unique mechanical behaviors caused by the multi-layer and multi-scale structure of plant fibers. Silva et al. **[48]** found that multiple failure modes including the damage of elementary fiber, the debonding between the elementary fibers and the debonding between cell walls occurred during the tensile loading for sisal fibers by observing the *SEM* morphologies of sisal fibers after tensile failure (**Figure 2.5**). Bos et al. **[153]** found that the primary and secondary cell walls of flax fibers presented different failure modes during the tensile failure process (**Figure 2.6**). The primary wall mainly underwent brittle fracture while the micro-fibrils in the secondary wall occurred bridging phenomenon. Dai et al. **[154]** pointed out that the initial crack of hemp fibers during tensile loading would be generated within the weaker primary cell wall of hemp fibers. With continuous loading in the tensile tests, the crack radially extended from S1 to S2 layer, which resulted in the damage of the secondary cell wall of hemp fibers. Newman et al. **[155]** also found that the micro-fibrils in S2 layer could be pulled-out in tensile experiments of Phormium fiber reinforced composites and the debonding between the elementary fibers could be observed from *SEM* fracture morphologies (**Figure 2.7**). Singleton et al. **[25]** studied the Charpy impact properties of *FFRCs* and multi-layer and multi-scale failure modes including fiber slipping, matrix cracking, fiber cracking, fiber splitting, fiber breakage and fiber pull-out were observed during the experiments (**Figure 2.8** (a)). It was pointed out that the primary cell wall of flax fiber firstly underwent brittle fracture and flax fiber splitting into separate units eventually presented with the crack initiation and propagation (**Figure 2.8** (b)).

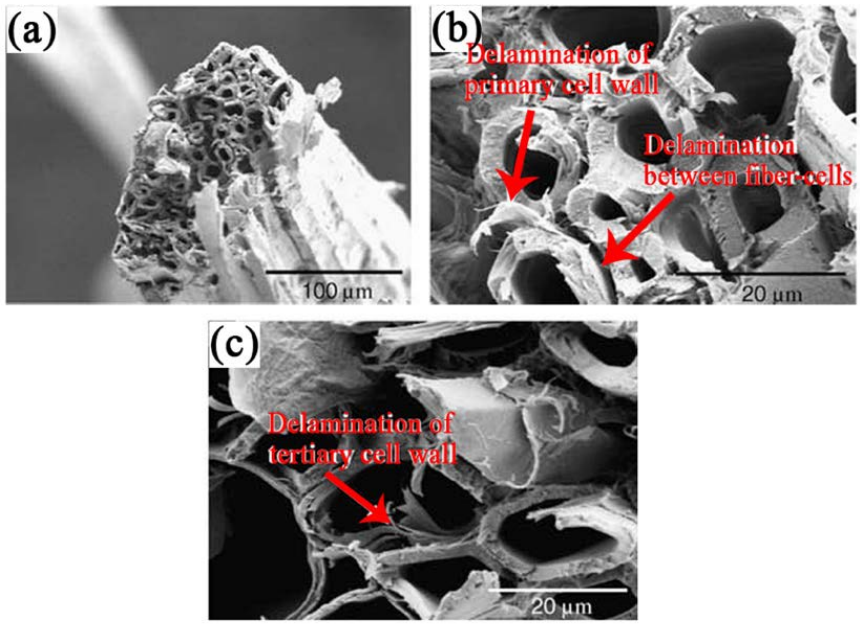

Figure 2.5 Fractography of sisal fibers after tensile failure: (a) overall morphology, (b) and (c) details of delamination within the cell walls and between cells **[48]**.

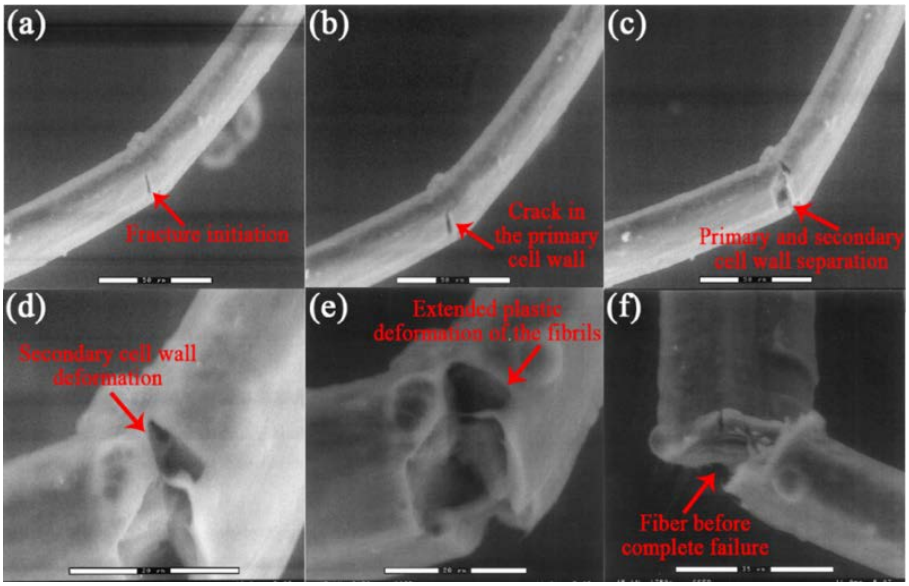

Figure 2.6 Initiation and development of fracture in an elementary flax fiber: (a) and (b) crack initiation in the primary cell wall, (c) separation between the primary and secondary cell walls, (d) the secondary cell wall deformation and the micro-fibrils bridging in S2 layer, (e) extended plastic deformation of the fibrils in the secondary cell wall and (f) the fiber before complete failure **[153]**.

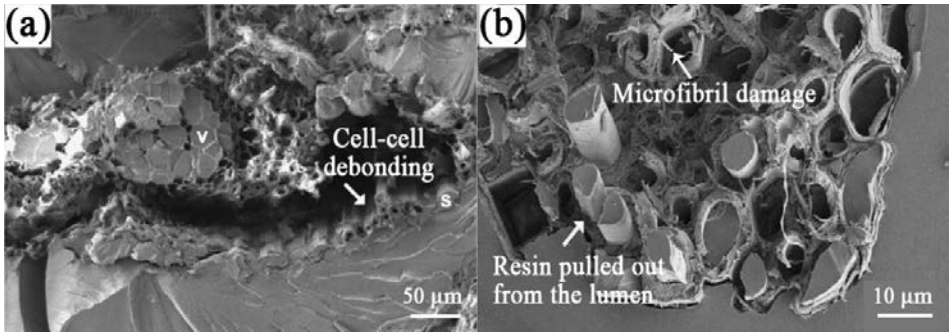

Figure 2.7 *SEM* images of Phormium fiber reinforced composites after tensile test: (a) cell-cell debonding and (b) the micro-fibrils pulled-out and resin pulled-out from the lumens of thin-walled cells **[155]**.

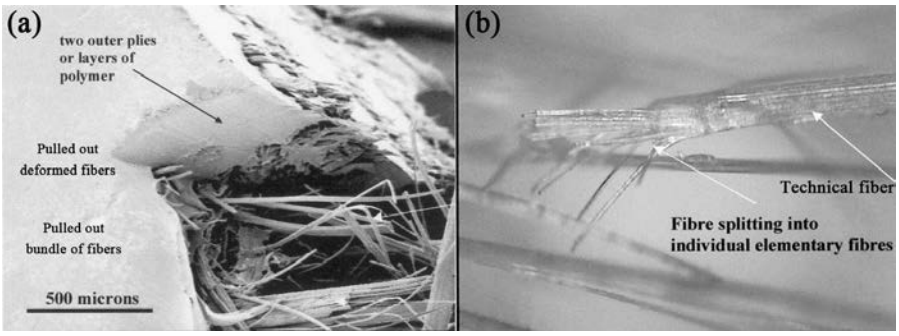

Figure 2.8 *SEM* morphologies of *FFRCs* after Charpy impact tests: (a) pulled out deformed fibers and fiber bundle and (b) splitting of a technical fiber followed by fracture of the elementary fibers **[25]**.

In our previous researches, we found the interfacial failure of *PFRCs* indeed presents the multi-layer and multi-scale feature (**Figure 2.9**) **[32, 33]**. Therefore, the unique multi-layer and multi-scale microstructure of plant fibers leads to the complex mechanical behaviors and failure modes when subject to the external load compared with traditional synthetic fibers. It is necessary to consider the unique characteristics of plant fibers and employ customized measurement and characterization techniques and interfacial mechanics model to evaluate the multi-interface performances in *PFRCs*.

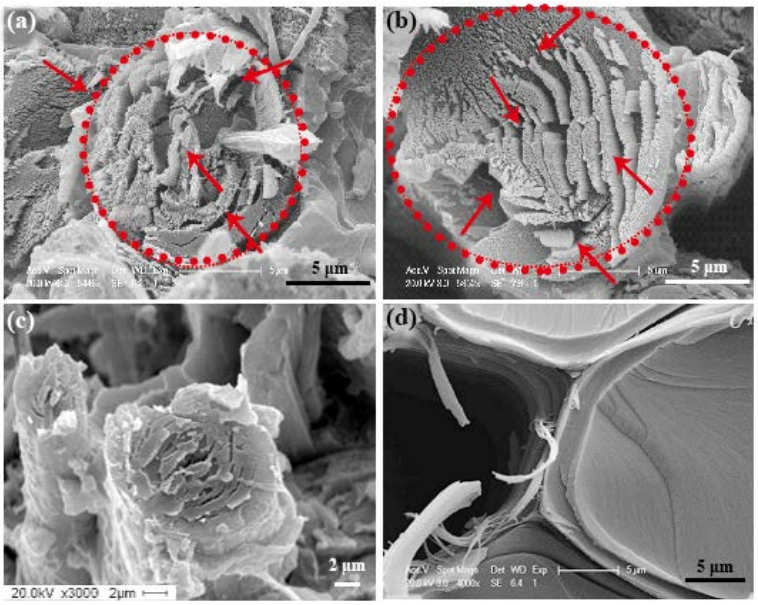

Figure 2.9 Multi-layer and multi-scale interfacial damage micrographs of *PFRCs* ((a)-(c) multi-layer damage of elementary fiber and (b) micro-fibril pull-out) **[32, 33]**.

2.5. Summary

In this chapter, the importance of fiber-matrix interface with regards to the mechanical properties of the composites is described firstly. Subsequently, the structural characteristics (i.e. chemical composition and microstructure) of synthetic fibers and plant fibers are comparably analyzed. The categories and distinct chemical compositions of plant fibers different from traditional synthetic fibers are introduced. Compared with synthetic fibers, the structure of plant fibers is reported to exhibit the multi-layer and multi-scale characteristics and plant fibers themselves can be regarded as a kind of composite material that based on cellulose as reinforcement and lignin and pectin as matrix. Then the prevailing methods on the evaluation of interfaces in *PFRCs* and *AFRCs* are briefly reviewed. Different experimental characterization

techniques have been developed to identify the interfacial properties of *PFRCs* and *AFRCs* from the macro-scale to nano-scale. Furthermore, the existing theoretical modelling and numerical simulation on *PFRCs* and *AFRCs* with respect to shear lag model and *CZM* are also presented. The unique structural characteristics of plant fibers lead to new interfacial mechanical problems. Although the interfacial properties have been effectively enhanced after the surface modification of plant fibers, the extent of improvement is limited caused by generally neglecting the existence of hierarchical structure of plant fibers. The interfacial modification method only applies to the interface between the fiber and matrix, not considering the interfaces within the plant fiber itself. Limitations on the usage of traditional evaluation methods and theoretical analysis to characterize the interfacial behaviors of *PFRCs* are proposed and discussed. The multi-layer and multi-scale damage of *PFRCs* have been observed in the tensile tests in macro-scale. The appropriate measurement on the multi-layer interface and sound theoretical basis for *PFRCs* with hierarchical structure have not been developed. Therefore, the above-proposed tasks will be attempted in this thesis by focusing on the multiple interfaces of *PFRCs*. Effects of the multi-layer and multi-scale structure on the interfacial failure mechanisms for *PFRCs* will be investigated with more rigorous experimental technique and theoretical calculation. Relationships between the multi-layer interface, mechanical properties and fracture performances of *PFRCs* are to be established and the criterions of multi-layer interfacial failure for *PFRCs* will be developed systematically and in depth by combining the exploration of the interface microstructure with the prediction of interfacial mechanical properties.

CHAPTER 3

Nanoscale Evaluation of Multi-Layer Interfacial Mechanical Properties of *PFRCs* by the Nanoindentation and *Nano-DMA* Technique

3.1. Introduction

As mentioned in previous two chapters, mechanical performances of *PFRCs* are largely dependent on the interfacial adhesion properties, which determine stress transfer efficiency at the interface. In Chapter 2, the microstructures of plant fibers are introduced in detail. Single plant fibers are described to possess a multi-layer and multi-scale structure, which is distinct from synthetic fibers with a homogeneous structure **[24]**. Such a hierarchical organization produces multi-interphase regions

with different morphological characterizations in the plant fibers. Without loss of generality, the interphase transition regions are usually small and often in the nanometer range, which induces challenges to achieve an accurate evaluation of the nanoscopic interfacial properties of plant fibers. Therefore, it is of necessity to characterize the interfacial properties of plant fibers and their reinforcing composites at the nanoscopic level. However, rare reported works are found to comprehensively quantify the interfacial properties of *PFRCs* in the nanoscopic perspective.

Amongst the nanoscopic evaluation methods regarding material interfacial properties, nanoindentation technique has emerged as promising tools in the applications for *CFRCs* or *GFRCs* as reviewed in Chapter 2 **[79-81]**. Such technique shows the availability on characterizing interfacial morphology and determining interfacial mechanical properties for the composites in nano-scale. However, limited studies have been carried out with regards to evaluating interfacial properties of *NFRCs* using the nanoindentation technique **[82-84]**. The existing studies are mainly focused on the basic mechanical or interfacial properties between the fiber and matrix of *PFRCs*, ignoring the distinct hierarchical structure (i.e., multi-layer and multi-scale) of plant fibers. Thus, relevant research endeavors in extending such a technique to the quantitative evaluation of hierarchical interfacial properties and interfacial failure of *PFRCs* with multi-layer and multi-scale interfaces are worthy of investigating and validating.

Meantime, study on *nano-DMA* was introduced in Chapter 2, which provides a new idea on investigating the nanofatigue behaviors of the multi-layer interfaces within

PFRCs by performing the fatigue tests at the nanoscopic scale. Currently, there exists a lack of understanding of failure processes occurring at the multi-layer interfaces of plant fibers when subject to external loads and the influence of fiber treatment on the global mechanical behaviors of *PFRCs*.

Inspired by the proven efficiency of the nanoindentation technique in evaluating interfacial properties of the *AFRCs* in nano-scale, sisal fibers as a typical plant fiber are selected in this chapter due to their large dimension and typical hierarchical structure. Present chapter is dedicated to quantitatively measuring the interfacial mechanical properties of *SFRCs* with a multi-layer and multi-scale structure by using the nanoindentation technology. To achieve this goal, firstly, a series of indents derived from the matrix to each layer of cell walls of the sisal fiber (S1, S2 and S3 layer) are employed to identify the transition zones of the multi-layer interfaces. Optical Microscopy (*OM*), Atomic Force Microscopy (*AFM*) and *SEM* characterizations are used to observe the multi-layer interface morphology of sisal fibers and the morphologies of indents. Secondly, single-step and multi-step nanoindentation measurement at various peak indentation loads are performed on the multi-layer interfaces of *SFRCs* to illustrate their distinct interfacial mechanical properties in terms of modulus and hardness, energy dissipation, crack initiation and propagation upon compressive loading. Then, interfacial fracture mechanisms of *SFRCs* are revealed by determining the transition zones of the multi-layer interfaces and the interfacial failure loads. Finally, the fatigue failure behaviors of the multiple interfaces within *SFRCs* in nano-scale are further examined and characterized by the *nano-DMA* technique. The differences of the dynamic nano-mechanical properties of

the multiple interfaces within *SFRCs* are analyzed by using the cyclic loading with varying applied indentation loads and frequencies.

3.2. Materials and experimental procedures

3.2.1. Materials and specimen fabrication for nanoindentation and *nano-DMA* measurements

The sisal fibers used for sample preparation in the nanoindentation experiment, with a density of 1.45 g/cm^3, were supplied by Guangxi Sisal Group Co., Ltd. The epoxy resin (NPEL-128), curing agent (EH-6303) and accelerator (EH-6412) were purchased from Shanghai Zhongsi Industry Co., Ltd. The epoxy resin was mixed with the curing agent (26 $wt.\%$) and accelerator (8 $wt.\%$) to produce a mixture with a volume density of 1.2 g/cm^3. The adopted single sisal fibers (also called technical fiber) were observed to possess diameters ranging from 100 to 300 μm and contain numerous elementary fibers of which diameters vary from 10 to 30 μm. Two types of cell walls were observed in the typical elementary fiber, named as the outer primary (P) and the inner secondary cell wall, respectively. The inner secondary cell wall is further separated as S1, S2 and S3 layers in nano-scale owing to their various thickness and structures. The reason for choosing sisal fibers is that sisal fibers possess larger diameters compared to other plant fibers, which makes it possible to identify transition region between cell wall layers (i.e., interface between S1 and S2 layer or that between S2 and S3 layer).

In the process of specimen preparation, pretreatment was first conducted on sisal fibers. To be more specifically, sisal fibers were immersed in the deionized water at 70 $^{\circ}C$ for 1 h to eliminate impurities and dirt. The treated fibers were firstly hackled and arrayed for straightening and subsequently heated in the vacuum oven at 105 $^{\circ}C$ for 2 h to remove the absorbed moisture in the pretreatment. From **Figure 3.1** (a)-(b), variation of the surfaces of the sisal fibers before and after treatment can be observed, that is, the clean surface of the sisal fibers after the pretreatment. The pretreated sisal fibers were designated as untreated fibers. The prepared fibers were separately embedded into a cylindrical silicon rubber mold with a dimension of 10 mm (diameter) × 3 mm (height). Mixed matrix was meticulously poured into the mold and submerged the whole fiber to fully impregnate the fibers as shown in **Figure 3.2**. The specimens were cured for 24 h at room temperature and post cured at 60 $^{\circ}C$ for 2 h. Prepared specimens were polished by sand papers (800#，1500#，2000#，3000# and 5000#) first and smoothed meticulously with polishing solution with particle sizes of 1, 0.1 and 0.03 μm, respectively. In order to minimize the influence of humidity on the mechanical properties of the sisal fibers, the polished specimens were also dried in the oven after polishing. Finally, the samples were attached to aluminium disks by super glue and the prepared specimens were fully dried in the oven before performing the nanoindentation tests.

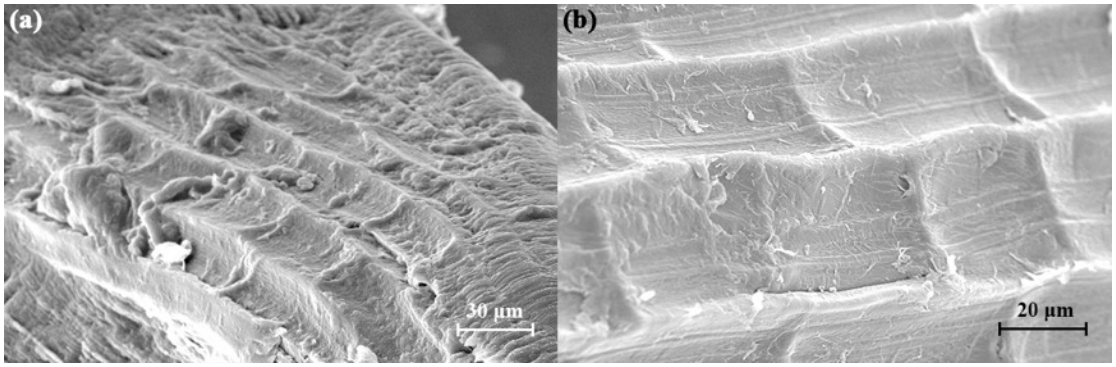

Figure 3.1 *SEM* photographs of the surface modification of the sisal fiber (a) before and (b) after pretreatment.

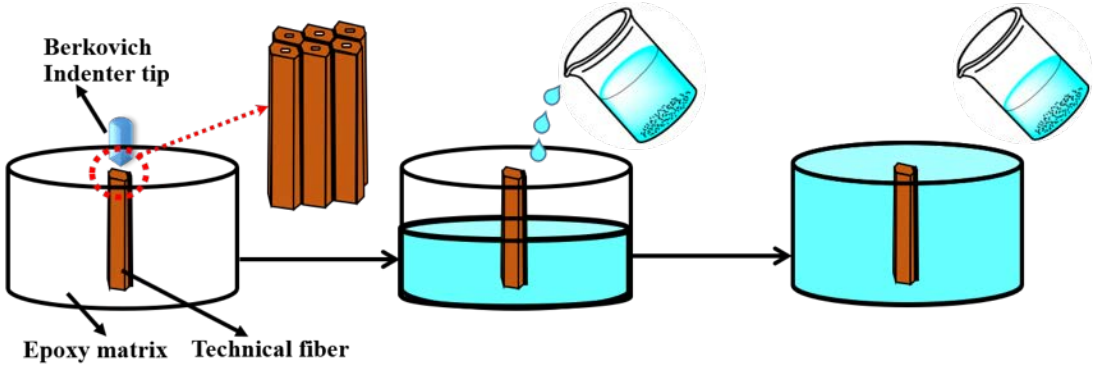

Figure 3.2 Schematic of the process of fiber impregnated.

3.2.2. Nanoindentation tests and morphology characterization

The typical specimen configuration (**Figure 3.3** (a)) and the schematic illustration of the indents (**Figure 3.3** (b)) for the nanoindentation experiments of *SFRCs* were presented in **Figure 3.3**.

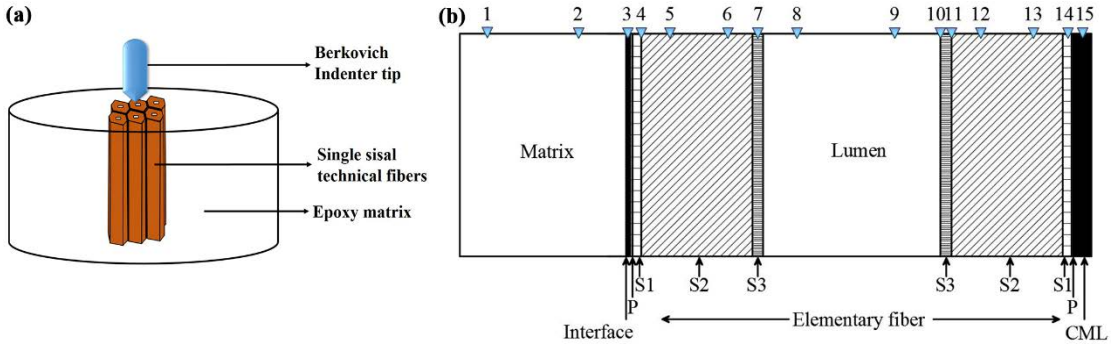

Figure 3.3 (a) Specimen configuration for nanoindentation test and (b) schematic illustration of nanoindentation position.

The nanoindentation experiments were carried out in Hysitron TI-950 Triboindenter (Hysitron Inc., MN) that equipped with a diamond Berkovich indenter tip (a three-sided pyramidal tip with a radius of 50 nm and a total included angle (the angle from one edge to the opposite side) of 142.35°) at 25 $^{\circ}C$ with ambient humidity of approximately 30 $\%$. The nanoindentation tests were conducted according to the following procedures: (1) the indenter approached the surface with a rate of 10 nm/s; (2) after contacted with the surface, the indenter tip was driven into the material with a constant loading rate until a designed maximum load P_{max}; (3) the peak load was held for 10 s to make the indenter steady; (4) unloading was carried out with the same constant rate as loading; (5) *OM* and *AFM*, equipped in the nanoindentation system, were employed to identify the position and quality of the indents. A series of indents were made on the cross-section of different cell wall layers of sisal fibers and epoxy matrix, as shown in **Figure 3.3** (b). The elastic modulus and hardness can be derived from the load-depth data based on the Oliver and Pharr method **[78]**, depicted as follows:

$$1/E_r = \left(1-\nu_I{}^2\right)/E_I + \left(1-\nu_S{}^2\right)/E_S \qquad \textbf{(3.1)}$$

$$H = P_{max} / A_C \quad \textbf{(3.2)}$$

where E_r is the reduced modulus of related indent regions measured in the experiments, and E_I is the indenter modulus with a value of 1140 GPa. Poisson's ratio ν_I is 0.07 for the standard diamond indenter probe in this study. E_S and ν_S are the elastic modulus and Poisson's ratio of each indent region in the *SFRCs*, respectively ($\nu_S = 0.16$ used for epoxy matrix and $\nu_S = 0.12$ used for S2 layer of the sisal fiber in current study **[21]**), where E_S can be derived by **Equation (3.1)**. In **Equation (3.2)**, H is the hardness of each indent region in the *SFRCs*, and A_C is the resultant projected contact area at the maximum indentation load P_{max}.

To quantify the interfacial properties of *SFRCs*, indents were produced in the proximity of the three types of interfaces, namely those between elementary fibers and epoxy matrix (*IF-FM*), those between elementary fibers (*IF-ELE*) and those between cell wall layers (*IF-CW*) (as displayed in **Figure 3.4**). To further illustrate the multi-layer interfacial failure processes of *SFRCs*, single-step nanoindentation experiments were first conducted on the three types of interfaces (repeated tests were conducted at six points for one type of interface at each nanoindentation load) by varying the maximum indentation loads from 200 to 9000 μN with an increase step of 200 μN (**Figure 3.5** (a)). Multi-step nanoindentation experiments applied increasing penetration forces at the same point of an interface each time from 200 to 9000 μN with an increase step of 200 μN (**Figure 3.5** (b)) and six repeated tests were conducted to minimize the measurement errors. The cyclic loading with a constant

peak load each time was subsequently applied on the three interfaces with the peak loads augmenting from 200 to 9000 μN with an increase step of 200 μN (**Figure 3.5** (c)). Microscopy observations (i.e., *OM* and *AFM*) were performed after the end of each cycle. Each indent position was recorded to identify them in subsequent *SEM* observation. The work of indentation (*WOI*), which can be used to indicate the interfacial failure, was calculated from the load-depth curve as illustrated in **Figure 3.5** (d). The area covered by loading curve represents the total work (W_t) while that of unloading curve stands for the reversible (elastic) work (W_{el}). The difference of these two works is termed as the irreversible (plastic) work (W_{pl}). The ratio of irreversible work to total work was expressed as follows:

$$W_{pl}/W_t = 1 - W_{el}/W_t \quad \textbf{(3.3)}$$

W_{pl}/W_t measured from the three interfaces by the single-step nanoindentation tests were compared to demonstrate the differences of the three interfaces in terms of energy dissipation capability, while W_{pl}/W_t for the three interfaces over cyclic cycles obtained from the multi-step and cyclic loading experiments were comparably obtained to present the distinct failure behaviors of the three interfaces.

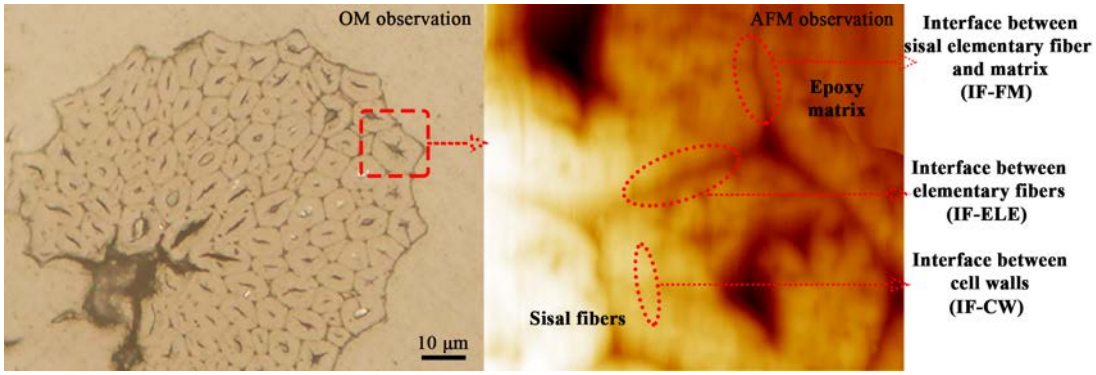

Figure 3.4 Schematic of three types of interfaces for the *SFRCs*.

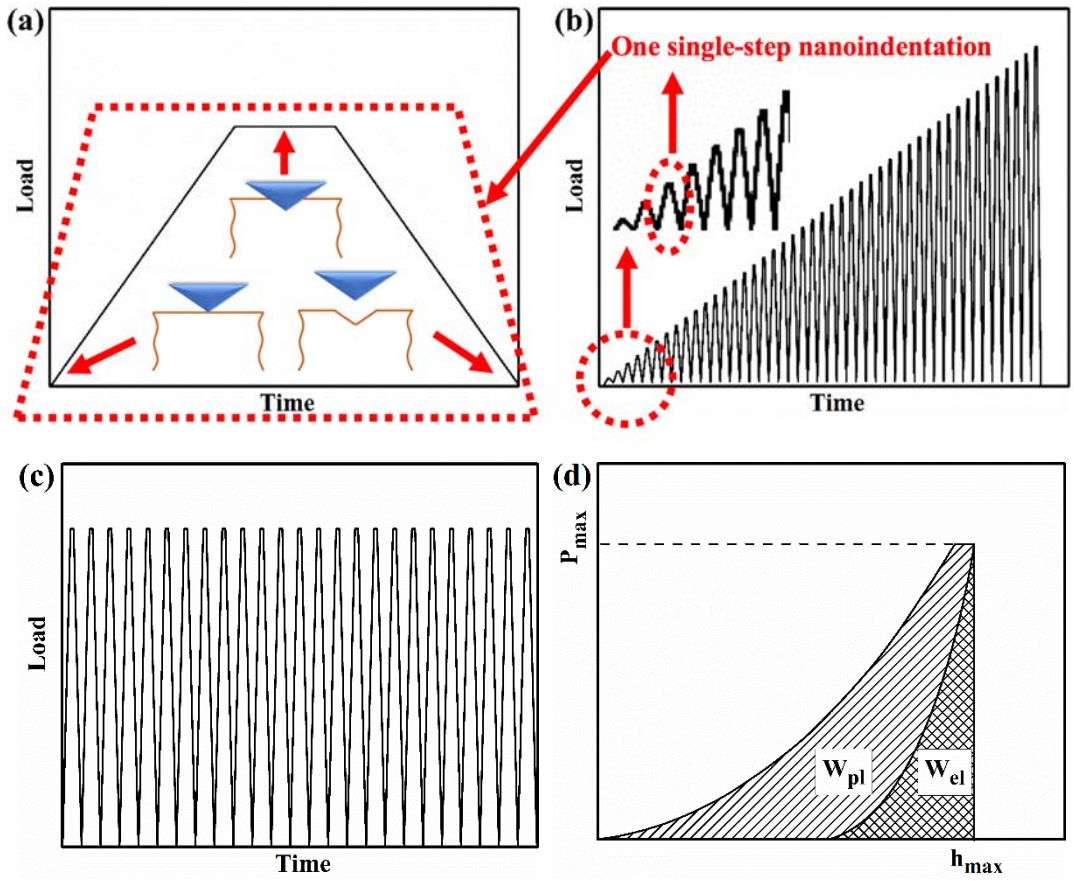

Figure 3.5 Schematic of typical loading function used in the (a) single-step, (b) multi-step and (c) cyclic nanoindentation and (d) plastic and elastic work calculated from load-depth curve of nanoindentation test.

The size of the indents was measured with the *OM* and *AFM*. The morphologies of cracks at the three interfaces upon the cyclic loading nanoindentation tests were observed by using a field emission *SEM* (FE-SEM, XL30 FEG, PHILIPS Co., Netherlands). The surfaces were coated with gold before observation.

3.2.3. Basis of *nano-DMA* theory and morphology characterization

All *nano-DMA* experiments were carried out using the dynamic mechanical analysis system in Hysitron TI-950 Triboindenter (Hysitron Inc., MN) equipment as mentioned

in previous section. The *nano-DMA* tests were conducted according to the following procedures: (1) a careful approach to the surface with an indenter rate of 10 nm/s; (2) after the indenter tip engaged with the sample surface, it was loaded to the designed maximum quasi static load P_{max} with a constant loading rate of 25 $\mu N/s$; (3) a dynamic load $P_{dynamic}$ covering a frequency range of 10-300 Hz or at a certain frequency was superposed on this load; (4) when the sweeping-frequency vibration was complete, the same constant rate as loading was applied for unloading; (5) *OM* and *AFM* in the machine itself were employed to evaluate the position and quality of the indents. The indents were made on the cell walls of sisal fibers and the three interfaces of *SFRCs*. The dynamic nano-mechanical properties including storage modulus, loss modulus and loss factor could be derived from the Pethica and Oliver method based on the continuous stiffness measurement (*CSM*) technique **[86]** described in the following part.

Figure 3.6 shows the schematic of a nanoscale fatigue test (**Figure 3.6** (a)) and loading cycles (**Figure 3.6** (b)) on *SFRCs* using the *CSM* technique, respectively. Force cycles were applied to the interface region, resulting in a cyclic stress. $P(t)$ is the cyclic load, P_{mean} is the mean load, P_{OL} is the oscillation load amplitude, and ω is the oscillation frequency. To obtain fatigue deformation and damage, large amplitude oscillations were used. The numbers of cycles could be determined from the elapsed time.

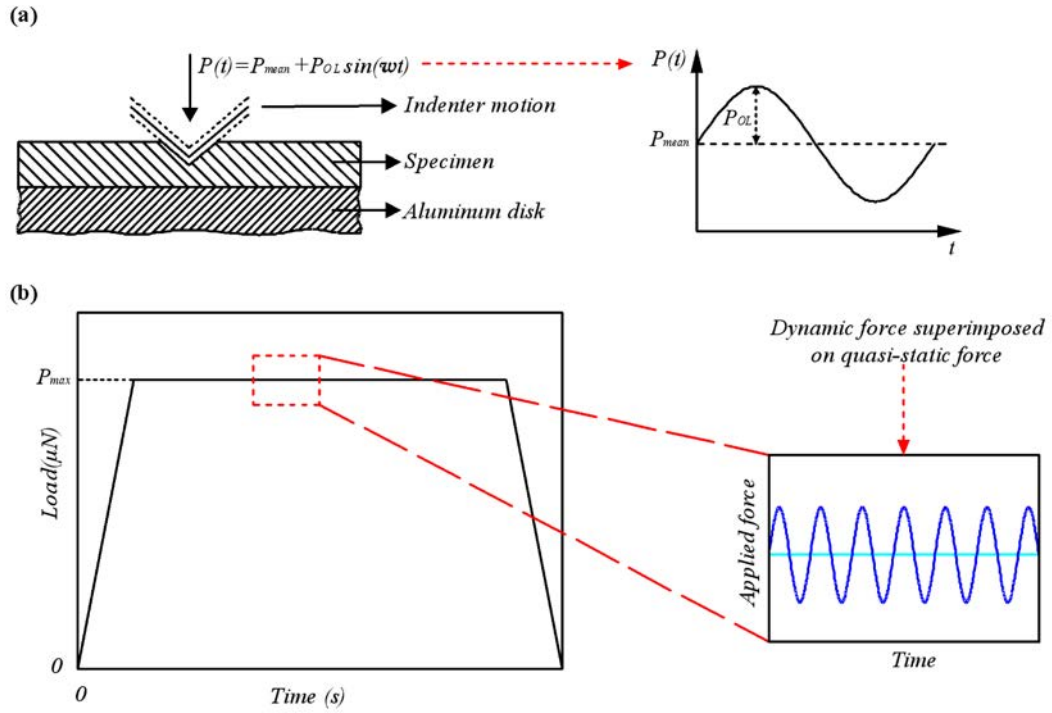

Figure 3.6 Schematics of (a) the nanoscale fatigue test and (b) the loading cycle by the *CSM* technique.

The interaction between the tip and the sample is usually described using a simplified mechanical model as illustrated in **Figure 3.7**. In **Figure 3.7** (a), P is the applied force, h_C is the contact depth and ϕ is the face angle of the indenter head. In **Figure 3.7** (b), m is the mass of the tip and shaft, K_I and K_S are the stiffness of the indenter and sample, respectively, and C_I and C_S represent the damping coefficients of the indenter and sample, respectively. Here, the tip is driven subject to the sinusoidal oscillation with the load amplitude F_0 at the oscillation frequency ω.

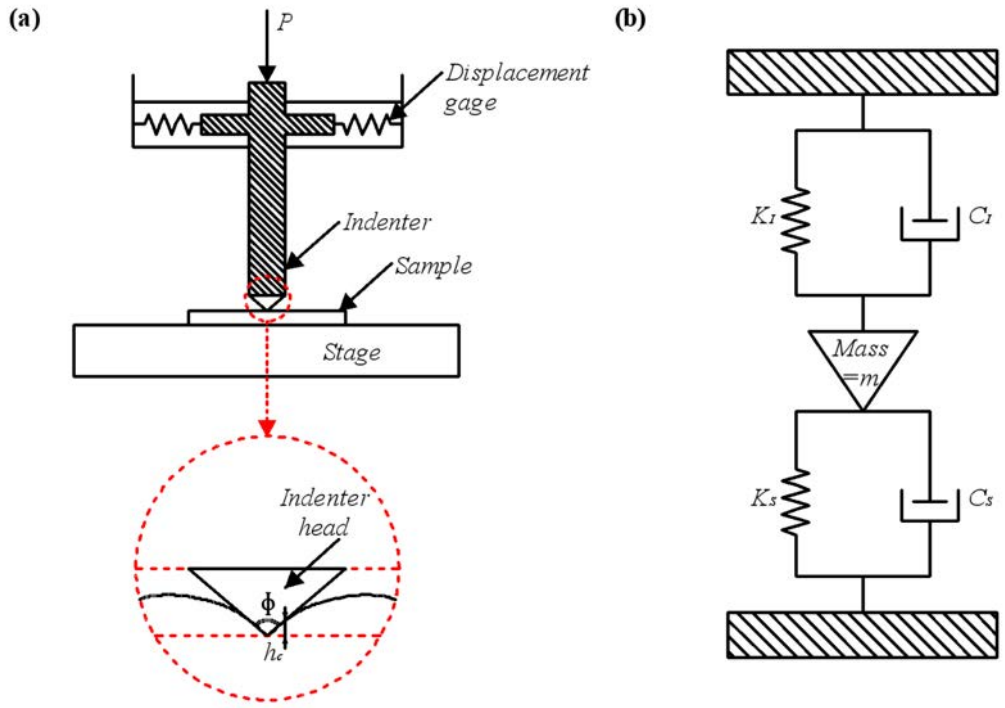

Figure 3.7 Schematic of (a) the nanoindentor-sample system and (b) the dynamic nanoindentation model.

Given the force equilibrium of this model system, an equation governing the motion of the indenter tip can be written as

$$m\ddot{x}+\left(C_I+C_S\right)\dot{x}+\left(K_I+K_S\right)x=F_0\sin\left(\omega t\right) \tag{3.4}$$

where $x(t)$ defines the position of the tip as a function of time and the overdots denote temporal derivatives. For the steady-state solution, the displacement varies at the same frequency and can be expressed in the following form:

$$x(t)=X\sin\left(\omega t-\varphi\right) \tag{3.5}$$

where X is the displacement amplitude and φ is the phase lag between the applied force and the tip displacement. Substituting **Equation (3.5)** into **Equation (3.4)** and simplifying, yields:

$$X = F_0 / \sqrt{\left(K_I + K_S - m\omega^2\right)^2 + \left(C_I + C_S\right)^2 \omega^2} \quad \textbf{(3.6)}$$

$$\varphi = \tan^{-1}\left(\left(C_I + C_S\right)\omega / \left(K_I + K_S - m\omega^2\right)\right) \quad \textbf{(3.7)}$$

These two equations relate the experimentally measured values, namely displacement amplitude X and phase lag φ, to the sample properties (K_S' and K_S'' are the storage and loss stiffness, respectively) which can be written as

$$K_S' = F_0 / X \cos\varphi + m\omega^2 - K_I \quad \textbf{(3.8)}$$

$$K_S'' = \omega C_S = F_0 / X \sin\varphi - C_I\omega \quad \textbf{(3.9)}$$

Note that the loss stiffness is defined as the product of the excitation frequency ω and the damping of the sample C_S. Both K_S' and K_S'' are directly obtained from the measured parameters of amplitude and phase without the use of any assumptions **[89]**. Thus, the differences of cell wall properties for plant fibers alone can be reflected by the measured quantities K_S' and K_S''.

In order to relate the measured quantities K_S' and K_S'' to those properties of the specimens themselves, a model to describe the contact mechanics between the tip and the sample is needed. Robust models have been developed for the cases when the sample is homogeneous and large in all directions relative to the contact area **[78]**. In this case, **Equations (3.10)-(3.11)** relate the measured storage stiffness and loss stiffness to the storage modulus E' and loss modulus E'' of the sample as

$$E' / \left(1-\nu^2\right) = K_S' / 2\sqrt{\pi / A_C} \quad \textbf{(3.10)}$$

$$E'' / \left(1-\nu^2\right) = K_S'' / 2\sqrt{\pi / A_C} \quad \textbf{(3.11)}$$

where A_C defines the contact area between the indenter tip and the sample. Note that indentation data are associated with the reduced modulus, which are related to the sample modulus through a factor of $1-\nu_S{}^2$ (ν_S is the Poisson's ratio as in section 3.2.2) **[78]**.

The surface morphology and microstructures of sisal fibers and the indent morphologies and size of the sample in the *nano-DMA* tests were observed with the aid of *OM*, *AFM* and *SEM* as in section 3.2.2.

3.3. Evaluation of nano-properties for pure epoxy matrix, cell wall layers and the multi-layer interphase in the *SFRCs*

To quantify the nano-properties (including geometry dimension and mechanical properties) of a sisal fiber with a multi-layer structure, dimension of transition region, elastic modulus and hardness of the epoxy matrix and cell wall layers are to be presented in what follows, then those of the interfaces in the *SFRCs* (e.g., *IF-FM*, *IF-ELE* and *IF-CW*) will be discussed.

Figure 3.8 presents the dependence of elastic modulus and hardness of epoxy matrix and S2 layer (a typical cell wall layer) on the indentation depths obtained from the single-step nanoindentation tests. To observe that the values of elastic modulus and hardness became steady when the nanoindentation depth exceeded 45 nm. While below 45 nm, a partial contact between the indentation tip and material caused by roughness of the material induced pressure-dependent measured values **[84, 156]**. Therefore, indentation depths used in the subsequent measurements were selected as more than 45 nm. It also can be seen from **Figure 3.8** that the stable modulus and hardness of the pure epoxy matrix are 4.75 GPa and 188.72 MPa, respectively, while those of S2 layer are 10.99 GPa and 378.72 MPa, respectively, which can serve as two baselines for evaluating related properties of *SFRCs*.

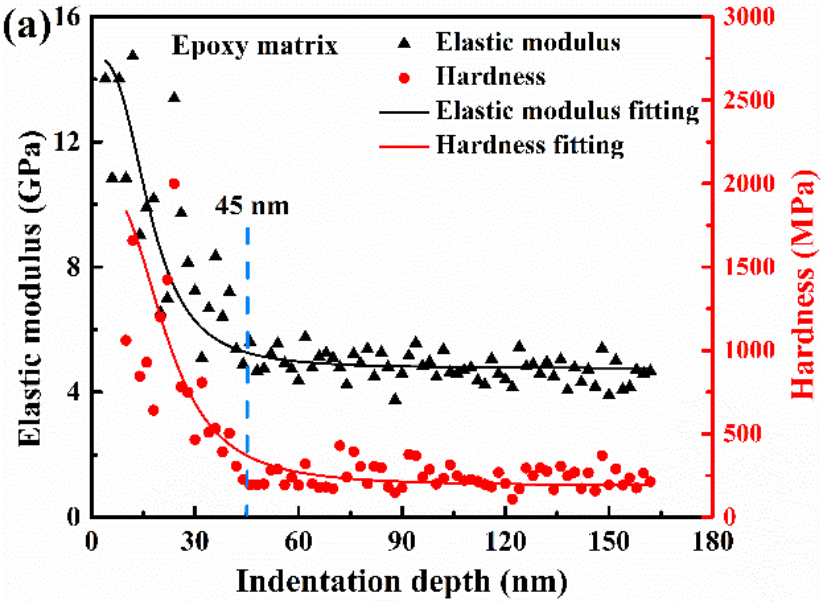

Figure 3.8 Elastic modulus and hardness measured at different indentation depths for (a) epoxy matrix and (b) S2 layer of the sisal fiber.

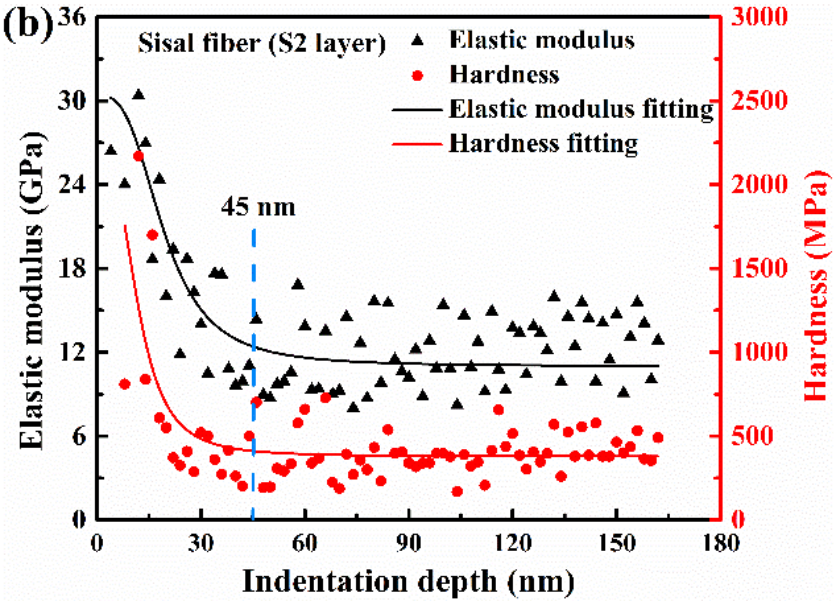

Figure 3.8 (continued).

Figure 3.9 depicts a series of load-depth curves obtained from indents at different locations from the single-step nanoindentation tests as highlighted in the insert and **Figure 3.3** (b). Results from the load-depth curves revealed distinct responses for the different measured points corresponding to different constituent materials (identified by *OM* observation), e.g., matrix or lumen, cell wall layers (P, S1, S2 or S3 layer) of sisal elementary fiber, *IF-CW* (P and S1, S1 and S2 or S2 and S3 layer), interfaces between the matrix and cell wall layer (P layer) or those between lumen and cell wall layer (S3 layer) and *CML* zone (*IF-ELE*).

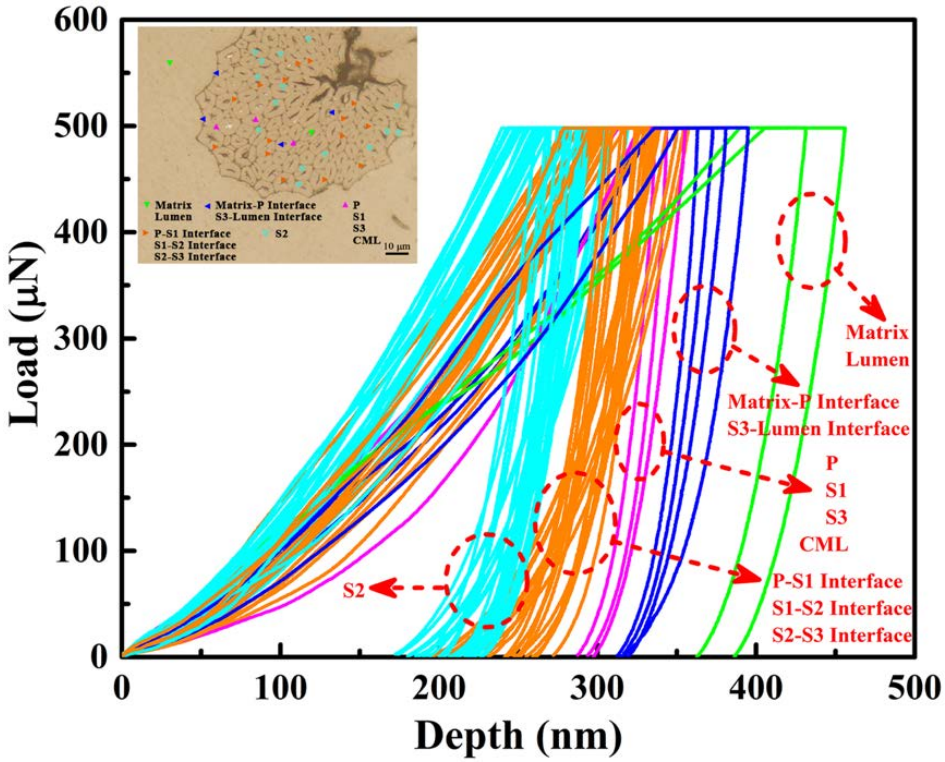

Figure 3.9 Load-depth curves obtained from different points.

To characterize variations of the nano-mechanical properties of each cell wall layer in detail, elastic modulus and hardness measured from different points (as indicated in **Figure 3.10** (a)) on the cross sections of *SFRCs* are plotted in **Figure 3.10** (c)-(d). *AFM* image of one typical indent with the geometry dimension is comparably shown in **Figure 3.10** (b). The indents were conducted with a spacing of 2 μm (**Figure 3.10** (a)) and a depth of 200 nm (**Figure 3.10** (b)) to avoid the effect of previous indentations on the subsequent indentations.

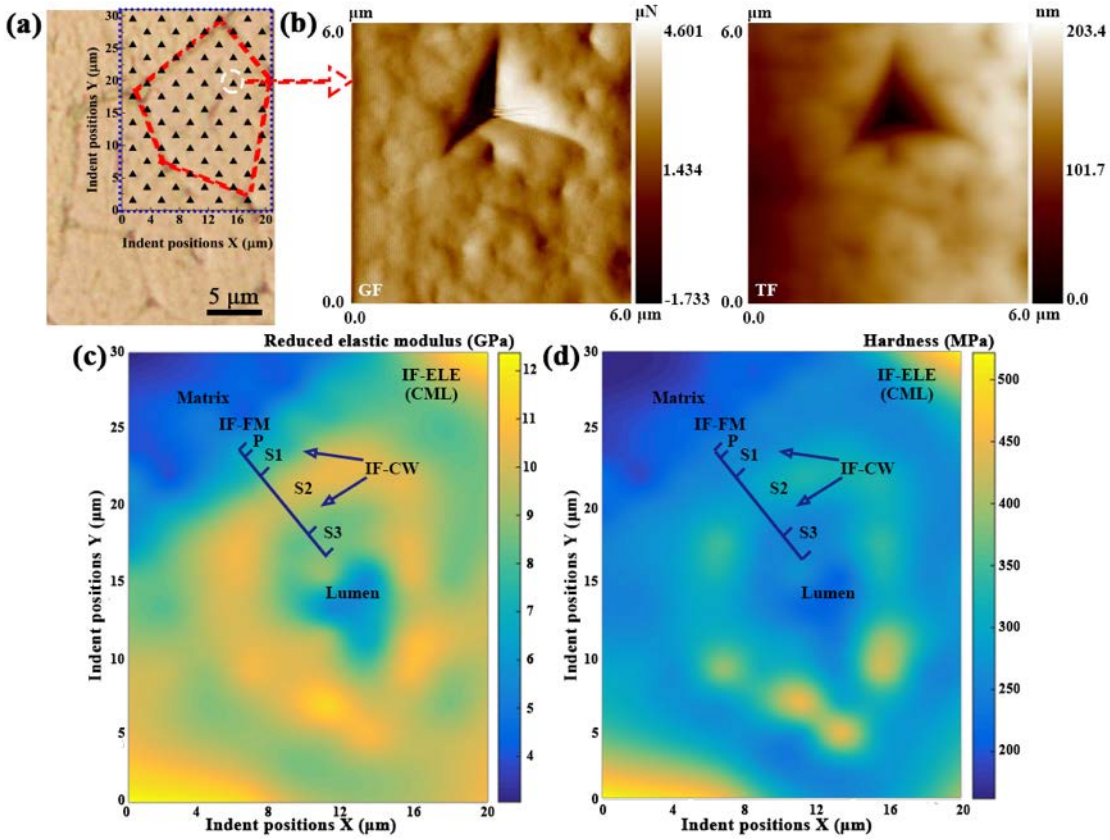

Figure 3.10 (a) Distributions of intents on the epoxy matrix and a sisal elementary fiber of the *SFRC*, (b) *AFM* image of a typical indent, cartography of (c) reduced elastic modulus and (d) hardness for the *SFRC*.

Figure 3.10 (c) and (d) depict the cartography (processed by commercial *MATLAB* software) of measured modulus (the reduced elastic modulus) and hardness at different points of the epoxy matrix and sisal elementary fiber, respectively. To note a good correlation between the fiber morphology (as shown in **Figure 3.10** (a)) and the reduced elastic modulus and hardness profiles (as shown in **Figure 3.10** (c) and (d)). The existence of lumen areas, as revealed by the cartography results, led to a significant decrease on the values of the reduced elastic modulus and hardness. In addition, the values measured in the lumen areas were close to those of the pure epoxy matrix, which indicated that the resin might penetrate into the fiber lumens during the manufacturing processing of the sample **[32]**. It can be noticed that the elastic modulus

and hardness augment with an increase of the distance away from lumen first (from S3 to S2 layer) and then reduced gradually (from S2 to P layer). The thickness of these layers (i.e., S3, S2, S1 and P layer) were quantitatively identified as 2, 5, 2 and 0.5 μm, respectively, featuring a multi-layer and multi-scale structure. As known, density distribution of the sisal fiber is not the same **[24]**, which is arising from two causes: random distributed voids and non-uniform distributions of the chemical compositions in different positions of natural fibers due to their natural growth characteristics. Therefore, the non-uniform density distribution further leads to the non-uniform distribution of modulus and hardness of the sisal fiber.

It can be seen in **Figure 3.10** (c) and (d) that the region associated with the S2 layer with the largest values of thickness, modulus and hardness, compared to other cell wall layers, was clearly identified in these two figures. Considering the S2 layer contains the most cellulose of the sisal fiber **[157]**, therefore, S2 layer plays an important role on determining the mechanical properties of the sisal fiber. To conclude, the modulus and hardness of epoxy matrix and each cell wall layer of the sisal elementary fiber in the *SFRCs* showed significant differences in between.

From previous analysis, different cell wall layers in the sisal elementary fiber possess distinct modulus and hardness. To achieve a quantitative analysis, the average reduced elastic modulus and hardness measured from scanning points starting from epoxy matrix to each cell wall layer of elementary fibers including related interfaces are comparatively calculated and depicted in **Figure 3.11**. The indents were performed with the same spacing and depth as described in **Figure 3.10**. Each point presented in

Figure 3.11 was the averaged result of at least 30 indents. The transition points regarding reduced modulus and hardness indicate transition positions between different constituents of the *SFRCs*, for instance the interfaces (i.e., *IF-FM* and *IF-CW*) from matrix to lumen and those from lumen to *CML* (i.e., *IF-CW* and *IF-ELE*), which were consistent with observations on the microstructure of *SFRC* as shown in **Figure 3.10**. Specifically, a transition region was first observed between the matrix and P layer (as circled in **Figure 3.11**), which possessed nano-mechanical properties intermediate between those for the matrix and P layer, which can be regarded as the interphase of *IF-FM*. Other two transition regions were observed between the S1 and S2 layer and between the S2 and S3 layer, respectively, referred to the interphases of *IF-CW*. Since *CML* connected each elementary fiber as described in previous illustration (**Figure 2.3**), the nano-mechanical properties of *CML* were considered to be the same as those of *IF-ELE*. In addition, combining the results illustrated in **Figure 3.10** and **Figure 3.11,** the reduced modulus and hardness of the *IF-FM* were lower than those of the *IF-ELE* and *IF-CW*, which was attributed to the weaker interfacial bonding between hydrophilic sisal fibers and hydrophobic epoxy matrix, while those of the *IF-ELE* was lower than those of the *IF-CW* due to that *CML* with relative low strength binds each elementary fiber. Regardless of difficulties in accurately measuring the interfacial properties of the three interfaces with thickness varying between 0.1 and 1 μm, the elastic modulus and hardness measured in the nanoindentation experiments were meaningful to quantitatively estimate the range of these regions.

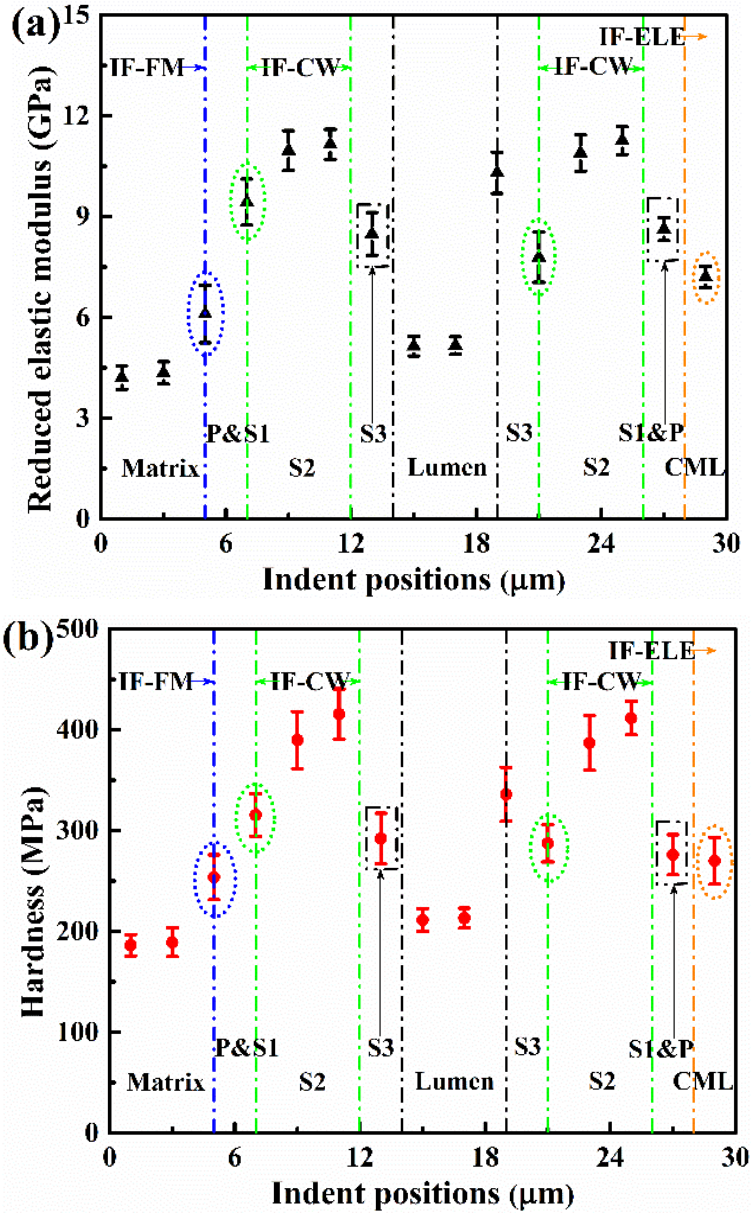

Figure 3.11 Distributions of (a) reduced elastic modulus and (b) hardness of the *SFRC* regarding indent positions.

3.4. Interfacial failure mechanisms of *SFRCs* in single-step and multi-step nanoindentation

Figure 3.12 (a) presents the variations of W_{pl}/W_t of the three types of interfaces in the *SFRCs* (as illustrated in **Figure 3.4**) upon subject to the maximum indentation

loads increasing from 200 to 9000 μN in the single-step nanoindentation experiments. W_{pl}/W_t obtained from the nanoindentation measurements was termed as the specific damping capacity in this study, reflecting the capability of energy dissipation **[158]**. It can be observed that the ratio of W_{pl}/W_t was on an overall increasing trend with the increases of indentation loads for all the three interfaces, which suggested that the interface underwent a plastic deformation and the plastic zone expanded with increasing indentation load. Notably the slope of the curves suddenly increased with an augment in the indentation load after critical indentation loads (2400 μN for *IF-FM*, 5200 μN for *IF-ELE* and 6800 μN for *IF-CW*), which can be attributed to the occurrence and propagation of cracks upon the indentation loads exceeded the fracture loads of the interface. Thus, the energy dissipation enhanced through synergistic effects of plastic deformation and crack initiation and propagation at these loading conditions. Meanwhile, W_{pl}/W_t of the *IF-FM* was found lower than that of the *IF-ELE* and *IF-CW*, which suggested the capability of energy dissipation for the *IF-FM* was weaker than the other two interfaces in the *SFRCs*. The weak capability of energy dissipation for the *IF-FM* led to a longer propagation distance of cracks, which was more prone to inducing the damage initiation in the *IF-FM*. Thus, the indentation load initiating the damage (i.e. crack) in the *IF-FM* was lower than that in the *IF-ELE* and *IF-CW*, suggesting the bonding of the *IF-FM* was weaker than the other two interfaces in the *SFRCs*. The earlier crack initiation and propagation in the *IF-FM* led to the enhancement of energy dissipation, which resulted in the faster increasing rate of the ratio of W_{pl}/W_t for the *IF-FM* as shown in **Figure 3.12** (a). **Figure 3.12** (b) plots relevant ratios of hardness to reduced elastic modulus (H/E_r) along with ratios of

W_{pl}/W_t obtained from **Figure 3.12** (a) on the three interfaces of *SFRCs*. The ratio of H/E_r can be used to describe the deformation properties of the materials **[158]**. Observations on **Figure 3.12** (b) reveal distinct mechanical properties of the three interfaces. *IF-FM* possessed a highest ratio of H/E_r compared to the other two interfaces, indicating the reversible (elastic) deformation was predominant, which resulted in the weakest capability of energy dissipation (a lowest ratio of W_{pl}/W_t) for the *IF-FM*. This phenomenon also evidences earlier damage initiation occurred in the *IF-FM*.

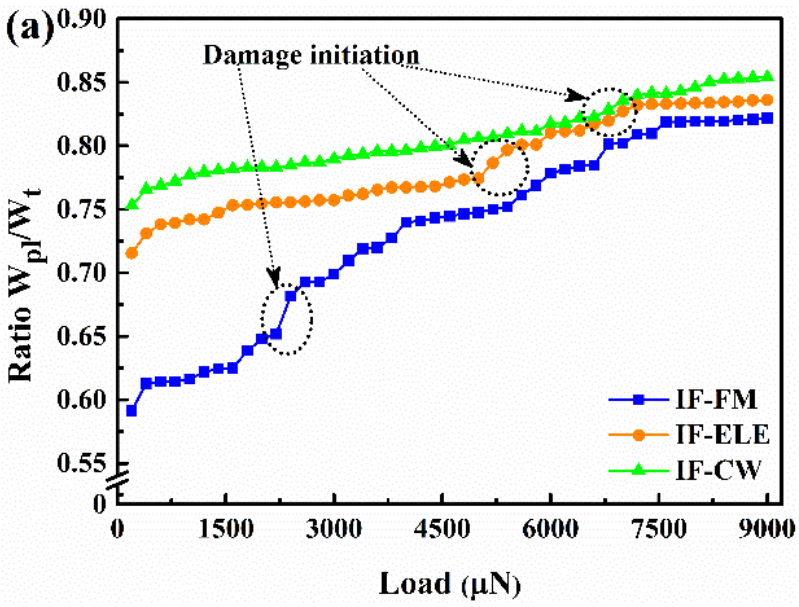

Figure 3.12 Comparison of relationships in terms of (a) W_{pl}/W_t *vs*. indentation loads and (b) W_{pl}/W_t *vs*. H/E_r for the three interfaces obtained from single-step nanoindentations.

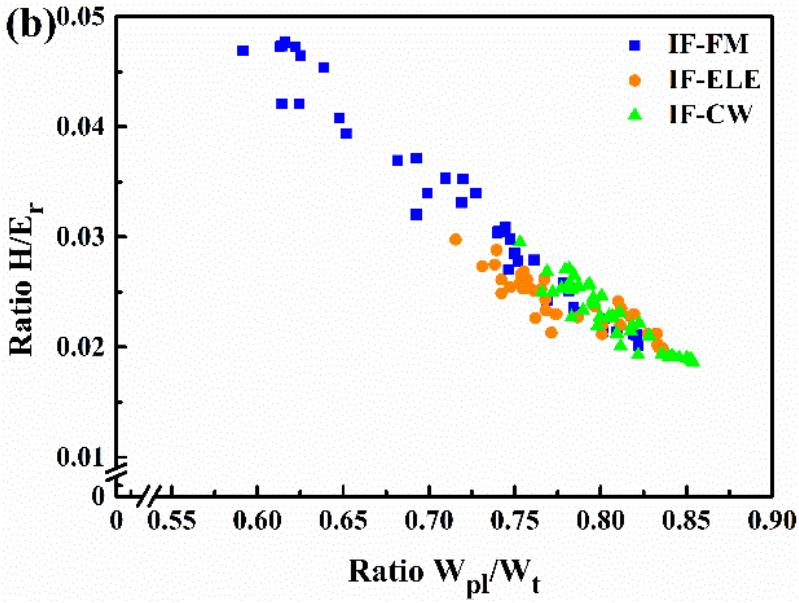

Figure 3.12 (continued).

Multi-step nanoindentation experiments could provide a rapid and direct evaluation of variation of nano-mechanical properties under cyclic fatigue loads. **Figure 3.13** (a) depicts the typical load-depth curves obtained from the three types of interfaces from the multi-step nanoindentation measurements. **Figure 3.13** (b) illustrates the change of the ratio of W_{pl}/W_t when the maximum indentation loads increased from 200 to 9000 μN as showed in **Figure 3.13** (a). From the results obtained by the multi-step nanoindentation experiments, a material hardening phenomenon presented for the three interfaces, manifested as decreasing ratios W_{pl}/W_t with increasing indentation loads. However, converse increasing trends occurred when the indentation loads exceeded specific values (4600 μN for *IF-FM*, 7000 μN for *IF-ELE* and 8000 μN for *IF-CW*), which can be attributed to the occurrence of cracks when the indentation load exceeded the material endurance. The transition points regarding the ratio of W_{pl}/W_t for the *IF-ELE* and *IF-CW* occurred at higher indentation loads compared

to that for the *IF-FM*. This indicated the weaker bonding of *IF-FM* and the conclusion was consistent with that from the single-step nanoindentation measurement. Notably the critical indentation loads obtained from the multi-step nanoindentation measurements were larger than those obtained in the single-step nanoindentation experiments, owing to the augment in the yield strength of interface induced by hardening, indicating progressively increasing nanoindentation loads could delay the occurrence of cracks in the interfaces of *SFRCs*.

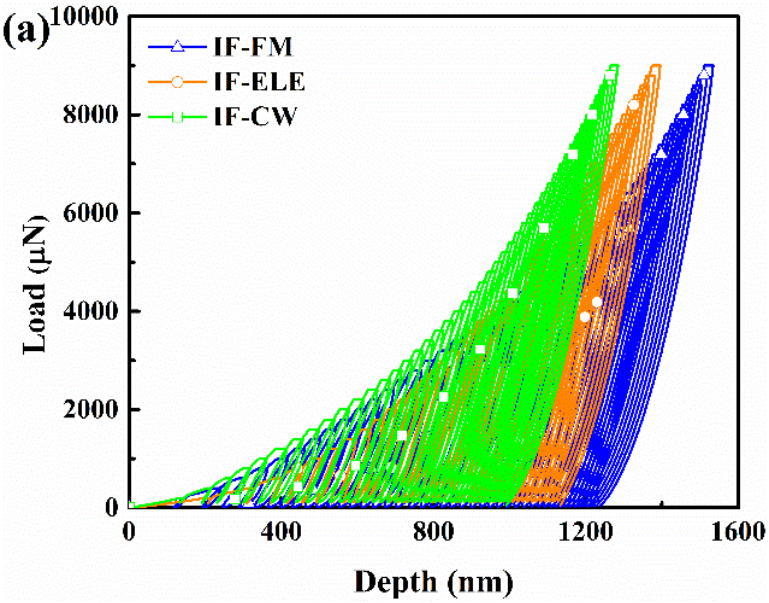

Figure 3.13 Comparison of (a) load-depth curves and relationships in terms of (b) W_{pl}/W_t vs. indentation loads for the three interfaces obtained from multi-step nanoindentations.

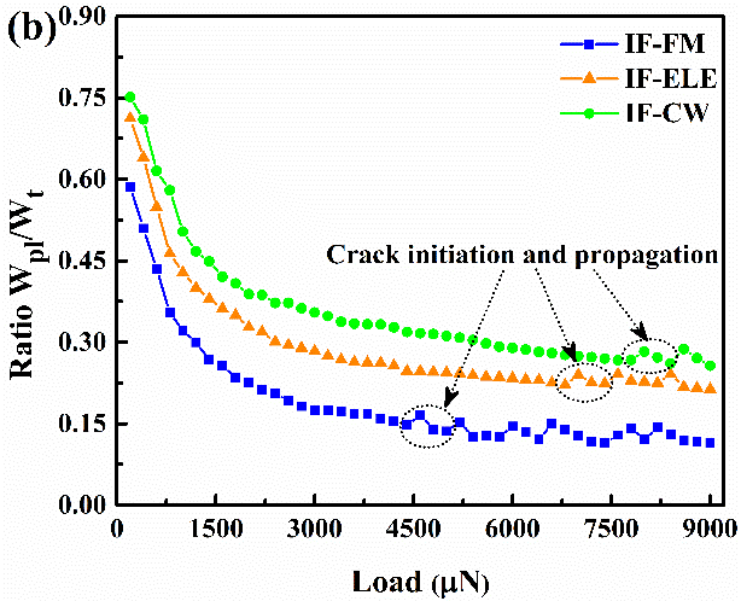

Figure 3.13 (continued).

Cyclic nanoindentation loading conducted in a localized region can provide accurate information regarding dynamic damage phenomena of distinct constituents in the *SFRCs* with a multi-layer structure. To clearly clarify the failure process of the three interfaces when subject to fatigue loads, the cyclic nanoindentation experiments were carried out on the three interfaces in the following part.

The failure process of the three interfaces subject to cyclic loadings with constant peak loads in the range from 200 to 9000 μN were investigated through the cyclic nanoindentation measurements. The ratios of W_{pl}/W_t at each cycle were comparably obtained from four cyclic loading tests with constant peak loads of 600, 2000, 4400 and 6200 μN on the three interfaces as showed in **Figure 3.14** (a)-(d), respectively. In **Figure 3.14** (a), the ratios of W_{pl}/W_t for the three types of interfaces under the peak indentation load of 600 μN all followed a declined trend, which was

a phenomenological demonstration of material hardening during deformation. While the highest ratio of the *IF-CW* and the lowest ratio of the *IF-FM* indicate the strong capability of energy dissipation and strong bonding for the *IF-CW* while the opposite trend for the *IF-FM* in the *SFRCs*, this agreeing with previous analysis. With the increase of the peak indentation loads (**Figure 3.14** (b)), obvious fluctuations of the ratio of W_{pl}/W_t on the *IF-FM* firstly occurred, which were associated with the initiation and propagation of the cracks. The cracks propagated after 10 loading cycles and induced an increase in the ratio W_{pl}/W_t. When the peak indentation load reached 4400 μN, the ratio of W_{pl}/W_t for the *IF-ELE* began to fluctuate after 13 loading cycles as plotted in **Figure 3.14** (c), which indicates that the cracks initiated later than those on the *IF-FM*. Finally, when the indentation load continued increasing to 6200 μN, as depicted in **Figure 3.14** (d), fluctuations in the ratio of W_{pl}/W_t presented for all three interfaces. In addition, notably the critical indentation loads obtained from the cyclic nanoindentation measurements were less than those obtained in the single-step nanoindentation experiments, indicating cyclic nanoindentation loading could accelerate the crack initiation and propagation in the interfaces of *SFRCs*. Since the bonding between the elementary fiber and epoxy matrix was weaker than the other two interfaces in the *SFRCs* as mentioned in section 3.3, cracks were more prone to initiate on the *IF-FM*. In other words, a weaker interfacial strength for the *IF-FM* resulted in a lower critical indentation load for the *IF-FM*. Fatigue resistance of the three interfaces differed from each other, due to different interfacial constituents which possessed distinct interfacial strengths. Therefore, when the *SFRC* was subject to fatigue loading, failures of *IF-FM*, *IF-ELE* and *IF-CW* caused by crack initiation

and propagation would not present at the same time, which could be further associated with multi-stage fatigue failure behaviors of *SFRC* laminates in macro-scale **[26, 159]**.

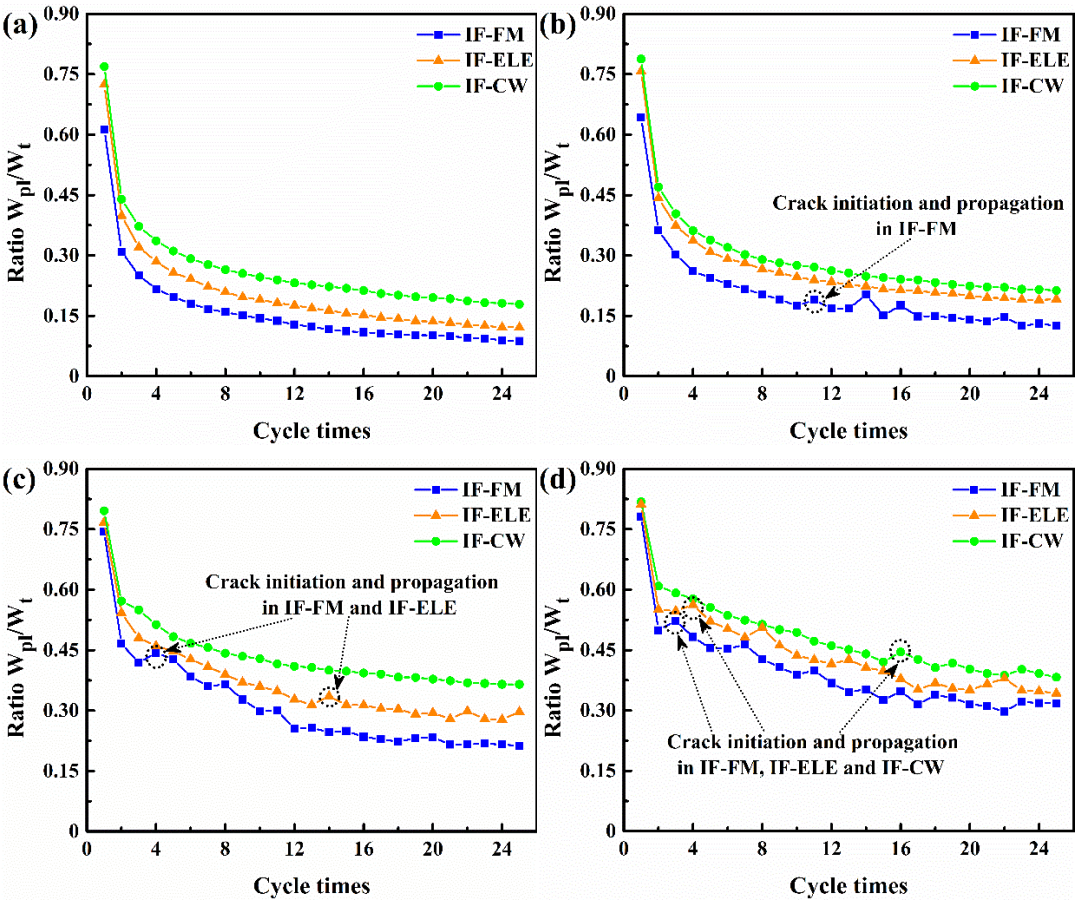

Figure 3.14 W_{pl}/W_t over cycle times obtained with indent forces of (a) 600, (b) 2000, (c) 4400 and (d) 6200 μN for the three interfaces.

To validate the previous discussion, the morphologies of cracks on the three interfaces of *SFRCs* upon subject to fatigue loading were illustrated by *SEM* observation as presented in **Figure 3.15** (a)-(c). The cracks first occurred on the *IF-FM* after 10 cycles with a peak fatigue load of 2000 μN at the lower loading zone (**Figure 3.15** (a)), then the cracks at the *IF-ELE* appeared at the middle loading zone after 13 cycles with a peak fatigue load of 4400 μN (**Figure 3.15** (b)), and finally the cracks could

be observed on the *IF-CW* at the higher loading zone (**Figure 3.15** (c)) after 15 cycles with a peak fatigue load of 6200 μN.

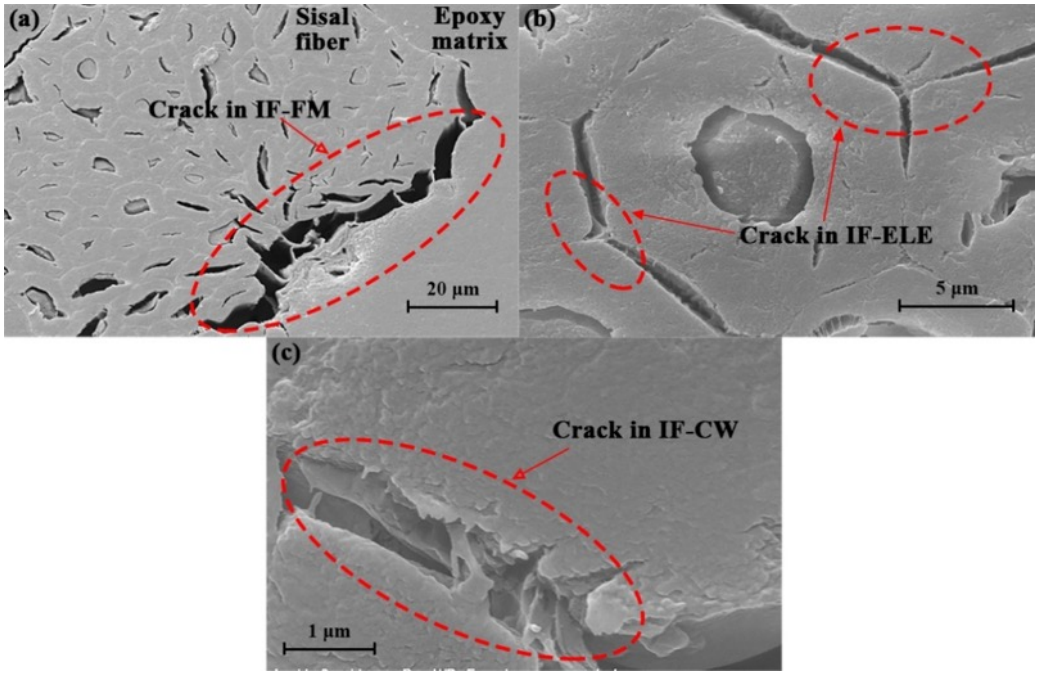

Figure 3.15 *SEM* photographs of cracks on the three interfaces: (a) *IF-FM*, (b) *IF-ELE* and (c) *IF-CW* for *SFRCs* subject to the cyclic indentation loads.

To conclude, the multi-layer and multi-scale structure of sisal fibers could effectively and progressively dissipate energy at the interfaces. Such phenomenon can delay the interfacial failure and improve the resistance abilities of *SFRCs* when subject to fatigue alternating loads.

3.5. Interfacial failure mechanisms of *SFRCs* in *nano-DMA*

Static nano-mechanical properties of *SFRCs* have been investigated in the last two sections. As discussed in section 3.4, the multi-step nanoindentation experiments

could be approximately equivalent to a kind of fatigue tests. The elastic modulus and hardness in each step were recorded but few data could be used to analyze the trends of nano-mechanical properties with the increase of cyclic loading. In addition, the static nanoindentation test is performed at a low frequency (about 1 Hz), and the effect of high frequency on the variation in material properties cannot be achieved. The appearance of dynamic indentation measurements could help provide some useful information on the change of nano-mechanical properties during the continuous loading process. Nanoscale fatigue also can be achieved by using the *CSM* technique in nanoindentation tests. The *CSM* technique provides force cycles of a sinusoidal shape at high frequencies that can be used to perform nanoscale fatigue tests. The evaluations of the multi-layer interfacial fatigue failure of plant fibers in nanoscale have sound significance on better understanding the interfacial failure mechanisms and damage behaviors of the composites in the macro-mechanical experiments. Based on the above, in this section, the time-dependent response and the viscoelastic and fatigue behavior of the multi-layer cell wall in *SFRCs* were measured by *nano-DMA*. The changes of the dynamic mechanical properties (i.e., storage modulus and loss factor $tan\ \delta$) in three types of interfaces (i.e., *IF-FM*, *IF-ELE* and *IF-CW*) as increasing of the frequencies in varying applied indentation loads (**Figure 3.16** and **Figure 3.17)** and those as increasing of the number of cycles in varying applied indentation loads (**Figure 3.18** and **Figure 3.19**) and oscillation frequencies (**Figure 3.20** and **Figure 3.21**) were captured with this approach.

This section firstly investigates the nano-dynamic mechanical performances of three types of interfaces in *SFRCs* over the oscillation frequency range from 5 to 285 Hz

with the increase amplitude of 5 Hz. Taking into account the results of the static multi-step nanoindentation experiment in section 3.4 and the high frequency under the dynamic nanoindentation test, the lower load conditions with the same oscillation load amplitude of 490 μN were selected for dynamic measurements in this section. **Figure 3.16** and **Figure 3.17** (a)-(c) show the variations of the storage modulus and loss factor $tan\ \delta$ on the three types of interfaces of *SFRCs* with the increasing oscillation frequency under different oscillation loads (500, 1000 and 1500 μN), respectively. It can be observed that the storage modulus of the three types of interfaces had no change under various oscillation loads and lower oscillation frequency, which mainly resulted from the fact that the storage modulus obtained in the dynamic nanoindentation test is essentially the Young's modulus. The storage modulus is the index of the rebound of the material after deformation and can reflect the ability of the material to store the elastic deformation energy. The results exhibited that the storage modulus of the *IF-FM* was the lowest, and that of the *IF-ELE* and *IF-CW* interface improved sequentially, which was consistent with the phenomena in section 3.3. It can be also seen that the abrupt decrease in storage modulus when the oscillation frequency reached a certain value under the same oscillation load. Under the lower oscillation load condition (500 μN as seen in **Figure 3.16** (a)), only the storage modulus of the *IF-FM* interface decreased at an oscillation frequency of 275 Hz, indicating that crack initiation and propagation may occur at this time. With the increase of oscillation load (1000 μN as seen in **Figure 3.16** (b)), the turning point for the decline of the storage modulus of the *IF-FM* interface was advanced to the oscillation frequency of 235 Hz, while that of the *IF-ELE* interface was at the

oscillation frequency of 265 Hz. Then the storage modulus of the three types of interfaces all showed a downward trend under the higher oscillation load condition (1500 μN as seen in **Figure 3.16** (c)), but occurring at the oscillation frequency of 205 Hz (*IF-FM*), 225 Hz (*IF-ELE*) and 250 Hz (*IF-C*W), respectively. In fact, the oscillation frequency is related to the number of cycles, and the effect of the increase of the number of cycles can be equivalent to the improvement of oscillation load. Therefore, the experimental phenomena obtained in the nano-*DMA* test were the same as those in the static multi-step nanoindentation test in the previous section, that is to say, the three types of interfaces for the *SFRCs* would not be simultaneously failure under dynamic indentation loading conditions. The loss factor is defined as the tangent of the phase difference between the strain and the stress cycle of the viscoelastic material under the alternating force field. It is the ratio between the energy dissipated per cycle and the maximum energy stored in a cycle, and also equal to the ratio of loss modulus to storage modulus of the material. The loss factor can demonstrate the state and the viscoelastic property of the material within a certain range. The smaller the loss factor, the greater the elasticity of the material, otherwise the greater viscosity. Meantime, the loss factor is positively related to the loss angle, and the magnitude of the loss angle represents the amount of energy loss under dynamic deformation. The loss factor can also reflect the damping performance of the material on another level. It is generally considered that the best damping performance of the material occurs when the loss modulus is equal to the storage modulus, that is, the loss factor tending to 1. The crack initiation and propagation can make the energy dissipation enhanced and increase the loss modulus, thus, the loss factor suddenly increased when the storage modulus abruptly decreased, as shown in **Figure 3.17**.

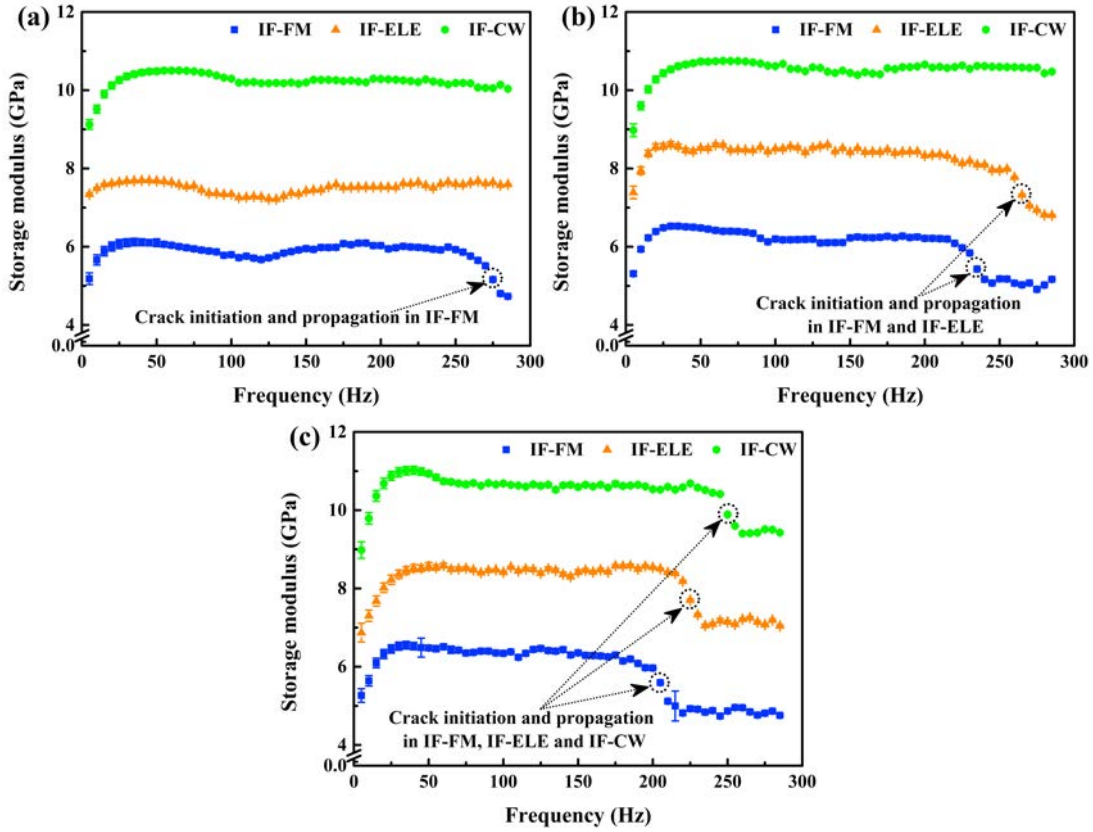

Figure 3.16 Storage modulus as a function of the oscillation frequencies on three types of interfaces for the *SFRCs* in different oscillation loads: (a) 500, (b) 1000 and (c) 1500 μN.

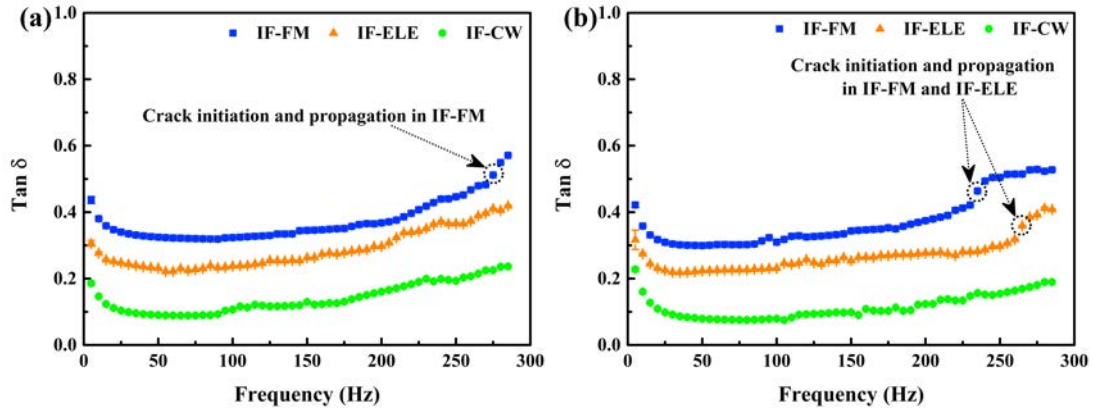

Figure 3.17 $Tan\ \delta$ as a function of the oscillation frequencies on three types of interfaces for the *SFRCs* in different oscillation loads: (a) 500, (b) 1000 and (c) 1500 μN.

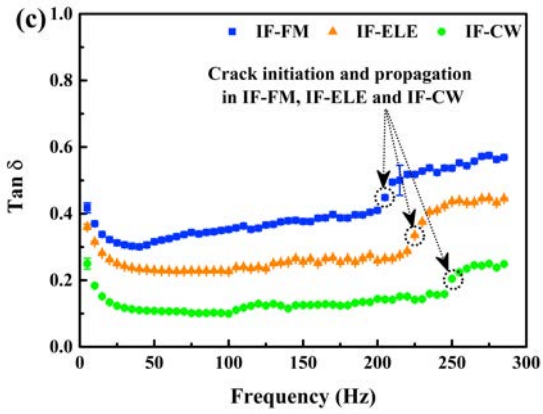

Figure 3.17 (continued).

Subsequently, in order to investigate the differences in the degree of fatigue accumulation between the three types of interfaces, referring to the above results on oscillation frequency, the value below the lowest frequency (205 Hz) where the interfacial failure occurs was selected as the oscillation frequency in the following test, while the oscillation loads were consistent with the above results. **Figure 3.18** and **Figure 3.19** (a)-(c) show the storage modulus and loss factor on the three types of interfaces of *SFRCs* performing the nanoscale fatigue experiments with the same oscillation frequency (180 Hz) but various oscillation loads (500, 1000 and 1500 μN). The different fatigue performance responses of three types of interfaces are clearly presented in **Figure 3.18** and **Figure 3.19**. The fatigue behaviors and interfacial failure properties of each interface within *SFRCs* are studied by monitoring the changes of storage modulus and detecting the differences in loss factor for the three types of interfaces. With the increase of the number of cycles, the earlier interfacial failure between technical fiber and matrix can be seen in **Figure 3.18** and **Figure 3.19** due to weaker bonding between hydrophilic sisal fibers and hydrophobic epoxy resin, which is consistent with the previous discussions. It can be seen that for the higher load conditions (**Figure 3.18** and **Figure 3.19** (c)), the decreased storage

modulus and the increased loss factor all occurred at the three types of interfaces when the number of cycles reached 104 (*IF-FM*), 158 (*IF-ELE*) and 183 (*IF-CW*) thousand cycles, respectively. This further confirmed the inconsistent fatigue failure sequence of the three types of interfaces.

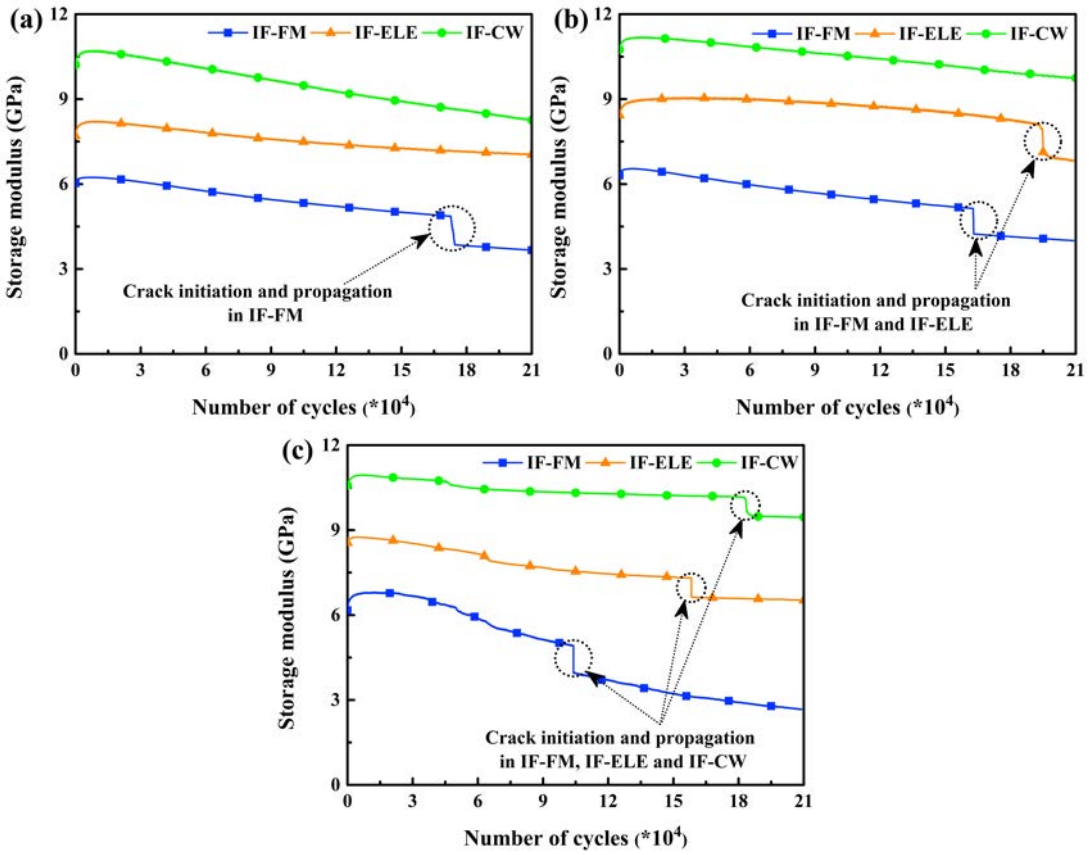

Figure 3.18 Storage modulus as a function of the number of cycles on three types of interfaces for the *SFRCs* in different oscillation loads: (a) 500, (b) 1000 and (c) 1500 μN .

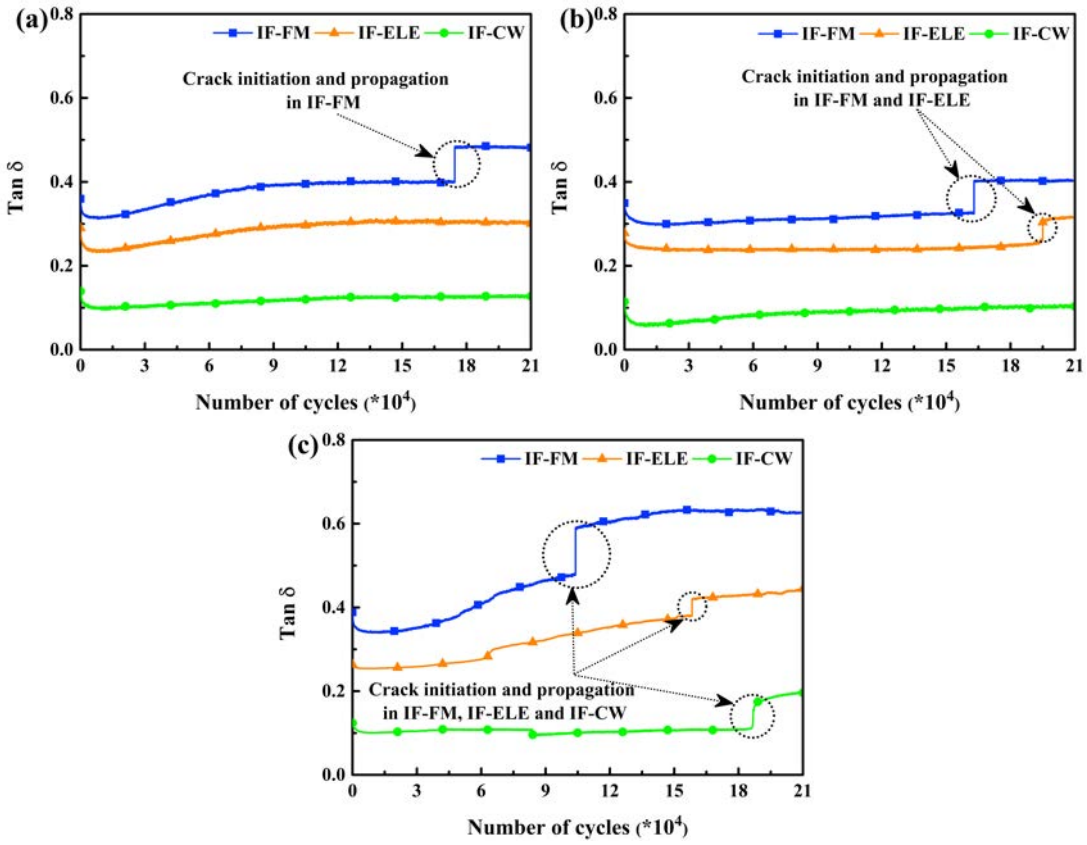

Figure 3.19 $Tan\ \delta$ as a function of the number of cycles on three types of interfaces for the *SFRCs* in different oscillation loads: (a) 500, (b) 1000 and (c) 1500 μN.

Furthermore, **Figure 3.20** and **Figure 3.21** (a)-(c) show the storage modulus and loss factor on three types of interfaces of *SFRCs* under the same oscillation load (500 μN) at different oscillation frequencies (180, 220 and 260 Hz). The different responses of the multi-layer interface structure with the change of the oscillation frequency were compared and analyzed. The results indicated that for the higher oscillation frequency (**Figure 3.20** and **Figure 3.21** (c)), the crack initiation and propagation on the *IF-FM*, *IF-ELE* and *IF-CW* interface appeared sequentially when the number of cycles reached 97 (*IF-FM*), 135 (*IF-ELE*) and 176 (*IF-CW*) thousand cycles, respectively. Conclusively, when the *SFRC* was subject to fatigue loading, failures of *IF-FM*, *IF-*

ELE and *IF-CW* caused by crack initiation and propagation would not present at the same time owing to their different interfacial properties. The phenomenon of interfacial failure in sequence indicated gradually energy dissipation at the interface of *PFRCs*, which can effectively improve the abilities of energy dissipation of *PFRCs* during the fatigue experiments and thus change the crack propagation mechanisms. The nano-fatigue data are of critical importance to the design of multi-layer interfaces of *PFRCs* and should receive more attention.

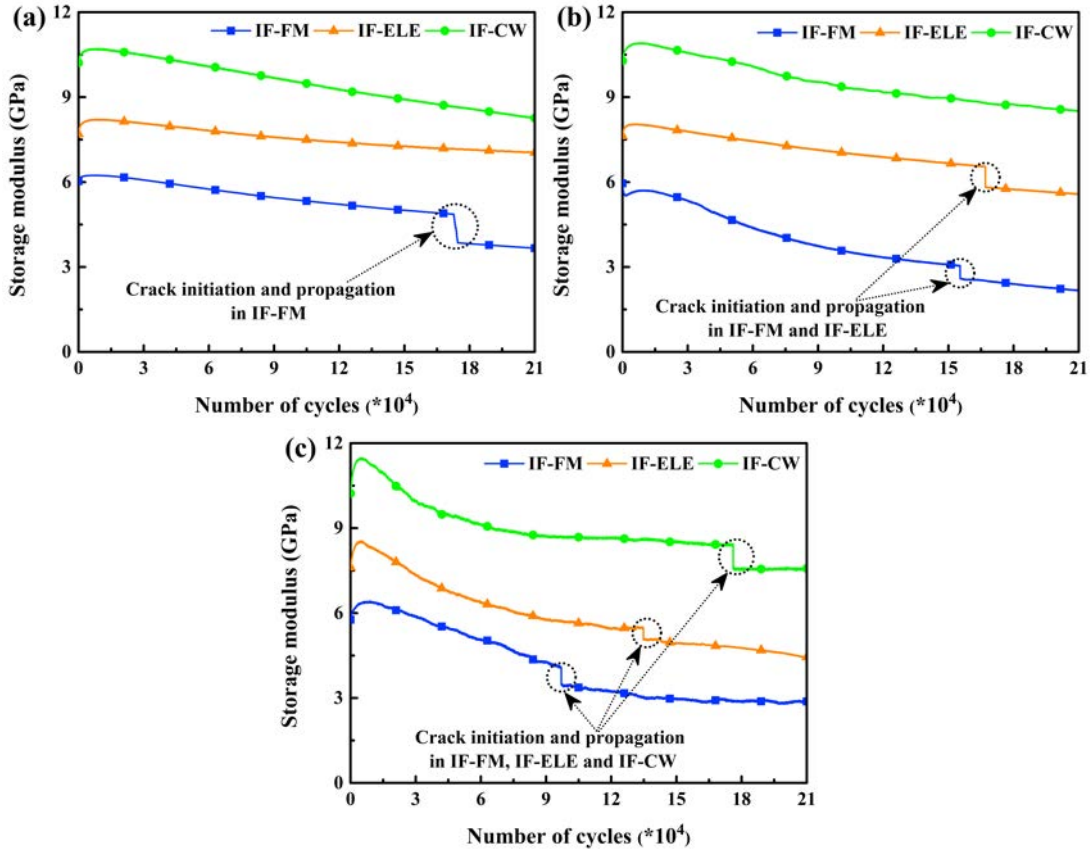

Figure 3.20 Storage modulus as a function of the number of cycles on three types of interfaces for the *SFRCs* in different oscillation frequencies: (a) 180, (b) 220 and (c) 260 Hz.

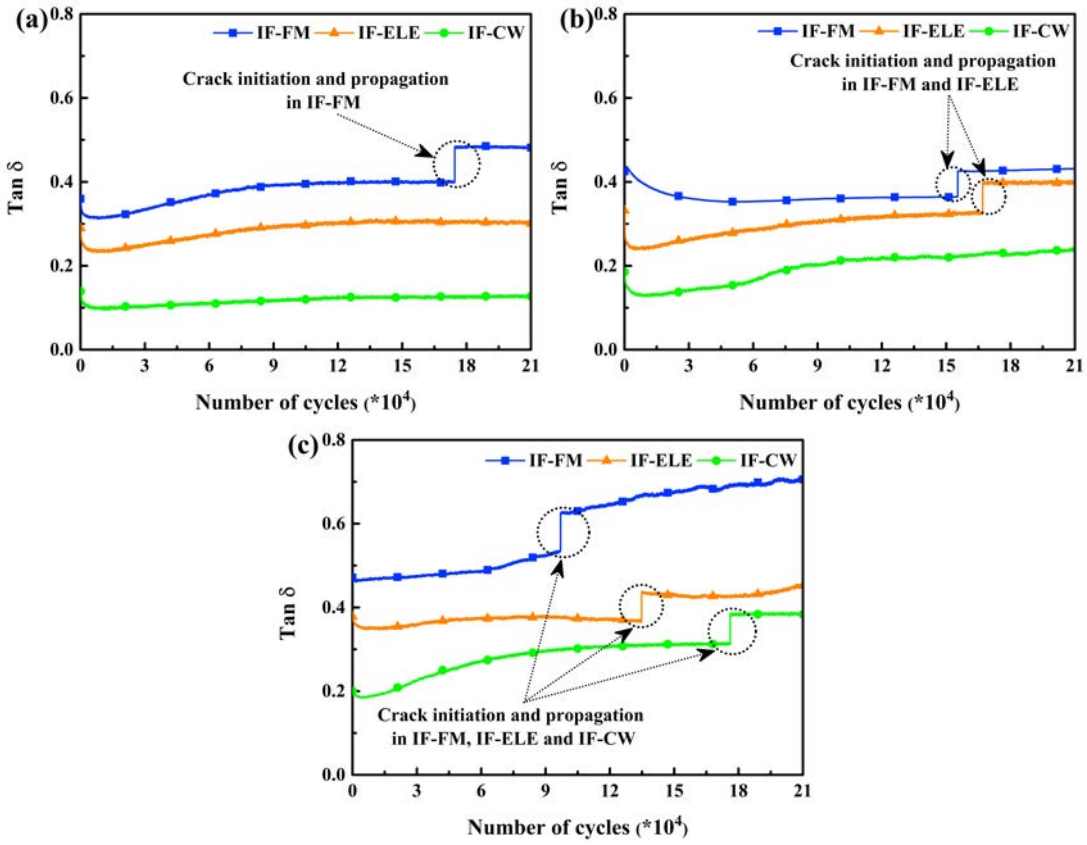

Figure 3.21 $Tan\ \delta$ as a function of the number of cycles on three types of interfaces for the *SFRCs* in different oscillation frequencies: (a) 180, (b) 220 and (c) 260 Hz.

3.6. Summary

The multi-layer structure of plant fibers has been revealed qualitatively by qualitative microscopic characterization and associated with multi-stage failure behaviors of *PFRCs*. To facilitate a better understanding of the multi-layer interfacial mechanical performances of *PFRCs*, this chapter measures the transition zones of the multi-layer interface and the interfacial failure load from a nanoscopic point of view, which consequently facilitates a quantitative analysis of fracture mechanisms for *PFRCs* with a multi-layer and multi-scale structure. The following conclusions can be drawn according to the experimental findings.

(1) The unique multi-layer structures of *SFRCs* were firstly presented quantitatively. The nanoscopic mechanical properties, including elastic modulus and hardness of the epoxy matrix and cell wall layers of the sisal fibers and the interfacial mechanical properties of the three types of interfaces, were quantitatively measured by applying the nanoindentation technique. The transition zones, i.e. the multi-layer interfaces of *SFRCs*, were identified by a series of indents derived from the matrix to each layer of sisal fiber cell walls (S1, S2, S3).

(2) The multi-layer and multi-scale structure of the sisal fibers makes their reinforcing composites present the multi-stage interfacial failure behaviors. The abilities of energy dissipation of the multi-layer interfaces and the multi-layer interfacial failure sequence and interfacial failure load were then respectively illustrated and ascertained by combining the single-step and multi-step nanoindentation measurements at various indentation loads. The multi-layer interfacial failure process was identified using multi-step nanoindentation method. New concepts and ideas were obtained to analyze the unique interfacial failure mechanism in *PFRCs*. Results from the single-step nanoindentation experiments indicated the distinct mechanical properties of the constituents of *SFRCs*, which featured a multi-layer and multi-scale structure with different modulus and hardness. The results also suggested the capacity of energy dissipation for the *IF-FM* was weaker than that for the *IF-ELE* and *IF-CW* due to the highest value regarding hardness to reduced elastic modulus of *IF-FM*.

(3) The multi-layer interfacial failure process was identified using multi-step nanoindentation method. The results obtained from the multi-step nanoindentation

experiments on the three interfaces showed a material hardening phenomenon, and the degrees of hardening were different between the three interfaces. The results from the cyclic loading nanoindentation and further observations from *SEM* revealed a multi-stage failure behavior of *SFRCs*. The interface between the sisal fibers and epoxy matrix with a weaker bonding firstly underwent the crack initiation and propagation, then the cracks occurred at the *IF-ELE* with increasing cyclic loading, and finally the cracks presented on the *IF-CW*. To sum up, the existence of multi-interfaces of *SFRCs* possessing distinct mechanical properties introduces the unique multi-layer and multi-scale failure behaviors of *SFRCs*. New concepts and ideas were obtained to analyze the unique interfacial failure mechanism in *PFRCs*.

(4) The evaluation of nano-fatigue properties of the multiple interfaces within *SFRCs* and their differences in the nanofatigue behaviors were achieved by using the cyclic loading with varying applied indentation loads and oscillation frequencies. The change of the oscillation load and oscillation frequency can lead to the different time on occurring the nanofatigue failures. At the same oscillation load and oscillation frequency, the initiation and propagation of cracks at the three types of interface were also different. This phenomenon can be helpful to explain the fatigue damage accumulation rate and crack propagation mechanism of *PFRCs* in fatigue tests compared with traditional *AFRCs*.

In summary, the existence of multiple interfaces of *SFRCs* makes them present unique multi-layer and multi-scale mechanical properties and failure behaviors.

CHAPTER 4

Experimental Investigation on Multi-Layer Interface Debonding Behaviors of Single *PFRC*s in the Pull-Out Test Using *AE* and Statistical Analysis

4.1. Introduction

In Chapter 3, nanoindentation technique has been used to present the multi-layer and multi-scale structural features of *PFRCs*, and to obtain nano-mechanical properties of the multi-layer interfaces of *PFRCs*. The results illustrate the rich designability of the interfaces within *PFRCs*. Researchers have been dedicated to investigating the interfacial properties of *PFRCs* and improving their relevant mechanical properties through modifications of fiber surfaces. However, limited promotion of mechanical

properties of *PFRCs* was reported in the published papers and few studies have comprehensively revealed the interfacial failure mechanisms of *PFRCs* by considering the hierarchical structure of plant fibers, which makes it difficult to obtain *PFRCs* with satisfactory mechanical properties and limits their large-scale industrial applications.

As we all know, the mechanical performances of composite materials, including *PFRCs*, are largely dependent on their interfacial properties owing to the decisive role of the interface in the stress transfer within composite structures **[16, 160]**. Varied micromechanical techniques have been developed to characterize and evaluate the interfacial behaviors of these composites, including single fiber pull-out **[61]**, push-out **[62]**, fragment testing **[63]** and micro-droplet testing **[64]**. Among these, the single fiber pull-out test is widely used in a rich body of academic literature to determine the interfacial debond stresses. Numerous literatures concluded interfacial debonding as an important source of energy absorption during the failure of a composite. *IFSS*, which controls the occurrence and propagation of fiber-matrix debonding, is one of the vital properties used to characterize the interface. During a typical pull-out test of synthetic fiber reinforced composites (i.e., *CFRCs* or *GFRCs*) **[111-113]**, the applied stress firstly increases linearly with increasing displacement until the onset of debonding, followed by a significant drop in the applied stress due to complete debonding of the interface between the fiber and matrix. Consequently, the pull-out test enables the quantitative evaluation of interfacial properties (i.e., fracture toughness, frictional coefficient) between the fiber and matrix.

Meantime, a great amount of studies on evaluating the interfacial failure behaviors of the composites by employing the *AE* method have been reviewed in Chapter 2. *AE* method is reported to exhibit its efficiency in qualitative detection of sudden changes (e.g., the occurrence and propagation of a crack) in a structure. In most reported studies, the macro-, micro- and nano-failure sources during the fracture progressing can be well identified by this nondestructive evaluation technique. Czigany **[161]** examined sensitivity to crack propagation in flax fiber-reinforced polypropylene composites of different moisture content with the help of *AE* method and revealed correlation between the number of acoustic events occurred during debonding and fracture. It indicated that *AE* could provide more likely the quantitative information on the interfacial adhesion and micro-failure. Although an examination of the literature with regards to the application of *AE* to monitor the micromechanical tests of *PFRCs* allows a sounder knowledge of the micro-failure modes, the results are still only focused on the adhesion between the plant fiber and matrix. Kocsis et al. **[162]** used *AE* to detect debonding between wood fibers and the matrix in tensile mode and reported that the number of *AE* counts tended to decrease in poor adhesion between the wood fibers and matrix. The *AE* count distribution showed two local maxima for the slipping of wood fiber and the fiber debonding, whilst the sole debonding was responsible for the large number of *AE* counts. Therefore, along the same line of thinking, *AE* technique can be extended to identify the possible multiple micro-failure behaviors of *PFRCs* caused by the hierarchical structure of plant fibers and to further elucidate the effects of multi-layer and multi-scale structure of *PFRCs* on their interfacial behaviors.

With above motivation, the interfacial debonding behaviors of *SFRCs* were investigated experimentally in this chapter. The single fiber pull-out experiments were applied on *SFRCs* with the multi-layer structure to obtain the load-displacement curves and the maximum debond stresses of *SFRCs* with different embedded fiber lengths. To facilitate the comprehending of the relationship between the fiber structure and the interfacial debonding behaviors of *SFRCs*, the failure process and mechanism of the *SFRCs* in the pulled-out test were monitored and characterized with *AE* technique. Time-frequency analysis on the original *AE* signals were comparably conducted by using Hilbert-Huang transform (*HHT*). The failure modes of the *SFRCs* in the fiber pull-out tests were observed by *SEM*. Finally, statistical analysis was applied to evaluate the probability of multiple debonding and pull-out behaviors and account for the interfacial fracture mechanism of *SFRCs*.

4.2. Sisal technical, elementary fibers and micro-fibrils pull-out experiments and characterizations

Sisal fibers and matrix formulated of epoxy resin, curing agent and accelerator used in this chapter are the same as in section 3.2.1.

The specimens for the single fiber pull-out test were prepared as follows **[32, 163]**. Firstly, the sisal fibers were washed in deionized water at 70 $^{\circ}C$ for 1 h to remove impurities and dried in a vacuum oven at 105 $^{\circ}C$ for 2 h. One thousand dried sisal fibers, the diameters of which were measured by *OM* (10XB-PC) at 100× magnification, were randomly selected (to obtain different fiber fracture modes) and

chopped into two adjacent fibers with 20 mm long. One was used for the single-fiber pull-out test, and the diameter of each fiber was measured by respectively focusing on the upper and lower edge of the fiber to take a picture, then overlap the two pictures to obtain the most accurate projection profile. The average value of three point for the embedded part was considered as the fiber diameter, which was employed on calculating the pull-out stress of each fiber. While the other fiber was used to prepare the metallographic specimens, and the diameter of each fiber was measured with the method illustrated in **Figure 4.1** by *OM*. The average diameters of the sisal fibers were statistically assessed using the Weibull distribution analysis, which were used in the theoretical calculation and numerical simulation in the following chapters. The prepared sisal fibers were separately fastened into a cylindrical silicon rubber mold with dimensions of 20 mm (diameter) $\times$ 20 mm (height) using a sewing needle. The embedded fiber lengths ranged from 100 to 500 μm (see **Figure 4.2**). The mixture of the epoxy resin, curing agent and accelerator was placed in the vacuum oven for 10 min to eliminate air bubbles and then cured in the mold at room temperature for 24 h. Finally, the specimens were carefully removed from the molds and fully post-cured at 60 $°C$ for 2 h.

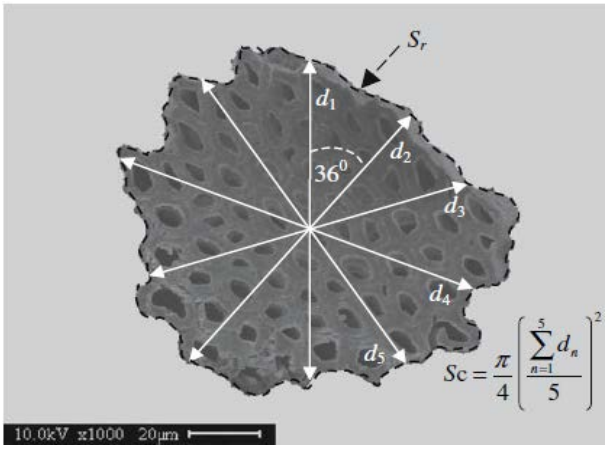

Figure 4.1 Measurement on the diameter of single sisal fiber.

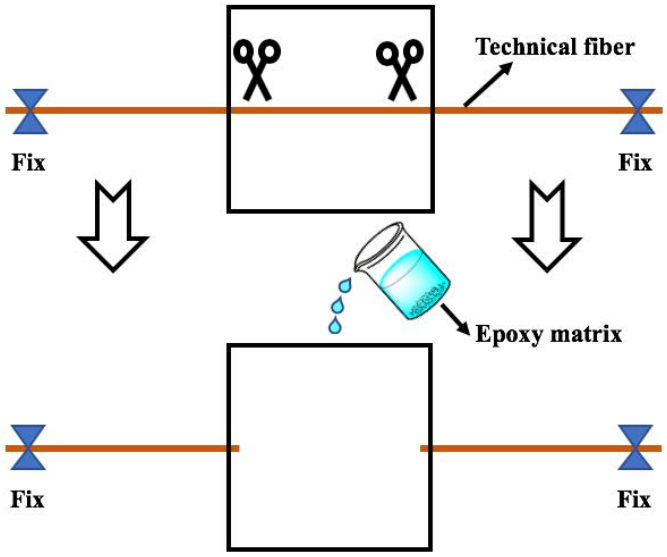

Figure 4.2 Specimen preparation for single sisal fiber pull-out measurements.

After the specimens were prepared, single sisal fiber pull-out tests were performed on a universal mechanical testing machine (Wance, Shenzhen, China) at a crosshead speed of 1 mm/min with a gauge length of 10 mm. The applied force and the displacement were recorded. Then, *AE* monitoring was simultaneously performed in the single sisal fiber pull-out tests to characterize the pull-out failure process of the *SFRCs* by applying an SAEU2S system (Soundwel Technology Co., Ltd, Beijing,

China), test strategy and mechanism of which were illustrated in **Figure 4.3**. *AE* measurements were carried out by employing single SR150M sensor with a resonant frequency range of 10 to 160 kHz and a preamplifier (40 dB) with a bandwidth of 10 kHz to 2 MHz. The threshold was set as 35 dB to exclude the majority signals of background noises. The changes of *AE* signals in the single sisal fiber pull-out tests were recorded at a sampling frequency of 2 MHz.

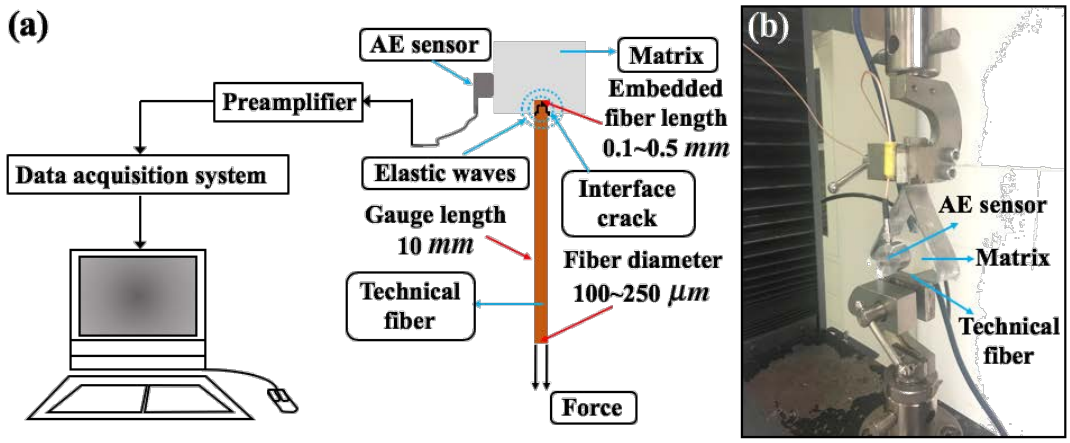

Figure 4.3 (a) Schematic illustration of the principle and mechanism and (b) experimental setup of *AE* in the single sisal fiber pull-out measurement.

After the pull-out tests, the debond lengths of the fibers were measured with an *OM*. The surface morphologic features, microstructures and failure modes of the pulled-out fibers were observed by *SEM* (Jeol-6490, Japan). The surfaces were coated with gold before observation. Based on the above results, statistical analysis was used to evaluate the probability of fiber pull-out and to gain insight into the multi-layer interfacial failure mechanisms of *SFRCs*.

4.3. Single sisal fiber pull-out behaviors of *SFRCs* monitored by *AE* technique

The stress-displacement curves obtained for the sisal fibers with the epoxy matrix during the single fiber pull-out tests are given in **Figure 4.4**. Three different types of stress-displacement curves were observed. At first, all these three curves show a monotonic and typically linear increase in stress until debonding was initiated, followed by an instantaneous stress drop, indicating complete debonding. Then the slowly stress decreasing part followed by the complete debonding was self-explanatory as the fiber was pulled-out from the matrix as presented in **Figure 4.4** (a). Whereas, the stress began to continue to improve as seen in **Figure 4.4** (b) and (c), but not as much as the first increase. The third rising and sudden declining could be observed in **Figure 4.4** (c), and at final, the gradually declining portion of the debond stress versus displacement curve occurred as duplicated in **Figure 4.4** (a). Probable reasons can be demonstrated from the observation of *SEM* (see **Figure 4.5**). Technical fiber (**Figure 4.5** (a)), elementary fibers (**Figure 4.5** (b)) and micro-fibrils (**Figure 4.5** (c)) in the *SFRCs* all can be pulled-out from the matrix.

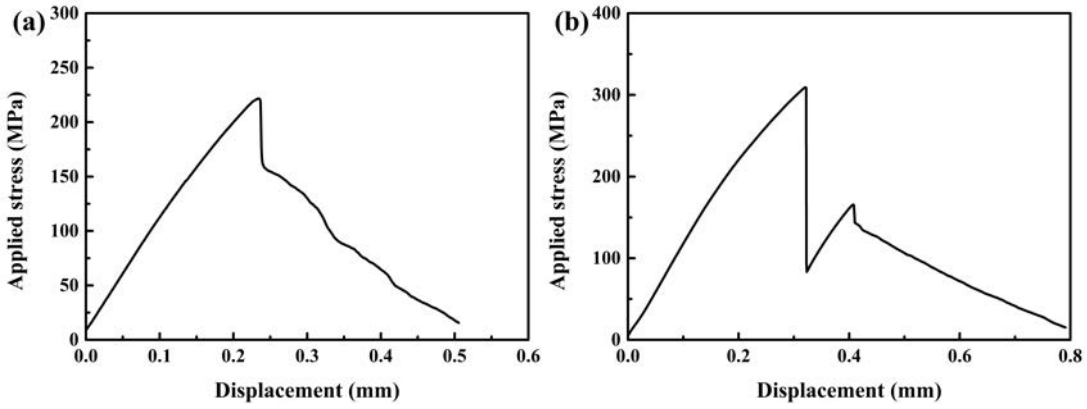

Figure 4.4 The applied stress-displacement curves for the single sisal fiber pull-out with (a) single-, (b) double- and (c) triple-stage pull-out and fracture.

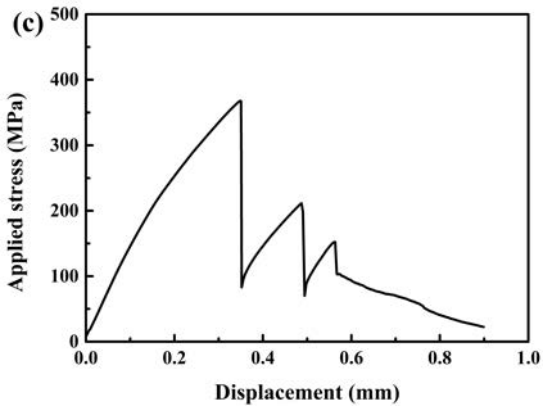

Figure 4.4 (continued).

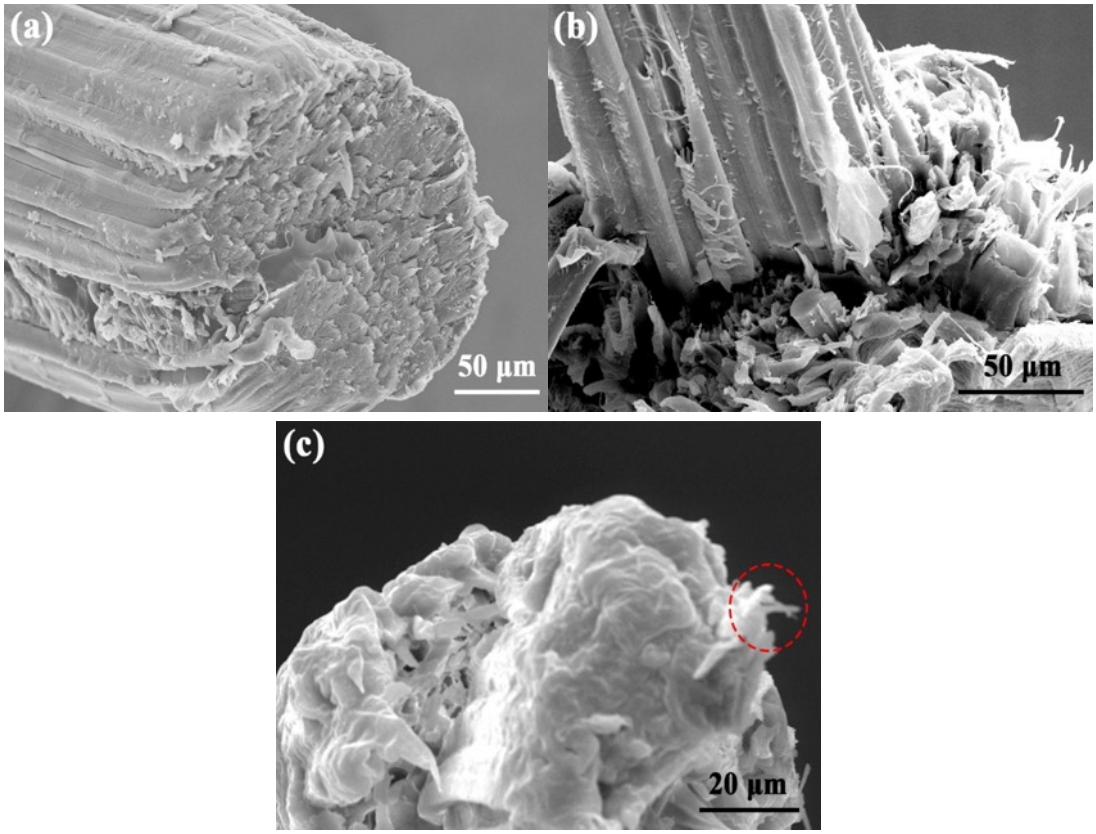

Figure 4.5 *SEM* photographs of pulled-out sisal fibers after single fiber pull-out tests: (a) technical fiber, (b) elementary fibers and (c) micro-fibrils pull-out.

To surveil the failure modes and fracture behaviors of *SFRCs* during the process of single fiber pull-out, the *AE* technique was employed on monitoring and characterizing. A series of plots were generated for the *AE* events to evaluate the

possible correlations with the failure behaviors of *SFRCs* following multi-stage pull-out and fracture (**Figure 4.4**). **Figure 4.6** shows the *AE* energy behaviors of *SFRCs* during the pull-out process. Variations in *AE* event energy reflected different damage mechanisms. There were two energy ranges of *AE* events for *SFRCs*, the interfacial debonding and breakage of sisal elementary fiber and micro-fibrils at higher energies, and sisal technical fiber, elementary fiber and micro-fibrils pulling-out at lower energies. It can be seen from **Figure 4.6** (a) that the *SFRCs* with the single-stage debonding had only one higher *AE* energy and following few lower energies during loading, which meant the *IF-FM* interface occurred fully debonding and the whole sisal technical fiber were pulled-out. Similarly, it can be found in **Figure 4.6** (b) and (c) that the *SFRCs* with the double- and triple-stage debonding had two and three higher *AE* energies emission events before the pull-out process, respectively, suggesting that the breakage of partial elementary fibers in sisal technical fiber and the micro-fibrils in the cell wall layer occurred at different time. Simultaneously, the energy emission for multi-stage debonding and fracture of the *SFRCs* was found to reduce gradually due to their decreased residual pull-out strength when subject to the tensile load. On the basis of the information captured from these *AE* signals, three typical failure processes of the *SFRCs* in the single fiber pull-out experiments can be concluded as follows. The first failure mode named as single-stage debond behavior in the present thesis can be seen in **Figure 4.4** and **Figure 4.6** (a), presenting one debonding process in this single-stage. In this process, debonding occurred between technical fiber and matrix, then technical fiber could be pulled out from the matrix with the increase of applied stress. The second failure mode as shown in **Figure 4.4** and **Figure 4.6** (b), could be categorized into two processes, namely Process 1 and

Process 2. Two types of interfacial failure were observed in the fiber pull-out test. As shown in *SEM* observation, technical fiber and elementary fibers both could be pulled-out from matrix, which led to two debonding processes obtained in this double-stage. During the Process 1, the interfacial debonding occurred at the *IF-FM*; whereas with the increase of applied stress, some elementary fibers broke; then during the Process 2, debonding occurred at the *IF-ELE*; finally, elementary fibers could be pulled-out. The third failure mode, as illustrated in **Figure 4.4** and **Figure 4.6** (c), could be described as technical fiber, elementary fibers and micro-fibrils were all pulled-out from the matrix, resulting in three debonding processes in this triple-stage debond behavior, namely Process 1, Process 2 and Process 3. With the same as double-stage, in the Process 1, the breakage of some elementary fibers occurred after the debonding between technical fiber and matrix. Then in the Process 2, debonding happened between the elementary fibers, but with the increase of applied stress, some micro-fibrils in the cell walls of partial elementary fibers broke. Finally, in the Process 3, debonding continued to occur between the cell walls and micro-fibrils were pulled-out.

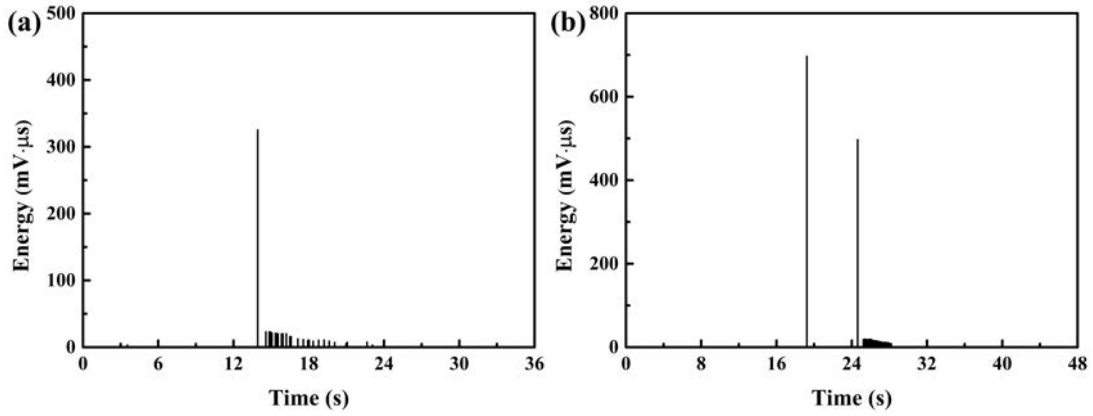

Figure 4.6 The *AE* response about energy versus time for the single sisal fiber pull-out with (a) single-stage debonding, (b) double- and (c) triple-stage debonding, fracture and pull-out.

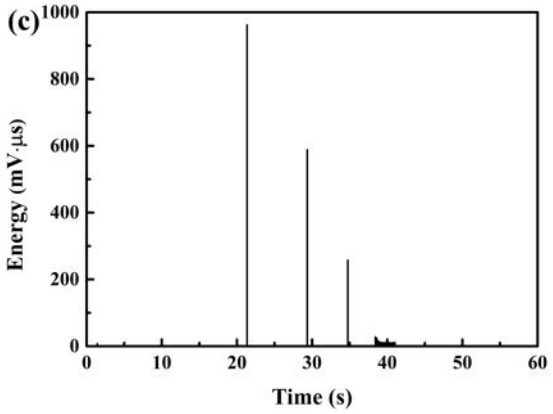

Figure 4.6 (continued).

4.4. Multi-interface debonding and multi-stage fiber component fracture and pull-out mechanisms of *SFRCs* characterized by *AE* signal analysis

A series of parameters defined from the characteristics of *AE* signals (i.e., amplitude, energy, rise time, counts and duration), are related to the severity of possible damage in the monitored structure to achieve an on-line detection. To achieve the evaluation of a monitored structure using *AE* signal characteristics, generation mechanism of *AE* signals and their relationship with the occurrence and severity of structural damage must be understood. For instance, the onset and growth of cracks in the material under external pull-out force is a complicated process. Cracks initiate and propagate in the multi-layer interface of plant fiber due to shearing force and followed by a tensional loading, during which *AE* generates with distinct signal characteristics. Previous research has illustrated that the generation of *AE* signals is physically linked to the asperities at the interface and the interfacial bonding status. The characteristics of *AE* signals produced by the interactions of interfaces with various surface characteristics

are different. *PFRCs* possess multi-layer interfaces (i.e., *IF-FM*, *IF-ELE* and *IF-CW* interfaces) and multi-scale structures (i.e., single technical fiber, elementary fibers and micro-fibrils). When the composites are subjected to external loads, three kinds of interfacial debonding failure and the fracture failure of fiber components in three scales could introduce *AE* signals with specific signal characteristics. During the single sisal fiber multi-stage pull-out process, a relative motion occurs between the interfaces due to sliding friction but with different contact durations in the three types of interfaces possessing different roughness, which are determined by the real contact area of the asperities. Larger asperities (i.e., *IF-CW* interface) could lead to a larger real contact area. As a result, *AE* signals with a longer duration (i.e., a lower centred frequency) are generated. Conversely, shorter-duration *AE* signals (i.e., a higher centred frequency) generate from the contacts between the smallest asperities (i.e., *IF-FM* interface). A reduce in contact area between asperities of interfaces, results in more frequency components with higher centred frequencies in the *AE* signals. Based on these, frequency-based analysis should be capable of characterizing *AE* signals generated from asperities with different sizes and identifying the contact behaviors at various interfaces with different roughness. With energy-based analysis, characteristics of *AE* signals can be linked to each interface at various stages. Therefore, from above descriptions, it can be inferred that upon the occurrence of the interfacial debonding in the composites, different failure processes naturally generate *AE* signals with distinct characteristics in terms of time durations and centred frequencies. Meantime, during the single sisal fiber multi-stage pull-out process, fiber components breakage (i.e., elementary fibers and micro-fibrils in cell walls) in the corresponding scale occurred after the interface debonding at each stage. Since sisal

fibers with different compositions (i.e., single technical fiber, elementary fibers and micro-fibrils) possess various fracture toughness, the released energy and frequency of breakage for different fiber components are varying. While, in conjunction with energy-based method, frequency-based method can be used to achieve the identification of the characteristics of *AE* signals generated from different interfaces (i.e., *IF-FM*, *IF-ELE* and *IF-CW* interfaces) and fractured fiber components (i.e., single technical fiber, elementary fibers and micro-fibrils) at various stages.

AE signals are generally nonstationary and nonlinear with unpredictable arrival times and waveforms. The use of traditional frequency-based analysis (e.g., fast Fourier transform, *FFT*) may result in false information when applied to process non-stationary or nonlinear mechanical fault signals (e.g., *AE* signal). In this backdrop, *EMD* method is a time-based analysis method that extracts features in the vibratory response of a structure but without any basic functions to be set **[164]**. From the theoretical derivation **[165, 166]**, when an *AE* signal is processed with *EMD*, a series of completed and orthogonal "intrinsic mode functions" (*IMFs*) (i.e., components with instantaneous frequencies) are decomposed, which represent the natural oscillatory modes in the original signal and are determined by the characteristics of the signal itself. *IMFs* make it applicable to process nonlinear and non-stationary signals without the need for spurious harmonics. Researchers found that from the comparison of performance between the traditional and *EMD*-based frequency analysis on the damage detection, the latter one was found to be more sensitive to damage compared to the former one, compromising its efficacy **[167]**. To facilitate a better understanding of procedure of *EMD* method, its flowchart is exhibited in **Figure 4.7**. The basic idea

of *EMD* is to decompose a time-domain wave with an irregular frequency distribution into multiple single-frequency waves and residual waves. To conduct *EMD* on a signal, the upper and lower envelops of the signal were first obtained by connecting local maxima and minima using a cubic spline function, respectively. The average of the maxima and minima envelopes m_{ij} is then obtained and subtracted from the original signal sequence $Y(t)$ to obtain the j^{th} "Proto-Intrinsic Mode Function", which is treated as a new original signal in the subsequent processes. This process is called the *EMD* sifting process. If the new data sequence h_{ij} has negative local maxima or positive local minima, it means that it is not yet an *IMF* and needs further 'sifting'. Then the above sifting process is repeated several times (j) until the new data set satisfying two conditions: 1) in the whole data set, the number of extrema and the number of zero crossings must either equal or differ at most by one; and 2) at any point, the mean value of the envelope fitted by the local maxima and the envelope fitted by the local minima is zero. Thus, this data set becomes the i^{th} *IMF* c_i. According to the above description of the generation mechanisms of *AE* signals, it should be pointed out that the first *IMF* is deduced to be associated with the shortest contact duration and the highest centred frequency, and then the frequency gradually decreases. The difference between the original function and the decomposed *IMF* is defined as the i^{th} residue function r_i, and then repeat the above sifting process until all *IMFs* of the original signal are obtained. The decomposition process is terminated until the residue becomes a constant, a monotonic function, or a function with only one maximum and one minimum. Finally, the original signal can be expressed with the sum of decomposed *IMFs* and the residue. To conclude, in the following case

studies, *EMD* method will be used to extract the *IMFs* of *AE* signals to recognize the failure behaviors at multiple interfaces with different roughness of *PFRCs* during the single fiber pull-out process.

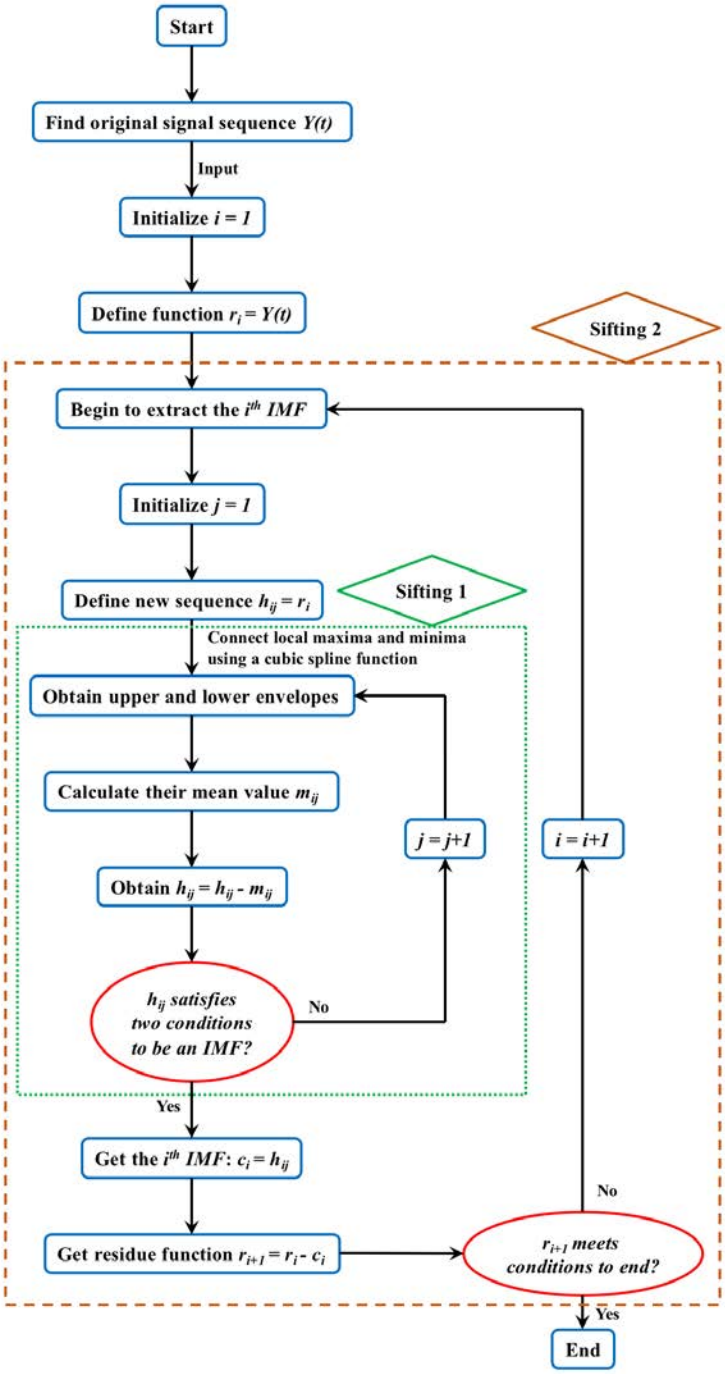

Figure 4.7 Flowchart of *EMD*.

From the above analysis, amplitude (energy)-based and frequency-based analyses are predicted capable of characterizing *AE* signals generated at the debonding of multi-layer interfaces with various asperities (i.e., *IF-FM*, *IF-ELE* and *IF-CW* interfaces) and further indicating the debonding process of the interfaces. To gain insight into the multi-layer interfacial failure behaviors of *SFRCs*, an *EMD* technique was applied to process the original *AE* signals (average of 100 signals) generated at the multi-stage debonding interfaces (i.e., *IF-FM*, *IF-ELE* and *IF-CW*) and those arising from different fiber components breakage, and extract their *IMFs* to characterize the debonding process (e.g., debonding and sliding friction) in the multi-layer interfaces and the fiber components breakage process of *SFRCs* undergone tensile stress, whereby to evaluate the debonding condition of the composites quantitatively. Three types of pull-out failure behaviors, namely single-, double- and triple-stage, were comparably used to exhibit the dependence of Wave energy attenuation (*WED*)-based method on the interface configurations. The original *AE* signals recorded in various interfacial debonding and different fiber components fracture or pull-out processes of various stage and their first two decomposed *IMFs* were respectively displayed in **Figure 4.8** and **Figure 4.9** and compared the differences in *IMFs* at different stages, then comparably studied to recognize the distinct characteristics of multi-interfacial failure in the *SFRCs*. Noted that S_i^T denotes the i^{th} *IMF* of the *AE* signals generated from the specimens under a process of T ($T = 11,\ 21,\ 22,\ 31,\ 32\ or\ 33$, that is, Process 1/2/3 of single-/double-/triple-stage). From these two sets of graphs, it can be observed that the original *AE* signal is more complicated while the decomposed *IMF* is more regular, and the first two *IMFs* in each figure are observed to possess

increasing periods. Meanwhile, the *AE* signal components of the *IF-FM* interface are relatively simple. As shown in **Figure 4.8**, the decomposed *IMFs* of the *AE* original signal for Process 1 of the three types of debonding and pull-out failure behaviors (i.e., single-, double- and triple-stage) present similar characteristics (see **Figure 4.8** (a), (b) and (c)), indicating these *AE* signals arise from the debonding at the *IF-FM* interface. Then, the similar *IMFs* between **Figure 4.8** (d) and (e) demonstrate these *AE* signals were generated from the debonding of the *IF-ELE* interface. **Figure 4.8** (f) shows the *AE* signals produced by the debonding of the *IF-CW* interface. As illustrated in **Figure 4.8** (c), (e) and (f), *AE* signals obtained in the triple-stage presented different envelope forms, confirming that three debonding processes occurred in different interfaces. In addition, from further observation on the results from the triple-stage pull-out behaviors, the periods of the *IMFs* from the debonding of the *IF-FM* interface to that of the *IF-CW* interface are observed to gradually decrease. The main reason is that the asperities at the interface of the *IF-FM* with larger roughness have more contact, leading to bigger contact area and longer contact duration. As the same condition with **Figure 4.8, Figure 4.9** (a), (b) and (c) represent the complete pull-out of sisal technical fiber due to fully debonding of the *IF-FM* interface, while **Figure 4.9** (d) and (e) exhibit the breakage of partial elementary fibers in sisal technical fiber, and **Figure 4.9** (f) is on behalf of the pull-out of non-fracture fiber components (i.e., elementary fiber and micro-fibrils in cell walls) in sisal technical fiber. However, the amplitude of the energy of the *AE* signals generated by the fiber components breakage is higher than that caused by the interface debonding. The signals from the fiber components breakage exhibit high damping characteristics and emit large amount of energy in a relatively short period of time. The waveforms of fiber breakage rose

quickly, after which the signal amplitude rapidly decayed, showing shorter time duration. In addition, fiber breakage also accompanied with higher energy emission. Whereas, the *AE* signals produced by the interfacial debonding had less release of elastic stress energy, then the waveforms of signals were more moderate and rose slowly and had the longer time duration. Through comparing **Figure 4.8** or **Figure 4.9** (a)-(f), it can be found that, with the increase of debonding interface or breakage process, the amplitude of energy gradually decreased.

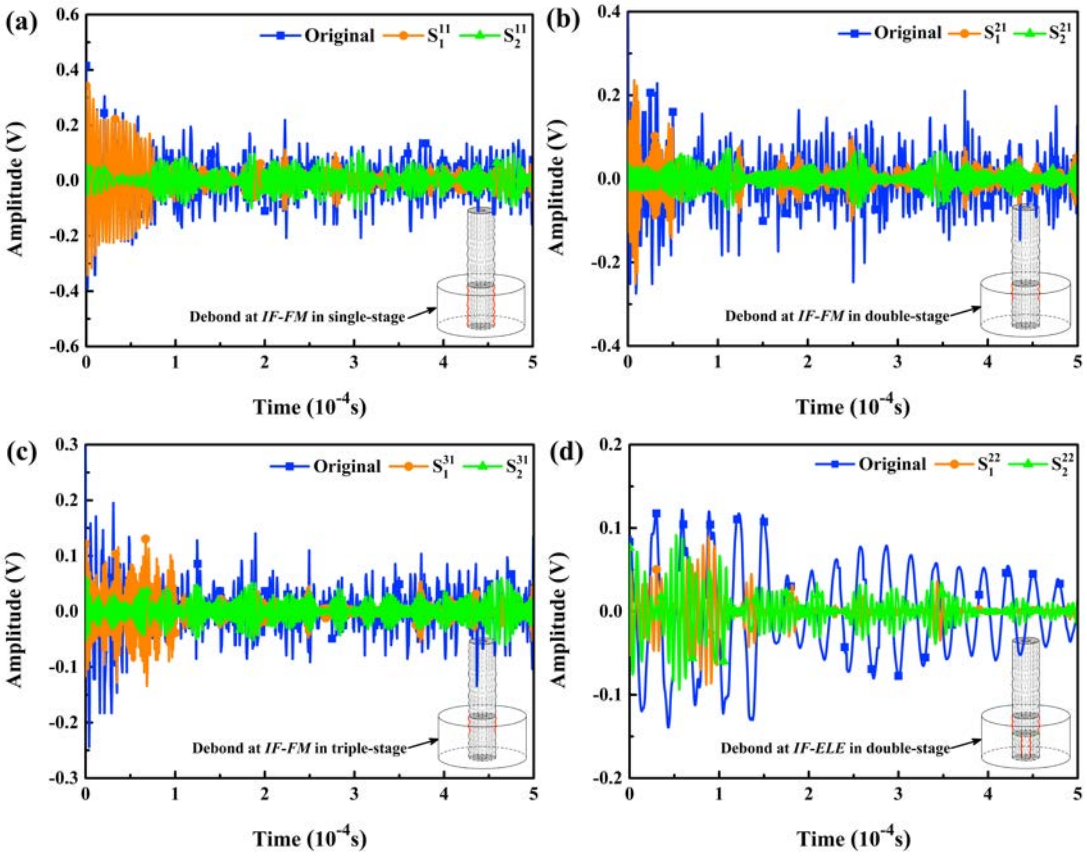

Figure 4.8 Time presentations of the original *AE* signal and its first two *IMFs* captured from multiple interfaces debonding during single sisal fiber pull-out process: *IF-FM* debonding (Process 1) in (a) single-stage, (b) double-stage and (c) triple-stage, *IF-ELE* debonding (Process 2) in (d) double-stage and (e) triple-stage, and *IF-CW* debonding (Process 3) in (f) triple-stage.

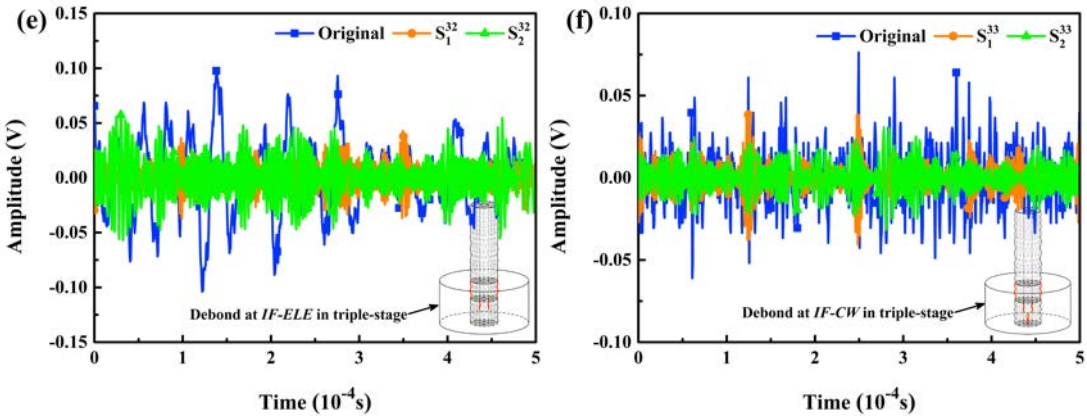

Figure 4.8 (continued).

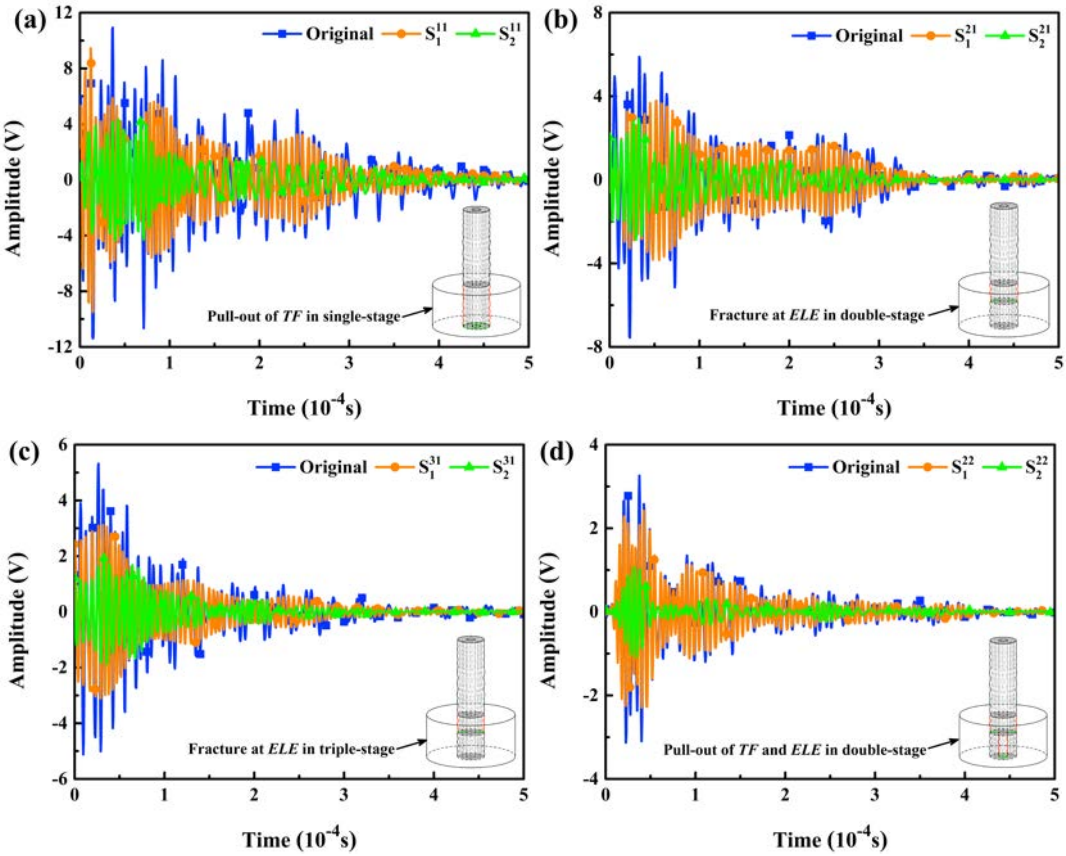

Figure 4.9 Time presentations of the original *AE* signal and its first two *IMFs* captured from the fiber component multi-stage fracture or pull-out during single sisal fiber pull-out process: (a) *TF* pull-out (Process 1) in single-stage, *ELE* fracture (Process 1) in (b) double-stage and (c) triple-stage, (d) *ELE* pull-out (Process 2) in double-stage, (e) *CW* fracture (Process 2) in triple-stage, and (f) *CW* pull-out (Process 3) in triple-stage.

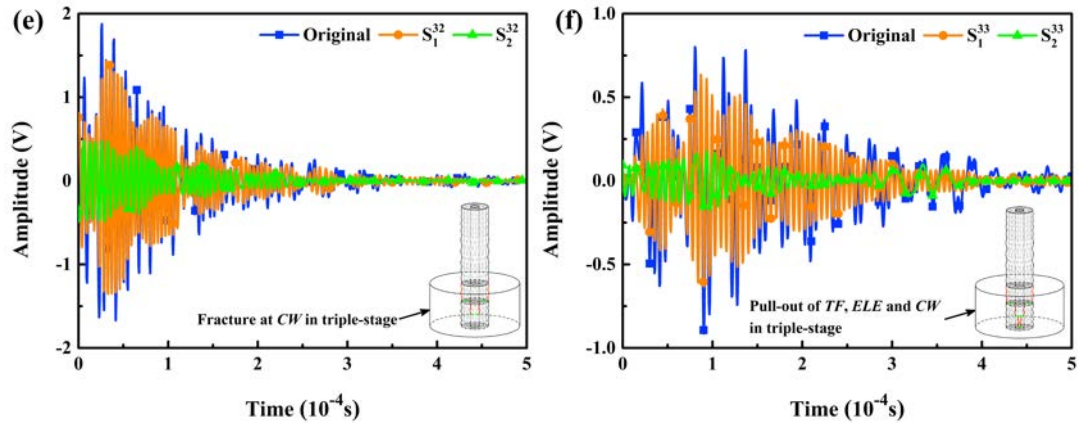

Figure 4.9 (continued).

AE descriptors such as amplitude, energy and frequency can be used to identify the micro-failure mechanisms. In order to obtain the time-frequency characteristics of *AE* signals generated by multi-interface debonding and multi-stage fiber components breakage, this section will employ *HHT* to perform time-frequency analysis of the original *AE* signals. Specifically, the first four decomposed *IMFs* of the original *AE* signals (the average of 100 signals) generated at the multiple interface debonding (i.e., *IF-FM*, *IF-ELE* and *IF-CW*) and multi-stage fiber components breakage during the single fiber pull-out measurements were ascertained via an *HHT*. The *HHT* spectra can provide accurate time-frequency characteristics of the *AE* signals, creating favorable conditions for monitoring the multi-stage failure behaviors of *SFRCs* using *AE* technique. To investigate energy shift in the signals generated from the interface debonding and fiber components breakage under different process, the corresponding *HHT* spectra presented with normalized energy of the two sets of time-domain signals (first four decomposed *IMFs* from the original signals in **Figure 4.8** (a)-(f) and **Figure 4.9** (a)-(f)) were comparatively displayed in **Figure 4.10** (a)-(f) and **Figure 4.11** (a)-(f), presenting relatively high time-frequency resolution. Meantime, the features of *AE* signals generated from multi-interface debonding and multi-stage fiber

components fracture were comparably investigated. The distributions of frequencies of the main energy of the *AE* signals produced by different failure modes were extracted. Each failure mechanism can be characterized by a different peak frequency. According to frequency analysis on the *AE* signals generated from these two types of failure modes (interface debonding and fiber components breakage), signals from the former contained a large peak in the high-frequency region (see **Figure 4.10**), mainly concentrating in the range of 50 to 500 kHz, while those from the latter presented a series of peaks in the low-frequency region (see **Figure 4.11**), mainly concentrating between 20 and 300 kHz. This was mainly due to the point-to-point contact for the interfacial debonding, exhibiting short duration and high frequency, while fiber components breakage usually released higher energy with longer duration, leading to lower frequency. Therefore, this study verified the application of *AE* technique in the recognition of different failure mechanisms of *SFRCs*.

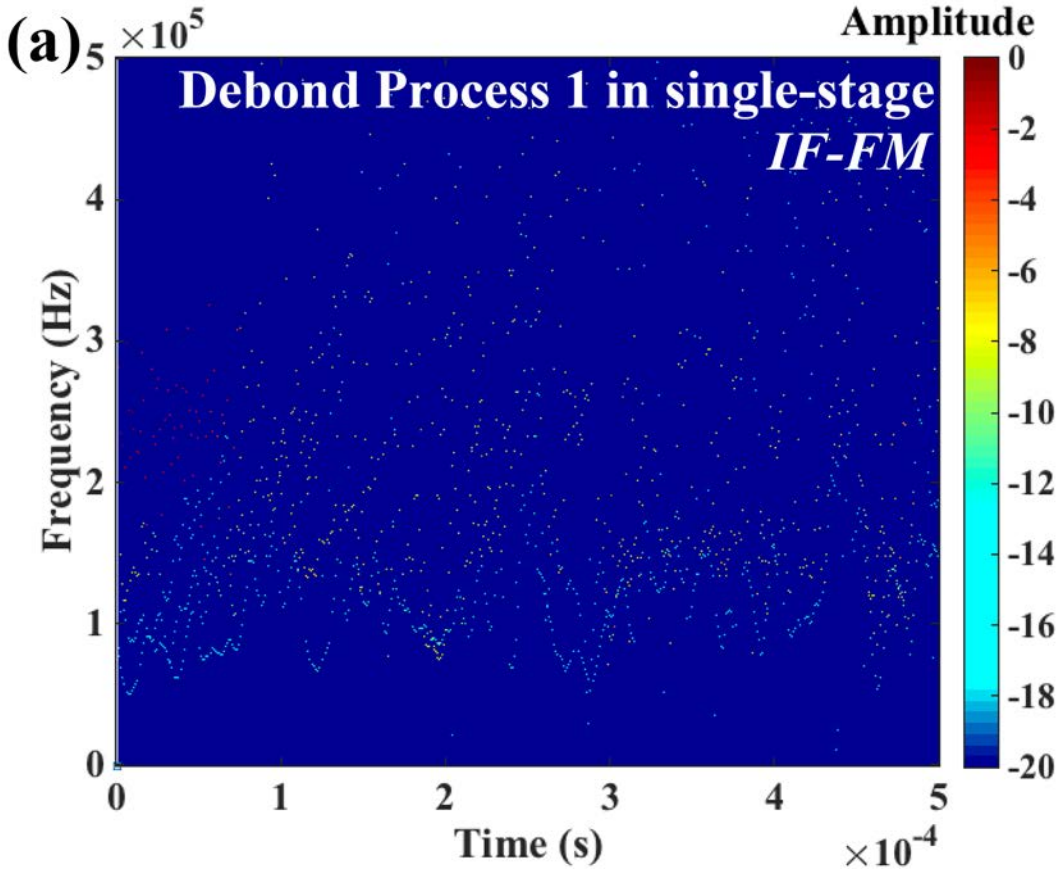

Figure 4.10 *HHT* spectra of the *AE* signals captured from the multiple interfaces debonding during the single sisal fiber pull-out process: *IF-FM* debonding (Process 1) in (a) single-stage (refer to Figure 4.8 (a)), (b) double-stage (refer to Figure 4.8 (b)) and (c) triple-stage (refer to Figure 4.8 (c)), *IF-ELE* debonding (Process 2) in (d) double-stage (refer to Figure 4.8 (d)) and (e) triple-stage (refer to Figure 4.8 (e)), and *IF-CW* debonding (Process 3) in (f) triple-stage (refer to Figure 4.8 (f)).

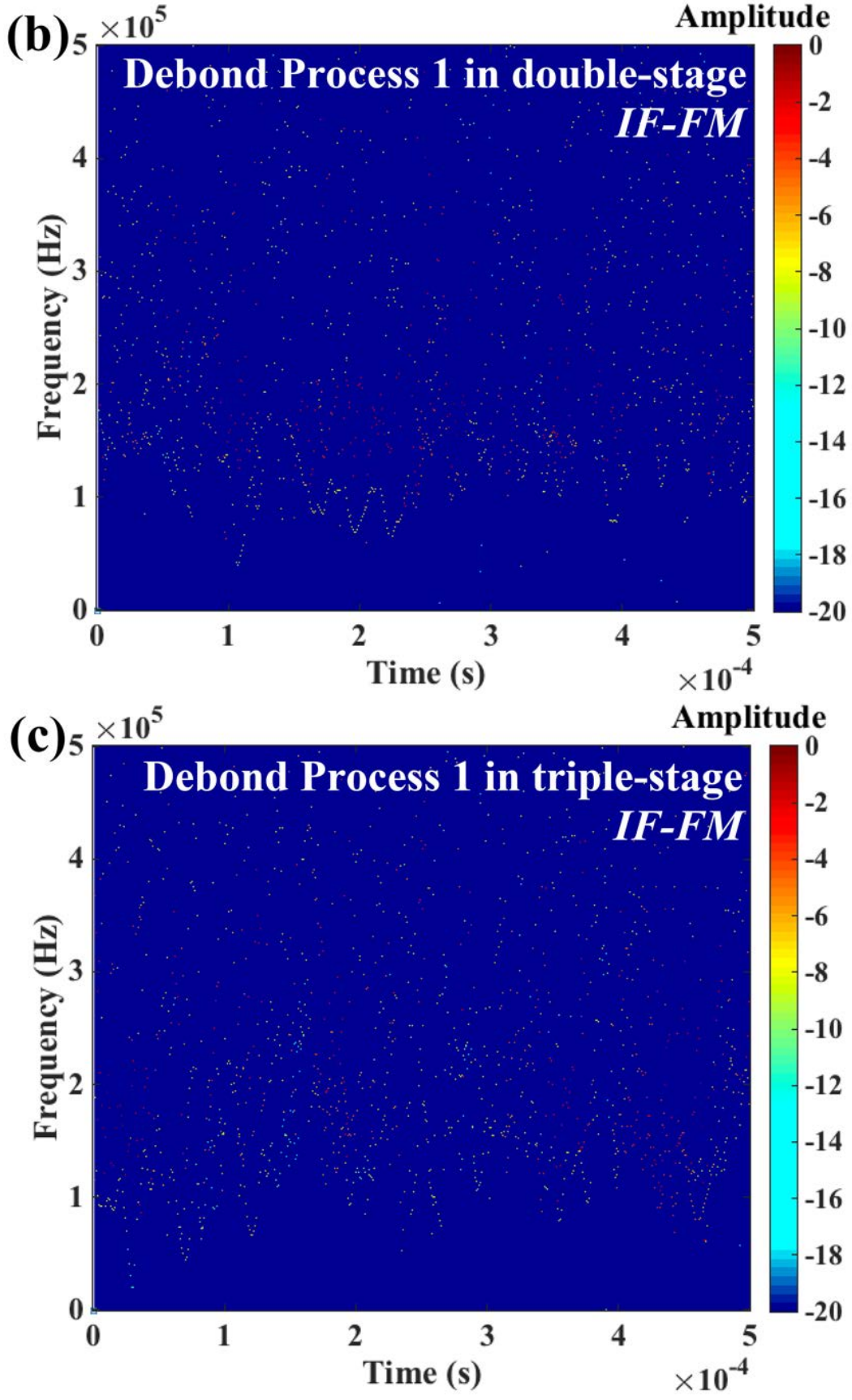

Figure 4.10 (continued).

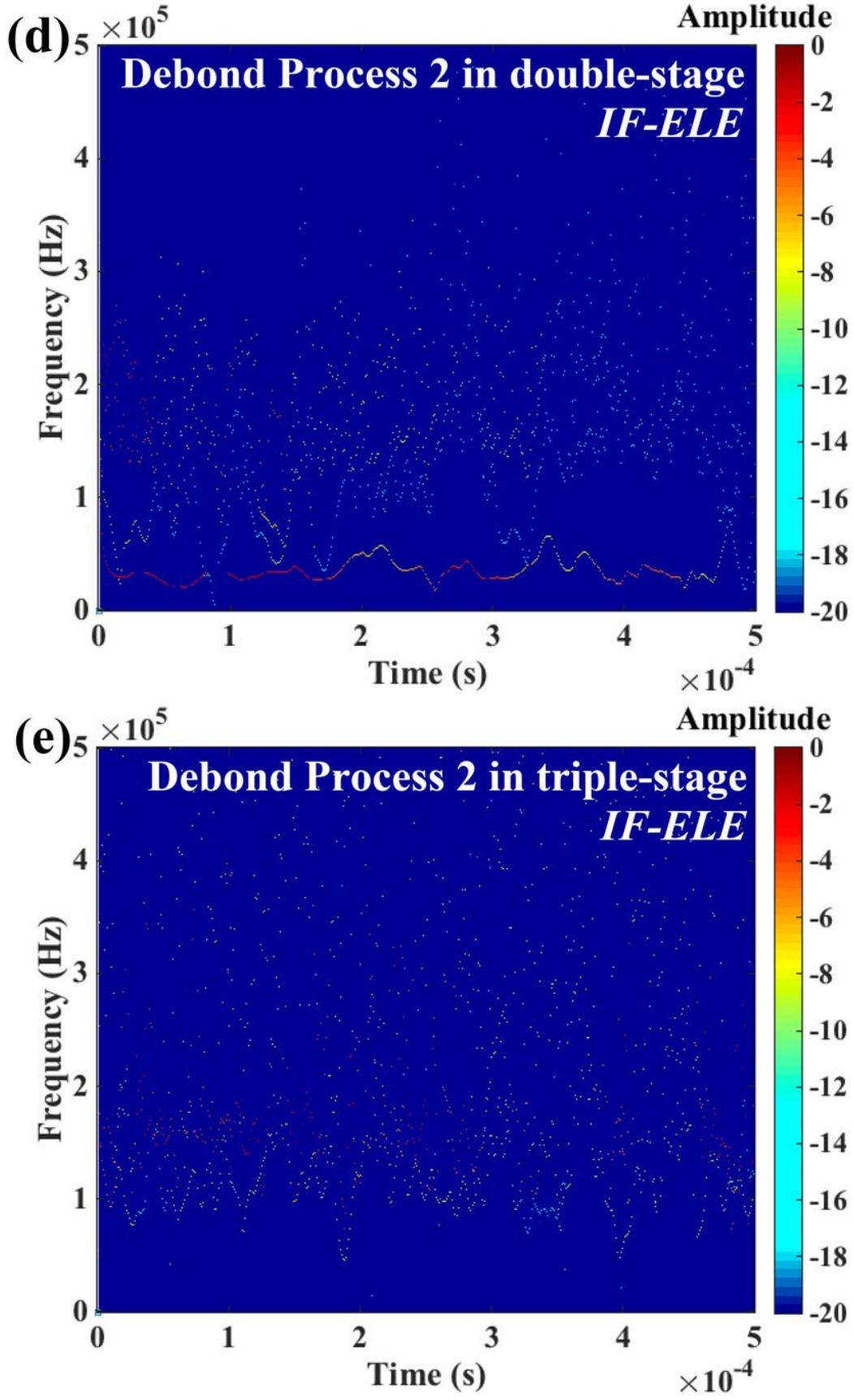

Figure 4.10 (continued).

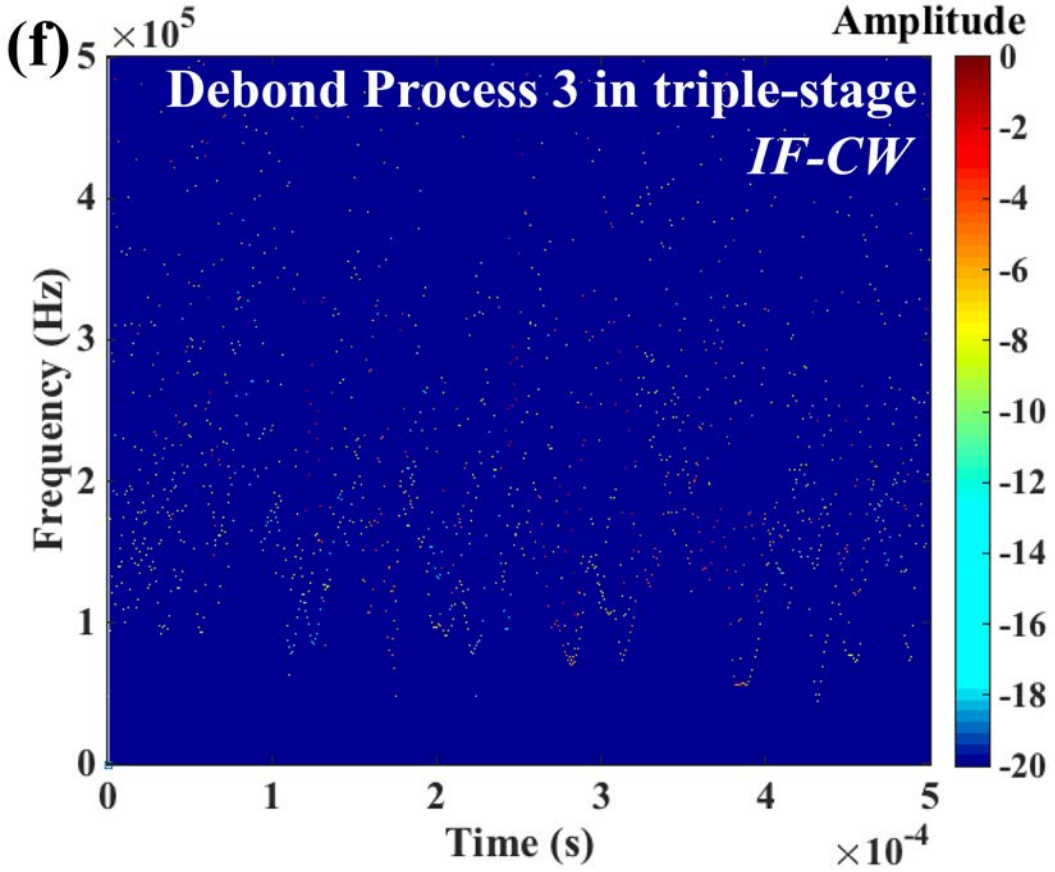

Figure 4.10 (continued).

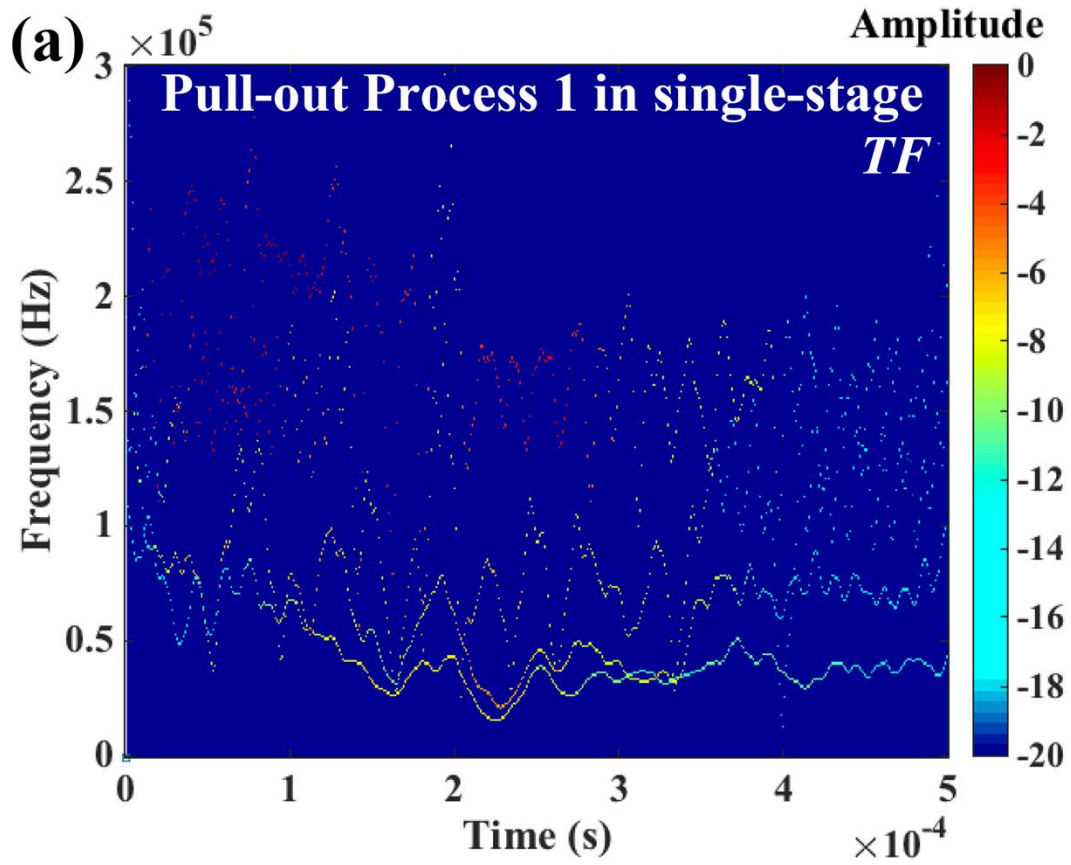

Figure 4.11 *HHT* spectra of the *AE* signals captured from the fiber components multi-stage fracture or pull-out during single sisal fiber pull-out process: (a) *TF* pull-out (Process 1) in single-stage (refer to Figure 4.9 (a)), *ELE* fracture (Process 1) in (b) double-stage (refer to Figure 4.9 (b)) and (c) triple-stage (refer to Figure 4.9 (c)), (d) *ELE* pull-out (Process 2) in double-stage (refer to Figure 4.9 (d)), (e) *CW* fracture (Process 2) in triple-stage (refer to Figure 4.9 (e)), and (f) *CW* pull-out (Process 3) in triple-stage (refer to Figure 4.9 (f)).

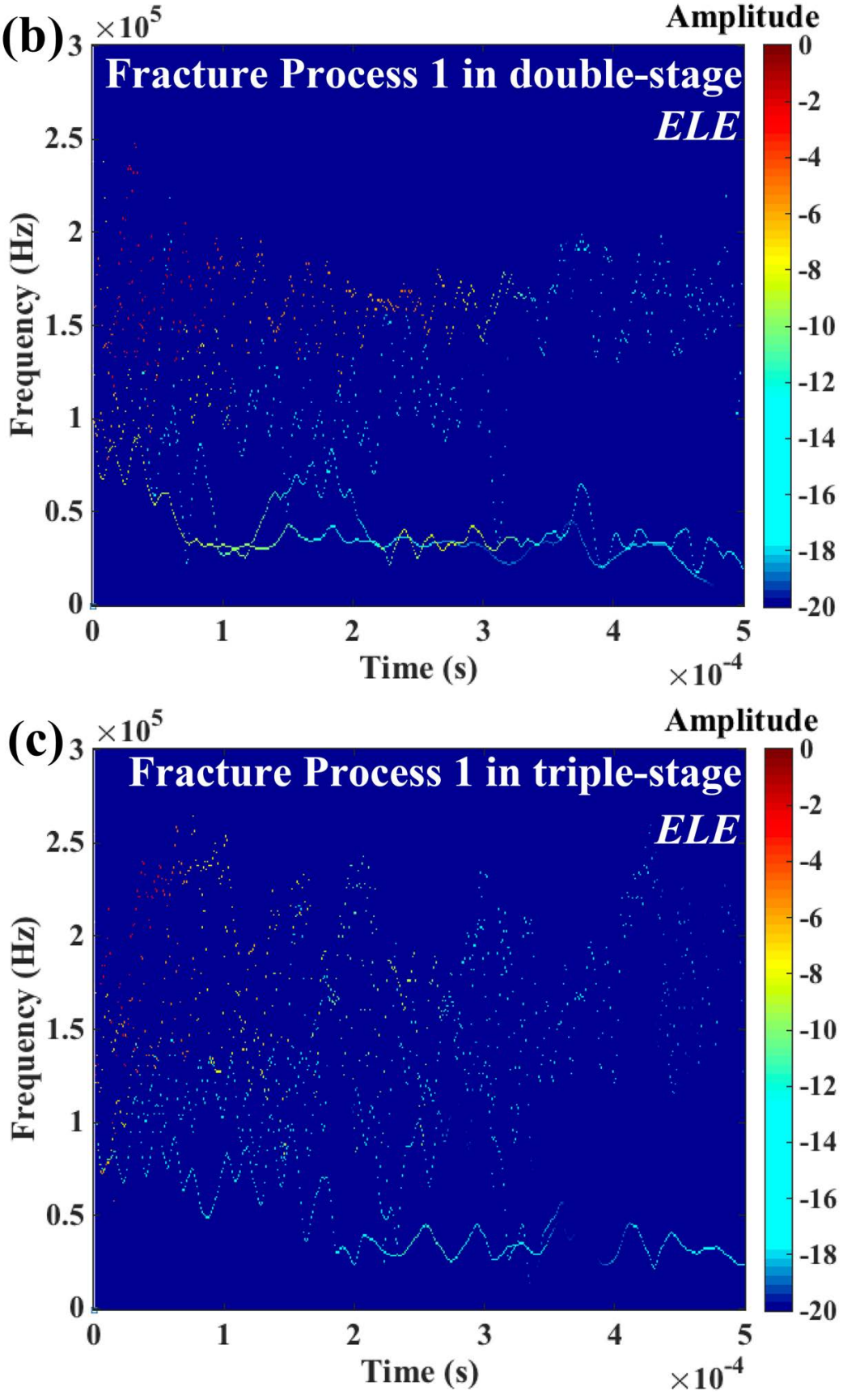

Figure 4.11 (continued).

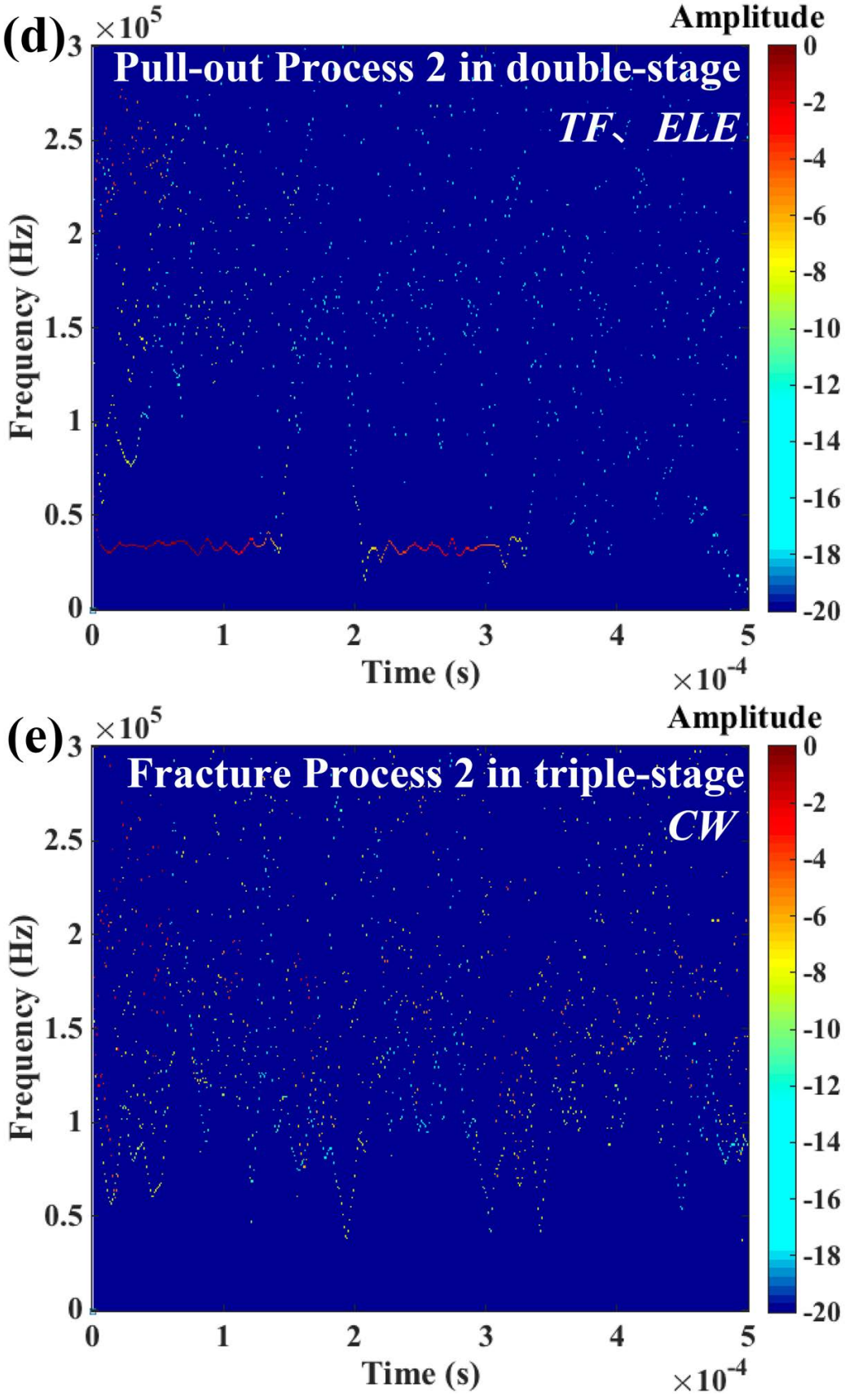

Figure 4.11 (continued).

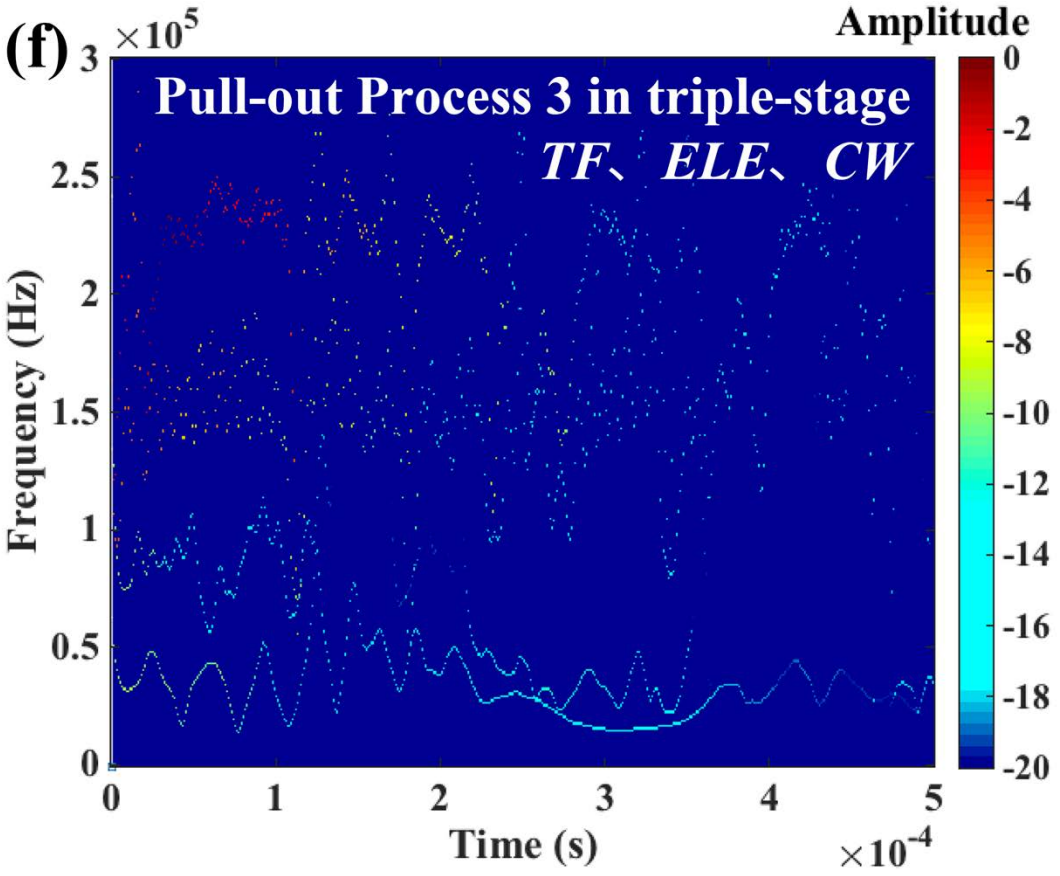

Figure 4.11 (continued).

From **Figure 4.10** (a), (b) and (c), it can be observed that the main energy of the *AE* signal generated by the debonding of the *IF-FM* interface dominates the frequency range between 50 and 500 kHz. Comparing the *HHT* spectra of the *AE* signals generated from the debonding failure of the *IF-FM* interface (**Figure 4.10** (a), (b) and (c)) to those generated from the *IF-ELE* (**Figure 4.10** (d) and (e)) and *IF-CW* (**Figure 4.10** (f)) interface debonding failure, it can be found that the frequencies of the *AE* signals induced by the *IF-ELE* and *IF-CW* debonding failure mainly distribute between 50 to 360 kHz and 50 to 240 kHz, respectively. It is worth noting that, differences in roughness and hardness between these three types of interfaces (*IF-FM*, *IF-ELE* and *IF-CW*) and the resin, single technical fiber, elementary fibers and micro-

fibrils (as described in Chapter 3) are supposed to be responsible for the diversity of their frequency distribution. It can be seen from the above results that the frequency distribution range of the three types of interfaces gradually decreases with the increase of the number of debonded interface. This is mainly due to the fact that, as described in Chapter 3, the *IF-CW* interface is rougher than the *IF-FM* interface, thus the debonding requires a longer duration, manifesting as a lower frequency. Through comparing the *AE* signals generated by the same type interfaces from different failure modes (i.e., single-/double-/triple-stage) in **Figure 4.10**, it can be found that the energy distributions of the *AE* signals are different. From single- to triple-stage, the energy ratio of low-frequency components (below 100 kHz) of the *IF-FM* interface (see **Figure 4.10** (a), (b) and (c)) or the *IF-ELE* interface (see **Figure 4.10** (d) and (e)) becomes larger with the increase of debonded interface, indicating that the duration of interface sliding continues to increase. Whereas, more energies required to be stored in the debonding process, illustrating the *SFRCs* with the double- or triple-stage debonding failure behavior possess stronger interfacial bonding in *IF-FM* interface or *IF-ELE* interface.

Simultaneously, comparing the *HHT* spectra of the *AE* signals generated from the single technical fiber or the remaining fiber components pull-out failure to those generated from the elementary fibers and micro-fibrils breakage failure in **Figure 4.11**, the main energies of the *AE* signals generated by the single technical fiber pull-out failure (**Figure 4.11** (a)) were observed to distribute in the frequency range between 20 and 220 kHz and had a high energy, while those induced by the elementary fibers (**Figure 4.11** (b) and (c)) and micro-fibrils (**Figure 4.11** (e)) breakage failure

dominated the frequency range between 20 to 260 kHz and 20 to 280 kHz, respectively, with relatively low energy, and the main energies of those generated from the remaining fiber components pull-out failure (**Figure 4.11** (d) and (f)) distributed in the frequency range between 20 to 300 kHz. The diversity of the frequency distribution of energy is related to the dimension of single technical fiber, elementary fibers and micro-fibrils (as described in Chapter 3). In addition, it can be observed in **Figure 4.11** that the energy distributions of the *AE* signals generated by the same kind of fiber component breakage from different failure modes (i.e., single-/double-/triple-stage) are different. From single- to triple-stage, the energy ratio of the elementary fiber breakage (see **Figure 4.11** (b) and (c)), the micro-fibrils breakage (see **Figure 4.11** (e)) or various fiber components pull-out (see **Figure 4.11** (a), (d) and (f)), gradually reduced with the increase of the form of fiber components breakage, which was ascribed to incomplete fracture of elementary fibers or micro-fibrils in different time for the *SFRCs* with the double- or triple-stage debonding failure behavior, indicating that the *AE* signals arise from the partial fracture exhibited lower energy.

Based on these, the features of *AE* signals can discriminate the multi-interface debonding and multi-stage fiber components breakage behaviors. An increase in the debonded interface or the form of fiber component breakage may cause the change of energy distribution at the corresponding frequency. This further illustrated that even though for the same untreated *SFRCs*, the adhesive strength of the same kind of interface would display different performances, which is precisely in line with a unique dispersion in the performance of the plant fiber itself within a certain range.

Marginal spectra of the *AE* signals captured from the multiple interfaces debonding and the fiber components multi-stage fracture or pull-out under different processes during single fiber pull-out test are shown in **Figure 4.12** and **Figure 4.13**, respectively, in which the energy ratio of middle- and low-frequency components (below 200 kHz) of the *IF-FM* interface (see S^{11}, S^{21}, S^{31}) or the *IF-ELE* interface (see S^{22}, S^{32}) becomes larger with the increase of debonded interface by comparing the curves in **Figure 4.12**. These phenomena are consistent with previous analysis in terms of the influence of the difference in the same type of interface for various processes of *SFRCs* on the resultant *AE* signal characteristics. To be more specifically, the *SFRCs* with the double- or triple-stage debonding failure behavior possess stronger interfacial bonding in *IF-FM* interface or *IF-ELE* interface and consequently the contact area of asperities increases and then more *IMFs* with longer durations (i.e., low centered frequencies) occurs. While as illustrated in **Figure 4.13**, from single- to triple-stage, the energy ratio of the elementary fibers breakage (see S^{21} and S^{31}), the micro-fibrils breakage (see S^{32}) or various fiber components pull-out (see S^{11}, S^{22} and S^{33}) gradually reduce with the increase of the form of fiber components breakage. The *AE* signals arise from the partial fracture of elementary fibers in single technical fiber or micro-fibrils in cell walls exhibited lower energy compared with those complete fracture.

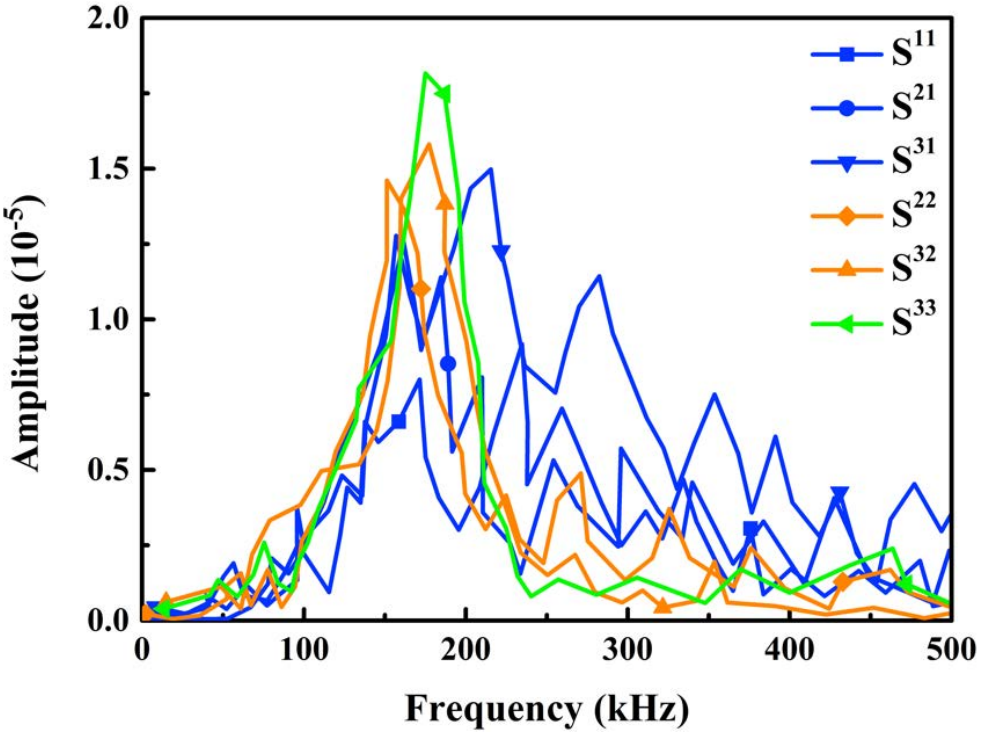

Figure 4.12 Marginal spectra of the *AE* signals captured from the multiple interfaces debonding during the single sisal fiber pull-out process.

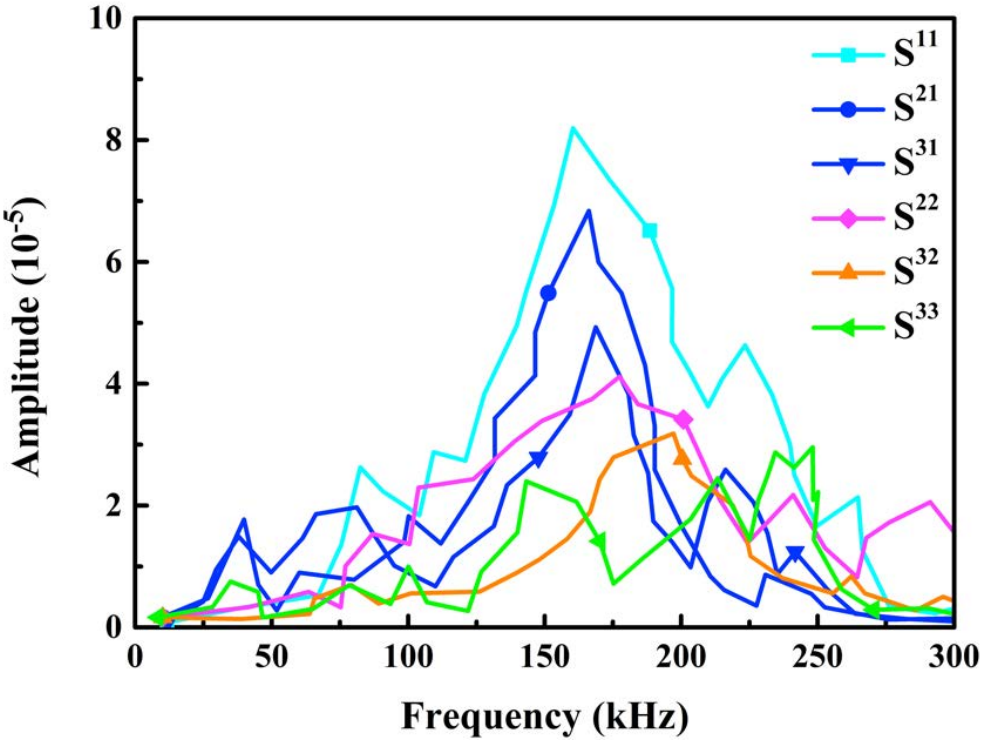

Figure 4.13 Marginal spectra of the *AE* signals captured from the fiber components multi-stage fracture or pull-out during the single sisal fiber pull-out process.

To achieve a quantitative analysis, energy ratio (R_k) of each *IMF* c_k with different centered frequency is calculated using the following equation:

$$R_k = E(c_k) / \sum_{k=1}^{n} E(c_k) \times 100\% \quad \textbf{(4.1)}$$

where $E(c_k)$ is the equivalent energy of *IMF* c_k , obtained by accumulating the squares of signal amplitudes of c_k in the time domain. The evolution of energy ratios of first three *IMFs* components of the *AE* signals generated from their summation (R_{1-3}) along with the ratio of residual *IMFs* ($R_{Residual}$) are obtained and displayed in **Table 4.1** and **Table 4.2**. It can be observed from these two tables that, R_{1-3} is found to increase for the interface debonding process when the pull-out process applied on the *SFRCs* changes from single- to triple-stage, while an observable decrease presents in R_{1-3} for the fiber components breakage process. By comparing these two tables, R_{1-3} for the multiple interface debonding is higher than that for the multi-stage fiber components breakage. Moreover, for the *SFRCs* with double- or triple-stage, during the interface debonding process, the energy ratios of residual *IMFs* gradually increase from *IF-FM* to *IF-ELE* or *IF-CW*, which indicates the high-frequency *IMFs* captured from the *AE* signals of the internal interface of *SFRCs* become weaken. While during the fiber components breakage and pull-out process, the energy ratio of residual *IMFs* decrease from technical fiber to elementary fibers or micro-fibrils, which indicates the high-frequency *IMFs* captured from the *AE* signals of the internal fiber component of *SFRCs* become more intensive. Compared with the results in *HHT* analysis, a considerable consistency in between can be concluded.

With usage of R_{1-3} and $R_{Residual}$, changes of processes of interface debonding or fiber breakage can be detected. Therefore, the above results exhibit that the energy ratios of *IMFs* decomposed from *EMD* can quantitatively reflect the status of the multiple interface debonding or multi-stage fiber components breakage or pull-out in various stage.

Table 4.1 Evolution of energy ratios of *IMF* components decomposed from the *AE* signals from the multiple interfaces under different debonding processes during the single fiber pull-out test of the *SFRCs* (unit: %).

Debonded interface		Single-stage	Double-stage	Triple-stage
IF-FM	R_1	19.58	16.18	15.99
	R_2	5.73	9.26	13.93
	R_3	9.08	10.55	11.95
	R_{1-3}	34.39	35.99	41.87
	$R_{Residual}$	65.61	64.01	58.13
IF-ELE	R_1	/	15.89	14.26
	R_2		6.22	12.41
	R_3		7.83	10.77
	R_{1-3}		29.94	37.44
	$R_{Residual}$		70.06	62.56
IF-CW	R_1	/	/	13.27
	R_2			11.42
	R_3			10.14
	R_{1-3}			34.83
	$R_{Residual}$			65.17

Table 4.2 Variation of energy ratios of *IMF* components decomposed from the *AE* signals from the fiber component multi-stage fracture under different fracture processes during the single fiber pull-out test of the *SFRCs* (unit: %).

Fractured fiber		Single-stage	Double-stage	Triple-stage
Elementary fibers	R_1	/	11.89	10.67
	R_2		6.45	7.99
	R_3		6.16	4.09
	R_{1-3}		24.50	22.75
	$R_{Residual}$		75.50	77.25
Micro-fibrils	R_1	/	/	10.27
	R_2			6.27
	R_3			6.88
	R_{1-3}			23.42
	$R_{Residual}$			76.58
Technical fiber pull-out or different fiber component fracture	R_1	12.52	10.80	9.26
	R_2	7.12	8.89	8.68
	R_3	5.83	6.35	8.67
	R_{1-3}	25.47	26.04	26.61
	$R_{Residual}$	74.53	73.96	73.39

4.5. Statistical analysis on the multi-stage fracture performance of *SFRCs*

Statistical method is a proper way to describe the dispersion characteristics of the events occurred in *SFRCs*. Based on the above results, in this section, statistical analysis was used to evaluate the probability of technical fiber, elementary fiber and micro-fibrils pull-out. The effects of the multi-layer interfaces on the interfacial failure behaviors and the pull-out performances of *SFRCs* were depicted. **Figure 4.14** (a) shows the distributions of the number of occurrences of single-, double- and triple-

stage debonding and pull-out of the *SFRCs* recorded via Weibull statistical analysis method and the corresponding Weibull distribution was illustrated in **Figure 4.14** (b). It can be seen that double- and triple-stage debonding occurred in the single fiber pull-out test for *SFRCs* due to the distinct structure of multi-layer interfaces, of which the double-stage debonding was the major failure mode. The statistical results indicated that technical fiber and elementary fiber were more prone to be pulled-out from matrix since the interfacial bonding between the sisal fiber and matrix and between the elementary fibers was relatively poor for the untreated sisal fiber, while micro-fibrils could also be pulled-out from the elementary fiber owing to the existence of the cell wall structure. So, for the *SFRCs*, appropriate embedded fiber length could not only make the debond and pull-out occurred, but also lead to multi-stage debond and pull-out owing to the existence of the multi-layer interface. Then the shape and scale parameter of Weibull distribution are as listed in **Table 4.3**. Three Weibull scale parameters as the typical embedded fiber length of three kinds of pull-out behaviors (i.e., single-, double- and triple-stage) were chosen to simulate the multi-stage debond and pull-out process of *SFRCs* in the following *FE* model in Chapter 6.

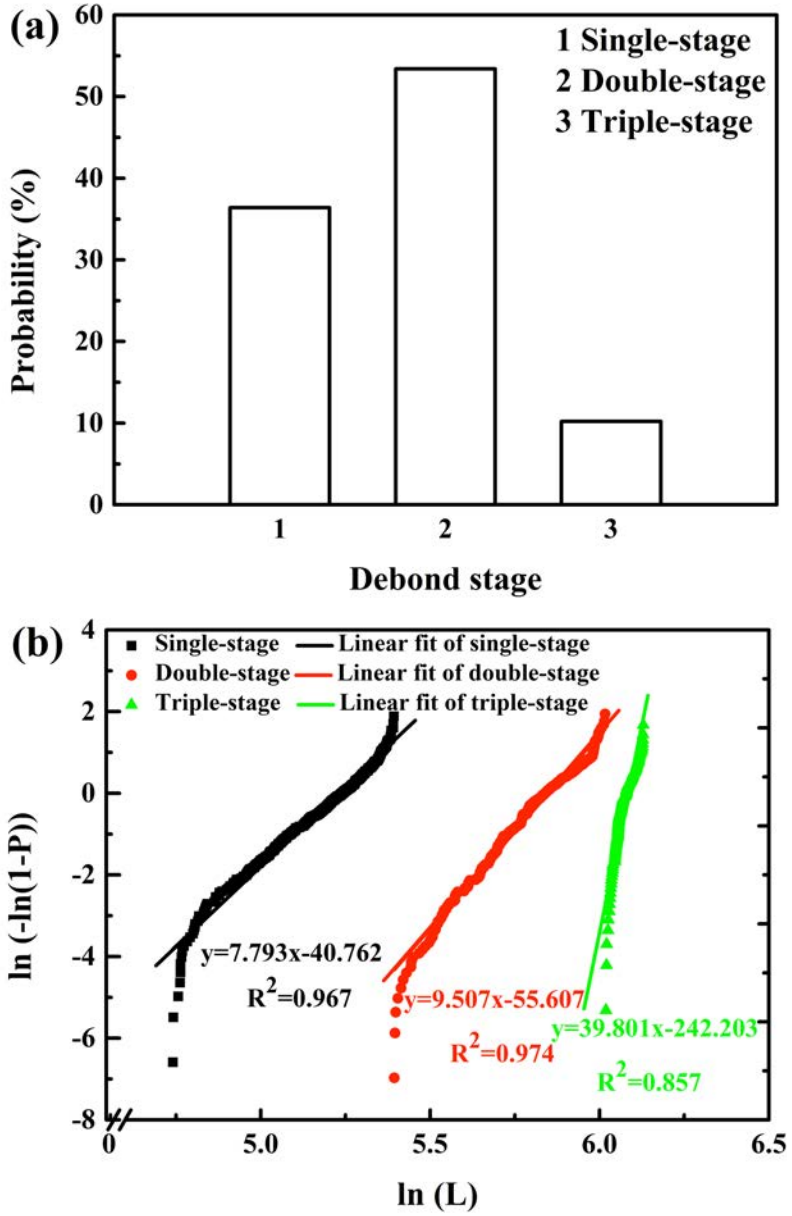

Figure 4.14 (a) Distribution of the number of occurrences of multi-stage debonding of the *SFRCs* and (b) corresponding Weibull distribution.

Table 4.3 Weibull distribution statistical parameters for the occurrence of multi-stage debonding of the *SFRCs*.

	Single-stage	Double-stage	Triple-stage
Shape parameter	7.793	9.507	39.801
Scale parameter (μm)	186.903 (187)	346.908 (347)	439.373 (440)

Through conducting the statistical analysis of the relationship between the maximum debonding force and the fiber embedded area at various stages of different fiber embedded lengths, as shown in **Figure 4.15**, the interfacial strengths of different interfaces in the single-, double- and triple-stage debonding of *SFRCs* were obtained by fitting the test data. It can be seen that as the number of the interface debonding stage increased, the interfacial strength in the same interface gradually improved. In the case of double- and triple-stage debonding process, the interfacial strength in the internal interface of sisal fibers was higher than that in the *IF-FM* interface. The determined interfacial strength in this chapter was used as the input parameter in the *FE* model of Chapter 5 for simulating the multi-stage debonding and pull-out process in the single fiber pull-out test of *SFRCs*.

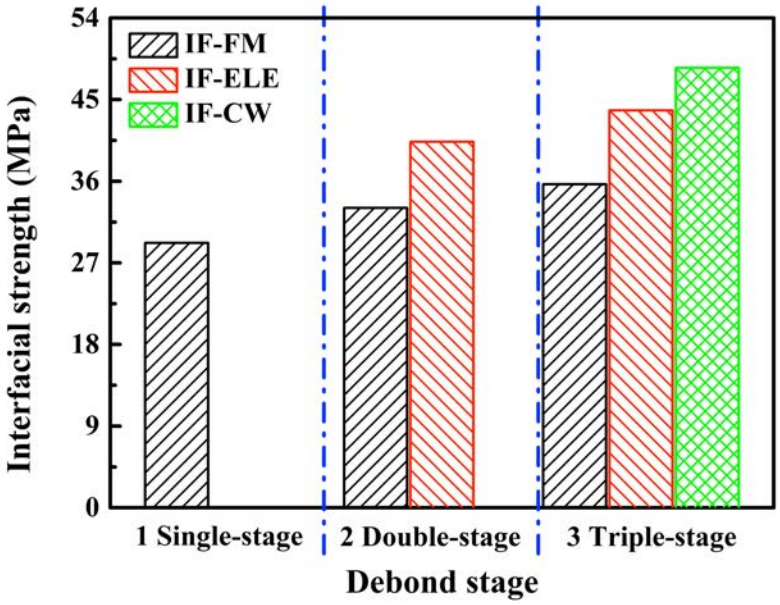

Figure 4.15 Distribution of the interfacial strength of different interfaces with occurrences of multi-stage debonding of the *SFRCs*.

4.6. Summary

In this chapter, the single fiber pull-out experiments were conducted on *SFRCs* to investigate the interfacial failure process of the *SFRCs* by monitoring with *AE* technique. This investigation discovers that the multi-layer and multi-scale structure of the sisal fibers made the interfacial debonding processes and the interfacial failure mechanisms in their reinforcing composites different from those of *CFRCs* or *GFRCs*. The probability of multiple failure modes was obtained from statistical analysis. The main research results can be presented as follows.

(1) The unique multi-stage interfacial failure and fiber components fracture behaviors of *SFRCs* were observed in the single fiber pull-out experiments. The residual pull-out strength of the *SFRCs* was found to gradually decrease when subject to tensile loading during the single sisal fiber pull-out test, after which the *SFRCs* presented multiple failure modes, including at the interface between the technical fiber and matrix, at the interface between the elementary fibers and at the interface between the cell walls. Interfacial debonding could occur between technical fiber and matrix, between elementary fibers and between cell walls for *SFRCs*. The measured maximum debond stresses increased with the increase of the embedded fiber length.

(2) The unique multi-stage interfacial failure behaviors of *SFRCs* can be well identified based on *AE* events recorded in the single fiber pull-out experiments, including interfacial debonding (i.e., *IF-FM*, *IF-ELE* and *IF-CW*), fiber components pull-out or breakage (i.e., technical fiber, elementary fiber and micro-fibrils). The

measured *AE* features were coupled with supplementary information such as microstructural observations of the test specimen. Meantime, the failure sequences of *SFRCs* were described with the help of *AE*, and the corresponding fracture mechanisms were characterized by in-situ *AE* technique. The energy emission for the multi-stage debonding and fracture performances of *SFRCs* observed in the pull-out process gradually decreased due to their declined residual pull-out strength.

(3) Furthermore, *EMD* is found as a promising tool and in conjunction with usage of *HHT* spectrum of the signal to provide accurate time-frequency signal characteristics and make it possible to monitor the multi-interface debonding and multi-stage fiber components breakage behaviors using *AE* signals in real practice. Based on this, this chapter proposed an effective method for accurately assessing the multi-layer and multi-scale pull-out behavior of *SFRCs* and determining the failure mode relying on the distribution of frequency and energy throughout the single sisal fiber pull-out process, which could be useful with the aim of failure mechanisms associated with multiple interface failure identification.

(4) Statistical analysis was employed to evaluate the probability of technical fiber, elementary fiber and micro-fibrils pull-out, which showed the technical fiber and elementary fiber were more prone to be pulled out from the matrix while micro-fibrils can only occasionally be pulled-out from cell wall. An appropriate embedded fiber length for the *SFRCs* could not only result in the debond between the technical fiber and matrix and pull-out behaviors of the technical fiber, but also lead to the multi-

stage debond and pull-out behaviors among the technical fiber, elementary fibers and cell wall micro-fibrils.

To conclude, the existence of multi-interfaces of *PFRCs* and the differences of their interfacial properties introduce the multi-layer and multi-scale mechanical failure behaviors of *PFRCs*.

CHAPTER 5

A Micromechanical Model of Interfacial Debonding between Technical and Elementary Fibers during the Pull-Out Test of Single *PFRCs*

5.1. Introduction

The hierarchical organization of plant fibers leads to multi-interface regions in their reinforced composites. Chapter 4 has presented a series of experimental exploration on the interfacial failure behaviors of single *SFRCs* in micro-scale, demonstrating that multiple interfacial failure modes can be observed in the fiber pull-out tests of single *SFRCs*. However, the traditional interfacial mechanics research methods, especially theoretical modelling, cannot accurately describe the interface mechanical properties

of *PFRCs*. Therefore, it is necessary to develop a theoretical analysis method suitable for *PFRCs* by taking into account the unique multi-layer and multi-scale structure characteristics of plant fibers.

Some micromechanical models (i.e. shear lag model) as the basis of the interface structural design have been respectively built and carried out to analyze the interfacial behaviors of fiber reinforced composites. Our understanding of the fiber pull-out behavior of fiber reinforced composites has already been enhanced by a rich body of literature based on theoretical modelling of the fracture of the fiber-matrix interfaces in *CFRCs* and *GFRCs* **[61, 113, 117, 118, 120]**. They comprehensively investigated the interface bonding conditions in composites. However, most reported studies with regards to the theoretical analysis of *PFRCs* in Chapter 2 mainly aim to evaluate their interfacial adhesion between the fiber and the matrix. There is no appropriate model for simulating the multi-layer and multi-scale failure of *PFRCs*. Notably, theoretical studies of the failure mechanisms of *PFRCs* have only considered the fracture of the interface between the technical fiber and matrix while ignoring the fracture of the interfaces between the elementary fibers **[27-29]**. To accurately reveal the interfacial debonding mechanisms of *PFRCs*, it is necessary to investigate and understand the influence of the multi-layer and multi-scale structure of plant fibers on the interfacial adhesion behaviors and the interfacial stress transfer mechanisms of *PFRCs* by combining the theoretical model with the experimental characterization. The present work in this chapter is expected to provide some guidance for the interface structural design of *PFRCs*, whereby to improve their overall mechanical performances and achieve their large-scale industrial applications.

With this motivation, the interfacial debonding behavior of *SFRCs* was respectively investigated theoretically and numerically in the following two chapters relying on the experimental results obtained in Chapter 4. In this chapter, based on the observed microscopic structure of the sisal fibers using *OM* and *SEM*, a double-interface theoretical model was proposed to simulate the interfacial failure process of *SFRCs* and investigate their fiber pull-out behaviors, interfacial bonding behaviors, damage modes and interfacial failure mechanisms. The effects of the interfacial roughness and residual clamping stress on the frictional pull-out stress of the fiber were considered using a fiber sliding model developed by the Fourier transformation approach. The developed model provided theoretical solutions of the interfacial fracture toughness, partial debond stress, maximum debond stress and initial frictional pull-out stress during the pull-out of *SFRCs*. The accuracy of the double-interface model in describing the double-layer interfacial failure of *SFRCs* was examined by comparison with experimental results.

5.2. Theoretical analysis of multi-layer interface debonding behaviors for single *PFRCs*

5.2.1. Basic governing equations for *PFRCs*

To describe the multiple interface debonding behaviors of *PFRCs*, a double-interface model based on the shear lag model **[61, 113, 117, 118]** was developed for single *PFRCs* subject to the pull-out tests, as shown in **Figure 5.1** (a). A plant technical fiber of radius a_1, composed of elementary fibers, is embedded in the center of the coaxial

matrix of radius b. The bundle of elementary fibers located in the center of the technical fiber, denoted the inner elementary fibers (*InEFs*), is equivalently treated as a single fiber of radius a_2. The remaining part of the technical fiber is denoted the outer elementary fibers (*OutEFs*). The axial and radial directions of the fiber are set as the z and r axes, respectively, to establish a general cylindrical coordinate system (r, θ, z). L is the total embedded length of the technical fiber. The matrix is fixed at the bottom end ($z = L$) and a tensile stress σ can be seen as being applied at the upper end ($z = 0$) of the embedded part of the technical fiber by neglecting the variation of the fiber axial stress for the extension part. The *OutEFs* and *InEFs* are assumed to possess the same mechanical properties (i.e., Young's modulus and Poisson's ratio) **[168]**, whereas the *IF-FM* and the *IF-ELE* are assumed to have different interfacial properties regarding the interfacial fracture toughness and friction coefficient. Therefore, for perfectly elastic and isotropic elementary fibers and matrix, the general stress-strain relationships can be written as **Equations (5.1)-(5.3)**.

$$\varepsilon_i^{\,z}(r, z) = \partial u_i^{\,z} / \partial z = \left\{\sigma_i^{\,z}(r, z) - \nu_i\left[\sigma_i^{\,r}(r, z) + \sigma_i^{\,\theta}(r, z)\right]\right\} / E_i + \alpha_i \Delta T \qquad \textbf{(5.1)}$$

$$\varepsilon_i^{\,\theta}(r, z) = u_i^{\,r} / r = \left\{\sigma_i^{\,\theta}(r, z) - \nu_i\left[\sigma_i^{\,r}(r, z) + \sigma_i^{\,z}(r, z)\right]\right\} / E_i + \alpha_i \Delta T \qquad \textbf{(5.2)}$$

$$\varepsilon_j^{\,rz}(r, z) = \partial u_j^{\,z} / \partial r = 2\left(1 + \nu_j\right) / E_j \tau_j^{\,rz}(r, z) \qquad \textbf{(5.3)}$$

where E and ν are Young's modulus and Poisson's ratio, respectively, and $i = m, f_1, f_2$ and $j = m, f_1$. The subscripts m, f_1 and f_2 refer to the matrix ($a_1 < r < b$), *OutEFs* ($a_2 < r < a_1$) and *InEFs* ($0 < r < a_2$), respectively, and the superscripts indicate the directions of material properties. Two types of interfacial failure are observed in the fiber pull-out test, as schematically summarized in **Figure**

5.1. The failure of *PFRCs* is consequently categorized into two processes, namely Process 1 (**Figure 5.1** (b)-(c)) and Process 2 (**Figure 5.1** (d)-(g)). During Process 1, the interfacial debonding occurs at the *IF-FM*, whereas during Process 2, debonding occurs at the *IF-ELE*.

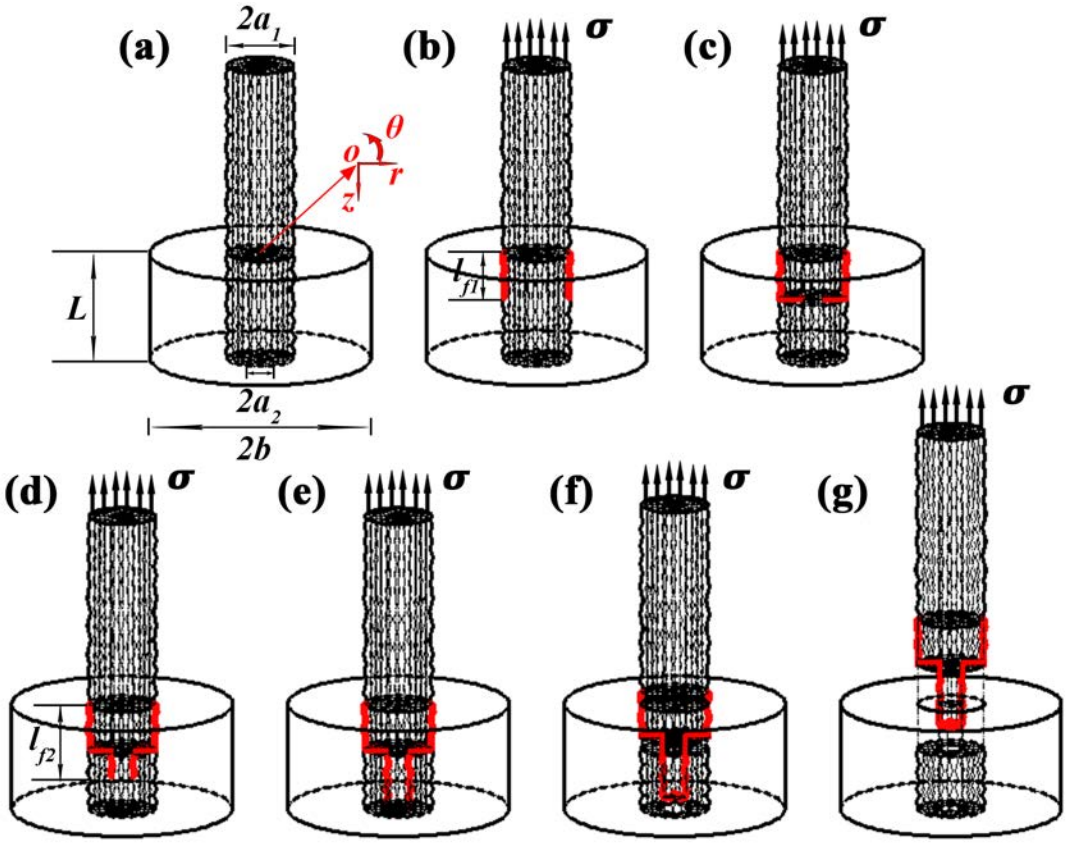

Figure 5.1 Schematic of the double-interface model describing pull-out behaviors of *PFRCs*: (a) original stage, (b)-(c) Process 1 and (d)-(g) Process 2.

The mechanical equilibria of the applied stresses (σ), internal stresses (σ_{f1},σ_{f2},σ_m) and interfacial shear stresses (τ_{i1}, τ_{i2}) are described by the following equations:

$$\sigma = \eta/(1+\eta)\sigma_{f2}{}^{z}(z)+\sigma_{f1}{}^{z}(z)/(1+\eta)+\sigma_{m}{}^{z}(z)/\gamma \tag{5.4}$$

$$\begin{aligned} d\sigma_{f2}{}^{z}(z)/dz &= -2/a_2\tau_{i2}{}^{rz}(z) \\ d\sigma_{f1}{}^{z}(z)/dz &= -2(1+\eta)/a_1\tau_{i1}{}^{rz}(z)+2\eta/a_2\tau_{i2}{}^{rz}(z) \end{aligned} \tag{5.5}$$

$$d\sigma_m{}^z(z)/dz = 2\gamma / a_1\tau_{i1}{}^{rz}(z) \quad \textbf{(5.6)}$$

in which $\eta\left(=a_2{}^2/\left(a_1{}^2-a_2{}^2\right)\right)$ and $\gamma\left(=a_1{}^2/\left(b^2-a_1{}^2\right)\right)$ are the volume ratio of the elementary fiber to the technical fiber and volume ratio of the technical fiber to the matrix, respectively.

In the following, the stress distributions of the *OutEFs* and *InEFs* during Processes 1 and 2 will be derived by considering the boundary conditions induced when the debonding occurs and propagates at the *IF-FM* and *IF-ELE*, respectively.

5.2.2. Process 1: Debonding between the technical fiber and epoxy matrix

5.2.2.1 Stresses in the bonded region ($l_{f1} < z < L$)

During Process 1, the axial stresses of the *OutEFs* and *InEFs* are the same, as they undergo identical deformations and have identical modulus values ($\sigma_{f1}{}^z(z) = \sigma_{f2}{}^z(z) = \sigma_f{}^z(z)$). In the bonded region, the fiber axial stress is calculated by the differential equation and boundary conditions in Appendix A as

$$\sigma_f{}^z(z) = \left[\begin{array}{l}\left(\sigma_{lf1} + (1+\eta)A_1/\eta\sigma + A_2\right)\sinh\left(\sqrt{A_3}(L-z)\right) \\ +\left((1+\eta)A_1/\eta\sigma + A_2\right)\sinh\left(\sqrt{A_3}(z-l_{f1})\right)\end{array}\right] \\ /\sinh\left(\sqrt{A_3}\left(L-l_{f1}\right)\right) - \left((1+\eta)A_1/\eta\sigma + A_2\right) \quad \textbf{(5.7)}$$

where σ_{lf1} represents the crack tip debond stress acting at the critical point ($z = l_{f1}$) separating the bonded and debonded regions. The other coefficients are functions of material properties and geometric factors, and the relevant details are given in

Appendix C. The resulting equations of the matrix axial stress $\sigma_m{}^z(z)$ and shear stresses $\tau_{i1}{}^{rz}(z)$, $\tau_{i2}{}^{rz}(z)$ are determined by **Equations (5.4)-(5.7)**.

5.2.2.2 Stresses in the debonded region ($0 < z < l_{f1}$)

In the debonded region of the *IF-FM*, the frictional shear stress is governed by the Coulomb friction law **[169]**, assuming a constant friction coefficient μ_1 along the debonded interface **[74]**:

$$\tau_{i1}{}^{rz}(z) = -\mu_1\left[q_{01} + q_{a1}(z) - q_{R1}(z)\right] \tag{5.8}$$

in which the expressions for q_{01}, $q_{a1}(z)$ and $q_{R1}(z)$ are described in Appendix B. q_{01} is the residual clamping stress caused by matrix shrinkage and the difference in thermal contraction or expansion between the constituents during fabrication. $q_{a1}(z)$ is the radial stress arising from the Poisson contraction of fibers subject to tension. $q_{R1}(z)$ is the additional radial stress due to the asperity mismatch between the technical fiber and matrix, i.e., the interfacial roughness.

Substituting **Equations (5.8)** into **(5.5)** and considering the stress boundary condition $\sigma_f{}^z(0) = \sigma$, the solution for the axial stress of the technical fiber is given by

$$\begin{aligned}\sigma_f{}^z(z) = {} & e^{A_5 z}\sigma + \begin{pmatrix}\left(1 - 2\mu_1\alpha\nu_{f1}A_4/(a_1A_5)\right)\sigma \\ -\mu_1\left(2q_{01} + k_1/a_1B_{01}\right)/(a_1A_5)\end{pmatrix}\left(1 - e^{A_5 z}\right) \\ & - \sum_{n_1=1}^{\infty} B_{n_1} 2\mu_1 k_1 A_5 L^2 / \left(a_1\left(A_5{}^2L^2 + n_1{}^2\pi^2\right)\right)\begin{pmatrix}\cos\left(n_1\pi z/L\right) - e^{A_5 z} \\ -n_1\pi/\left(A_5 L\right)\sin\left(n_1\pi z/L\right)\end{pmatrix}\end{aligned} \tag{5.9}$$

where the corresponding coefficients are defined in Appendices B and C. The solutions for the matrix axial stress $\sigma_m{}^z(z)$ and shear stresses $\tau_{i1}{}^{rz}(z)$, $\tau_{i2}{}^{rz}(z)$ at the interface can be solved by applying **Equations (5.4)-(5.6)** and **(5.9)**.

5.2.2.3 Debonding criterion of *IF-FM* and solution for the external applied stress

Fracture mechanics and the Griffith energy balance equation are used to determine the interfacial debonding criterion **[170]**.

$$G_{ic1} = 1/\left(2\pi a_1\right)\partial U_{t1}/\partial l_{f1} \tag{5.10}$$

The total elastic strain energy U_{t1} is expressed as the sum of the elastic strain energies of the technical fiber U_f and the epoxy matrix U_m.

$$U_{t1} = U_f + U_m \tag{5.11}$$

The interfacial debonding criterion between the technical fiber and epoxy matrix can be expressed as **Equation (5.12)** by substituting **Equations (5.7)** and **(5.9)** into **Equation (5.10)** and rewriting the energy balance expressed in **Equation (5.10)**.

$$2\pi a_1 G_{ic1} = p_1\sigma^2 + p_2\sigma + p_3 \tag{5.12}$$

where p_1, p_2 and p_3 are listed in Appendix C. Therefore, the external stress applied on the technical fiber during the onset and spread of debonding can be calculated by rearranging **Equation (5.12)** as

$$\sigma = \left(2\pi a_1 G_{ic1}/p_1 + \left(p_2{}^2 - 4p_1p_3\right)/\left(4p_1{}^2\right)\right)^{1/2} - p_2/\left(2p_1\right) \tag{5.13}$$

Using the boundary condition $\sigma_f{}^z\left(l_{f1}\right)=\sigma_{lf1}$ in the debonded region, the partial debonding stress $\sigma_{d1}{}^p$ during Process 1 is given by

$$\sigma_{d1}{}^p=\left(\sigma_{lf1}-A_7\right)/A_6 \tag{5.14}$$

5.2.3. Process 2: Debonding between the elementary fibers

5.2.3.1 Stresses in the bonded region ($l_{f2}<z<L$)

During Process 2, stress is redistributed due to the sudden partial breaking of the *OutEFs*. The axial stresses of the *OutEFs* and *InEFs* are no longer equal due to the displacement discontinuity. The equilibrium between the applied stress and the internal stress distribution is rewritten as

$$\sigma=\sigma_{f2}{}^z(z)+\sigma_{f1}{}^z(z)/\eta+(1+\eta)/(\gamma\eta)\sigma_m{}^z(z) \tag{5.15}$$

where $\sigma_{f1}{}^z(z)=\sigma_{f2}{}^z(z)=\sigma_f{}^z(z)$ is used for the bonded region of Process 2.

A method similar to that of Process 1 is used to represent the solution for the fiber axial stress.

$$\sigma_f{}^z(z)=\begin{bmatrix}\left(\sigma_{lf2}+A_1\sigma+A_2\right)\sinh\left(\sqrt{A_3}\left(L-z\right)\right)\\+\left(A_1\sigma+A_2\right)\sinh\left(\sqrt{A_3}\left(z-l_{f2}\right)\right)\end{bmatrix}/\sinh\left(\sqrt{A_3}\left(L-l_{f2}\right)\right)-\left(A_1\sigma+A_2\right) \tag{5.16}$$

where σ_{lf2} is defined as the debond stress at the crack tip ($z=l_{f2}$). The corresponding matrix axial stress and shear stresses can be obtained by substituting **Equations (5.16)** into **(5.5), (5.6)** and **(5.15)**.

5.2.3.2 Stresses in the debonded region ($0 < z < l_{f2}$)

During Process 2, as shown in **Figure 5.1** (d), the existence of the debonded *IF-FM* (produced during Process 1) influences the stress distribution at the *IF-ELE* due to the residual axial stress of the *InEFs* during Process 1. Consequently, the debonded region during Process 2 is divided into two parts along the z axis, namely Part 1 ($0 < z < l_{f1}$) and Part 2 ($l_{f1} < z < l_{f2}$).

The fiber axial stress, the matrix axial stress and the shear stresses at the *IF-ELE* in Part 1 can be solved following a similar procedure to that described in section 5.2.2.2. In Part 2, the axial stresses of the *OutEFs* differ from those of the *InEFs* due to stress rearrangement and the difference in the displacements ($\sigma_{f1}{}^{z}(z) \neq \sigma_{f2}{}^{z}(z)$). The Coulomb friction law is used to determine the frictional shear stress between elementary fibers with a constant friction coefficient μ_2:

$$\tau_{i2}{}^{rz}(z) = -\mu_2 \left[q_{02} + q_{a2}(z) - q_{R2}(z) \right] \quad \textbf{(5.17)}$$

in which q_{02} is assumed to equal q_{01} (i.e., neglecting differences in the thermal contraction or expansion between the *OutEFs* and *InEFs*), $q_{a2}(z)$ is the radial stress and $q_{R2}(z)$ is the additional radial stress due to the asperity mismatch between the *OutEFs* and *InEFs* induced by the interfacial roughness. The expressions for $q_{a2}(z)$ and $q_{R2}(z)$ can be found in Appendix B.

Combining **Equations (5.5)** and **(5.17)** in conjunction with the stress boundary conditions $\sigma_{f1}{}^{z}\left(l_{f1}\right)=0;\ \sigma_{f1}{}^{z}\left(l_{f2}\right)=\sigma_{f2}{}^{z}\left(l_{f2}\right)=\sigma_{lf2};\ \sigma_{f2}{}^{z}\left(l_{f1}\right)=\sigma_{f2lf1}$, the axial *OutEFs* ($\sigma_{f1}{}^{z}(z)$) and *InEFs* ($\sigma_{f2}{}^{z}(z)$) stresses are given by

$$\begin{aligned}\begin{pmatrix}\sigma_{f1}{}^{z}(z)\\ \sigma_{f2}{}^{z}(z)\end{pmatrix}&=\begin{pmatrix}C_8\\ F_2\end{pmatrix}\sigma+\begin{pmatrix}C_9\\ -F_3\end{pmatrix}+\left(C_1\sigma+C_2\right)\begin{pmatrix}C_3\\ 1\end{pmatrix}e^{r_1 z}\\ &+\begin{pmatrix}D_3\sigma+D_7\\ -D_5\left(C_1\sigma+C_2\right)\end{pmatrix}\begin{pmatrix}C_4\\ 1\end{pmatrix}e^{r_2 z}+\begin{pmatrix}D_4\sigma+D_8\\ +D_6\left(C_1\sigma+C_2\right)\end{pmatrix}\begin{pmatrix}C_5\\ 1\end{pmatrix}e^{r_3 z}\\ &+\begin{pmatrix}C_6\\ D_9\end{pmatrix}\sum_{n_2=1}^{\infty}B_{n_2}\cos\left(n_2\pi z/L\right)-\begin{pmatrix}C_7\\ -F_1\end{pmatrix}\sum_{n_2=1}^{\infty}B_{n_2}\sin\left(n_2\pi z/L\right)\end{aligned}\qquad\textbf{(5.18)}$$

which yields the corresponding expressions for the matrix axial stress $\sigma_{m}{}^{z}(z)$ and the shear stresses $\tau_{i1}{}^{rz}(z)$, $\tau_{i2}{}^{rz}(z)$ at the two interfaces according to **Equations (5.5)**, **(5.6)**, **(5.15)** and **(5.18)**. The relevant coefficients C_i, D_i, F_i are all presented in Appendix C.

5.2.3.3 Debonding criterion of *IF-ELE* and solution for the external applied stress

Following the similar procedure in section 5.2.2.3, the total elastic strain energy (U_{t2}) is taken as the sum of the elastic strain energies of the matrix (U_m), the *OutEFs* (U_{f1}) and *InEFs* (U_{f2}), which are expressed in Appendix C. The same method as during Process 1 is used to determine the partial debonding stress $\sigma_{d2}{}^{p}$ during Process 2 by using the boundary condition $\sigma_{f2}{}^{z}\left(l_{f2}\right)=\sigma_{lf2}$:

$$\sigma_{d2}{}^{p}=\left[\begin{array}{l}\sigma_{lf2}+F_3-C_2\mathrm{e}^{\eta l_{f2}}+\left(C_2D_5-D_7\right)\mathrm{e}^{r_2l_{f2}}-\left(C_2D_6+D_8\right)\mathrm{e}^{r_3l_{f2}}\\-D_9\sum_{n_2=1}^{\infty}B_{n_2}\cos\left(n_2\pi l_{f2}/L\right)-F_1\sum_{n_2=1}^{\infty}B_{n_2}\sin\left(n_2\pi l_{f2}/L\right)\end{array}\right]\\ /\left(C_1\mathrm{e}^{\eta l_{f2}}+\left(D_3-C_1D_5\right)\mathrm{e}^{r_2l_{f2}}+\left(D_4+C_1D_6\right)\mathrm{e}^{r_3l_{f2}}+F_2\right) \quad \textbf{(5.19)}$$

The frictional pull-out stress σ_{fr} is calculated by considering that $\sigma_{f2}{}^{z}=0$ at $z=l_{f2}-s$ (s is the fiber sliding distance).

$$\sigma_{fr}=\left[\begin{array}{l}F_3-C_2\mathrm{e}^{\eta\left(l_{f2}-s\right)}+\left(C_2D_5-D_7\right)\mathrm{e}^{r_2\left(l_{f2}-s\right)}-\left(C_2D_6+D_8\right)\mathrm{e}^{r_3\left(l_{f2}-s\right)}\\-D_9\sum_{n_2=1}^{\infty}B_{n_2}\cos\left(n_2\pi\left(l_{f2}-s\right)/L\right)-F_1\sum_{n_2=1}^{\infty}B_{n_2}\sin\left(n_2\pi\left(l_{f2}-s\right)/L\right)\end{array}\right]\\ /\left(C_1\mathrm{e}^{\eta\left(l_{f2}-s\right)}+\left(D_3-C_1D_5\right)\mathrm{e}^{r_2\left(l_{f2}-s\right)}+\left(D_4+C_1D_6\right)\mathrm{e}^{r_3\left(l_{f2}-s\right)}+F_2\right) \quad \textbf{(5.20)}$$

5.3. Evaluations of interfacial parameters and maximum debond stresses of *SFRCs*

As shown in **Figure 5.2**, the Weibull shape parameter and scale parameter for the diameters of the sisal fibers in this study were 4.54 and 186 μm, respectively. The volume ratio of the elementary fiber to the technical fiber and volume ratio of the technical fiber to the matrix were measured by the *OM* and *SEM* observation. The pulled-out elementary fibers were considered as a bundle of elementary fibers. The distribution ratio of pulled-out and residual elementary fibers inside each technical fiber can be calculated by measuring the corresponding area with the image analysis software (MiVnt, Shanghai Optical Instrument Factory, China). The Young's modulus

of the sisal fiber was obtained by the linear part in the curve of single fiber pull-out test in Chapter 4 while that of the matrix was based on the result in section 3.3. The Poisson's ratio of the sisal fiber and matrix were referred to section 3.2.2. The other basic material constants, including the thermal expansion coefficient of the sisal fiber and matrix and their temperature range, summarized in **Table 5.1**, were reference for other literatures **[74, 168, 171]**. The determination of the interfacial properties for two interfaces of the *SFRCs* will be discussed in the following section. Finally, the tensile strength of the sisal fibers was 411.73 ± 99.76 MPa **[32]**.

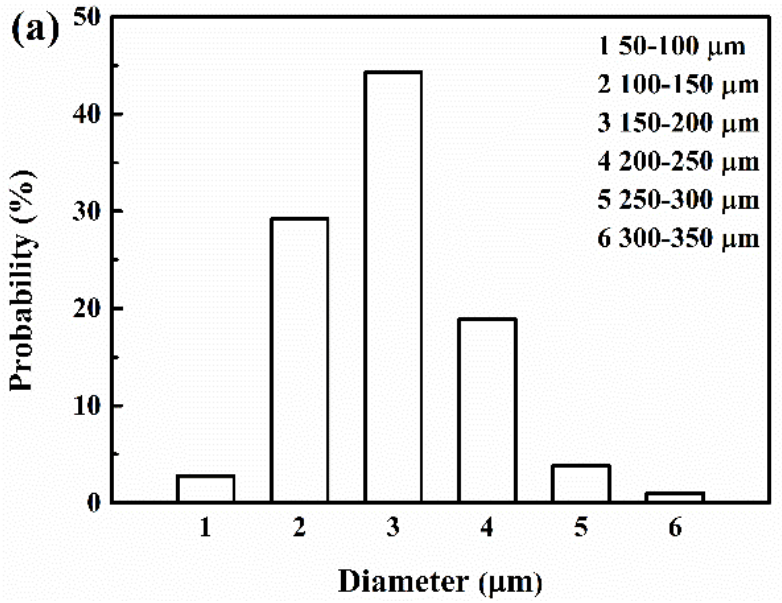

Figure 5.2 (a) Distribution of diameters of the sisal fibers and (b) corresponding Weibull distribution.

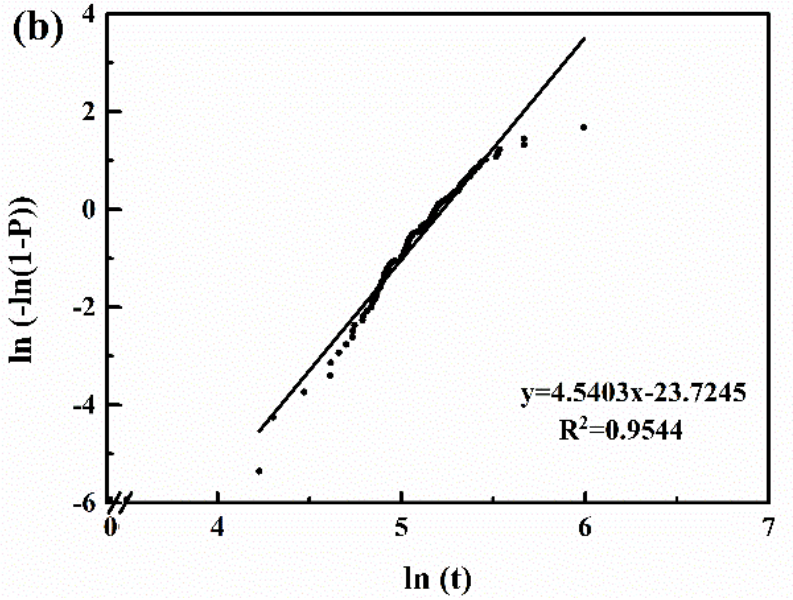

Figure 5.2 (continued).

Table 5.1 Material properties and geometric factors used in the model.

	Properties of fibers			Properties of matrix	
Type	Fiber type	*OutEFs*	*InEFs*	Matrix type	Epoxy
Young's modulus	$E_{f1}\ (GPa)$	10.06		$E_m\ (GPa)$	4.75
Poisson's ratio	ν_{f1}	0.12		ν_m	0.16
Radius	$a_1 / a_2\ (mm)$	0.093	0.065	$b\ (mm)$	10
Thermal expansion coefficient	$\alpha_{f1}\ (10^{-6}/°C)$	10.8		$\alpha_m\ (10^{-6}/°C)$	70.8
Interfacial properties					
Interface type	*IF-FM*			*IF-ELE*	
Embedded fiber length $L\ (mm)$	0.1~0.5				
Coefficient of friction μ_1 / μ_2	4.42			1.12	
Temperature change $\Delta T\ (°C)$	-100				
Fracture toughness G_{ic1} / $G_{ic2}\ (J/m^2)$	133			181	

From the *SEM* observation, the technical fibers and elementary fibers of the sisal fiber both possessed rough surfaces. The roughness of the two interfaces was simulated

with the same average wavelength of 2 μm and maximum amplitude d_{max} of 0.1 μm and were generated randomly based on these parameters, as depicted in **Figure 5.3**.

Figure 5.3 Simulated rough interface with d_{max} of 0.1 μm.

From the experimental curves, the maximum debond stresses in different embedded fiber length could be obtained. The interfacial properties, including the coefficient of friction and fracture toughness, were calculated through the fitting of the experimental results and theoretical predictions regarding the maximum debond stresses as functions of the embedded fiber length as shown in **Figure 5.4**. The maximum debond stresses were found to increase with increasing embedded fiber length. It could also be seen in **Figure 5.4** that the debond behavior is dependent on the embedded fiber length. The fibers were directly pulled-out from the matrix when the embedded length was less than 220 μm. In every case, this phenomenon did not occur during Process 2, because the maximum debond stresses of the *IF-ELE* were far less than the tensile strength of the sisal fibers. Conversely, when the embedded fiber length exceeded 460 μm (i.e., the critical fiber length), the fiber would break at a position above the embedded part and no debonding or pull-out processes occurred.

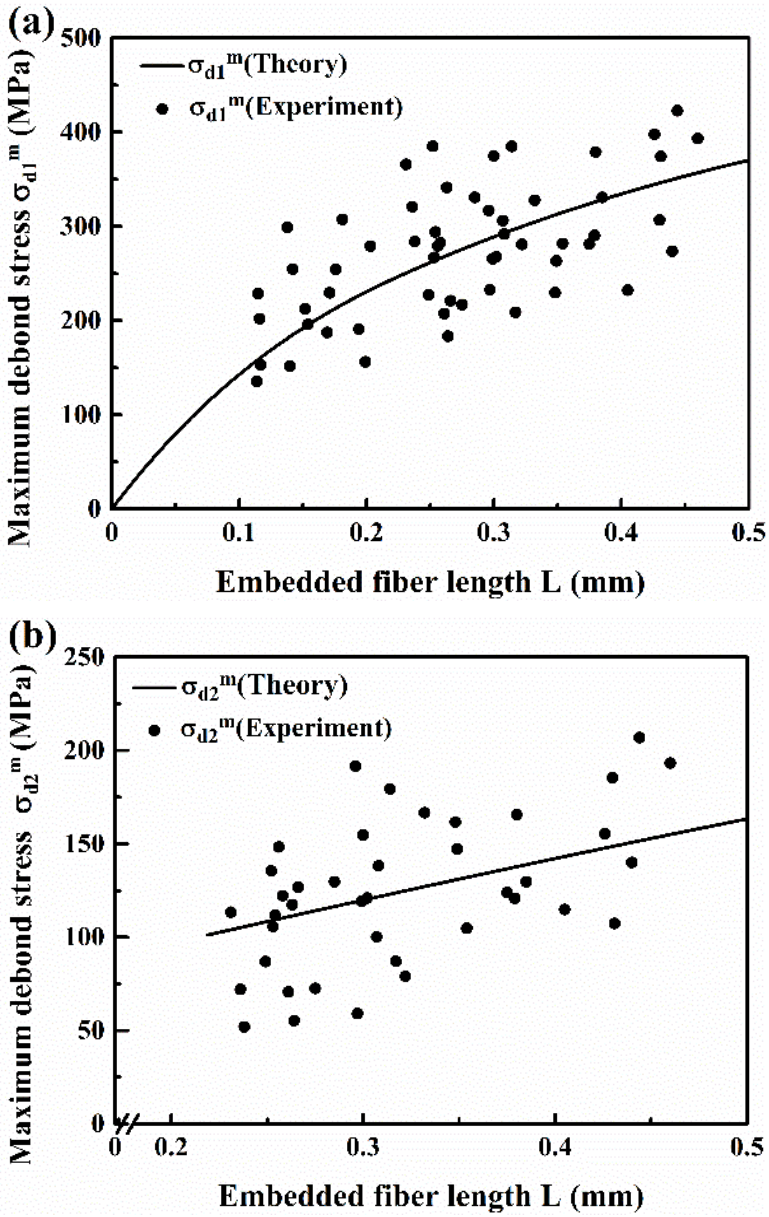

Figure 5.4 Maximum debond stress of *SFRCs* with different embedded fiber lengths during (a) Process 1 and (b) Process 2.

5.4. Comparisons of the applied stresses on sisal technical fiber between experiment and theory

The experimental applied stresses versus displacement curve for *SFRCs* with different embedded fiber lengths are plotted in **Figure 5.5** (a). Using **Equations (5.1), (5.14),**

(5.19) and **(5.20)**, the theoretical applied stresses were solved at different stages (see **Figure 5.1**) with various embedded fiber lengths and are shown together in **Figure 5.5** (b), where the displacement was calculated as the sum of the deformation of the external fiber and the embedded fiber.

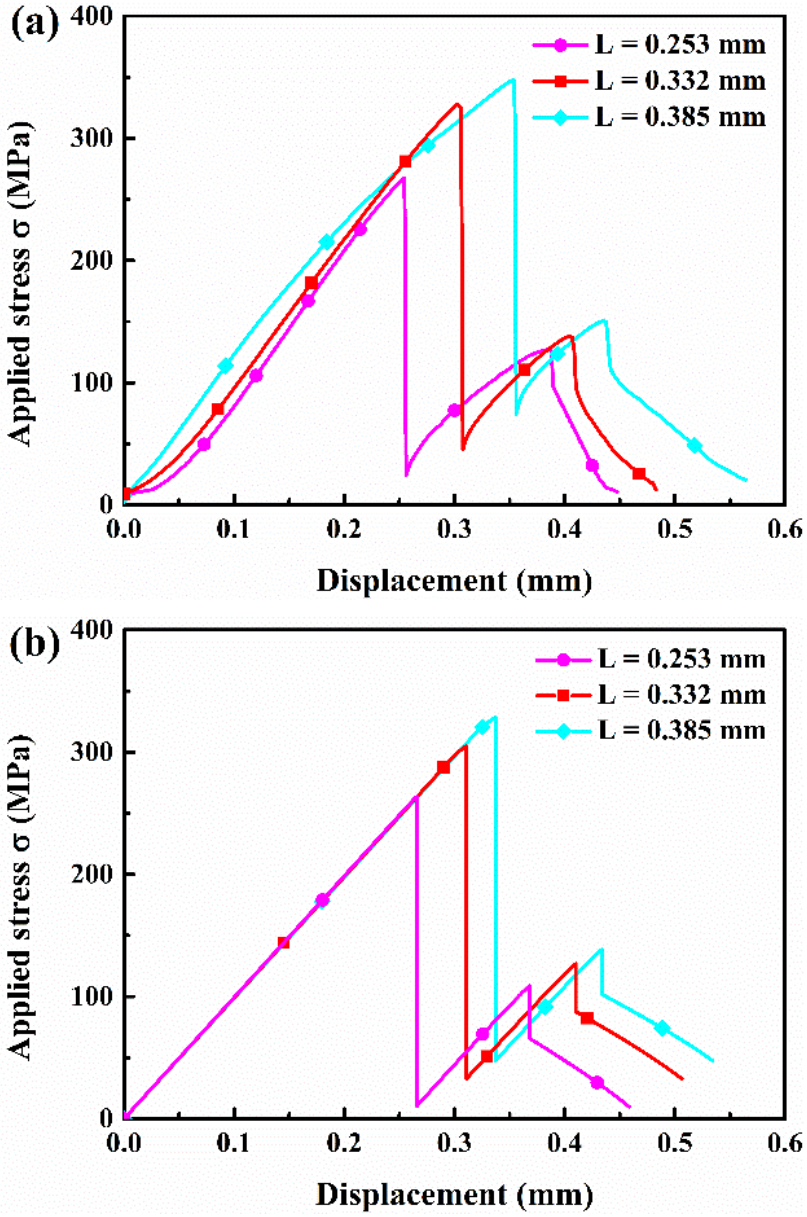

Figure 5.5 Applied stress-displacement curves in the single fiber pull-out behaviors of single *SFRCs* obtained from (a) experiment and (b) theory.

From the results in **Figure 5.5** (b), it is clear that the *PFRCs* subject to tensile loading underwent a multi-stage failure mode that proceeded through the sequential fracture of the two interfaces. During Process 1, the loading of the composite induced elastic deformation, followed by the partial debonding of the interface between the technical fiber and matrix. The partial debond stress, $\sigma_d{}^p$, increased with the increase of the debond length, as calculated by **Equation (5.14)**. When the applied stress reached the maximum debond stress, $\sigma_d{}^m$, as shown in **Figure 5.1** (c), the elementary fibers began to break, as the applied stress exceeded the limit of the tensile strength. During Process 2, the residual elementary fibers continued to support loading, whereas debonding began at the *IF-ELE*, as demonstrated in **Figure 5.1** (d). The applied stress then dropped abruptly when all of the elementary fibers had been broken. We emphasize that the theoretical analysis was consistent with the experimental data regarding the applied stress-displacement curve from the pull-out tests. The maximum debond stresses in both Processes 1 and 2 increased as the embedded fiber length L increased, due to the greater radial asperity pressure.

The morphologic features of the fracture surfaces of the sisal fibers after the pull-out tests, as observed by *SEM* (see **Figure 5.6**), further confirmed the validity of the present double-interface model in predicting the fracture behavior of *PFRCs* subject to the tensile loading. Specifically, debonding occurred at the *IF-ELE* (**Figure 5.6** (a)), as predicted. Moreover, some elementary fibers were observed being pulled-out from the technical fiber in the specimen for which pull-out was predicted based on its

embedded fiber length (**Figure 5.6** (b)). Therefore, the multi-layer structure of the sisal fiber led to multiple interfacial failure modes of *SFRCs* in the pull-out tests.

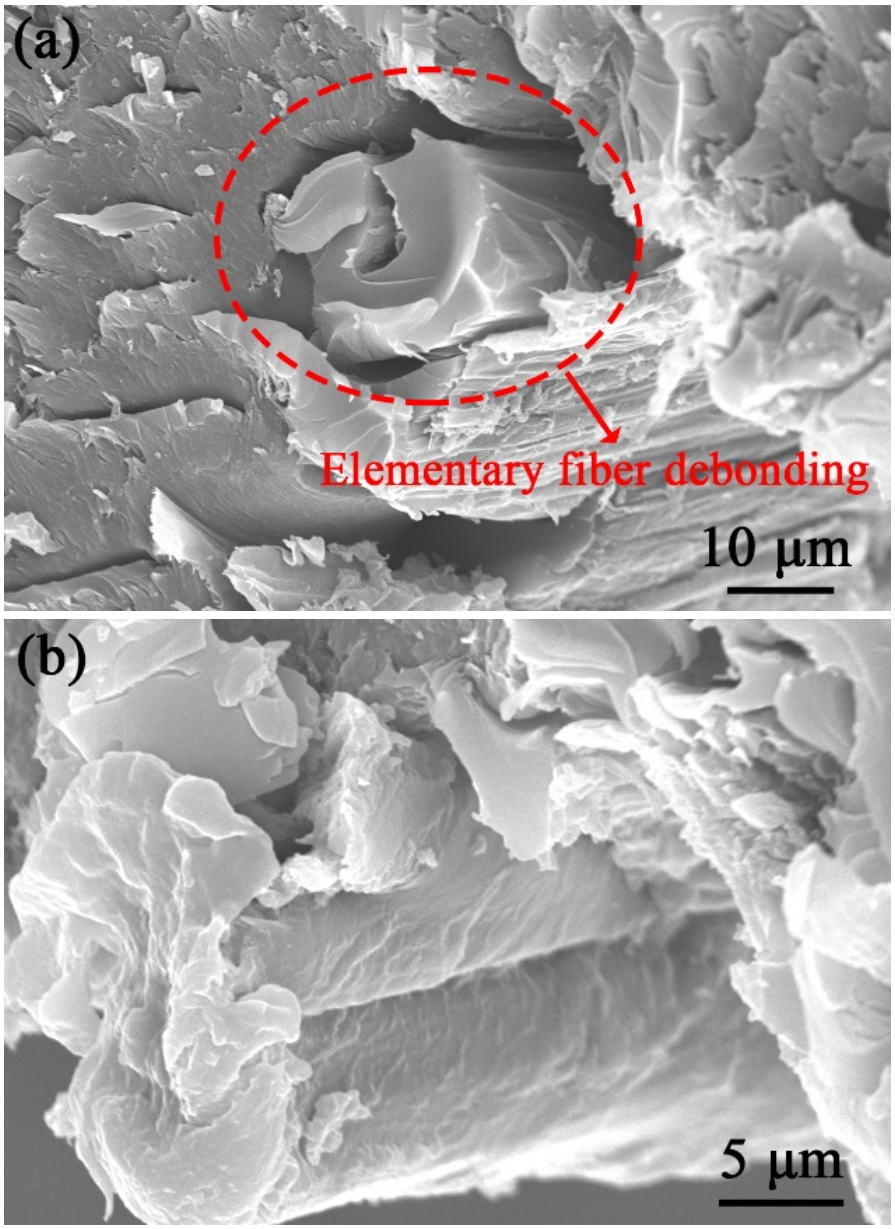

Figure 5.6 *SEM* photographs of pulled-out sisal fibers after single sisal fiber pull-out tests: (a) elementary fiber debonding and (b) elementary fiber pull-out ($L = 0.332\ mm$).

As shown in **Figure 5.7**, the accuracy of the double-interface model was also compared with that of the traditional single-interface model for predicting the multi-stage debonding behavior of *SFRCs*. The results of the former were found to be more consistent with the experimental results than those of the latter, showing that the double-interface model developed in this work provided a more accurate description of the multi-layer and multi-scale interfacial damage behaviors of *SFRCs*.

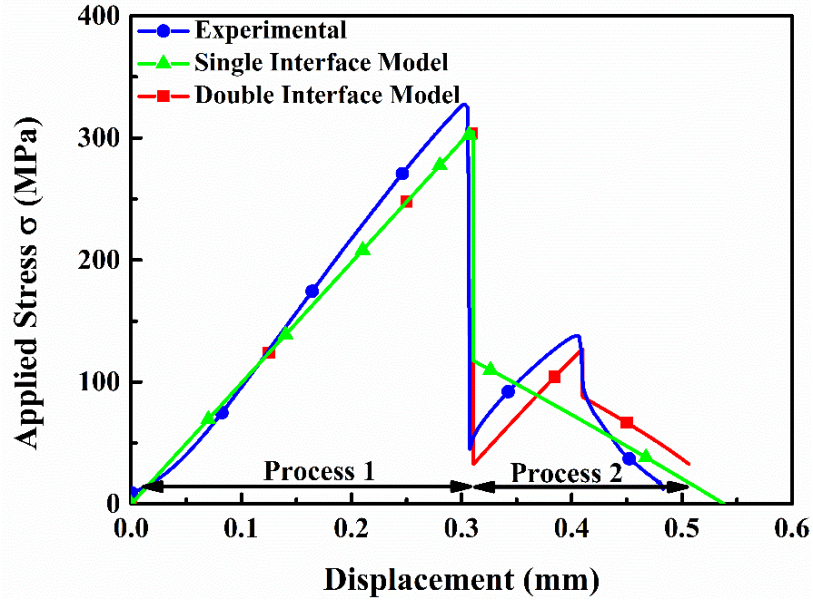

Figure 5.7 Applied stress-displacement curves obtained from experiment, single- and double-interface model in a typical case $L = 0.332\ mm$.

5.5. Double-stage fracture mechanisms of *SFRCs*

To investigate the influence of the double-interface on the debonding behavior of *SFRCs*, the stress distributions in the sisal fibers, epoxy matrix and two interfaces were calculated and will now be discussed with reference to the failure mechanisms of the *SFRCs*. **Figure 5.8** depicts the axial stress distribution of the fiber and matrix and the shear stress distribution of the two interfaces, as a function of the ratio z/L,

for *SFRCs* with different embedded fiber lengths subject to the maximum debond stress. During Process 1, the axial stresses of the technical fiber decreased rapidly from the free end to the bottom end while the matrix axial stresses increased from the free end to the embedded end. The stress gradient in the bonded region was greater than that in the debonded region. In addition, the embedded length L was found to directly affect the rate of change of these two stresses. With the increase of the embedded fiber length, the stress gradient in the bonded region increased, whereas that in the debonded region remained unchanged. The distributions of the interfacial shear stresses in the two interfaces were both discontinuous at the critical point separating the debonded region and bonded region, with a sudden rise at the debond crack tip. Inspection of **Figure 5.8** (e) shows that the shear stress of the *IF-FM* was larger than that of the *IF-ELE* and reached the *IFSS* of *SFRCs*, identifying that the debonding first occurred in the *IF-FM*. During Process 2, the axial stresses of the *OutEFs* and *InEFs* differed in the region $l_{f1} < z < l_{f2}$ but were equal in all other regions. The axial stresses of the *OutEFs* and matrix decreased abruptly at the position at which $z = l_{f1}$, because of the partial breaking of elementary fibers at the end of Process 1. The broken *OutEFs* and the resin matrix functioned together as a new "matrix" in the debonding of Process 2. The matrix axial stresses in the other regions $\left(0 < z < l_{f1},\ l_{f2} < z < L\right)$ displayed similar trends during Process 2 to those of Process 1. The results in **Figure 5.8** (f) reveal that the shear stresses of the *IF-ELE* became larger than those of the *IF-FM* in the region $l_{f1} < z < l_{f2}$, which resulted in the debonding of the *IF-ELE*. To conclude, the differences between the interfacial properties of the *IF-FM* and *IF-ELE* induced multi-stage fracture of the two interfaces

in this work. The residual pull-out strength and internal stress redistribution following the failure of the *IF-FM* influenced the subsequent failure behavior of the *IF-ELE*. Therefore, the existence of multiple interfaces of *SFRCs*, and their multi-stage fracture, can lead to multiple failure modes.

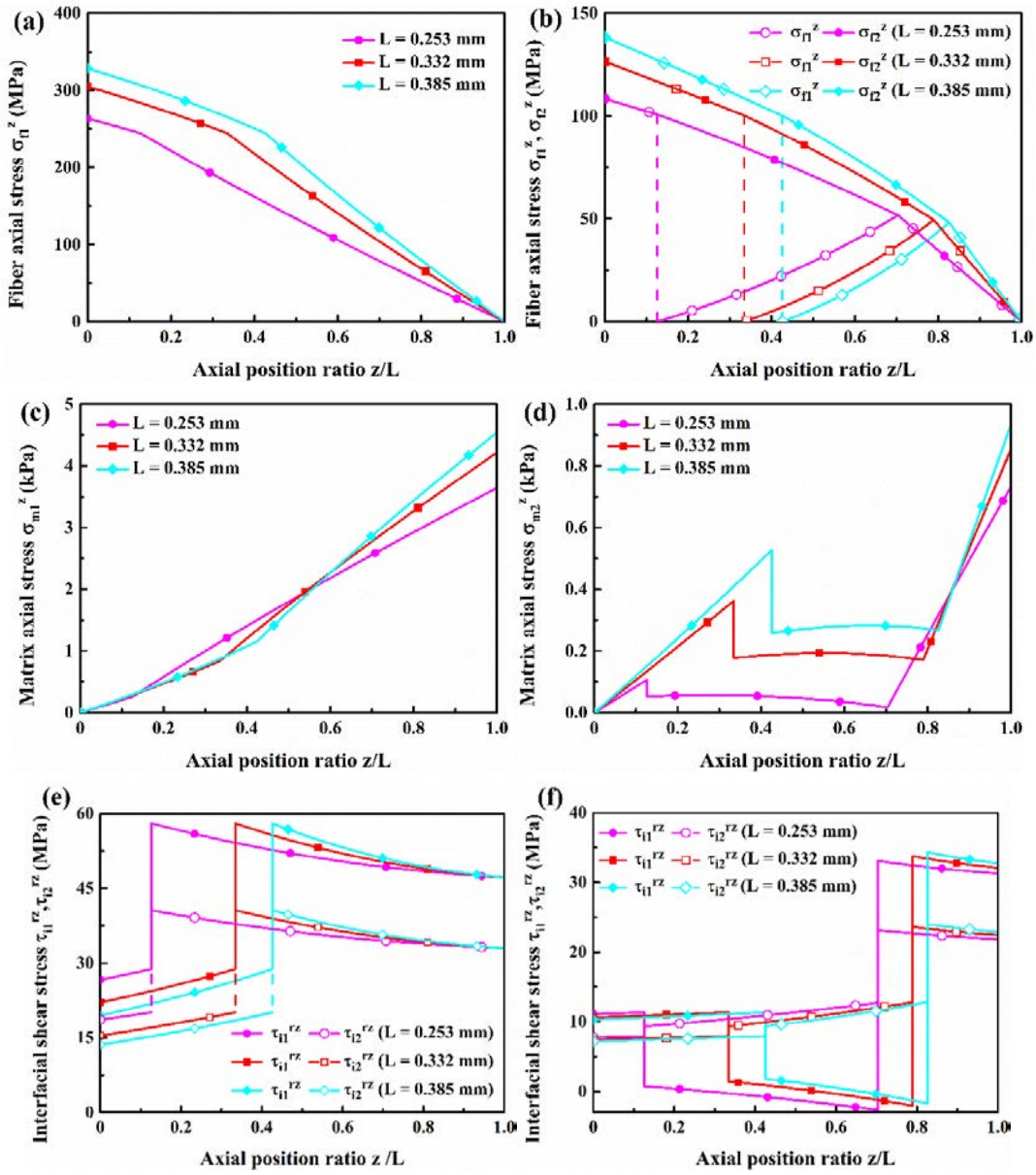

Figure 5.8 Distributions of (a) and (b) axial fiber stress, (c) and (d) axial matrix stress and (e) and (f) interfacial shear stress in the single fiber pull-out behaviors of single *SFRCs* ((a), (c) and (e) for Process 1 and (b), (d) and (f) for Process 2).

5.6. Summary

In this chapter, a double-interface model that considering the effects of interface roughness and thermal residual stress is proposed for the single sisal fiber pull-out test on the basis of a Fourier transformation approach, Coulomb friction law and the Griffith energetic debond criterion. The interfacial debonding criterions and the solutions for the axial stress distributions, the partial debond stresses, the maximum debond stresses, the external applied stresses and the initial frictional pull-out stresses in the pull-out processes of *PFRCs* are obtained. The presented model provided a more reasonable and accurate description of debonding process in the single sisal fiber pull-out test. The major results from this chapter are shown below:

(1) Due to the multi-layer and multi-scale structure of sisal fibers, their reinforced composites have different interfacial failure mechanisms from those of *CFRCs* or *GFRCs*. The multi-interface debonding processes of *SFRCs*, including the debonding between the technical fiber and matrix and that between the elementary fibers, could be adequately described by the double-interface model that incorporated the effects of interfacial roughness and thermal residual stress. The distinct interfacial properties of *SFRCs* and process of stress transfer across the multi-layer interface were presented.

(2) The calculated and measured maximum debond stresses increased with the increase of the embedded fiber length. The experimental curves and the calculated results both showed that residual pull-out strength for *SFRCs* was gradually reduced due to the existence of the unique multi-layer structures for plant fibers and this kind

of multi-layer damage mode. Good agreement was achieved between the theoretical predictions of the proposed double-interface model and the experimental measurements of fiber pull-out, which indicated that the proposed model could predict the stress distribution and provide guidance for the experiment procedure. Upon further comparison, the double-interface model was found to produce more accurate results than the existing single-interface model, indicating that the former provided a better description of the multi-layer and multi-scale interfacial damage mechanisms of *PFRCs*. Using the proposed model, the failure mechanisms of *PFRCs* in the pull-out tests were analyzed in further detail.

(3) The axial stress distributions at the maximum debond stress with different embedded fiber length were different in two processes due to the different interfacial bond conditions. During the Process 1, the shear stress of the *IF-FM* was larger than that of the *IF-ELE*, so that debonding first occurred at the *IF-FM*. During the Process 2, the shear stresses in the debonded region of the *IF-ELE* became larger than that of the *IF-FM*, which resulted in the debonding of the *IF-ELE*.

(4) Compared to the pull-out process of *CFRCs* or *GFRCs*, the multiple interface failure mode will delay the interfacial damage of *PFRCs*, which may make the plant fibers not directly pulled out from the matrix. The unique multi-layer damage failure derived from the distinct microstructure of plant fibers has great influence on the interfacial strength and toughness in the *PFRCs*, as well as benefit for the high energy absorption in the impact damage and the slow crack propagation in the fatigue damage.

CHAPTER 6

An *FE* Model of Multi-Layer Interface Debonding Behaviors for Single *PFRCs* during the Pull-Out Test

6.1. Introduction

Chapter 4 has illustrated that after the single sisal fiber pull-out experiment, the *SFRCs* presented multi-failure modes at the three interfaces of *SFRCs*, namely the interface between the technical fiber and matrix, that between the elementary fibers and that between the cell walls. Whereas, Chapter 5 mainly discussed the interfacial performances between the fiber and matrix and those between the elementary fibers by establishing a double-interface theoretical model. Since elementary fibers possess the multi-layer microstructure characteristics and moreover the debonding between the cell walls has already been observed in Chapter 4, it is necessary to further

consider the interfacial failure between the cell walls of plant fibers and to study its important role during the overall failure of *PFRCs*. Rare research work was found to quantitatively describe the relationship between the hierarchical structure of plant fibers and the interfacial mechanical properties of *PFRCs* and develop the *FE* model of *PFRCs* by considering the multi-layer interface. Accurate understanding of the multi-layer interfacial debond mechanisms of *PFRCs* by numerical modelling so as to assess their multi-layer interfacial load-carrying capacity, will remain a worldwide challenge, especially for *3D* problems with the complex interfacial interactions.

FE modelling has been widely used to simulate fiber pull-out behaviors and understand various intricacies of the fiber-matrix interface debonding process **[172-175]**. Liu et al. **[173]** have developed *FE* simulations for a single carbon fiber pull-out process and obtained solutions for the fiber axial stress, fiber displacement, and applied pull-out stress versus fiber displacement. Chapter 2 has summarized that numerical modelling of *CFRCs* or *GFRCs* for demonstrating their whole fiber pull-out process has been conducted in a rich body of literature **[125-130]**. However, these researches all only concluded the interface between the fiber and matrix owing to the uniform homogeneous characterization of traditional synthetic fibers. Therefore, it is necessary to combine the exploration of the interface microstructure with the prediction of interfacial mechanical properties and to develop the failure criterions for *PFRCs*, whereby accurate numerical model can be proposed to analyze the interfacial failure behaviors of *PFRCs* with the multi-layer and multi-scale characteristics.

To comprehensively display the multiple debonding processes of *PFRCs* in the pull-out test, relying on the single fiber pull-out experiments performed in Chapter 4 and the *CZM* method, a three-interface *FE* model, regarding multi-stage fracture of the three interfaces, was established to interpret the multi-layer failure phenomenon and estimate the stress variation of *SFRCs* (a typical *PFRC*) during the single sisal fiber pull-out process. Based on the proposed numerical model, three typical embedded fiber lengths obtained from statistical analysis in Chapter 4 were applied to simulate the multiple debond and pull-out behaviors of single *SFRCs*. Quantitative comparisons between the numerical simulation and experimental results of multi-stage debonding and pull-out were performed by using the applied stress as reference. The failure in *IF-FM*, *IF-ELE* and *IF-CW* was simulated to facilitate the comprehending of the relationship between the multi-layer structure of plant fibers and the interfacial mechanical properties of *SFRCs*. Finally, stress distributions during the debond process of *SFRCs*, including the axial stress and the shear stress at the multi-layer interfaces along the embedded direction were determined by *ABAQUS* model to reveal the mechanisms of the fracture behaviors of *SFRCs*.

6.2. Numerical analysis of multi-layer interface debonding behaviors for single *SFRCs*

In order to analyze multi-layer failure phenomenon of *PFRCs* in the single fiber pull-out experiments, previous chapter has firstly developed a double-interface theoretical model for single *PFRC* on the basis of existing traditional shear lag model, Coulomb friction law, fracture mechanics concept and Griffith energy balance equation. While,

from the results of Chapter 4, there still exists the third layer interfacial failure, that is, the interface between the micro-fibrils in the cell walls. To verify the theoretical model and enhance the understanding of the multi-layer and multi-scale failure modes of *PFRCs*, a three-interface *FE* model of single *PFRCs* relying on single fiber pull-out test was further established in this chapter to simulate the failure process and investigate interfacial failure mechanism.

Based on the experimental results obtained in Chapter 4, three kinds of failure modes of *PFRCs* and corresponding different debonding processes can be concluded in **Figure 6.1-Figure 6.3**. First, as shown in **Figure 6.1**, the technical fiber can be pulled out from matrix in single fiber pull-out experiments, thus one debonding process can be seen in this first failure mode, named as single-stage debond behavior. In Process 1, debonding occurs between technical fiber and matrix (see **Figure 6.1** (b)). With the increase of applied stress, technical fiber can be pulled out (see **Figure 6.1** (c)). Second, as illustrated in **Figure 6.2**, technical fiber and elementary fibers both can be pulled out from matrix, then two debonding processes can be observed in the second failure mode, named as double-stage debond behavior. In Process 1, debonding occurs between technical fiber and matrix (see **Figure 6.2** (b)). With the increase of applied stress, some elementary fibers break (see **Figure 6.2** (c)). Then in Process 2, debonding happens between elementary fibers (see **Figure 6.2** (d)). Finally, elementary fibers can be pulled out (see **Figure 6.2** (e)). Third, as exhibited in **Figure 6.3**, technical fiber, elementary fibers and micro-fibrils all can be pulled out from the matrix, so three debonding processes can be seen in the third failure mode, named as triple-stage debond behavior. With the same as double-stage, in Process 1, debonding

occurs between technical fiber and matrix and some elementary fibers break (see **Figure 6.3** (b)-(c)). Then in Process 2, the following debonding happens between elementary fibers (see **Figure 6.3** (d)), but with the increase of applied stress, some cell walls break (see **Figure 6.3** (e)). Finally, in Process 3, debonding continue to occur between cell walls and micro-fibrils can be pulled out (see **Figure 6.3** (f)-(i)).

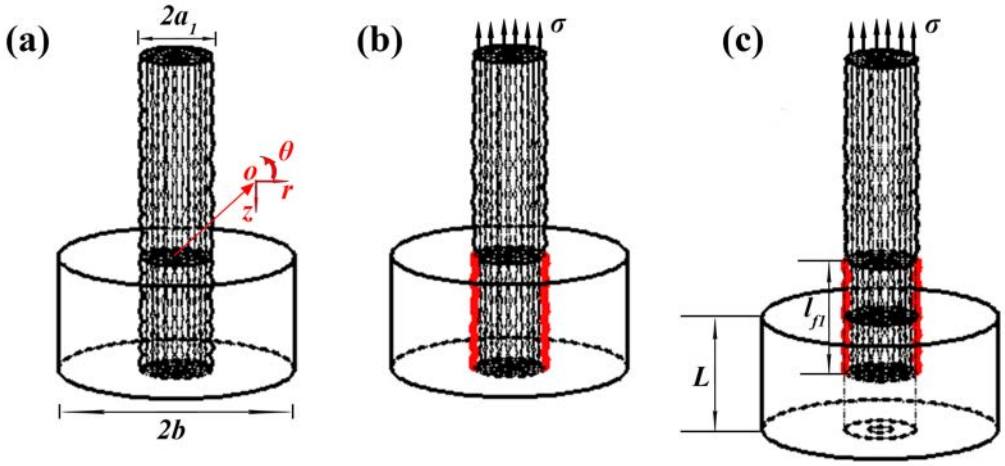

Figure 6.1 Schematic of the triple-interface model describing single-stage debond behavior of *PFRCs*: (a) original process, (b) *IF-FM* interfacial debond process and (c) pull-out process.

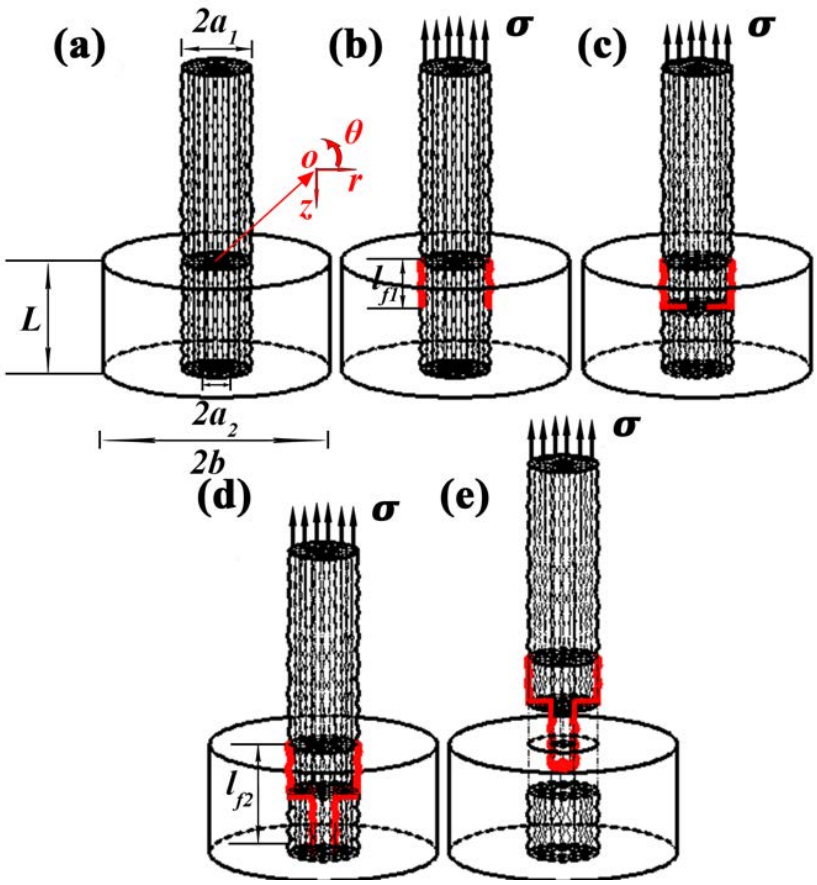

Figure 6.2 Schematic of the triple-interface model describing double-stage debond behavior of *PFRCs*: (a) original process, (b) *IF-FM* interfacial debond process, (c) partial elementary fibers fracture process, (d) *IF-ELE* interfacial debond process and (e) pull-out process.

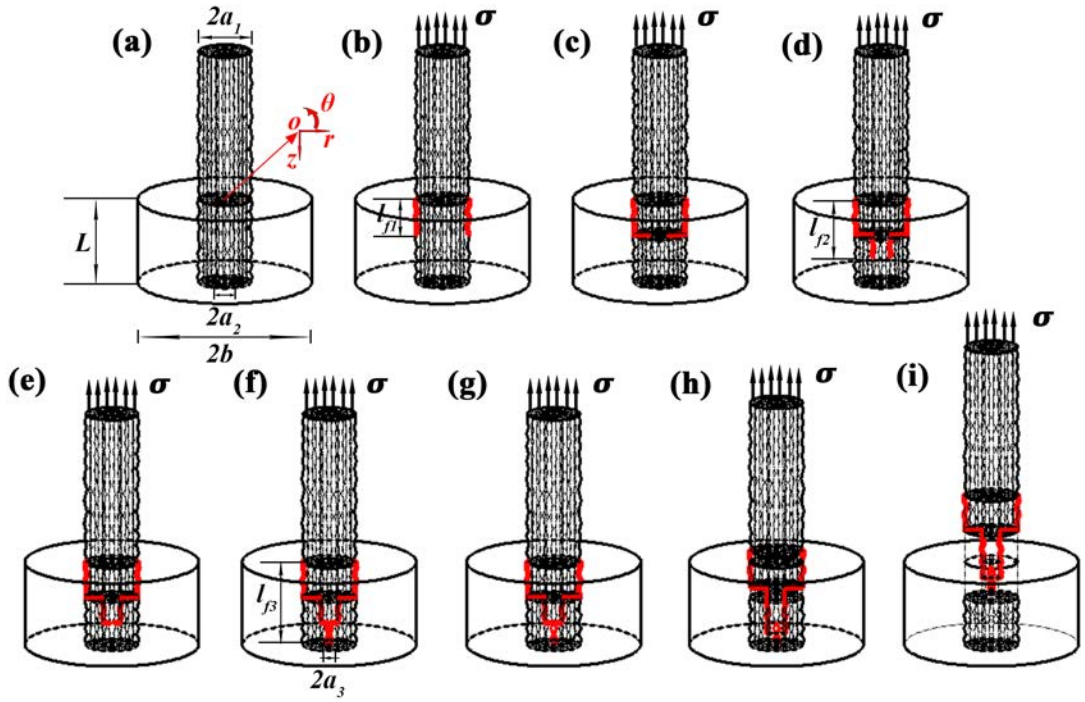

Figure 6.3 Schematic of the triple-interface model describing triple-stage debond behavior of *PFRCs*: (a) original process, (b) *IF-FM* interfacial debond process, (c) partial elementary fibers fracture process, (d) *IF-ELE* interfacial debond process, (e) partial cell wall micro-fibrils fracture process, (f)-(g) *IF-CW* interfacial debond process and (h)-(i) pull-out process.

In order to simulate the process of multi-stage fiber pull-out measurements and obtain the stress distributions in whole pull-out procedure, an *FE* method was employed to perform the numerical simulation via the commercial *FE* structural analysis software *ABAQUS* (*ABAQUS* 6.14). A *3D FE* model with three interfaces as above described was developed using the *ABAQUS* code to simulate the single sisal fiber pull-out tests. In current study, single, double and triple-stage debond and pull-out behaviors were presented based on the experimental phenomenon of single sisal fiber pull-out tests. Both geometric and material nonlinearity were included in the *FE* analysis. The physical problem of a typical fiber pull-out test can be treated as a cylindrical fiber embedded in a matrix with semi-infinite dimension. The illustration of the *FE* model

is shown in **Figure 6.4**. The components of different types of fiber and interfaces were modelled as separate parts as presented in **Figure 6.4**. A technical fiber with radius of a_1 that consists of elementary fibers is embedded in the centre of the coaxial matrix with radius of b and each elementary fiber possesses cell walls. Partial technical fiber (that is the bundle of elementary fibers) is denoted by the outer elementary fibers, within the outer radius of circular ring of a_1. The remaining part of the technical fiber is denoted by the inner elementary fibers with two part of cell wall layers. The cell wall layers located in the center of the technical fiber are equivalently treated as S2/S3 layer (containing micro-fibrils) of radius a_3, while those located in the outer of the micro-fibrils are denoted by the cell wall layers P/S1 with the outer radius of circular ring of a_2. L is the total embedded length of the technical fiber.

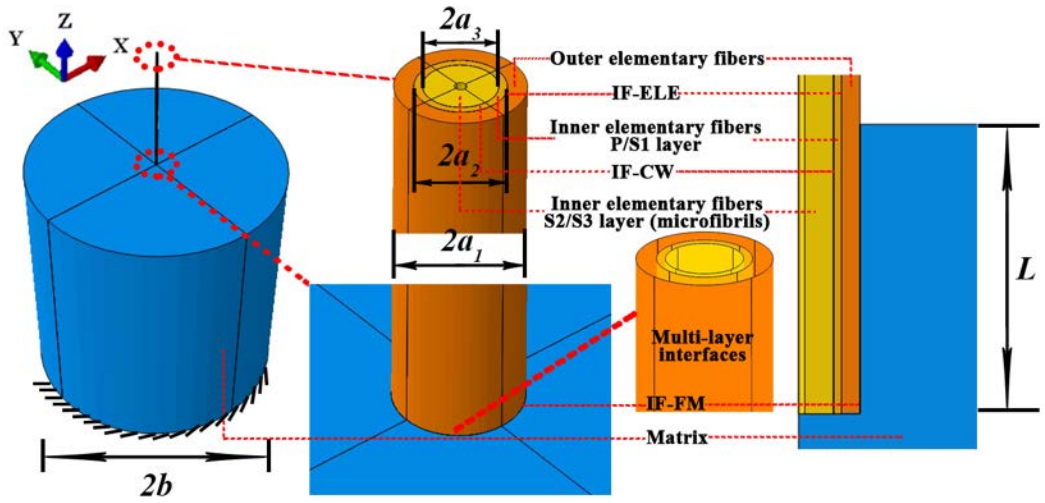

Figure 6.4 The full view of *FE* model with multi-layer interfaces for the single sisal fiber pull-out.

Due to the symmetry of the geometric characteristics of sisal fibers and the loading conditions of the single sisal fiber pull-out problem, to simplify the calculation process,

one quarter *3D* symmetric *FE* model with mesh is constructed and employed on the specific *FE* analysis in present study as displayed in **Figure 6.5**. The magnified *FE* mesh of the specimen used in the numerical analysis is also presented. The components are modelled as separate parts as presented in **Figure 6.5**. Different components of the fiber (as shown in the orange part of the figure) are meshed with the eight-node *3D* continuum shell element SC8R with reduced integration stiffness available in *ABAQUS* library, assuming that each component is a composite structure with a single ply. Whereas matrix (as shown in the blue part of the figure) is meshed with the eight-node *3D* solid brick element C3D8R with reduced integration stiffness available in *ABAQUS* library. Each node has three translational degrees of freedom (*DOF*) in the directions of *X*, *Y* and *Z*. This element can be employed for the nonlinear analysis, containing the problems on contact, large deformation, plasticity and failure. Considering the calculation accuracy and calculation cost simultaneously, after several meshing attempts, the model eventually contains a total of 31428 eight-node hexahedral elements. Whereas the eight-node *3D* cohesive element COH3D8 with zero thickness is used to define the cohesive zone and simulate the multi-layer interfaces of *SFRCs*, designed for modelling bonded interfaces and potential cracks. Although the thickness of the interface can be set as required, the interface of the composites is usually very thin, which may have a trouble when using such a small size in the numerical simulation. Therefore, to facilitate the calculation, the interface is set to zero thickness. For these elements, the interface opening displacement is defined as the relative displacement between the sharing nodes of the connected above and below element. The nodes of the upper and lower interfacial surface are coincident (that is, all elements in the whole interface have no thickness) without loading. Three

types of interfaces were all discretized by using eight-node cohesive elements. To save the computational time and without affecting the accuracy of the result, as shown in **Figure 6.5**, the mesh is chosen to be fine in the regions closer to the interface and coarse in the regions away from interface. A very fine mesh with the smallest elements of 7 μm is used at the region around the interfaces (i.e., *IF-FM*, *IF-ELE* and *IF-CW*) to ensure the accuracy of the numerical results. The coarse mesh is applied as an overall maximum size of 0.95 mm.

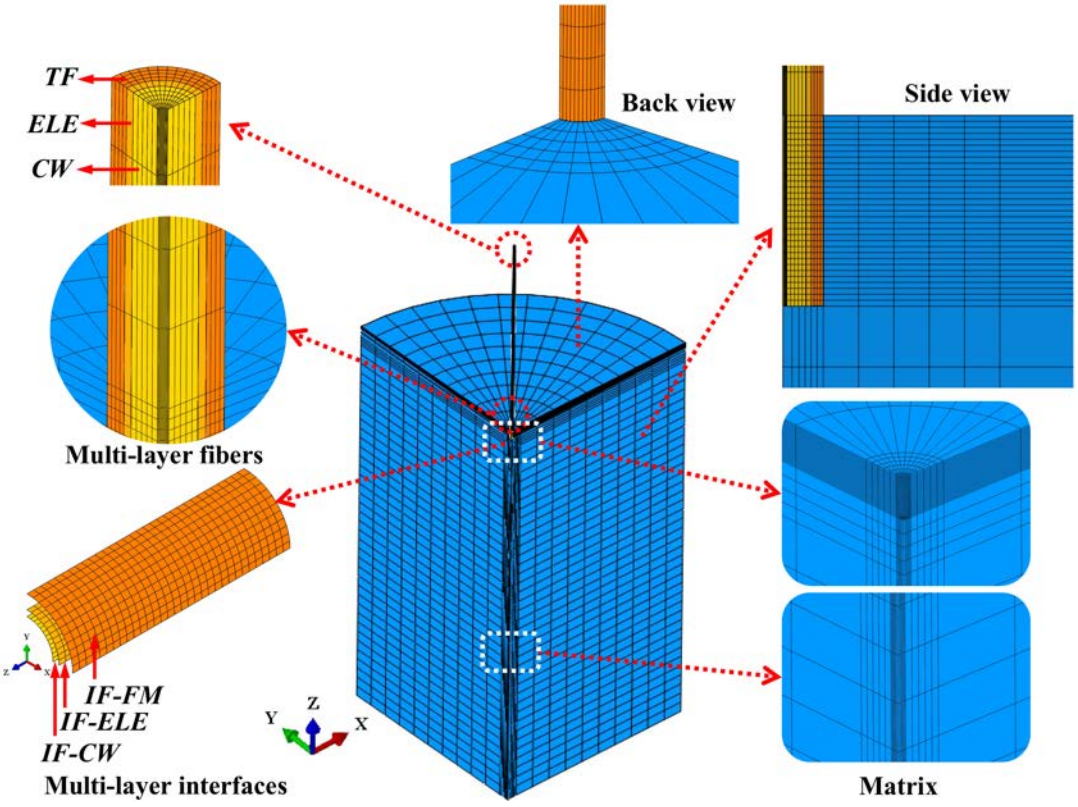

Figure 6.5 One quarter *3D* discretized *FE* model with mesh for the single sisal fiber pull-out with multi-layer interfaces (fine mesh around the interface).

Compared with the shear lag theory model used for the theoretical analysis model in the previous chapter, the *CZM* was selected for *FE* simulation in this chapter. The

main reason is that the *CZM* itself can consider the interfacial performance characteristics including the interface stiffness, interface strength, and so on, which is more suitable to obtain the stress variations during the interface debonding process in the *FE* calculation. Thus, more complex problems that cannot be achieved directly in the experiment can be solved, further receiving and predicting the performance parameters of the unique multi-layer interfaces of *PFRCs*. The cohesive elements in *ABAQUS* were used to mesh the cohesive layer (i.e., interface), which were based on the cohesive zone model by establishing the traction-separation relation for the interface. The constitutive response of cohesive elements, defined in terms of traction-separation laws, assumes an initially linear elastic behaviour followed by the initiation and evolution of damage. The elastic behaviour of the element is written in terms of elastic constitutive matrix that relates the nominal stress to the nominal strain. The traction across the interface increases and reaches a peak value, then decreases and eventually vanishes, permitting a complete decohesion **[176]**. Once the damage criterion is reached, the stiffness of the material degrades following the softening law. The element will be removed from the mesh when the stiffness at all integration points reaches the maximum degradation.

The traction-separation law in *ABAQUS* first assumes that the two parts connecting by the cohesive element are perfectly bonded before the damage of the cohesive element. The properties of the cohesive elements are also defined by the traction-separation law. The constitutive relation between these traction stresses and strain (separation) is given by a linear elastic response **[95, 113, 121, 125, 126, 129, 130, 177]**:

$$\tau = \begin{Bmatrix} \tau_n \\ \tau_s \\ \tau_t \end{Bmatrix} = \boldsymbol{K}\varepsilon = \begin{bmatrix} K_{nn} & K_{ns} & K_{nt} \\ K_{sn} & K_{ss} & K_{st} \\ K_{tn} & K_{ts} & K_{tt} \end{bmatrix} \begin{Bmatrix} \varepsilon_n \\ \varepsilon_s \\ \varepsilon_t \end{Bmatrix} \quad \textbf{(6.1)}$$

where τ is the nominal stress vector of the cohesive element; τ_n is the traction stress in the normal direction (the thickness direction of the cohesive element); τ_s and τ_t are traction stresses in the first and second shear directions, respectively; $\boldsymbol{K}$ is the elastic constitutive nominal stiffness matrix; ε is the nominal strain vector for the cohesive element; ε_n is the strain in the normal direction; ε_s and ε_t are strains in the first and second directions, respectively. In this chapter, the uncouple traction type was used, that is, the normal and shear components are uncoupled and the stiffness $K_{nt} = K_{sn} = K_{st} = K_{tn} = K_{ts} = K_{tt} = 0$. The penalty stiffness K_{nn}, K_{ss} and K_{tt} are artificial parameters used to constrain the separation (or interpenetration) between the crack faces and have perfect bonding between components before debonding onset. While the values of K_{nn}, K_{ss} and K_{tt} were assumed to be same and listed in next section according to the results of static nanoindentation test in Chapter 3.

And ε_n, ε_s and ε_t are defined as:

$$\varepsilon_n = \frac{\delta_n}{T_0},\ \varepsilon_s = \frac{\delta_s}{T_0},\ \varepsilon_t = \frac{\delta_t}{T_0} \quad \textbf{(6.2)}$$

where δ_n is the separation in the normal direction; δ_s and δ_t are separations in the first shear and second shear directions, respectively; T_0 is the initial constitutive thickness of the cohesive element (different from the actual thickness of the upper and lower surfaces of the cohesive element). In order to avoid the strain singularity

produced from calculating the damage of material when using the zero-thickness cohesive element, the constitutive thickness T_0 is used instead of the actual geometric thickness of the cohesive layer, which is generally taken as 1. Therefore, the strain of the cohesive element has the same value as the corresponding displacement.

Subsequently, when the stress or strain of the cohesive element satisfies an initial damage criterion, damage begins to occur, which also means that the degradation of the material begins. There are four main damage initiation criteria **[132]**:

(1) Maximum nominal stress criterion: It is assumed that when the stress in any one of the three directions reaches its critical stress, the cohesive element starts to damage, which is implemented as follows:

$$max\left\{\frac{\langle \tau_n \rangle}{\tau_n^c}, \frac{\tau_s}{\tau_s^c}, \frac{\tau_t}{\tau_t^c}\right\} = 1 \tag{6.3}$$

where τ_n^c, τ_s^c, and τ_t^c are damage stress thresholds (i.e., strength) in the normal, the first shear and second shear directions, respectively. $\langle\ \rangle$ is the Macaulay brackets, indicating that neither compressive stress nor compressive stress can cause damage of the cohesive element.

(2) Maximum nominal strain criterion: It is assumed that when the strain generated in any one of the three directions reaches its damage strain threshold, the damage of the cohesive element appears, which is implemented as follows:

$$max\left\{\frac{\langle \varepsilon_n \rangle}{\varepsilon_n^c}, \frac{\varepsilon_s}{\varepsilon_s^c}, \frac{\varepsilon_t}{\varepsilon_t^c}\right\} = 1 \tag{6.4}$$

where ε_n^c, ε_s^c and ε_t^c are the damage strain thresholds in the normal, the first shear and second shear directions, respectively.

(3) Quadratic nominal stress criterion: It is assumed that when the sum of squares of the ratio of the actual stress and the corresponding damage threshold in each direction reaches 1, the damage occurs, which is implemented as follows:

$$\left\{\frac{\langle \tau_n \rangle}{\tau_n^c}\right\}^2 + \left\{\frac{\tau_s}{\tau_s^c}\right\}^2 + \left\{\frac{\tau_t}{\tau_t^c}\right\}^2 = 1 \quad \textbf{(6.5)}$$

(4) Quadratic nominal strain criterion: It is assumed that when the sum of squares of the ratio of the actual strain and the corresponding strain threshold value in each direction reaches 1, the damage initiated, which is implemented as follows:

$$\left\{\frac{\langle \varepsilon_n \rangle}{\varepsilon_n^c}\right\}^2 + \left\{\frac{\varepsilon_s}{\varepsilon_s^c}\right\}^2 + \left\{\frac{\varepsilon_t}{\varepsilon_t^c}\right\}^2 = 1 \quad \textbf{(6.6)}$$

Through comparing the results derived from different damage initiation criterion calculated by the previous established *FE* model, the quadratic nominal stress criterion as shown in **Equation (6.5)** was eventually used as the damage initiation criterion for the cohesive layer in the current chapter, to obtain more fitting results.

Finally, after the initiation criteria was reached, the damage evolution was described by different damage propagation criteria for cohesive elements available in *ABAQUS*, including bilinear, exponential, sinusoidal and parabolic, etc. The damage evolution

manifested that the stiffness of the cohesive element begins to decrease at a certain rate. The general expression is:

$$\tau_n = \begin{cases} (1-D)\overline{\tau_n} & \overline{\tau_n} \geq 0 \\ \overline{\tau_n} & \text{no damage evolution to compressive stiffness} \end{cases}$$
$$\tau_s = (1-D)\overline{\tau_s} \quad \textbf{(6.7)}$$
$$\tau_t = (1-D)\overline{\tau_t}$$

where τ_n, τ_s and τ_t are the normal and shear stresses in the three directions as previously mentioned; $\overline{\tau_n}$, $\overline{\tau_s}$ and $\overline{\tau_t}$ are contact stress components in the normal, first and second shear directions predicted by the linear elastic traction-separation behavior for the current separation without damage, respectively. Once the damage has initiated, the damage evolution is described by introducing a stiffness degradation parameter, D. D is a scalar damage variable that represents the overall damage at the contact point. The value of D ranges from 0 (no damage) to 1 (complete damage) and can be described by either linear or exponential evolution.

In the *ABAQUS* analysis, due to the softening and stiffness degradation of the material, the convergence of the calculation is usually difficult. The way to overcome it is to use the viscous regularization parameter of the structural equations, which leads to the positive shear stiffness matrix of the softening material in sufficiently small amount of time increment. The regularization process involves the use of viscosity stiffness degradation variables D_v and defines the following evolution equations $\dot{D}_v$:

$$\dot{D}_v = \frac{1}{\mu}(D - D_v) \quad \textbf{(6.8)}$$

where μ is the viscosity coefficient describing the relaxation time of the viscous system and D is the damage variable in the model without viscosity. The damage response of the viscous material is:

$$t = (1 - D_v)\bar{t} \tag{6.9}$$

Displacement type in conjunction with the linear softening law was used to describe the damage evolution after the initiation criteria was reached. The displacement type of damage evolution requires a maximum displacement d^f at which the cohesive layer completely failed.

Displacement and energy type in conjunction with each type of evolution criterion were used to describe the damage evolution. For the bilinear softening law relying on displacement and energy type, the evolutions of damage variable D are both given by

$$D = \frac{\delta_m^f \left(\delta_m^{max} - \delta_m^c\right)}{\delta_m^{max} \left(\delta_m^f - \delta_m^c\right)} \tag{6.10}$$

where δ_m^f and δ_m^c are the effective separations at complete failure and damage initiation, respectively and δ_m^{max} is the maximum value of effective separation attained during loading history. However, if the calculation is based on the displacement type, the effective separation δ_m needs to be introduced to describe the damage evolution of the interface under normal and shear stress when the cohesive element generates mixed-mode deformation:

$$\delta_m = \sqrt{\langle \delta_n \rangle^2 + {\delta_s}^2 + {\delta_t}^2} \tag{6.11}$$

And if the calculation is based on the energy type, the damage evolution is defined as the energy dissipated during failure, namely the fracture energy or energy release rate. The fracture energy is equal to the area under the traction-separation curve. Therefore, the fracture energy criterion is:

$$\left\{\frac{G_n}{G_n^C}\right\}^{\beta}+\left\{\frac{G_s}{G_s^C}\right\}^{\beta}+\left\{\frac{G_t}{G_t^C}\right\}^{\beta}=1 \tag{6.12}$$

where the total mixed fracture energy G^C is defined as $G^C=G_n+G_s+G_t$ when the above conditions are satisfied, that is, when the cohesive unit is complete failure; G_n, G_s and G_t are the work along the normal and the two shear directions, respectively; G_n^C, G_s^C and G_t^C are the fracture energy along the normal and the two shear directions, respectively; β is energy coefficient. While, $\delta_m^f=2G^C/\sigma_{eff}^c$, where σ_{eff}^c is the effective traction at damage initiation.

For the exponential damage evolution criterion, if the calculation is based on the displacement type, the evolution of damage variable D is calculated as below:

$$D=1-\left(\frac{\delta_m^c}{\delta_m^{\max}}\right)\left\{1-\frac{1-\exp\left\{-\alpha\left[\left(\delta_m^{\max}-\delta_m^c\right)/\left(\delta_m^f-\delta_m^c\right)\right]\right\}}{1-\exp(-\alpha)}\right\} \tag{6.13}$$

where α is the dimensionless parameters describing the rate of damage evolution. If the calculation is based on the energy type, the evolution of damage variable D is given by:

$$D=\int_{\delta_m^c}^{\delta_m^f}\frac{\sigma_{eff}^c d\delta}{G^C-G_0} \tag{6.14}$$

where G_0 is the elastic energy at the damage initiation.

Since the shape of the traction-separation curve has little effect on the final numerical results when using the cohesive force model to model the interaction between the fiber and matrix **[128, 178, 179]**, a bilinear cohesive law in conjunction with fracture energy criterion was implemented to describe the interface damage evolution in this chapter, as illustrated in **Figure 6.6**, which saves the computational time to the minimum and reduces the artificial compliance inherent in the intrinsic cohesive zone model **[179]**. In the figure, τ_i is the interfacial shear stress and the relative displacement across the interface is denoted as δ. δ_n^c, δ_s^c and δ_t^c are respectively the fiber separation displacement of crack initiation in the normal, the first shear and second shear directions, where crack surfaces start to separate at the peak stress. τ_n^c, τ_s^c and τ_t^c are the interfacial crack initiation stress in the three directions, respectively. δ_n^f, δ_s^f and δ_t^f are respectively the fiber complete separation displacement, where the crack surfaces separate completely. The interfacial debonding during single fiber pull-out test is a pure Mode II fracture problem. The Mode II cohesive law to describe the interfacial debonding can be represented as

$$\tau_i = \begin{cases} \dfrac{\tau_n^c}{\delta_n^c}\delta & 0 \le \delta \le \delta_n^c \\ \dfrac{\tau_n^c}{\delta_n^f - \delta_n^c}\left(\delta_n^f - \delta\right) & \delta_n^c \le \delta \le \delta_n^f \end{cases} \tag{6.15}$$

Correlating to energy-based fracture mechanics, the fracture energy G^C is the area under the traction-separation curve illustrated in **Figure 6.6**, which can be calculated as

$$G_c = \frac{1}{2}\tau_n^c \delta_n^f \tag{6.16}$$

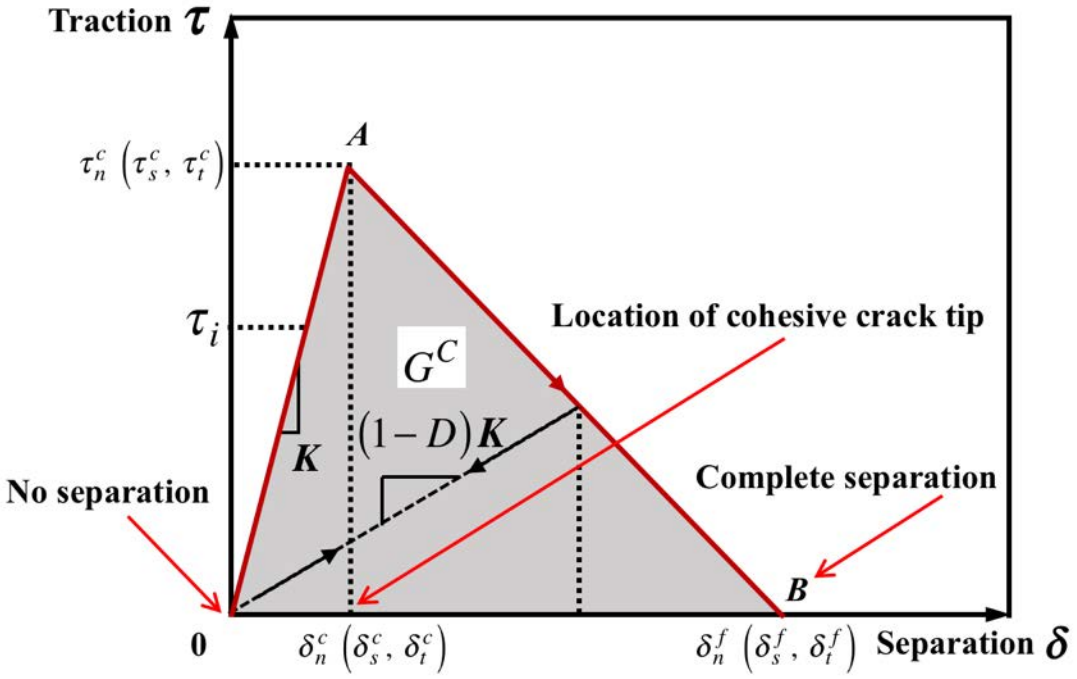

Figure 6.6 Schematic illustration of typical bilinear traction-separation cohesive law for modeling cohesive failure and its damage evolution.

This chapter assumes that the energy release rate G_n^C, G_s^C and G_t^C in the normal and the two shear directions satisfied $G_n^C = G_s^C = G_t^C = G^C$ and the interfacial crack initiation stress in the three directions τ_n^c, τ_s^c and τ_t^c satisfied $\tau_n^c = \tau_s^c = \tau_t^c = \tau^C$.

Subsequently, the loading, boundary, interaction and constraint conditions of fiber, matrix and multi-layer interfaces for the *FE* model of the single sisal fiber pull-out are

illustrated in **Figure 6.7-Figure 6.8. Figure 6.7** shows the loading and boundary conditions of fiber and matrix. In the single fiber pull-out experiment, a tensile stress σ is applied on the top end of the fiber in the axial direction using displacement control. So, for the simulation of the stress variation of the pull-out process, axial displacement loading condition was employed in the *FE* model of this chapter. Loading was upward enforced displacement applied to the top surface of the fiber as shown in **Figure 6.7**. Fiber nodes at the free-end of fiber were given a uniform displacement-controlled load in the axial direction to simulate the pull-out movement of the fiber. The applied displacement was linearly increased by amplitude function. The loading rate can be varied by using different amplitude functions, however, in order to facilitate the comparison between the theoretical calculations and the experimental results later, the same loading rate (i.e., 1 mm/min) as in the real experiment was used to simulate in this chapter. In order to completely simulate the pulled-out process of the fiber at different stages, the displacement applied to the fiber at each stage was just the pulled-out length of the fiber at each corresponding stage in the length direction, and the loading time in different stages was determined accordingly. The loading displacement and time at various stages will be discussed in the following section. The bottom of matrix was applied for fully fixed boundary condition (*BC*) in XOY plane, being constrained in both the radial and axial directions. Because of using one quarter *3D* symmetric *FE* model for calculation, the symmetrical *BCs* were applied to the surfaces at the symmetric planes of the various fibers and the matrix, that is, the nodes on the symmetric plane were symmetrically constrained. Once the interface of the composites is debonded, the contact-friction behavior between the two connecting parts of the interface is activated and influences the

occurrence of fiber slip and pull-out due to their relative motion, which need to handle the interaction of multiple components. The multiple contact pairs of multiple components need to be set in general *FE* software for the contact behavior. Therefore, the interaction between components is very important and needs to be considered. Appropriate constraints were used to describe the interaction between components. Meantime, three types of friction model, including the Coulomb friction model, the interface constitutive equation and the rough-lubrication model, can be used to achieve the friction behavior. In this chapter, the same Coulomb friction model as in the previous chapter is used for the *FE* calculation. The Coulomb friction model can be applied at each point of a continuum (i.e., the contact interface). Therefore, taking into account the experimental phenomenon as realistic as possible, as shown in **Figure 6.8**, the contact-friction behaviors of the three types of interfaces (i.e., *IF-FM*, *IF-ELE* and *IF-CW*) in the *FE* simulation were modelled using a cohesive surface behavior (surface-to-surface contact with finite sliding) in this chapter. The friction coefficients in these interactions were set as discussed in the following section. As shown in **Figure 6.8**, tie constraints were established between the nodes on the upper and lower surfaces of each type of interface and the surface of adjacent matrix or fiber to eliminate the relative slip between these two surfaces. Thus, the displacement and stress on both sides of the cohesive element can be coordinated with those on the surface of adjacent matrix or fibers.

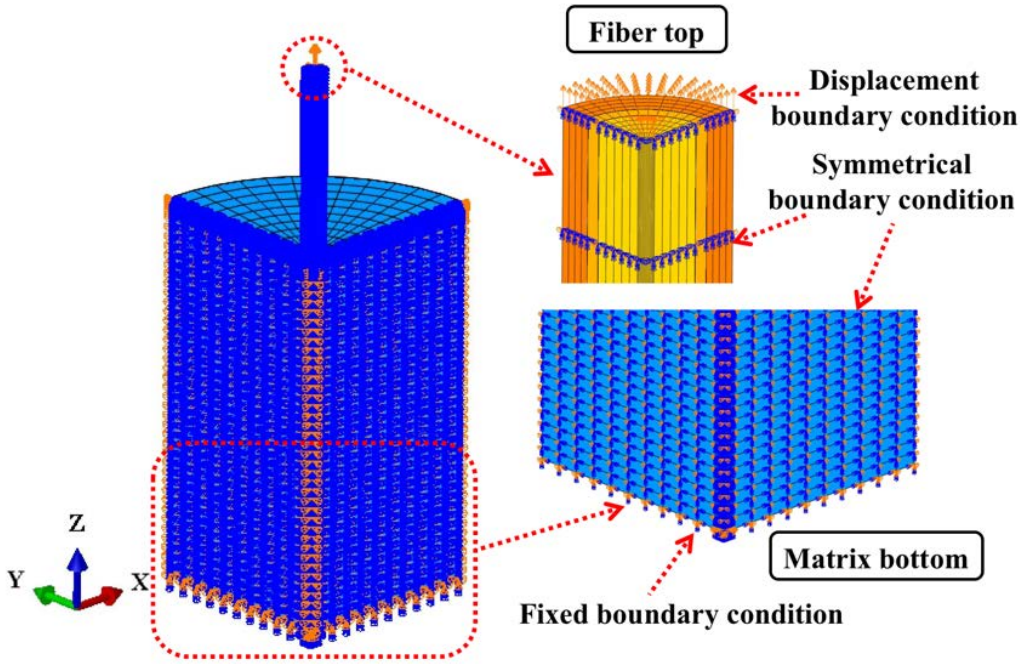

Figure 6.7 Load and boundary conditions of fiber and matrix for the *FE* model of the single sisal fiber pull-out with multi-layer interfaces.

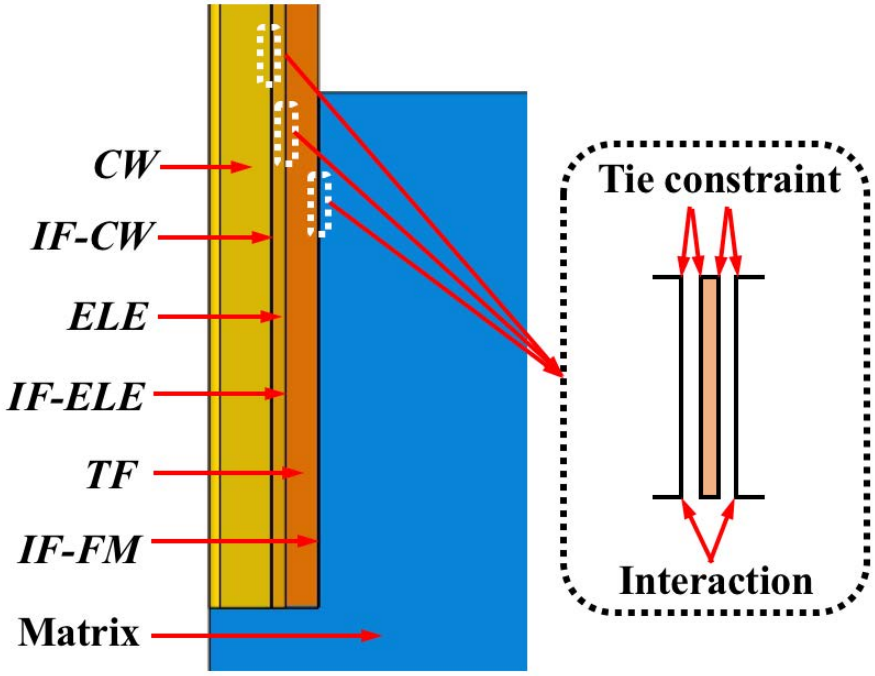

Figure 6.8 Interaction and constraint conditions of multi-layer interfaces (i.e., *IF-FM*, *IF-ELE* and *IF-CW*) for the *FE* model of the single sisal fiber pull-out.

As previous discussion, there are four stages during a single sisal fiber pull-out, which include elastic deformation stage before debonding, debonding stage, fracture stage and sliding stage. While, there are not only one debonding and fracture stage for different embedded fiber length. As illustrated in **Figure 6.9**, taking the triple-stage pull-out process for example, in the first stage, the fiber and the matrix are well bonded. As the pull-out force increases, a crack propagates along the interface between the technical fiber and the matrix, leading to a partial debonding, which is the debonding stage. Then the breakage of partial outer technical fiber occurs, namely fracture stage. After that, the second debonding happened on the *IF-ELE*. And the second fiber fracture, the third debonding and the third fiber fracture continue to occur. In the last stage, the inner technical fiber slides out from the matrix, with friction acting between the two newly formed surfaces. Therefore, in order to simulate the process of multi-stage debonding and fracture of single sisal fiber, this paper combines solving method *ABAQUS* standard and *ABAQUS* dynamic explicit to simulate. In this investigation, a static debond and pull-out process is assumed, which corresponds to the cases with a low pull-out rate, using *ABAQUS* standard solution method. To approximate the non-linear behavior of the multi-layer interface, a mixed 'cohesive' and 'Coulomb-friction' model was proposed. The use of such a model enables us to simulate the entire pull-out process. As debonding occurs between the two contact surfaces, it may go through stages of debonding, slip and separation during the fiber pull-out process. After debonding, only the stress continuity across the sliding contact elements is preserved. During the solving process, the large deformation and time automatic sub-step were turned on. Meantime, the size of the time increment in the calculation was controlled and set small enough to more clearly exhibit the bonding conditions of multi-layer

interfaces during the entire process of fiber pull-out. Then the result of each increment was output, thus showing the whole damage process of the cohesive element. *ABAQUS* dynamic explicit analysis is popularly applied for the problems of crack, progressing damage and failure of material, etc, showing to be a powerful solution scheme and very efficient for discontinuous medium, contact interaction and large deformation problems, thus it is appropriate for pull-out test simulation. In this study, the *ABAQUS* dynamic explicit analysis method was employed to simulate the fiber breakage process. First, the stress field from the last time step solved by *ABAQUS* standard was loaded into the model through a restart analysis and predefined stress field. Dynamic explicit analysis is a time control method. The size of the time increment is then determined dependent on the mesh size and material properties. The analysis time can be reduced by using mass scaling or increasing the loading rate. The approach of mass scaling was applied in this study. Different mass scaling factors have been tried and the most appropriated factor was determined as 5 on the basis of ensuring the accuracy of simulation results and computational efficiency. Finally, to facilitate the query of results in the post-processing, the slip was measured as the relative displacement between the nodes on the multi-layer interfaces, and the load was measured as the total reaction acting on the loading surface. The flowchart of *FE* model for solving the multi-stage debonding and fracture process was presented in **Figure 6.10**.

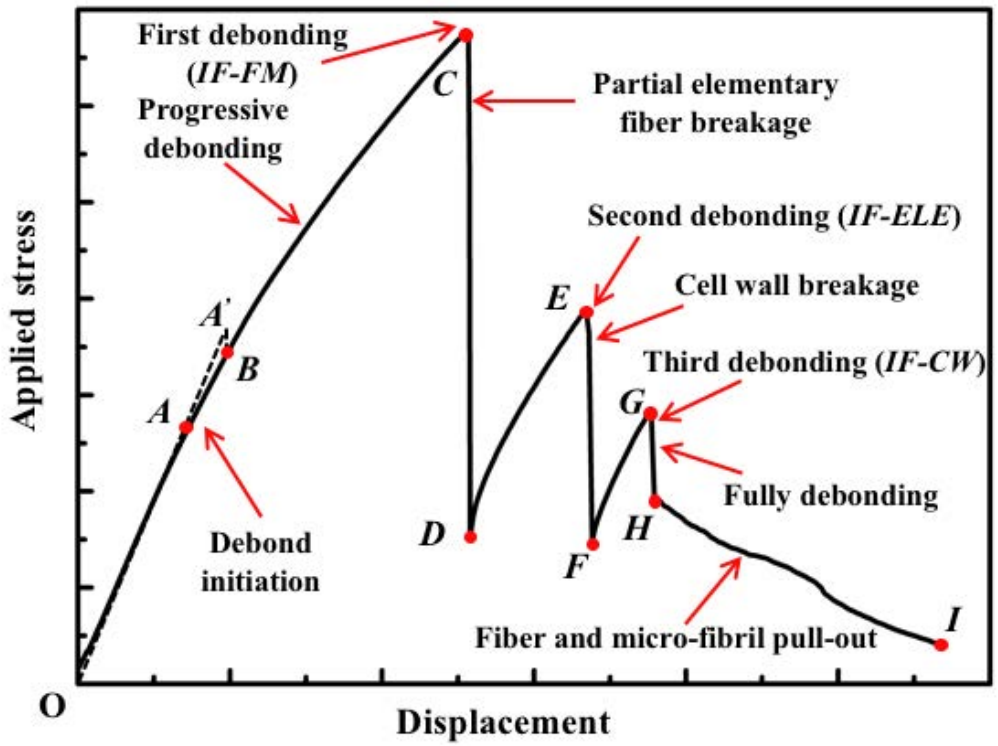

Figure 6.9 Schematic of typical stress-displacement behavior during single sisal fiber pull-out process with multi-stage debonding and fiber fracture and pull-out.

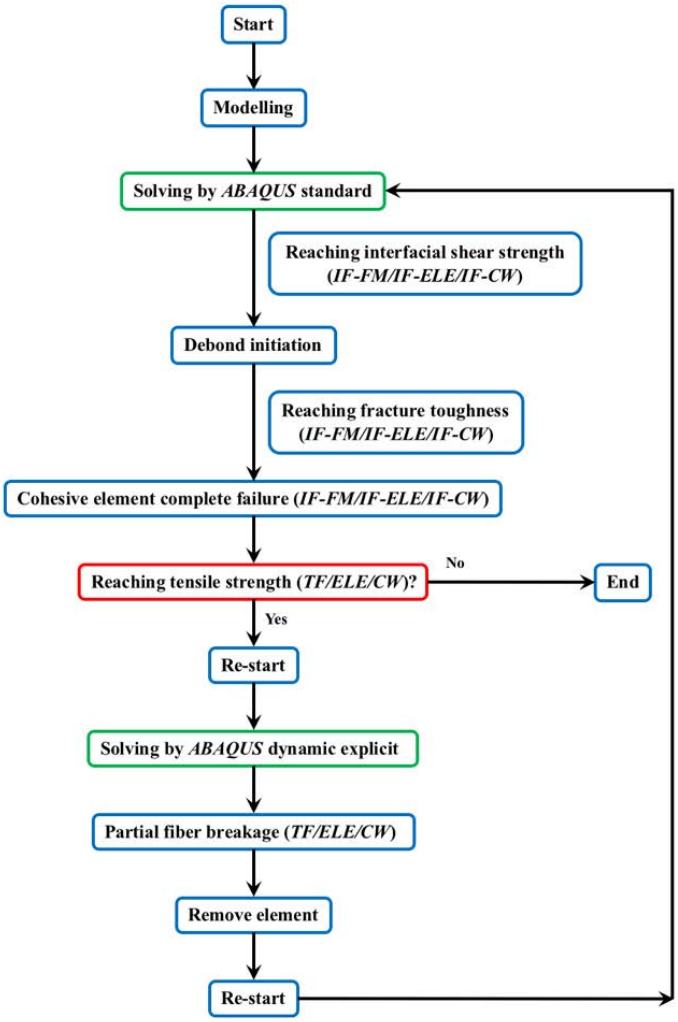

Figure 6.10 Flowchart of the proposed *FE* model for solving the multi-stage debonding and fracture process.

6.3. Effects of the interfacial parameters on the interfacial failure behaviors of *SFRCs*

The geometric parameters and the basic material properties of sisal fiber, epoxy matrix and multi-layer interfaces and other input parameters required for numerical simulation are summarized in **Table 6.1** according to our pre-research work and results obtained in previous chapters. The extended length of fiber and the depth of the matrix are respectively set as 10 mm and 20 mm according to the single fiber pull-

out experiment in Chapter 4. The radius (10 mm) and depth (20 mm) of the matrix are much larger than the radius dimensions of the fiber (0.093 mm) and fiber embedded length (smaller than 0.5 mm) in the numerical models so as to simulate a semi-infinite matrix body. The fiber embedded length was determined to be 0.187, 0.347 and 0.440 mm based on the results obtained from the statistical analysis in Chapter 4. The radii of single technical fiber, elementary fibers and micro-fibrils, the elastic modulus and Poisson's ratio of fibers and matrix and the longitudinal elastic modulus of the interface were ascertained relying on the results of static nanoindentation test in Chapter 3. The tensile test was performed to get the properties of original and impregnated fibers. The shear moduli were determined by the comparison of the experimental and numerical curves from tensile tests in our pre-research work. The density of fiber and matrix was obtained from our pre-research work as described in section 3.2.1. Due to symmetry in geometry, loading and boundary conditions, the technical fiber, elementary fibers, micro-fibrils and matrix all considered as linear elastic material, satisfying the linear elastic constitutive relationship. The technical fiber, elementary fibers and micro-fibrils exhibit anisotropic properties, while the matrix displays isotropic property. The technical fiber, elementary fibers and micro-fibrils are assumed to possess different ultimate tensile strength so as to simulate the breakage of fiber between multiple debonding processes, whereas the *IF-FM*, *IF-ELE* and *IF-CW* are assumed to have different interfacial properties regarding the interfacial modulus (stiffness), interfacial strength, interfacial fracture toughness (energy release rate) and friction coefficient. Therefore, different interface debonding criteria and axial stress distribution, partial debonding stress, maximum debonding stress, externally applied stress and initial frictional pull-out

stress during the pull-out process of *PFRCs* can be obtained. The friction coefficient referred to the theoretical analysis in Chapter 5. Interfacial properties play a prominent role in the fracture mechanism of composites. If interfacial bonding is too strong, then ductile fibers will break at some point before fully debonding and most embedded portions of the ductile fibers have no chance to develop plastic deformation and dissipate energy. However, if there exists a weak interfacial bonding instead, the fibers will be pulled out of matrix and only the frictional force can take limited energy out of the system. So, the length of fiber embedded in the matrix is assumed to be less than the critical embedded length for debonding so that the fiber will not break before the debonding occurs. The debonding is assumed to initiate at each interface and propagate longitudinally along the fiber. The thermal residual stresses of the pull-out sample due to curing are considered. Thermal expansion coefficient and temperature change were determined according to the parameters in Chapter 5. The interfacial properties used in the debonding failure criterion are also given in **Table 6.1**. A viscous regularization parameter (viscosity coefficient = 0.0005) has been used to overcome convergence difficulties that arise during material softening and stiffness degradation. Energy type in conjunction with the bilinear softening law is used to describe the damage evolution after the initiation criteria is reached. The energy type of damage evolution requires a maximum energy release rate G^C at which the cohesive layer has completely failed. In this study, with the use of the proposed numerical model, different values of the critical stresses (τ_n^c, τ_s^c and τ_t^c) and the energy release rate (G^C) at failure are tried, and the values that gave the best agreement between the analysis and experiment stress-displacement curves are listed in **Table 6.1**.

Table 6.1 Material constants and geometric parameters for sisal fibers and their composites used in the *FE* model.

Properties of sisal fibers			
Fiber type	Technical fiber	Elementary fibers	Micro-fibrils
Embedded fiber length $L\ (mm)$		0.187/0.347/0.440	
Radius $a_1 / a_2 / a_3\ (mm)$	0.093	0.065	0.053
Density $\left(g / cm^3\right)$		1.45	
Young's modulus $\left[E_{11} / E_{22} / E_{33}\ (GPa)\right]$	10.06/6.2/6.2	8.62/5.31/5.31	11.07/6.42/6.42
Shear modulus $\left[G_{12} / G_{13} / G_{23}\ (GPa)\right]$	4.49/4.49/2.7	3.85/3.85/2.33	4.94/4.94/2.99
Poisson's ratio $v_{f1}\left[v_{12} / v_{13} / v_{23}\right]$		0.12/0.12/0.14	
Thermal expansion coefficient $\alpha_{f1}\ \left(10^{-6} / °C\right)$		10.8	
Properties of matrix			
Matrix type		Epoxy	
Radius $b\ (mm)$		10	
Density $\left(g / cm^3\right)$		1.2	
Young's modulus $E_m\ (GPa)$		4.75	
Poisson's ratio v_m		0.16	
Thermal expansion coefficient $\alpha_m\ \left(10^{-6} / °C\right)$		70.8	
Properties of multi-layer interfaces			
Interface type	*IF-FM*	*IF-ELE*	*IF-CW*
Density $\left(g / cm^3\right)$		1.5e-3	
Tensile stiffness $\left[K_{nn} / K_{ss} / K_{tt}\ (GPa)\right]$	6.1/6.1/6.1	7.2/7.2/7.2	9.4/9.4/9.4
Coefficient of friction $\mu_1 / \mu_2 / \mu_3$	4.42	1.12	1.02
Temperature change $\Delta T\ (°C)$		-100	
Shear strength $\left[\tau_n^c / \tau_s^c / \tau_t^c\ (MPa)\right]$	35/35/35	43/43/43	48/48/48
Fracture toughness $G_1^C / G_2^C / G_3^C\ \left(J / m^2\right)$	133	181	412

6.4. Comparisons of the applied stresses on sisal technical fiber with multi-layer interface between experimental test and numerical simulation

Relying on the statistical analysis of the pull-out behavior of different failure modes for single *SFRCs* in section 4.5 of Chapter 4, the experimental and numerical applied stresses versus displacement curve for *SFRCs* with three embedded fiber lengths ($L = 0.187\ mm / 0.347\ mm / 0.440\ mm$) are plotted in **Figure 6.11**. The total reaction acting on the node of loading surface was first measured as the final applied load, and then the stress was calculated based on the geometrical dimension of the fiber. Combining the static and dynamic simulation results for different debonding and fracture processes, the numerical applied stresses were solved at different stages (see **Figure 6.1-Figure 6.3**) with various embedded fiber lengths and are plotted together in **Figure 6.11** (a)-(c).

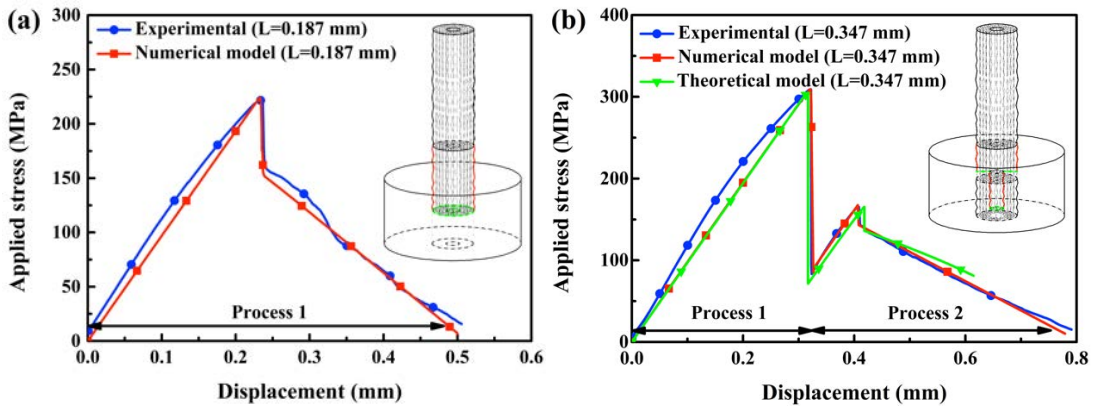

Figure 6.11 Applied stress-displacement curves obtained from numerical simulation and experimental test for the multi-stage pull-out of single *SFRCs* with various embedded fiber length: (a) single-stage ($L = 0.187\ mm$), (b) double-stage ($L = 0.347\ mm$) and (c) triple-stage ($L = 0.440\ mm$).

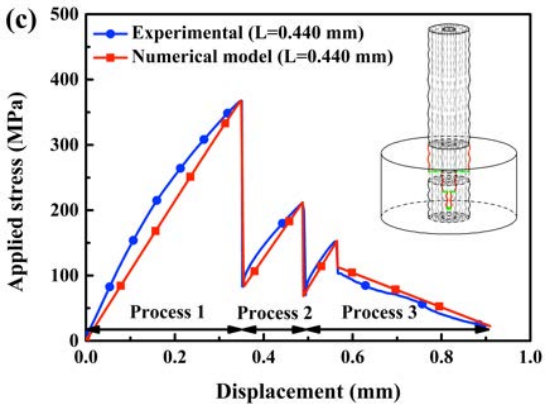

Figure 6.11 (continued).

The applied stresses at different stages in *FE* model were compared with those in experimental results. For the single-stage fiber pull-out behavior that occurred with a shorter embedded fiber length, one debonding and pull-out procedure can be observed as shown in **Figure 6.11** (a). The interface debonding between technical fiber and matrix and the pull-out of technical fiber occurred. For the double-stage pull-out behavior with a medium embedded fiber length, two debonding processes can be seen as displayed in **Figure 6.11** (b). At first, as analyzed in the double-interface theoretical model in Chapter 5, the interface between technical fiber and matrix begins partial debonding. When the stress reaches the tensile strength of the sisal fiber, some elementary fibers break and the applied stress suddenly drops to a certain value. Afterwards, the remaining elementary fibers can continue to be loaded and debonding between elementary fibers occurs. When all elementary fibers break, the applied stress further decreases, and the fibers start with frictional pull-out. The phenomenon in which some elementary fibers were pulled-out from technical fiber in the double-stage was also observed and verified by *SEM*. **Figure 6.11** (b) also compared the stress-displacement curve of the single sisal fiber pull-out at the same embedded fiber length calculated from the double-interface theoretical model in the previous chapter. It can

be seen that the result calculated from the triple-interface *FE* model with one more interface was more consistent with the experimental result. Whereas, as presented in **Figure 6.11** (c), three interface debonding and fiber breakage processes occur in the triple-stage pull-out behavior with a longer embedded fiber length. With the increase of the applied stress, since each elementary fiber possesses the multi-layer cell wall structure as described in Chapter 3, the interface debonding between the cell walls happened and micro-fibrils in the cell wall can be pulled-out after the cell wall breaks. The distinct multi-layer failure behavior of sisal fiber in the triple-stage was also exhibited in *SEM* observation. Thus, with the increase of embedded fiber length, the maximum debonding stress of Process 1 gradually improved from the single- to triple-stage, which indicated that the interfacial strength gradually increased. Results (i.e., the applied stress-displacement curves) obtained from numerical simulation were found to be in accordance with the experimental applied stress in the single fiber pull-out tests, showing the validity of the triple-interface *FE* method developed in the present chapter.

From the above analysis, the influence of different embedded length on the interfacial failure behaviors and the interface properties was investigated. It was found that the interfacial strength varies with the embedded fiber length of sisal fiber, which is related to the multi-interface failure modes of *SFRCs*. When the uniaxial tensile stress was applied on the single *SFRCs* with multi-layer and multi-scale structure, multiple interfacial failure modes of *SFRCs* were clearly presented in the pull-out tests, which was produced by the sequential failure of the three types of interfaces (i.e., *IF-FM*, *IF-ELE* and *IF-CW*). Therefore, for single *PFRCs*, the embedded fiber length not only

determines the interfacial properties, but also decides the occurrence of different debonding and fracture stages. Further, compared with the accuracy of the double-interface model established in the last chapter for predicting the multi-stage fracture behavior of *SFRCs*, the triple-interface *FE* model with one more hierarchical structure could more comprehensively analyze the complex multi-layer and multi-scale interfacial bonding conditions and interfacial failure behaviors of *PFRCs* to obtain more accurate results.

6.5. Multi-stage fracture mechanisms of *SFRCs*

Relying on the triple-interface *FE* model established in this chapter, the pull-out process of single sisal fiber was simulated, calculating the stress and displacement of fiber and matrix and the damage of the cohesive element in each interface during the multi-stage pull-out of sisal fiber and the frictional behavior of the interface after the damage process. As plotted in **Figure 6.12**, the distributions of stress nephogram on sisal fibers and multi-layer interfaces were obtained by simulating the triple-stage debond, fracture and pull-out process of single *SFRCs* in *FE* model. In particular, as described in section 6.3, since the radius and depth of the matrix are much larger than the dimensions of the fiber in the numerical models so as to simulate a semi-infinite matrix body to ignore the effects of stress changes in the matrix during the pull-out process. Therefore, the stress distribution of the epoxy matrix will not be discussed. Considering the structural characteristics of presented model, all results (i.e., stresses, displacements, etc.) were output in the cylindrical coordinate system in this section.

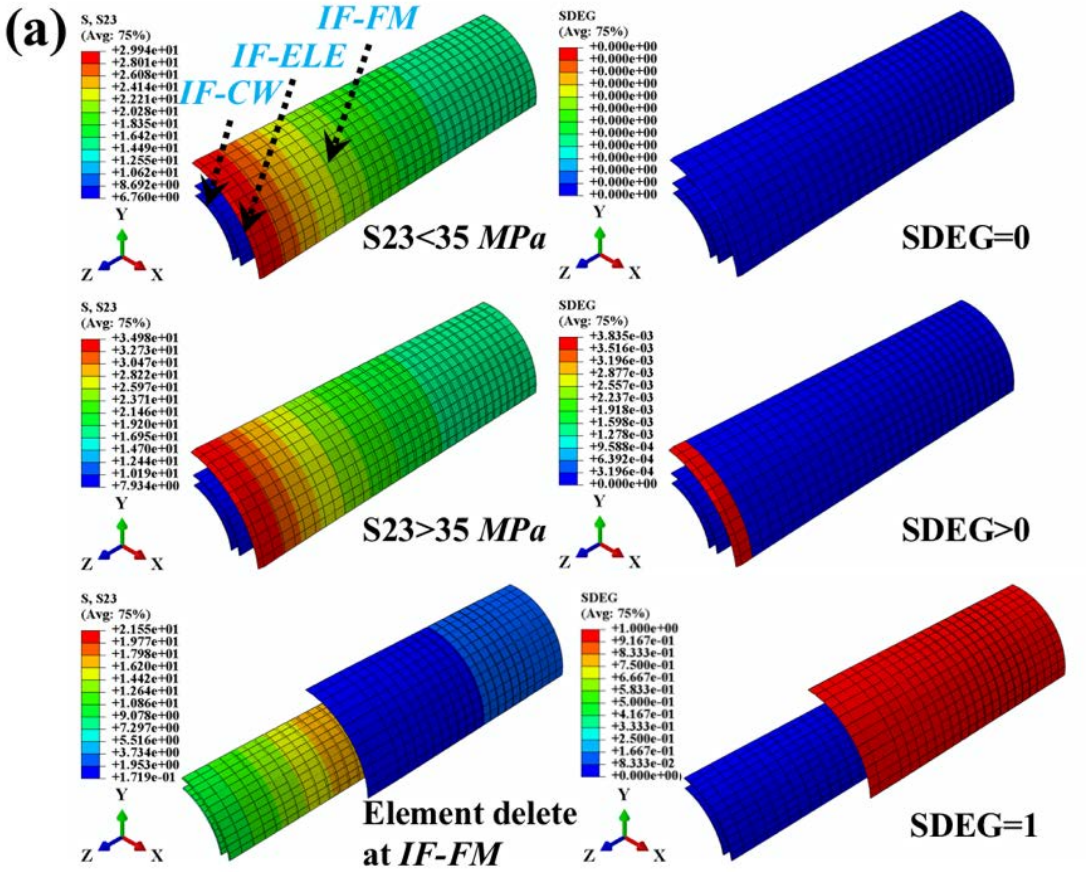

Figure 6.12 Stress distributions on sisal fibers and multi-layer interfaces in triple-interface *FE* model describing multi-stage debond, fracture and pull-out behaviors of single *SFRCs*: (a) the *IF-FM* interface debonding, (b) the outer single technical fiber *TF* breakage, (c) the *IF-ELE* interface debonding, (d) the P/S1 layer of cell wall for the inner elementary fiber *ELE* breakage, (e) the *IF-CW* interface debonding and (f) pulling-out.

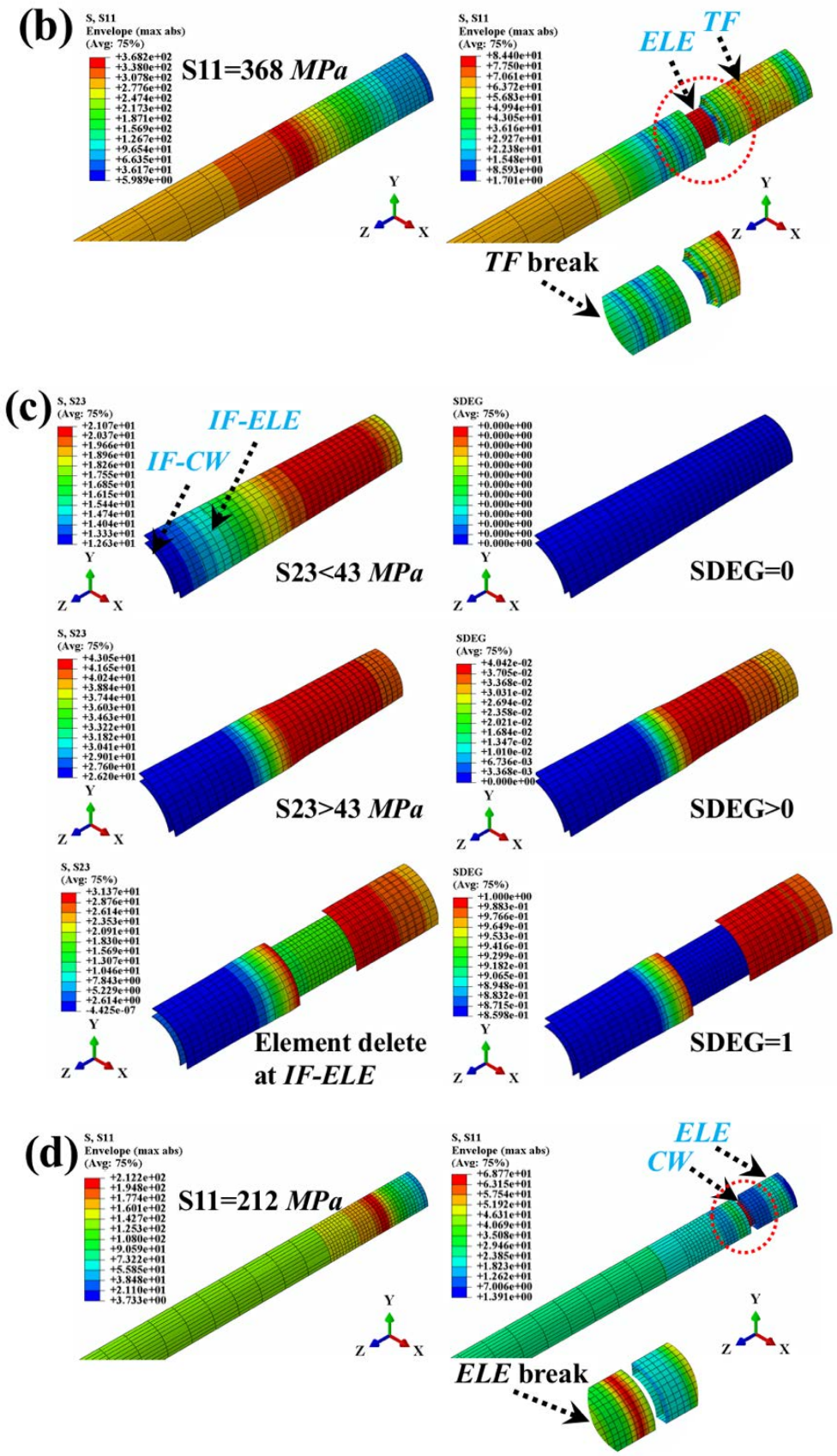

Figure 6.12 (continued).

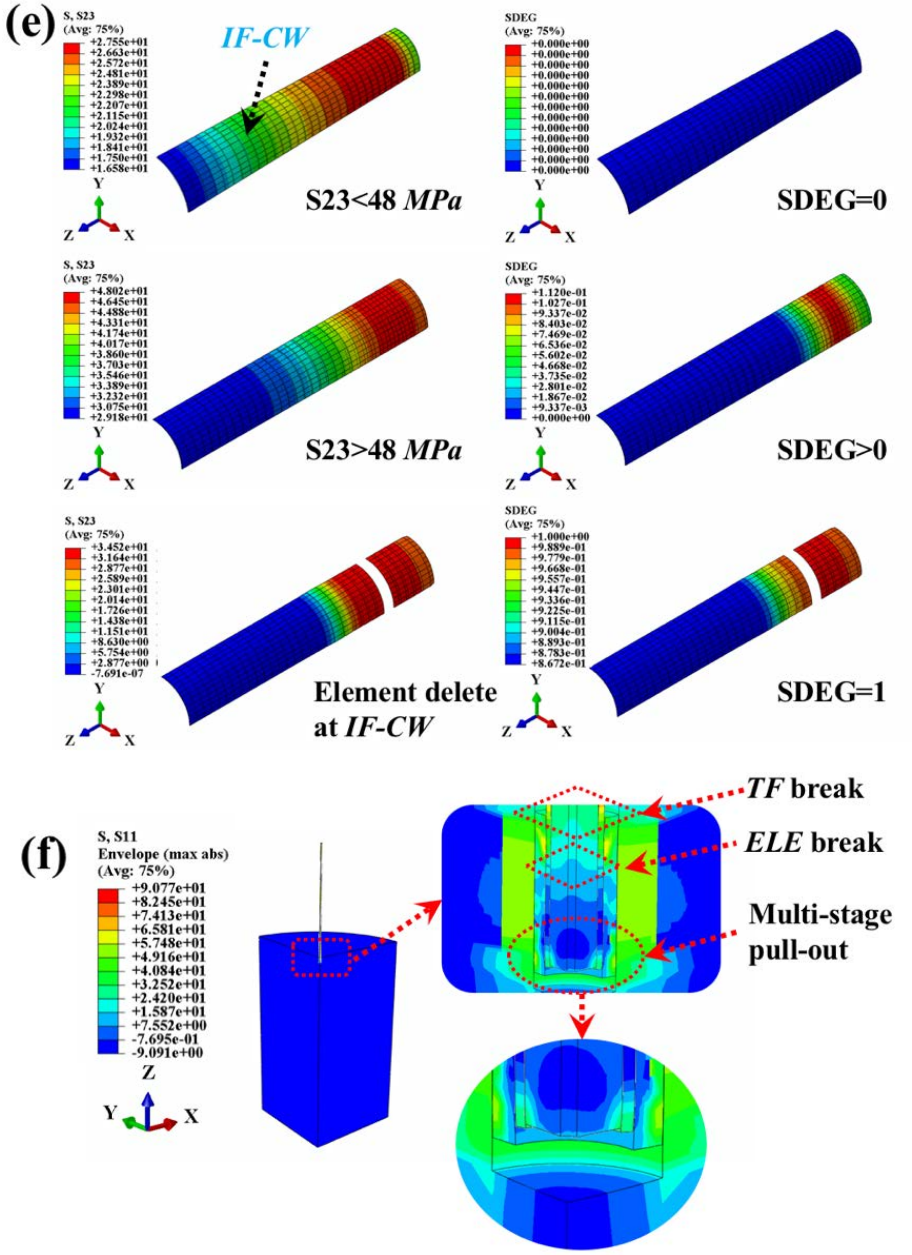

Figure 6.12 (continued).

6.6. Summary

Based on experimental characterization and theoretical analysis in the above two chapters, this chapter mainly investigated the multi-layer interfacial failure behaviors of *SFRCs* numerically. *FE* models utilizing cohesive damage modelling for multi-layer interface debonding and multi-stage fiber fracture and pull-out were developed,

being consistent with the experimental results. It is expected to provide a more effective method for the interface design of *PFRCs* via *FE* analysis of the single fiber pull-out problem. And some important conclusions are summarized as follow:

(1) An appropriate three-interface *FE* model utilizing cohesive damage modelling is developed for the multi-layer interfacial behavior during the single sisal fiber pull-out test. The debonding process of single *SFRCs* with multi-layer interfaces was successfully simulated by using the cohesive force model and the deactivate and reactivate element technique in *ABAQUS*. The solving methods of *ABAQUS* standard and *ABAQUS* dynamic explicit were combined to precisely simulate the process of multi-stage debonding and fracture of single sisal fiber. And a mixed 'cohesive' and 'Coulomb-friction' model was proposed to simulate the entire pull-out process.

(2) With the use of the proposed numerical model, the interfacial performance parameters such as the interfacial modulus, interfacial strength and interfacial energy release rate of the *SFRCs* were studied, analyzing the mechanism of the influence of the interface properties on the pull-out behavior. And then the multi-layer and multi-scale interfacial failure criteria of the *SFRCs* were determined.

(3) Numerical analysis and experimental results of the applied stress-displacement curves can reach a good agreement, showing the validity and accuracy of the developed triple-interface *FE* method. The interfacial strength varies with the multi-interface failure modes of *SFRCs*, which is related to the embedded fiber length of sisal fiber. When the single *SFRCs* were subjected to uniaxial tensile load, the failure

of three types of interfaces, including the interfaces between fibers and matrix, between elementary fibers, and between cell walls, occurred sequentially.

(4) The stress distributions of the components in single *SFRCs* (i.e., sisal fibers, matrix and multi-layer interfaces) can be obtained via the numerical model calculation to present precise derivation of the interface stresses. Referring to the status of the interfacial failure during the pull-out process, the multi-interfacial failure process and mechanisms of single *SFRCs* in the pull-out tests were further revealed and accounted for. The stress distribution obtained from numerical simulation deepens the understanding of multi-layer interface failure behavior of *SFRCs*. Therefore, compared with the accuracy of the double-interface model built in the last chapter for predicting the multi-stage debonding and fracture behaviors of *SFRCs*, the triple-interface *FE* model with one more hierarchical structure could more comprehensively and intuitively describe and analyze the complex multi-layer and multi-scale interfacial bonding conditions and interfacial failure behaviors of *PFRCs* for providing more accurate solutions and precise derivation of the interface stresses.

In conclusion, the presented study provides a theoretical foundation, relying on which numerical analysis can be accurately conducted to facilitate the tasks of multi-layer failure identification in a variety of interfacial structure types. Using the formulations and models developed in the last chapter and this chapter, one can analyze the performance of a *PFRC* for different interfacial properties and provide guidelines for their design and preparation, further achieving more widely application in practical engineering for *PFRCs*.

CHAPTER 7

An *FE* Model of Multi-Layer Interlaminar Fracture Behaviors for Laminated *PFRCs* during the *DCB* Test

7.1. Introduction

The preceding chapters with the nanoindentation and single fiber pull-out technique have illustrated that plant fibers possess complex multi-layer and multi-scale microstructure characteristics and *PFRCs* present the complicated multi-layer interfaces. These chapters have presented both theoretical analysis and experimental validation of the multiple interfacial failure behaviors of plant fibers and single *PFRCs* at the nanoscopic and microscopic scale. From the perspective of practical applications of fiber-reinforced composites, macroscopic interfacial mechanical properties and failure behaviors deserve more attention. For laminated composites,

the weakest failure mode is delamination, which limited the application of composites as the main load-bearing components. So, *ILFT* is very important for a material. Test methods based on fundamental mechanics have been developed to evaluate the interlaminar fracture resistance of laminated composites. Although macroscopic interfacial mechanical properties of fiber-reinforced composites have been studied for more than half a century, more efforts are still required when modelling the mechanical behaviors of the laminated *PFRCs* by considering the multi-layer and multi-scale interfaces. Meantime, the relationship between the microstructure parameters and macroscopic interfacial mechanical properties of *PFRCs* need to be explored by proposing the multi-layer and multi-scale mechanical failure modes, which are of great significance to accurately model the mechanical behaviors of *PFRCs* and to contribute to manufacturing high-performance plant composites.

Chapter 2 has pointed out that numerous overseas and domestic scholars have determined the interlaminar fracture performance of fiber-reinforced composites through experimental investigation and theoretical analysis. Our previous experimental results on the interlaminar fracture behaviors of *PFRCs* have showed that the hierarchical macroscopic mechanical failure modes can be constructed by employing hybrid technology and nano-modification techniques, which indeed brings in the improved interfacial properties and high mechanical performances of *PFRCs*. And the experimental findings also suggest that the *ILFT* of *PFRCs* is significantly higher than that of *AFRCs* (i.e., *GFRCs*). However, the real interlaminar fracture mechanisms of *PFRCs* and the multi-layer and multi-scale interfaces within plant fibers still rare have been considered in the reported theoretical modelling of *PFRCs*.

Therefore, from the perspective of composite structural design, this chapter intends to make full use of the unique microstructure characteristics of plant fibers to reveal the multi-stage interfacial failure mechanisms of *PFRCs*, which can be expected to provide design guidance for the *PFRCs*.

In order to making better interfacial design for the *PFRCs*, this chapter will experimentally and numerically investigate the effects of the hierarchical structure of plant fibers on the interfacial failure behaviors (i.e., the Mode I *ILFT*) of laminated *PFRCs* (continuous unidirectional sisal fiber and epoxy matrix) in the macro-scale through the *DCB* experiments. The *FE* model describing the multi-layer interlaminar fracture behaviors of laminated *PFRCs* is developed in *ABAQUS* software with designed *CZM* in the crack front based on the theory of micromechanics and cohesion model of composite materials. The effect of the multi-layer and multi-scale structure on the improvement of delamination or damage resistance of *PFRCs* can be revealed. A quantitative relationship among the microstructure characteristic, *ILFT* and parameters of the mechanical model is to be investigated based on the design principle of composite structures in this chapter.

7.2. *DCB* experiments for laminated *SFRCs*

Sisal fibers and epoxy resin system were same as in section 3.2.1. The glass fibers with a density of 2.45 g/cm^3 were supplied by Zhejiang Mengtai Composite Co., Ltd. The peel ply (SC01), sealing tape (AT200Y), infusion net (GF100), vacuum bag (L500Y) and draft tube were supplied by Shanghai SINO composite Co., Ltd.

Firstly, the cluster sisal fibers were washed and straightened in water, then dried in an oven as in section 3.2.1. Next, the well arrayed, hackled sisal fibers were chopped to desired length for making unidirectional fabrics as the reinforcing material by sewing method as shown in **Figure 7.1**. Subsequently, the sisal fibers were first sewed on one paper, and finally the paper was tore off to get the unidirectional sisal fabrics.

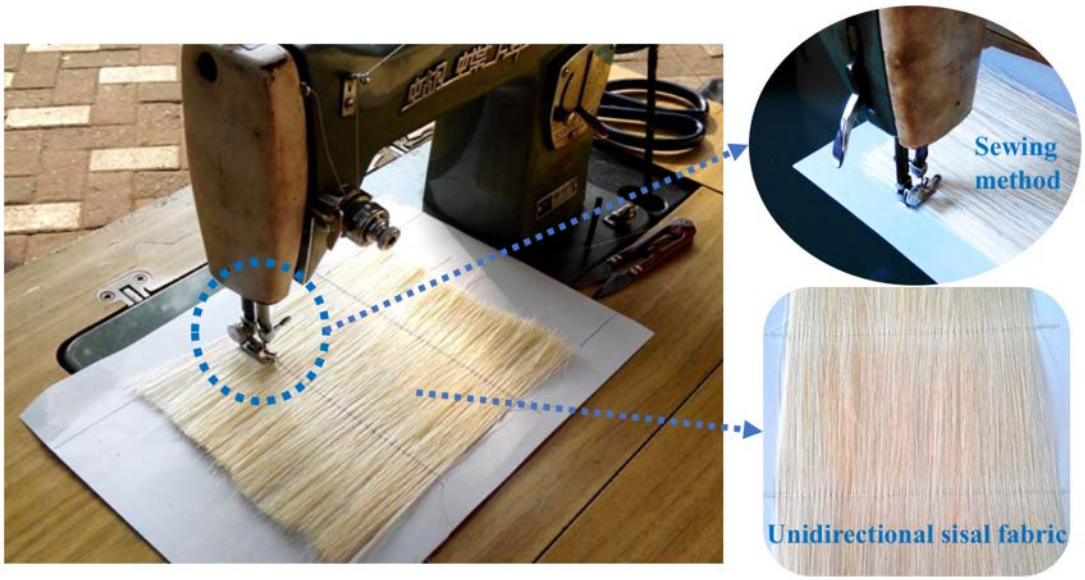

Figure 7.1 Sewing fabrication method of unidirectional sisal fiber fabrics.

The laminated *SFRCs* were manufactured by vacuum assistant resin infusion (*VARI*) process with a layup of $[0°]_{8s}$. To introduce a 50-mm-long pre-crack for *DCB* test, a 15-μm-thick polytetrafluoroethylene (*PTFE*) film was inserted the front section of the prepreg (mid-plane, that is, between the 8th and 9th layer). The *VARI* molding process flow diagram was shown in **Figure 7.2**. First of all, the glass plate was taken as the lower mold in the molding process. Before placing the material, the surface of glass platform was carefully cleaned with acetone to ensure the smooth glass platform,

waiting until the acetone volatilizes. Then a release agent with a thin layer was evenly spread on the glass platform. The mold was painted with a release agent twice, which served in preventing the composite panel from adhering to the mold surface. The material was then laid out neatly from the bottom to the top in the order of peel ply-sisal fiber-peel ply-infusion net. The peel ply was used to prevent the adhesion of the fibers and infusion net. The infusion net assisted the resin flow process. After the placement was completed, a rectangular sealing tape was attached, and two draft tubes were respectively connected to the infusion resin device (resin inlet) and the vacuum pump (vacuum supply) to settle to supply the resin and the vacuum. The stacked fabrics were sealed with the vacuum bag film, setting a suitable height ear at the position of the draft tube to ensure that the entire setup was covered with the vacuum bag. The draft tube was initially closed off, and then the pump was turned on and all the air inside the vacuum bag was removed. Further, it needed to ensure that the entire vacuum bag film was sealed tightly, and carefully check the air-tightness of the vacuum bag. The experimental set-up and the sealed vacuum bag were presented in **Figure 7.3**. The epoxy resin was injected to impregnate the pre-laid sisal fiber fabrics with this *VARI* technique. Prior to impregnation, the mixed epoxy resin was degassed in a vacuum oven for 10 min to remove air bubbles. After ensuring the air-tightness, the infusion draft tube was then inserted into the resin mixture and opened up the vacuum pump. Epoxy resin was drawn into the vacuum bag at a constant pressure of -0.1 MPa. The resin infusion flow rate should be uniform. Once all the fibers were wetted, the infusion draft tube was closed off and the vacuum pump was turned off. The resin infusion end and the vacuum end were tightly squeezed to maintain the vacuum pressure in the bag. Then the impregnated fabrics were cured at room

temperature for 24 h and post-cured at 60 $^{\circ}C$ for 8 h in the vacuum oven to ensure full cure of the epoxy resin after the mold was released. The *VARI* process was conducted under 25 $^{\circ}C$ at 58 $\%$ relative humidity. In order to comparing the Mode I *ILFT* and interlaminar fracture behavior of laminated *PFRCs* and *AFRCs*, the same molding process and curing parameters were employed to prepare laminated *GFRCs*. A total of 16 layers of unidirectional glass fiber fabrics were laid and the same *PTFE* film was laid on the mid-plane (between the 8th and 9th layer) to form an initial pre-crack. The fiber volume contents of the laminated *SFRCs* and *GFRCs* were both around 48 $\%$.

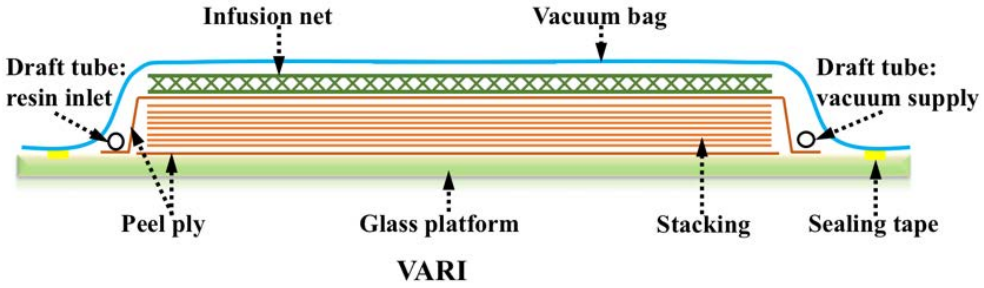

Figure 7.2 Schematic illustration of *VARI* technique for preparing the laminated *SFRCs* and *GFRCs*.

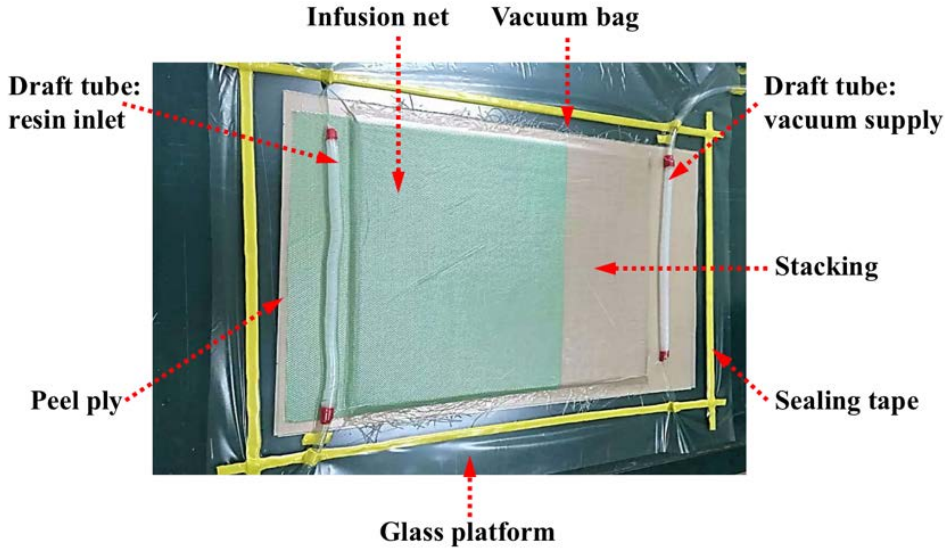

Figure 7.3 Experimental setup of *VARI* for the unidirectional sisal fiber reinforced composite laminate.

According to *ASTM* D-5528, Mode I *ILFT* of the composite laminate was evaluated by *DCB* test, performing at a crosshead speed of 2 mm/min with a load cell of 500 N on a universal mechanical testing machine, ETM204C, manufactured by Wance Testing Machine Co. Ltd., Shenzhen, China. Five specimens with the nominal dimensions of 150 mm × 25 mm × 5 mm were tested. Aluminium load blocks were then bonded to the top and bottom of the arms of specimens as prescribed by *ASTM* D-5528. All bonding surfaces were lightly polished, sandblasted and wiped with acetone-soaked cloth before application of adhesive. Before testing, both edges of the specimen just ahead of the insert were coated with a thin layer of water-based typewriter correction fluid to aid in visual detection of delamination onset and propagation. The crack length Δa (distance from crack tip to initial crack end) varied from 0 to 40 mm. Mark the first 10 mm from the insert on either edge with thin vertical lines every 1 mm. Mark the remaining 40 mm with thin vertical lines at the interval of 5 mm. When the specimen is continuously loaded, the increased crack

propagation length with their corresponding load and displacement was recorded. The crack propagation was monitored visually during the test by means of a similar travelling microscope (combining a high-definition camera with a magnifying glass), and the initiation fracture toughness was obtained by this visual onset method. And propagation toughness was determined directly from the R-curve.

Mode I *ILFT* can be evaluated using various methods as outlined in *ASTM* D-5528, including the modified beam theory (*MBT*), compliance calibration method (*CC*) and modified compliance calibration method correction (*MCC*), etc. The Mode I *ILFT* G_{IC} in this chapter was deduced by using the *MBT* method with providing conservative results and calculated by

$$G_{IC} = \frac{k_n P \delta}{2ba} \tag{7.1}$$

where $k_n = 3$ based on *MBT*. P and δ are the opening load and the crosshead displacement of the test machine at loading point, respectively. Moreover, b and a are the width of specimen and the delamination length ($a = a_0 + \Delta a$, a_0 =50 mm in this research), respectively. With the results calculated, an R-curve was drawn for each specimen which illustrated the variation trend of G_{IC} against Δa. On the whole, the R-curves presented a plateau region after Δa reached a certain value (normally 10 mm for the specimens in this research), which indicated stable crack propagation. The average G_{IC} value of the plateau region (typically as Δa varied from 10 to 40 mm) was calculated for each specimen, defined as G_{ave}. Thus, the Mode I *ILFT* of the laminates for the following simulation could be input by the value of G_{ave}.

The morphologies of cracks were observed, and the crack propagation length was measured by *OM* (10XB-PC). The failure modes of the composites were observed with the aid of a field emission *SEM* (FE-SEM, XL30 FEG, PHILIPS Co., Netherlands). The surfaces were coated with gold before observation.

7.3. Numerical simulation of multi-layer interlaminar fracture behaviors for laminated *SFRCs*

Figure 7.4 shows the macroscopic failure morphologies of interlaminar fracture for laminated unidirectional *SFRCs* obtained from the experiment in section 7.2. The phenomenon of in-plane fiber bridging across the delamination plane of the *SFRCs* can be clearly seen during *DCB* test., which is closely related to the micro-structure of fiber in the reinforcing fabric. As described in the previous chapters, sisal fibers exhibit multi-layer structural characteristics of technical fiber, elementary fibers and cell walls. The multi-layer failure during the loading process makes it possible to eventually appear bridging between each component. In order to analyze the phenomenon of multiple interfacial failure of *PFRCs* occurred in the *DCB* experiment, this chapter established a *3D FE* model with three interfaces for laminated *PFRCs* by employing the commercial *FE* structural analysis software *ABAQUS* (*ABAQUS* 6.14). The developed *FE* model was used to simulate the loading process of *DCB* experiment for laminated *SFRCs*, presenting unique multi-layer interlaminar fracture behaviors and obtaining the stress distributions during the entire interlaminar cracking process. Referring to the *DCB* test of *SFRCs* conducted in section 7.2, a *DCB* test specimen

model with the same plies stacking condition ($[0°]_{8S}$) and geometrical dimension (the fixed dimension of 5 *mm* thickness, 25 *mm* width and 50 *mm* initial crack length) was plotted in **Figure 7.4**. The composite laminate was divided into the upper and lower body models with the thickness of both 2.5 *mm*. Especially, the two layers near the midsection interlaminar layer where the upper and lower laminates are joined were subdivided into different layers with the smaller size as exhibited in **Figure 7.4**, including the elementary fiber layer and the cell wall layer. Although each layer in the laminate is actually consisted of several technical fibers, in order to simplify the calculation, elementary fibers contained in the single technical fiber and the cell walls in the elementary fiber are equivalent to different layers with various thickness. The symbols of the corresponding geometrical dimension are marked in **Figure 7.4**, and the specific values will be given in the following section.

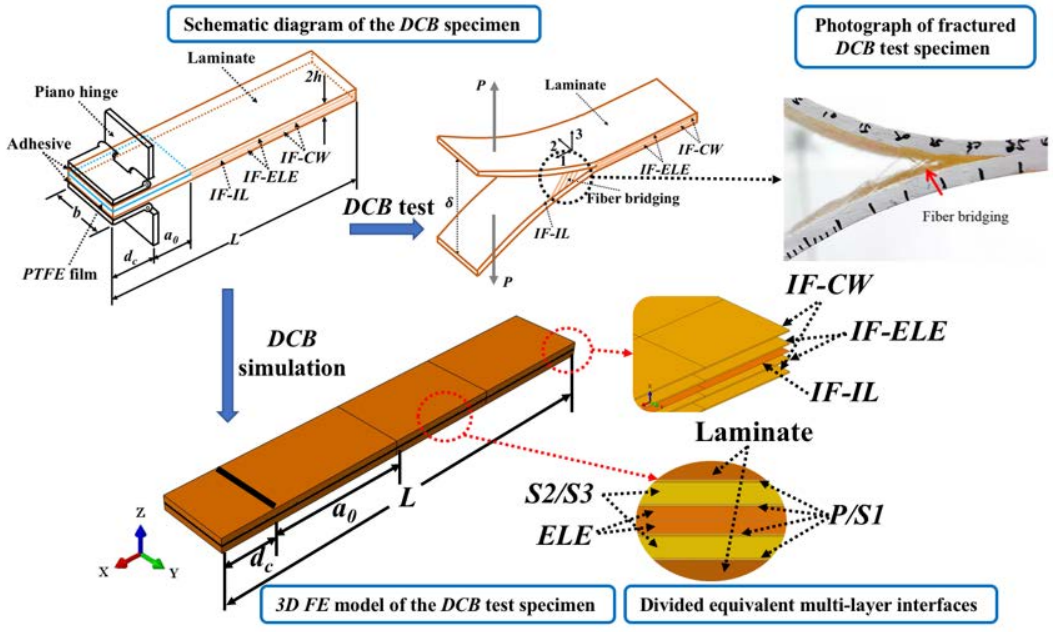

Figure 7.4 Schematic presentation of *DCB* specimen geometry and dimensions and the full view of *FE* model with multi-layer interfaces for simulating the interlaminar fracture of laminated *SFRCs*.

The multiple interlaminar fracture scenarios of the laminated *SFRCs* as tested in the experiment are built as shown in **Figure 7.5**. **Figure 7.5** (a) represents the original status of *FE* model of the *DCB* specimen. Firstly, as illustrated in **Figure 7.5** (b), the interlaminar cracking occurs between the layers along the interface with the pre-crack (defined as *IF-IL* interface (interfaces between interlaminar layer)). With the increase of applied load, partial elementary fibers in one layer near the interface with the pre-crack break (see **Figure 7.5** (c)), which makes the interlaminar cracking continue to happen along the *IF-ELE* interface (see **Figure 7.5** (d)). When micro-fibrils within the outer cell wall layer break (see **Figure 7.5** (e)), the crack propagation will be along the *IF-CW* interface (see **Figure 7.5** (f)). At final, micro-fibrils within the cell wall layer can be pulled out due to the breakage of cell walls (see **Figure 7.5** (g)). The exposed micro-fibrils and the fiber bridging are obviously observed in the fractured morphology of *SFRCs* after the *DCB* experiment. However, this chapter did not simulate the process of micro-fibrils pulling-out as shown in **Figure 7.5** (g).

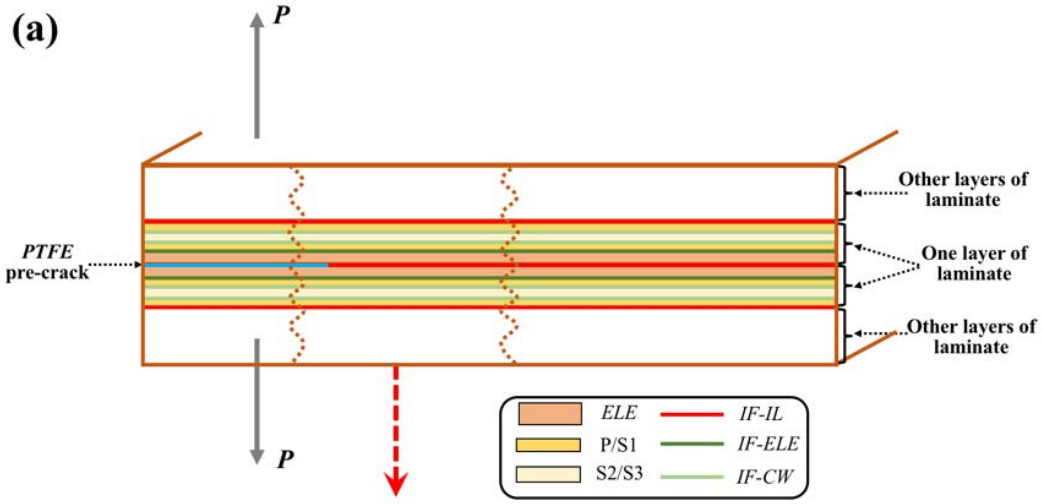

Figure 7.5 Schematic of the multiple interface model describing multi-stage Mode I interlaminar fracture behaviors of *PFRCs*: (a) original status, (b) *IF-IL* cracking, (c) elementary fibers breaking, (d) *IF-ELE* cracking, (e) cell walls breaking, (f) *IF-CW* cracking and (g) micro-fibrils pulling-out.

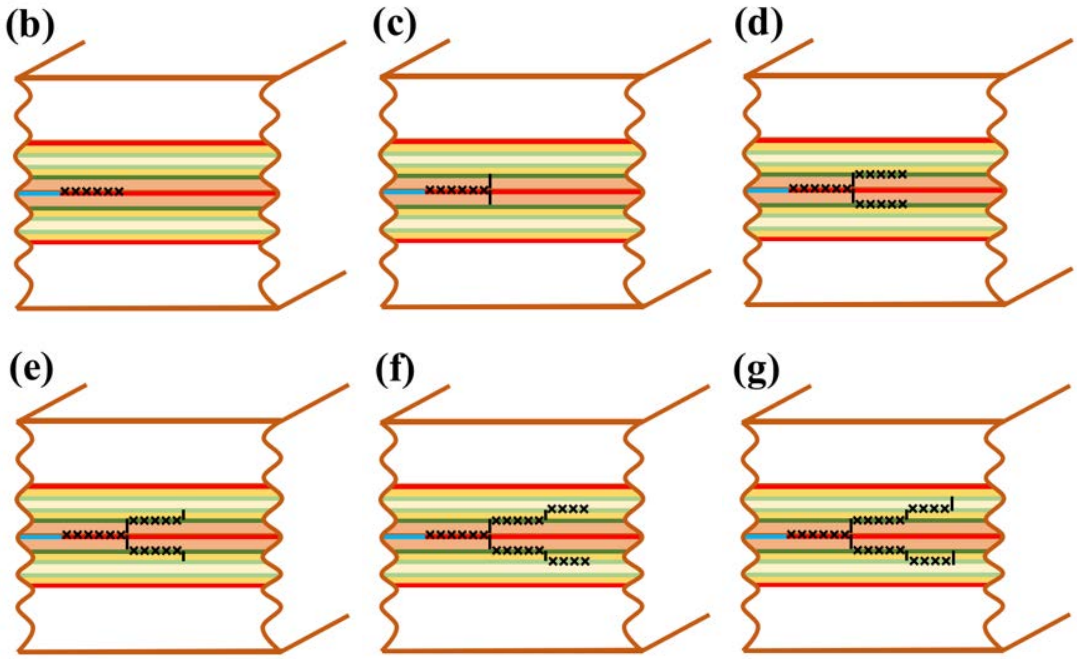

Figure 7.5 (continued).

Taking into account the symmetry of the geometric characteristics and the loading conditions of the *DCB* test specimens, the upper and lower laminates were meshed symmetrically in the specific *FE* analysis as displayed in **Figure 7.6**. The magnified *FE* mesh of the specimen used in the numerical analysis is also presented. Different components were simulated using different types of elements. In the *FE* model, the upper and lower laminates, elementary fiber and cell wall layers (as shown in the orange part of the figure) were all meshed with the eight-node quadrilateral in-plane continuum shell elements SC8R with reduced integration stiffness available in *ABAQUS* library to model the unidirectional *SFRCs* with a composite layup. The mesh number in the thickness direction of the upper and lower laminates, elementary fiber and cell wall layers was set as 1 to facilitate the lay-up. To both preserve numerical accuracy whilst minimizing computational expense, the mesh was chosen to be fine in the cracking regions of the upper and lower laminates, elementary fiber and cell

wall layers, while coarse applied at the non-cracking area of *3D FE* model of the *DCB* test specimen. Considering that the ultimate load is significant sensitive to finite element mesh size, after several meshing attempts, the model eventually contains a total of 60800 eight-node hexahedral elements. Whereas the interface is set to zero thickness with the same as the last chapter. In this study, delamination is modeled using *ABAQUS* cohesive element. The eight-node *3D* cohesive element COH3D8 with zero thickness was used to define the cohesive zone and simulate the multi-layer interfaces of *SFRCs*, designed for modelling potential crack propagation and interface delamination. And a 50 *mm* -long crack is preset in the front of the midsection interlaminar layer. Three types of interfaces were all discretized by using eight-node cohesive elements. Meantime, the mesh size in the cohesive zone was determined based on the rule for the cohesive zone length proposed by Harper et al. **[180]**. A matched mesh size was used for each type of interface (i.e., *IF-IL*, *IF-ELE* and *IF-CW*) and the both neighboring continuum shell element and cohesive element. A very fine mesh with the smallest elements of 0.5 *mm* were used at the region around the interfaces to ensure that the element is small enough to capture the change in stress gradient at the tip of the crack, thus ensuring the accuracy of the numerical results.

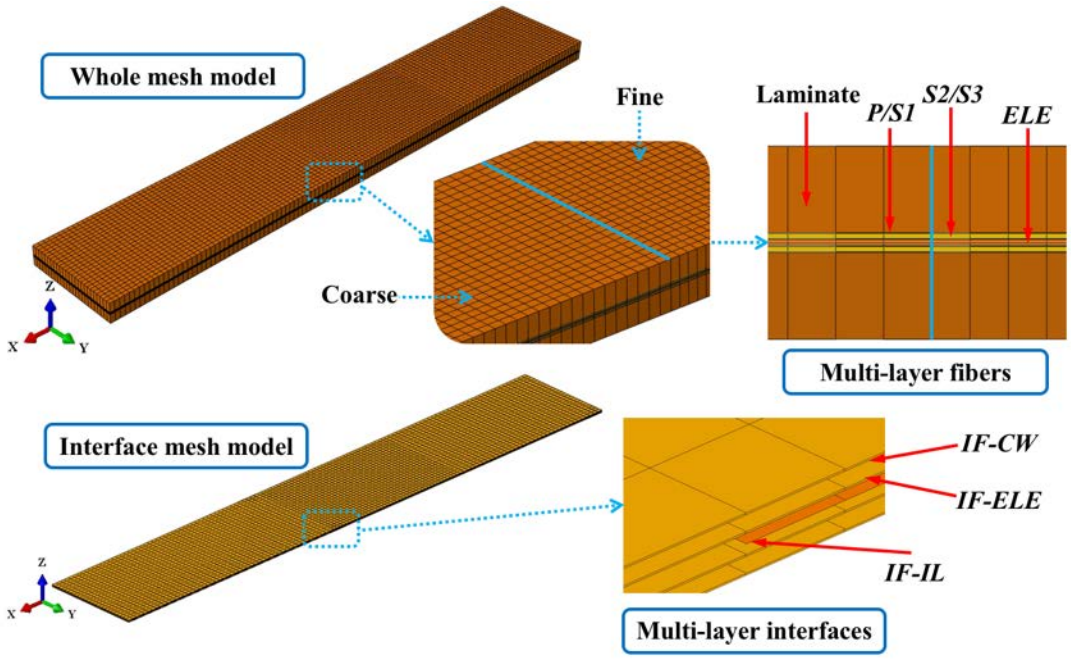

Figure 7.6 *3D* discretized *FE* model with mesh for the Mode I interlaminar fracture of laminated *SFRCs* with multi-layer interfaces (fine mesh at the cracking zone).

In general, there are two methods to solve the fracture problem, one is based on the model of classical fracture mechanics, while the other is based on the damage mechanics model. The fracture mechanics model is based on the linear elastic fracture mechanics and the elasto-plastic fracture mechanics developed on the basis of linear elastic fracture mechanics. The damage mechanics model refers to the method developed based on the damage mechanics. When the element reached the failure condition, the stiffness continuously reduced, and then complete failure achieved with forming a fracture zone. Currently, cracking criteria applied to crack growth simulation include *VCCT* (Virtual crack closure technique) and cohesive behavior. *VCCT* may be viewed as more fundamentally based on linear elastic fracture mechanics. It is suitable for simulating brittle fracture propagation and can only assume an existing flaw. Damage initiation and evolution are both based on fracture energy, available only in *ABAQUS* standard. This technique is developed by Irwin's

energy theory, which is to assume that the energy released by the crack propagation is equal to the energy of the crack closure. Crack propagates when strain energy release rate exceeds fracture toughness. Whereas, the *CZM* is a damage mechanics model that can avoid the singularity of the crack tip. Cohesive behavior can be used to separate the element as individual component. Not only can they simulate fracture occurring along a well-defined crack front, but also can model crack initiation on a surface where cracks do not exist. Crack initiates when cohesive traction exceeds critical value and release critical strain energy when fully open, being available in *ABAQUS* Standard and *ABAQUS* Explicit analysis. Therefore, it is very suitable for simulating the internal interface cracking of the plant fiber and fiber multi-stage fracture phenomena in this chapter. Meanwhile, the *CZM* needs to customize the elastic parameters (interface stiffness), bonding strength and critical traction cracking values of the bonding surface and uses the fracture energy only during damage evolution. It is more conducive to determining the multi-layer interface cracking criteria of *PFRCs* and its performance parameters that cannot be obtained by experimental methods and the interfacial stress variations during simulating the interface cracking behavior in *FE* calculation. Therefore, referring to the analysis of the *CZM* in the previous chapter, for presenting the interlaminar failure behavior of unidirectional *SFRCs* laminates, the *CZM* with wider application range is still employed in this chapter to simulate the interface crack propagation in the laminate and model the fiber bridging effect encountered during Mode I fracture of unidirectional *SFRCs* laminates. Relying on the observation in the experiment, there is generally involving more than one interface cracking behavior during the interlaminar fracture process of *PFRC*. From experimental results as shown in **Figure**

7.7, the presence of an R-curve demonstrated that the toughness measured during crack propagation increases until reaching a steady-state value. As reviewed in Chapter 2, it was found that the value of *ILFT* of *PFRCs* was higher than that of traditional *AFRCs* (i.e., *GFRCs*). The use of a traction-separation law with a nonlinear softening law is necessary to capture the R-curve effect **[181]**. The trilinear traction-separation cohesive law is used in order to model the R-curve effect of *ILFT* of *PFRCs* and the unique changes in the R-curve of *PFRCs* due to the large-scale in-plane fiber bridging that occurs during the delamination propagation process **[60, 132]**. Hence, the trilinear cohesive law (bilinear softening) as seen in **Figure 7.8** is used to obtain more accurate results in this chapter. This law is obtained from superposition of two bilinear cohesive laws with their own specific characteristics for modeling the effect of fiber bridging, as shown in **Figure 7.8**. Accordingly, the superposition parameters of the cohesive laws extracted from the experimentally obtained R-curves is determined using a semi-analytical relation **[181]**. The superposition parameters of m and n (**Figure 7.8**) for the unidirectional *SFRCs* laminate in the trilinear cohesive law can be calibrated by the R-curve obtained in the experiment. While m and n are defined as follows:

$$\begin{aligned} &G_1 = mG^C,\ G_2 = (1-m)G^C \\ &\tau_1 = n\tau^C,\ \tau_2 = (1-n)\tau^C \end{aligned} \qquad \textbf{(7.2)}$$

where G and τ represent the Mode I *ILFT* and cohesive strength, respectively. According to the experimental R-curve of the unidirectional *SFRCs* (**Figure 7.7**), the average initiation value of Mode I critical strain energy release rate (G_1) was 0.672 kJ/m^2 and the steady-state value (G^C) was 1.514 kJ/m^2, which was reached at

approximately 10 mm of crack propagation afterwards. Thus, $m = G_1 / G^C = 0.4439$ can be solved by **Equation** (7.**2**). In order to identify the other parameter, n, it is necessary to establish a relationship between the characteristic length of the process zone for the trilinear cohesive law (l_{ctr}) and the characteristic length of each primary bilinear cohesive law (l_{cbi}, $i = 1,\ 2$). There are special cases existed in this relation **[181]**, which are as follows:

1) The sum of two bilinear laws is a bilinear law when $m = n$;

2) If one of the two bilinear cohesive laws do not have associated fracture toughness (i.e., either $m = 0$ or $m = 1$), the contribution of that particular cohesive law is ignored;

3) If the strength of a bilinear cohesive law with a non-zero fracture toughness tends to zero (i.e., either $n \to 0$ or $n \to 1$), the superposition process zone will tend to infinity;

4) The order of the superposition of the two bilinear laws is irrelevant.

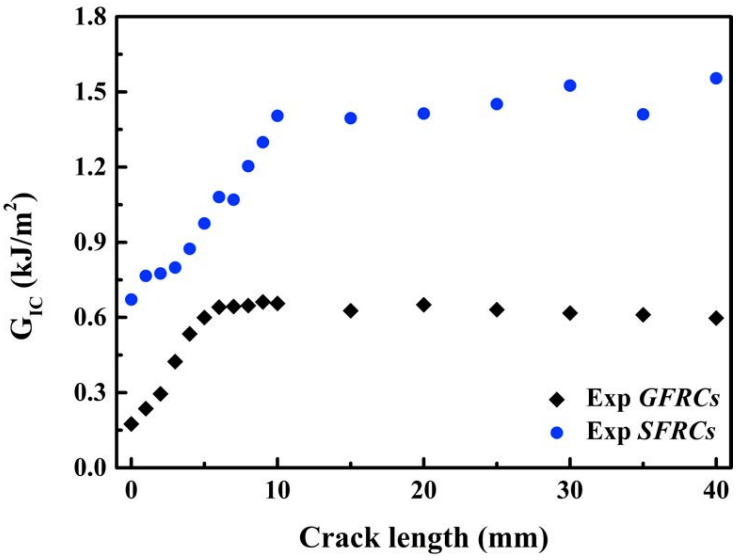

Figure 7.7 R-curve in experiment for unidirectional laminated *SFRCs* and *GFRCs*.

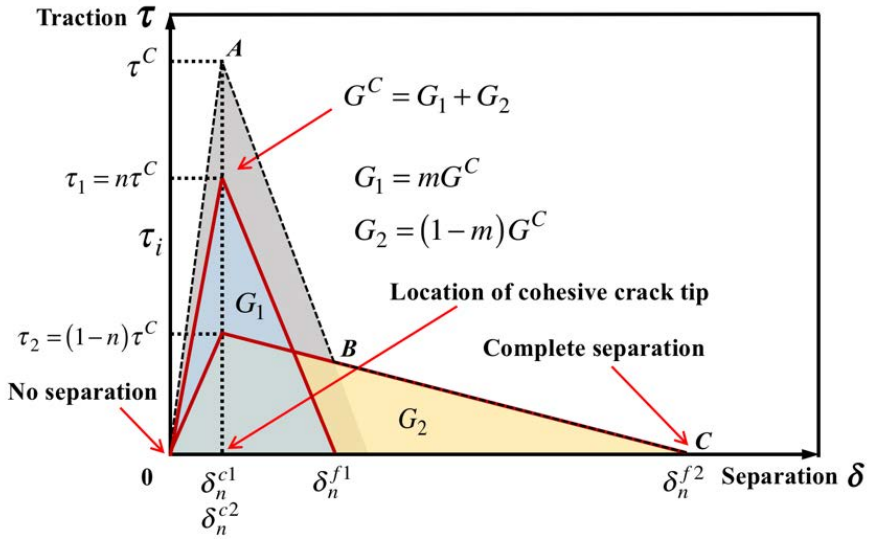

Figure 7.8 Schematic illustration of typical resultant trilinear traction-separation cohesive law (superposition of two bilinear cohesive laws) for modeling cohesive failure and its damage evolution.

These special cases for the characteristic length of process zone for the trilinear cohesive law (l_{ctr}) can be stated as:

$$\begin{aligned} &l_{ctr}(n,\, n) = l_{cb} \\ &l_{ctr}(n,\, m=0) = l_{cb2} \\ &l_{ctr}(n,\, m=1) = l_{cb1} \\ &\lim_{n\to 0 \text{ or } 1} l_{ctr} = \infty \\ &l_{ctr}(n,\, m) = l_{ctr}(1-n,\, 1-m) \end{aligned} \tag{7.3}$$

Then, based on the superposition parameters m and n, the characteristic length of the process zone for the trilinear cohesive law (l_{ctr}), can be calculated using the following interaction equation **[181]**:

$$l_{ctr}(n,\, m) = \left[\frac{m^2}{n^2} + \left(\frac{1-m}{1-n}\right)^2 - \frac{m(1-m)}{n(1-n)}\right] l_{cb} \tag{7.4}$$

in which all the conditions of **Equation (7.3)** are satisfied. In **Equation (7.4)**, l_{cb} refers to the characteristic length of the material, which is an intrinsic fracture property of material. The characteristic length l_{cb} is usually estimated as **[182]**:

$$l_{cb} = \gamma \frac{E^{'} G}{\left(\tau^{C}\right)^{2}} \tag{7.5}$$

where G and τ^{C} are the fracture toughness and strength of the material, respectively. γ is a non-dimensional parameter and depends on the damage or yielding process. The modulus $E^{'}$ under plane stress condition is governed by:

$$E^{'} = 2E_{22}\left(\sqrt{2\left[\sqrt{\frac{E_{22}}{E_{11}}} - \nu_{12}\right] + \frac{E_{22}}{G_{12}}}\right)^{-1} \tag{7.6}$$

where E_{22} and G_{12} are the transverse Young's modulus and shear modulus, E_{11} is the axial Young's modulus, and ν_{12} is the in-plane Poisson's ratio, respectively. In general, the length of process zone under steady-state propagation is estimated by the characteristic length ($l_{pz}^{ss} \approx l_{cb}$). However, this estimation is valid only when the material characteristic length l_{cb} is smaller than the structural dimension, which is because the value of γ in **Equation (7.5)** is noticeably affected by the structural dimension. Based on the above, considering the influence of structural thickness is essential for predicting the steady-state process zone length. Thus, using the empirical relation of **Equation (7.7)** proposed by the literature **[181]**, the thickness correction was applied on the characteristic length in the superposed cohesive law (l_{ctr}) obtained from **Equation (7.4)**:

$$l_{pztr}^{ss} = \left(\frac{t_{lam}}{t_{lam} + l_{ctr}} \right)^{\beta} l_{ctr} \quad \textbf{(7.7)}$$

where t_{lam} is the block thickness (thickness of plies stacking in the same orientation) and β is a non-dimensional parameter. The nonlinear relation of **Equation (7.7)** leads to the solution of l_{ctr}, in which $t_{lam} = 2.5\ mm$ and the steady-state process zone length is $l_{pztr}^{ss} = 30\ mm$ (estimated by experimental R-curve). Finally, using the calculated values of parameters m and l_{ctr}, the parameter n can be iteratively solved by substituting the nonlinear **Equation (7.4)**, the result of which is $n = 0.7808$.

To conclude, the trilinear cohesive law with the calculated values of $m = 0.4439$ and $n = 0.7808$ was applied to the cohesive elements of the *FE* model of the *DCB* specimen in this chapter.

Then, in this chapter, the penalty stiffness $K_{nt} = K_{sn} = K_{st} = K_{tn} = K_{ts} = K_{tt} = 0$ and the determination of the stiffness K_{nn}, K_{ss} and K_{tt} of each crack interface were the same as in section 6.2 and the specific values were listed in next section.

Meantime, the quadratic nominal stress criterion as shown in **Equation (6.5)** of the previous chapter was used as the damage initiation criterion for the cohesive layer in the interlaminar to model the damage (delamination onset) initiation. Once it is satisfied, delamination is initiated. Then, interface damage evolution (delamination propagation) is specified based on a fracture energy criterion and the bilinear softening law. The trilinear traction-separation cohesive law is implemented using a *UMAT*

subroutine. The brittle fracture response and the maximum longitudinal stress failure criterion were used in the *UMAT* subroutine to determine the fiber failure under tension.

Subsequently, the loading, boundary, interaction and constraint conditions of the upper and lower laminates, the elementary fiber layers, the cell wall layers and multi-layer interfaces in the *FE* model of the *DCB* specimen are illustrated in **Figure 7.9-Figure 7.10. Figure 7.9** shows the loading and boundary conditions imposed on the whole laminate based on the loading method in *DCB* experiment. In the *DCB* experiment, the force is applied on the top laminate in the vertical direction using displacement control while fix on the bottom laminate. So, for the simulation of the stress variation of the interlaminar fracture process, vertical displacement loading condition was employed in the *FE* model of this chapter. Loading along the Z-axis was upward enforced displacement applied to the center node (the reference point) of the top surface of the laminate in one side with the pre-crack, while constraining the center nodes of the bottom surface. These boundary conditions only released the rotation displacement R2, while other *DOF* of the nodes were restricted. The applied displacement was linearly increased by amplitude function. The loading rate can be varied by using different amplitude functions, however, in order to facilitate the comparison between the theoretical calculations and the experimental results later, the same loading rate (i.e., 2 mm/min) as in the real experiment was used to simulate in this chapter. In order to completely simulate the interlaminar cracking process of the multi-layer interfaces at different stages of the laminate, the applied displacement at each stage was just the cracking length of the interface at each corresponding stage in

the cracking direction, and the loading time in different stages was determined accordingly. The specific loading displacement and time at various stages will be discussed in the following section. Once the interface of the laminate is cracking, the relative movement between the two connecting parts of the interface leads to the contact behavior, which need to handle the interaction of multiple components. Therefore, taking into account the experimental phenomenon as realistic as possible, as shown in **Figure 7.10**, the contact behaviors of the three types of interfaces (i.e., *IF-IL*, *IF-ELE* and *IF-CW*) in the *FE* simulation were modelled using a cohesive surface behavior (node-to-surface contact with finite sliding) in this chapter. The cohesive layer with zero thickness was located between the *IF-IL*, *IF-ELE* and *IF-CW* as illustrated in **Figure 7.10**. As shown in **Figure 7.10**, tie constraints were established between the nodes on the upper and lower surfaces of each type of interface and the surface of adjacent fiber ply to eliminate the relative slip between these two surfaces. Thus, the displacement and stress on both sides of the cohesive element can be coordinated with those on the surface of adjacent fiber ply.

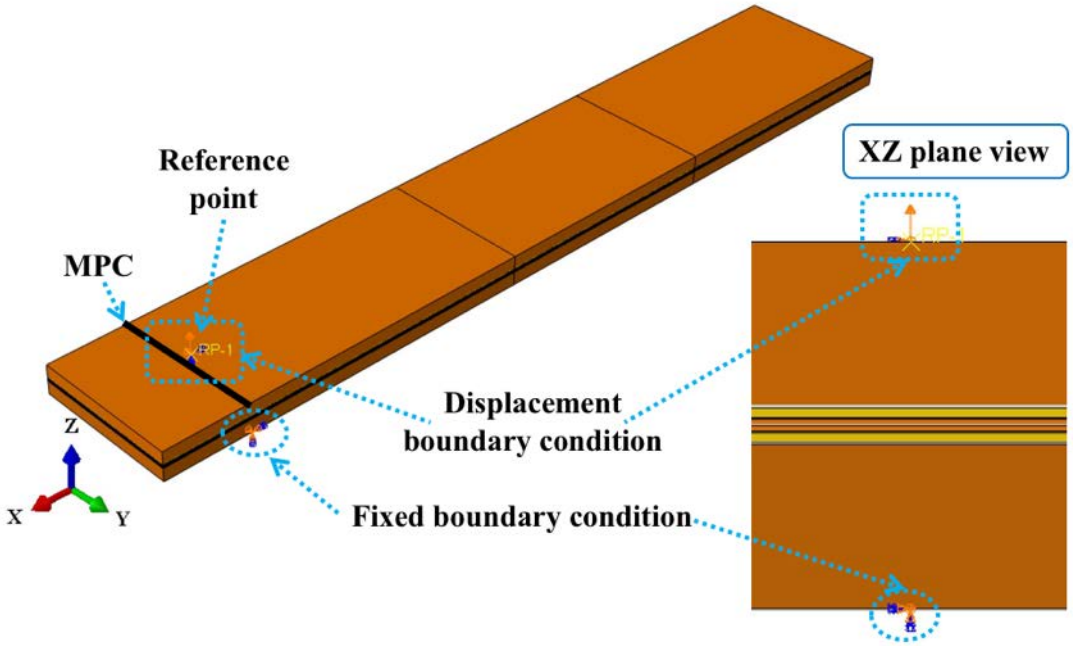

Figure 7.9 Load and boundary conditions of whole laminate for the *FE* model of the Mode I interlaminar fracture in *DCB* test specimen of *SFRCs* with multi-layer interfaces.

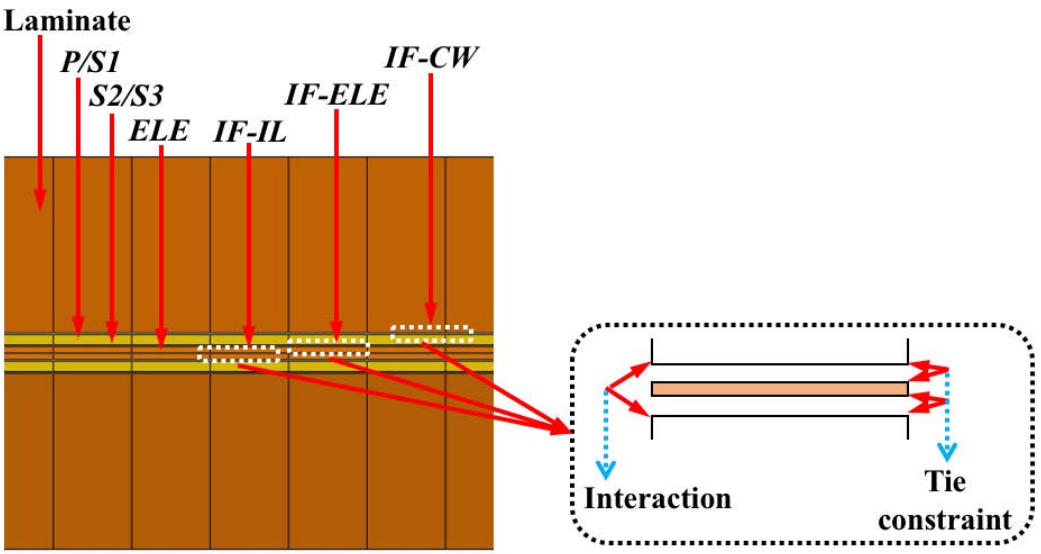

Figure 7.10 Interaction and constraint conditions of multi-layer interfaces (i.e., *IF-IL*, *IF-ELE* and *IF-CW*) for the *FE* model of the Mode I interlaminar fracture in *DCB* test specimen of *SFRCs*.

To model the interlaminar failure behavior of the *SFRCs* with the multi-layer interfaces, two fracture mechanisms associated with delamination propagation are considered: (1) decohesion of interlaminar interface (resin-rich layer between the fiber plies) at delamination front and (2) bridging traction of in-plane fibers in the wake of the crack (delamination) tip caused by the multiple interlaminar cracking, which are modeled using trilinear cohesive law. The implementation of the model and the proposed procedure can be summarized as, the parameters of the trilinear cohesive law are calibrated using the experimental results of the *SFRCs*, and the multiple interlaminar failure of *SFRCs* laminate is modeled using cohesive elements with a nonlinear softening law in order to model the large-scale fiber bridging occurred during delamination. Therefore, in order to simulate the process of multiple interlaminar cracking of the unidirectional laminated *SFRCs* discussed previously and obtain the final R-curve and force-displacement response (as shown in **Figure 7.11**-**Figure 7.12**), this paper combines solving method *ABAQUS* standard and *ABAQUS* dynamic explicit to simulate and analyze the *3D FE* model of the *DCB* test specimen (**Figure 7.4**-**Figure 7.5**) used to study delamination in unidirectional *SFRCs* laminates. In this investigation, a static interlaminar cracking process is assumed using *ABAQUS* standard solution method to simulate relying on the trilinear cohesive law discussed earlier. During the solving process, the large deformation and time automatic sub-step were turned on. Meantime, the size of the time increment in the calculation was controlled and set small enough to more clearly exhibit the bonding conditions of multi-layer interfaces during the entire process of interlaminar cracking. Then the result of each increment was output, thus showing the whole damage process of the cohesive element. *ABAQUS* dynamic explicit analysis method was employed to

simulate the fiber breakage process. The stress field from the last time step solved by *ABAQUS* standard was loaded into the model through a restart analysis and predefined stress field. The size of the time increment is then determined dependent on the mesh size and material properties. The analysis time was reduced by using mass scaling. Different mass scaling factors have been tried and the most appropriated factor was determined as 5 on the basis of ensuring the accuracy of simulation results and computational efficiency. Finally, to facilitate the query of results (the R-curve and force-displacement curve) in the post-processing, the interface cracking length was measured as the number of the elimination of cohesive elements on the multi-layer interfaces, and the load and displacement were respectively measured as the reaction and displacement in the loading direction acting on the reference point. The flowchart of *FE* model for solving the multiple interlaminar cracking and multi-stage fiber fracture process was presented in **Figure 7.13**.

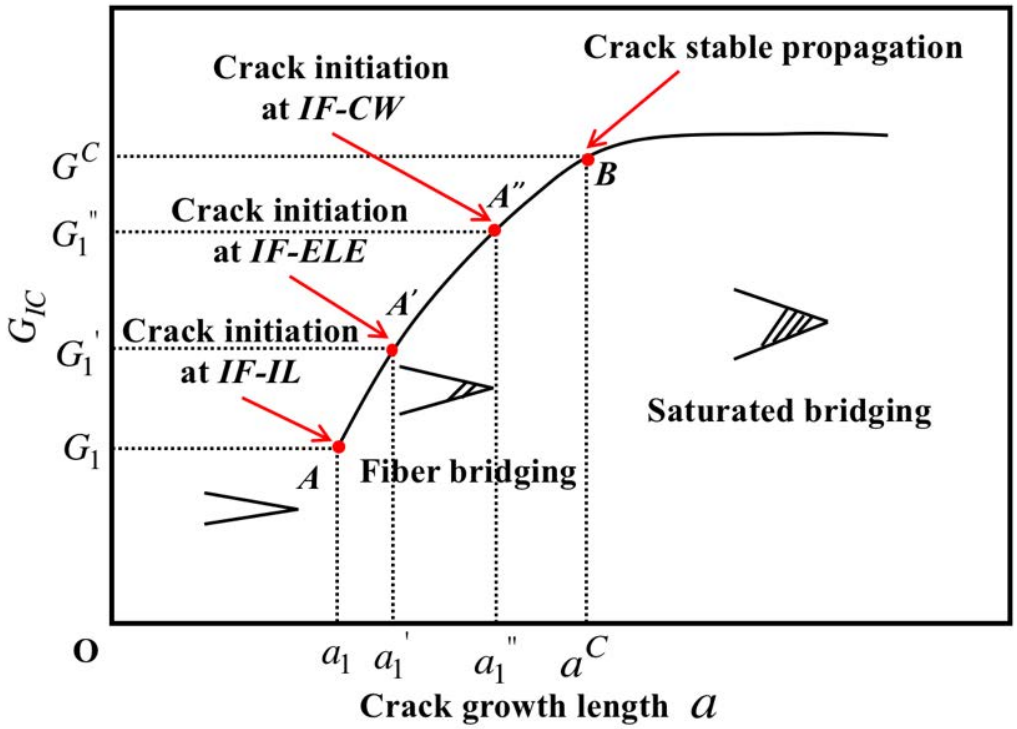

Figure 7.11 Schematic showing of typical R-curve behavior during multi-stage interlaminar cracking process of unidirectional *SFRCs* laminate.

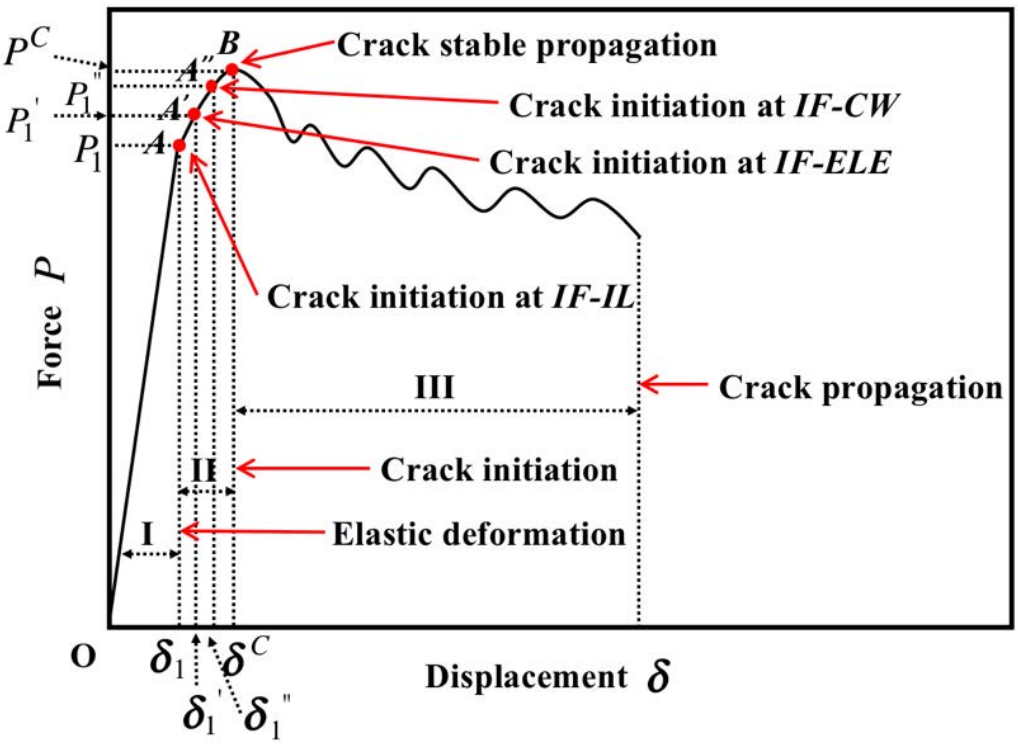

Figure 7.12 Schematic of typical force-displacement response behavior during multi-stage interlaminar cracking process of unidirectional *SFRCs* laminate.

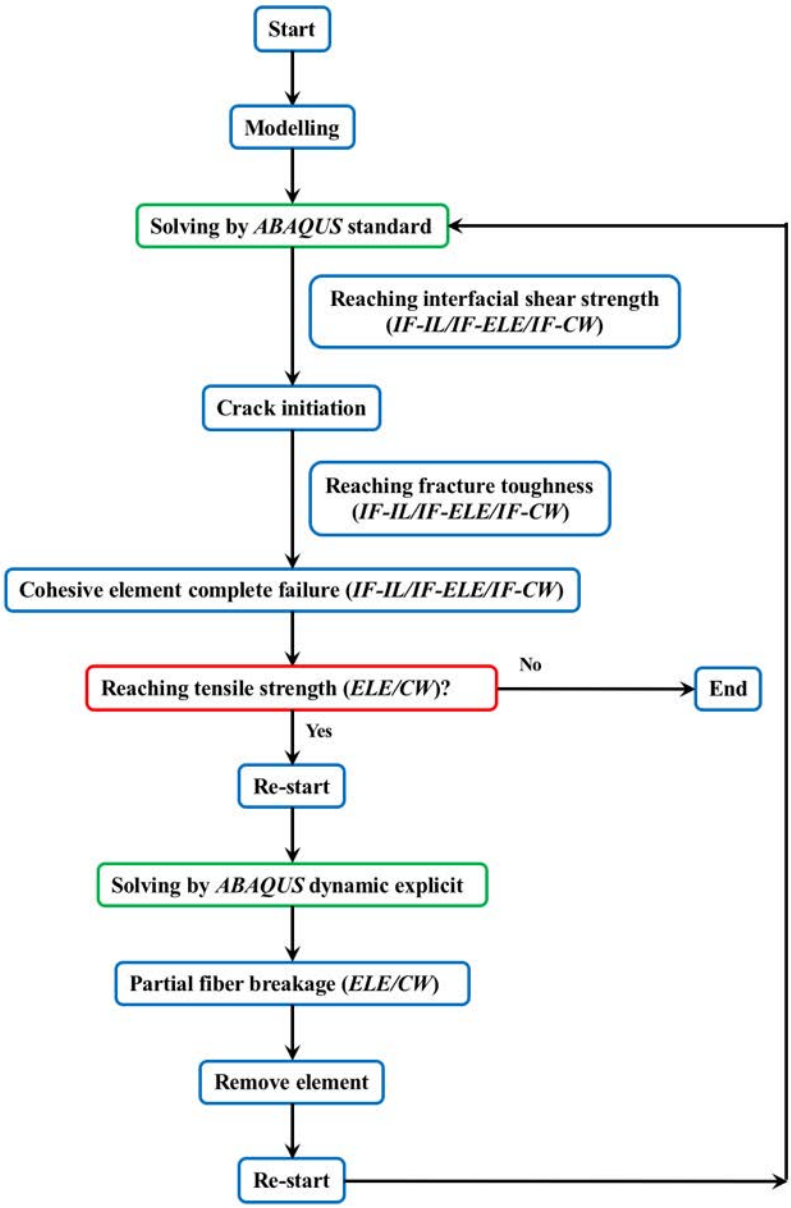

Figure 7.13 Flowchart of the proposed *FE* model for solving the multi-stage interlaminar cracking process.

7.4. Effects of the interfacial parameters on the interlaminar failure behaviors of *SFRCs*

According to the research work and results obtained in our previous chapters, the geometric parameters and the basic material properties of various types of fiber (i.e.,

technical fiber, elementary fibers and cell wall micro-fibrils) and multi-layer interfaces (i.e., *IF-IL*, *IF-ELE* and *IF-CW*) and other input parameters required for the numerical simulation of *DCB* test specimen are given in **Table 7.1**. The geometric dimension and lay-up of laminate referred to the data in previous *DCB* experiment. The thickness of the subdivided fibrous layers (elementary fibers, P/S1 and S2/S3 cell wall layer) was ascertained according to the proportion of components in the multi-interface pull-out model in Chapter 6. The density, elastic modulus, shear modulus and Poisson's ratio of elementary fibers and cell wall layers and the interfacial modulus were determined relying on the parameters of multi-interface pull-out model in Chapter 6. The density, elastic modulus, shear modulus and Poisson's ratio of laminate were obtained from our pre-research work. The laminate, elementary fibers and cell wall layers exhibit anisotropy. The technical fiber, elementary fibers and cell wall layers are assumed to possess different ultimate tensile strength so as to simulate the breakage of fiber between multiple cracking processes, whereas the *IF-IL*, *IF-ELE* and *IF-CW* are assumed to have different interfacial properties regarding the interfacial modulus (stiffness), interfacial strength and interfacial fracture toughness (energy release rate). Therefore, different interface cracking criteria and stress distribution during the interlaminar fracture process of *PFRCs* can be obtained. The interfacial properties used in the cracking failure criterion are also shown in **Table 7.1**. A viscous regularization parameter (viscosity coefficient = 0.0005) has been used to overcome convergence difficulties that arise during material softening and stiffness degradation. Energy type in conjunction with the trilinear softening law was used to describe the damage evolution after the initiation criteria was reached. The energy type of damage evolution requires a maximum energy release rate G^C at which the

cohesive layer completely failed. The Mode I interlaminar energy release rate of the laminated *SFRCs* was experimentally derived through *DCB* test. In this study, with the use of the proposed numerical model, different values of the critical stresses (τ_n^c, τ_s^c and τ_t^c) and the energy release rate (G^C) at failure were tried based on the values in Chapter 6, and the values that gave the best agreement between the analysis and experiment load-displacement curves were listed in **Table 7.1**.

Table 7.1 Material constants and geometric parameters for sisal fibers and their composites used in the *FE* model.

Properties of *SFRCs*				
Fiber type	Laminate	*ELE* layer	P/S1 layer	S2/S3 layer
Thickness L (mm)	2.1875	0.0940	0.0202	0.1781
Density $\left(g/cm^3\right)$	1.45			
Young's modulus $\left[E_{11}/E_{22}/E_{33}\ (GPa)\right]$	10.06/6.2/6.2		8.62/5.31/5.31	11.07/6.42/6.42
Shear modulus $\left[G_{12}/G_{13}/G_{23}\ (GPa)\right]$	4.49/4.49/2.7		3.85/3.85/2.33	4.94/4.94/2.99
Poisson's ratio $\left[\nu_{12}/\nu_{13}/\nu_{23}\right]$	0.12/0.12/0.14			
Properties of multi-layer interfaces				
Interface type	*IF-IL*		*IF-ELE*	*IF-CW*
Density $\left(g/cm^3\right)$	1.5e-3			
Tensile stiffness $\left[K_{nn}/K_{ss}/K_{tt}\ (GPa)\right]$	6.1/6.1/6.1		7.2/7.2/7.2	9.4/9.4/9.4
Shear strength $\left[\tau_n^c/\tau_s^c/\tau_t^c\ (MPa)\right]$	15/15/15		20/20/20	24/24/24
Initial fracture toughness $G_1^C/G_2^C/G_3^C\ \left(J/m^2\right)$	672		1070	1299
Propagated fracture toughness $G_f^C\ \left(J/m^2\right)$	1514			

7.5. Comparisons between experimental and numerical results on Mode I interlaminar fracture of laminated *SFRCs* with multi-layer interface

Figure 7.14 presents the force-displacement response for the *DCB* specimen of laminated *SFRCs* calculated by single- and triple-interface model with trilinear cohesive law. Meantime, the experimental results of *SFRCs* and the existed data of traditional *AFRCs* (i.e., *GFRCs*) were compared. It can be seen that the numerical simulation in the curves of force-displacement using the triple-interface model with trilinear cohesive law was very close to the experimental value. The experimental findings between *SFRCs* and *GFRCs* and the results of single-interface *FE* model established in this work suggest that the introduce of multi-layer interface for plant fiber was effective and can improve the load capability of their composite laminates. With the increase of the applied load, a pre-crack was initiated. When the load reached a level to make the composite laminate delaminated, the crack started to propagate. The higher the *ILSS*, the higher the load needed to make the crack initiate and propagate. By contrast, with the increase of the crack propagation, the force versus displacement plots demonstrated that the maximum force required for the unidirectional *SFRCs* to cause crack propagation was higher than that for the unidirectional *GFRCs*. The main reason is that, compared with traditional synthetic fibers, plant fibers possess a unique multi-layer and multi-scale structure, thus, the failure modes of their reinforcing composites depend on both the interfacial properties between the plant fiber and matrix and the cohesion of the internal interfaces of plant

fiber. For the fracture toughness of composite materials, it is generally believed that the interlaminar fracture behavior of composites is closely related to the fiber bridging between the composite layers. In general, the typical failure modes of the unidirectional fiber reinforced composite in *DCB* experiment are matrix cracking and interface debonding. Relying on the investigation of Mode I *ILFT* of unidirectional *PFRCs*, it was found that the fiber bridging phenomenon which was attributed to the distinct microstructure of plant fibers was more pronounced, suggesting that the process of crack propagation was more complicated than that of *AFRCs*. The higher peak load caused by the fiber bridging in the force-displacement curve indicated that the unique multi-layer interface characteristics of *PFRCs* play a crucial role in the crack propagation front of *DCB* specimen. Generally, in the presence of fiber bridging, the damage process zone is extended by inducing bridging traction over the wake of the crack tip, which leads to a significant increase in the crack growth resistance of fiber-reinforced composites.

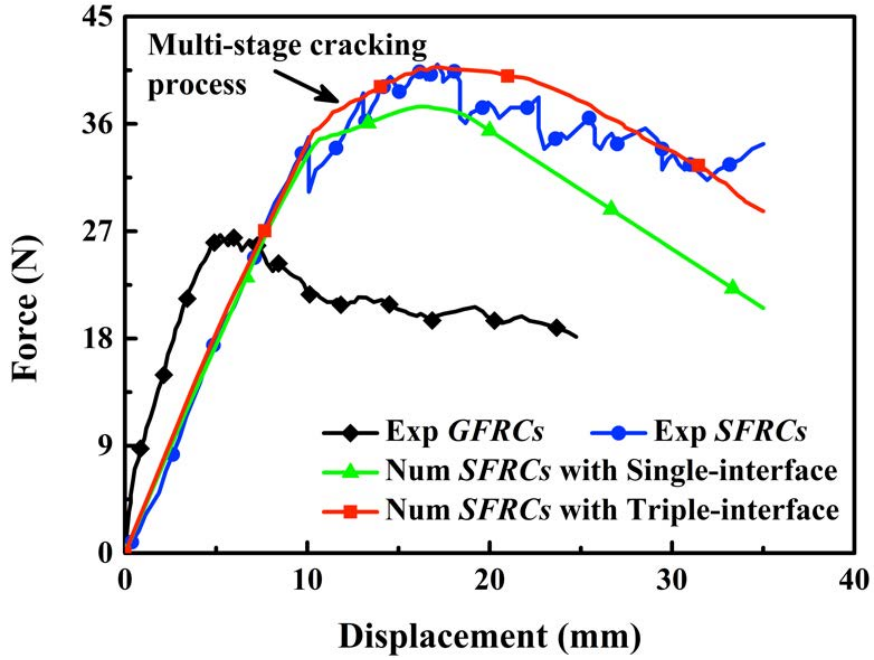

Figure 7.14 Comparison of the force-displacement response between the experimental results and the numerical results for the *DCB* test specimen of composite laminates (i.e., *SFRCs* and *GFRCs*).

From the perspective of fracture mechanics, the *ILFT* expressed in terms of the critical strain energy release rate, which is an important resistance property to the crack propagation, can be used to evaluate the interlaminar fracture characteristics of laminated composites. Usually a crack resistance curve, called R-curve is used to evaluate the fracture resistance of a fiber reinforced composite material. **Figure 7.15** compares the delamination resistance curves (R-curves) of the variation of strain energy release rate with the delamination crack propagation length obtained from experiment and numerical simulation of Mode I *ILFT* for unidirectional *SFRCs* with multi-interface, which was also compared with those for the traditional *GFRCs*. It can be seen that the strain energy release rate of *SFRCs* appeared a plateau and reached a stable value after the crack propagation reaching 10 *mm* where the crack growth propagated in a constant manner while earlier cracking occurred in *GFRCs* at 6 *mm*.

Unlike *GFRCs*, the R-curves of laminated *SFRCs* showed significant ups and downs in the crack propagation stage (crack propagation length from 0 to 10 mm), which implied unstable crack propagation. Observed by side views of the specimens in *DCB* test of *GFRCs*, the crack tips of *GFRCs* laminates were basically at the mid-plane of the specimens. In contrast, crack tips of *PFRCs* would shift far away from the mid-plane, which also demonstrated the unsaturated crack propagation implied by the R-curves. During the whole process of crack propagation, the strain energy release rate of *SFRCs* was higher than that of *GFRCs*. When the crack began to propagate, it first propagated along the *IF-IL* interface where the pre-crack was located. The initial fracture toughness of the *IF-IL* interface can be determined by *FE* simulation as 0.672 kJ/m^2. With the increase of applied opening displacement, the elementary fiber layer close to *IF-IL* interface can be broken, then the crack will continue to propagate along the interface between the elementary fibers (i.e., *IF-ELE*). The initial fracture toughness of the *IF-ELE* interface can be ascertained as 1.070 kJ/m^2. With the propagation to a certain extent, the outer cell wall micro-fibrils layer in the elementary fiber layer broke, and then the crack propagation occurred along the *IF-CW* interface. The initial fracture toughness of the *IF-CW* interface can be confirmed as 1.299 kJ/m^2. Finally, the crack reached a saturated propagation and the averaged propagated fracture toughness was 1.514 kJ/m^2. Therefore, the strain energy release rate values obtained from the R-curves were 0.635 kJ/m^2 for the *GFRCs* which was the lowest and 1.514 kJ/m^2 for the *SFRCs*. It could also be seen that more energy was needed for the initiation of the cracks for the *SFRCs* compared with the *GFRCs*. The numerical results showed that the higher interfacial properties of the internal

interface of *SFRCs* enhanced the resistance to crack propagation when the initial crack propagates at the interface, making the initial fracture toughness of the three interfaces of *SFRCs* gradually improved. Meantime, it indicated that the trilinear cohesive law is able to accurately predict the initiation and the final steady-state propagation values of the fracture toughness for each interface in laminated *PFRCs*. The *FE* analysis results showed reasonably good agreement with the experimental results and the prediction of the Mode I critical strain energy release rate for the initiation and propagation phase of the delamination was within the range of the measured values. Therefore, it was shown that the shape of R-curve, i.e., the relation between the fracture toughness and the crack length, was not material property but depended on the geometry of the specimen. The multi-stage failure induced by the multi-layer interfaces made large-scale fiber bridging occurred across the delamination plane, which captured a much wider range of unsaturated stage.

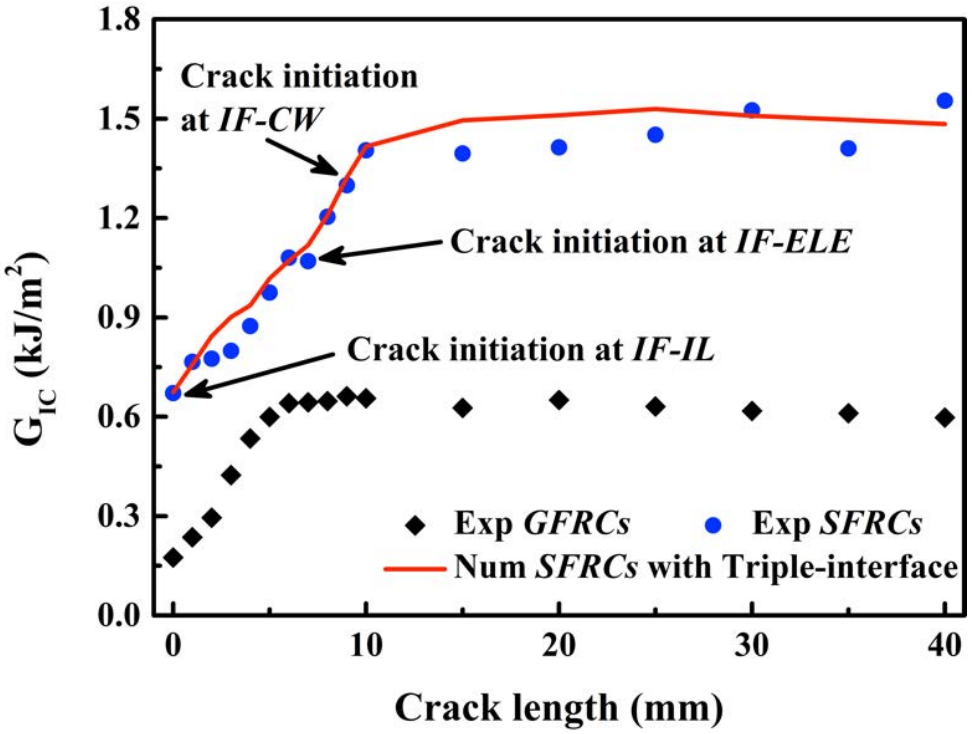

Figure 7.15 Comparison of R-curves (measured fracture toughness values of the composite versus crack length) between the experimental results and the *FE* analysis results for the *DCB* test specimen of composite laminates (i.e., *SFRCs* and *GFRCs*).

The evolution of the crack propagation length against the opening displacement obtained by experimental and *FE* simulation of *DCB* test specimens was compared in **Figure 7.16**. It was found that the model appeared to be able to give a satisfactory prediction of the multi-interface interlaminar failure behavior of laminate. The fit between the numerical predicted and experimental measured crack lengths for the *SFRCs* agreed very well. The numerical model showed that the crack propagation toke place at a similar rate to the experimental result. The difference between the predicted crack length and the experimental measured data against the opening displacement was mainly attributed to the discrepancy between the ratio of fiber component and the location in the presence of multi-interfaces between the actual specimens and the *FE* model.

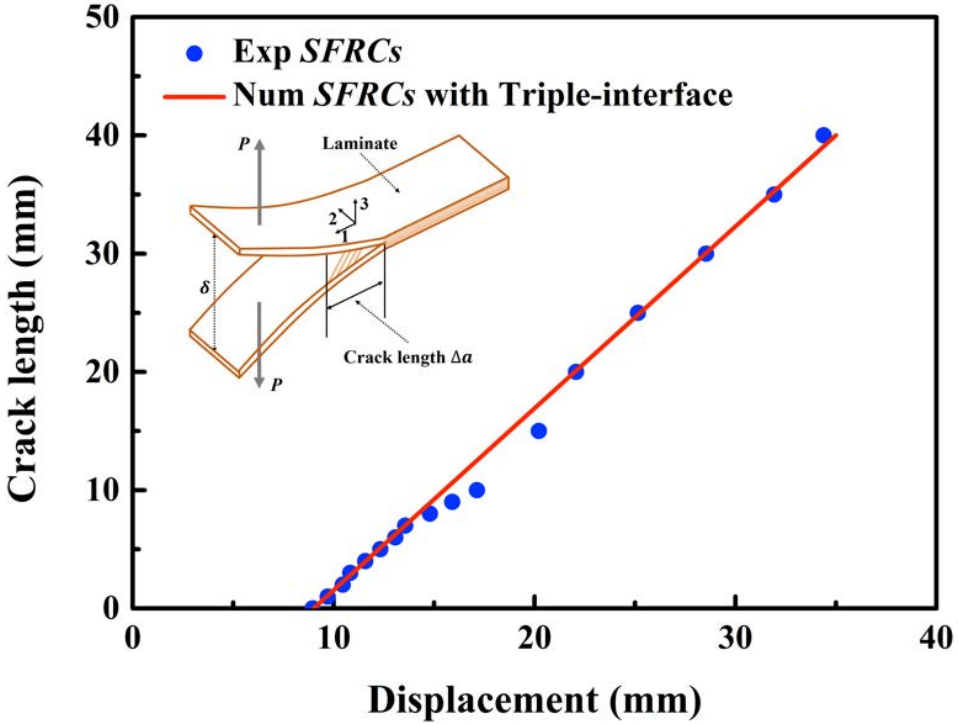

Figure 7.16 Comparison of change in crack length against opening displacement between the experimental and *FE* analysis results for the *DCB* test specimen of *SFRCs*.

To sum up, considering a more complex failure mechanism of composite caused by multi-layer and multi-scale structure, the multi-interface initiation fracture toughness values of *PFRCs* were modelled and determined with the proposed trilinear traction-separation cohesive law. The experimental results are used to calibrate the parameters of the cohesive law. Good consistency between the numerical simulation and the experiment results in the curves of force-crack opening displacement, strain energy release rate-crack length and crack length-opening displacement verified the efficiency of *CZM* in modelling the multi-layer failure behaviors of laminated *PFRCs*. The experimental findings between *SFRCs* and *GFRCs* and the results of single-interface *FE* model established in this work suggest that the introduce of multi-layer interface for plant fiber was effective and can improve the load capability and the

Mode I critical strain energy release rate (that is, steady-state *ILFT*) of their composite laminates. There were three initiation fracture toughness values in the three stages before reaching the saturated propagation fracture toughness value, corresponding to the toughness of the three types of interfacial cracking. And it is crucial to consider the effects of in-plane fiber bridging to have an accurate prediction of the values of Mode I *ILFT* for the *PFRCs* with hierarchical structure.

7.6. Multi-stage interlaminar fracture mechanisms of *SFRCs*

When the interfacial stress reached the interfacial strength of the composite laminate, the interface began to damage. Then with the increase of the displacement, the load-bearing capacity of the interface decreased, resulting in the appearance of interfacial micro-cracks. After that, the interlaminar delamination occurred when the elements of the interface cannot be loaded, and the stress distribution changed and redistributed. Moreover, details of the stress distribution around the crack tip and the crack propagation pattern across the width of the *DCB* specimen could be investigated using the *FE* method via the cohesive element. **Figure 7.17** plots the distributions of stress nephogram on the components of sisal fiber layers and the cracking zones of multi-layer interfaces in triple-interface *FE* model describing multi-stage cracking and fracture behaviors of laminated *SFRCs*.

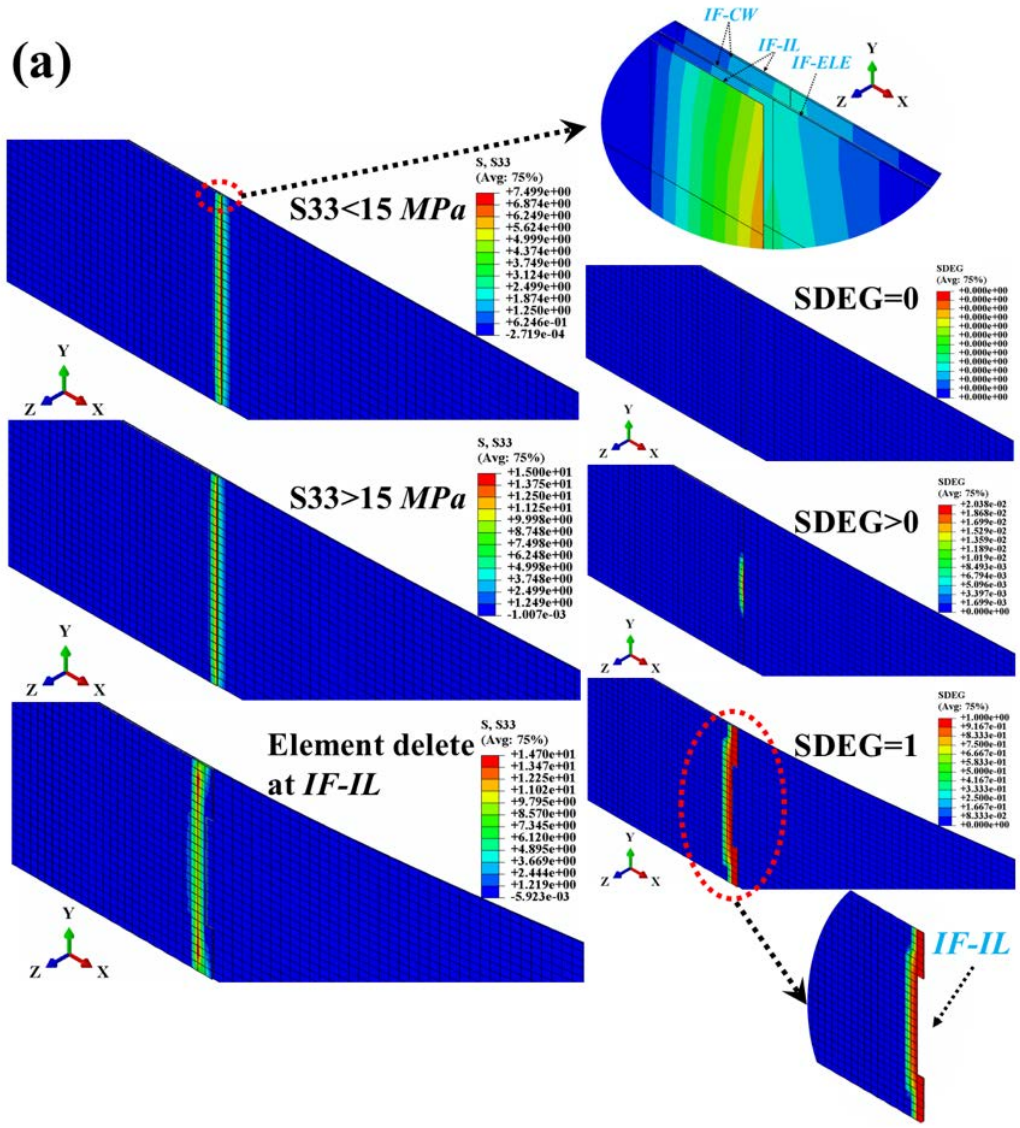

Figure 7.17 Stress distributions on sisal fiber layers and multi-layer interfaces in triple-interface *FE* model describing multi-stage cracking and fracture behaviors of laminated *SFRCs*: (a) the *IF-IL* interface cracking, (b) the elementary fiber layer *ELE* breakage, (c) the *IF-ELE* interface cracking, (d) the P/S1 layer of cell wall for the inner elementary fiber breakage and (e) the *IF-CW* interface cracking.

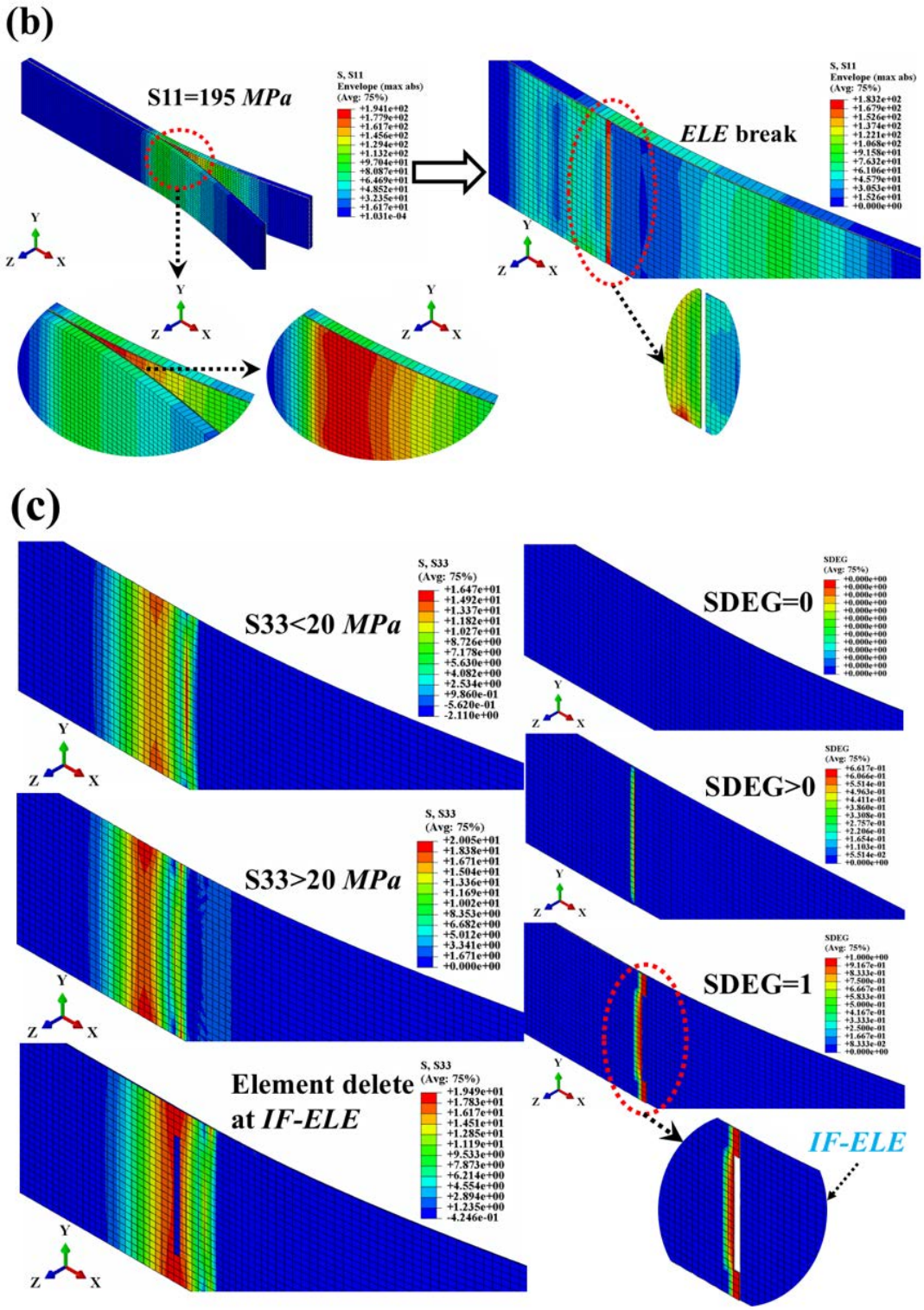

Figure 7.17 (continued).

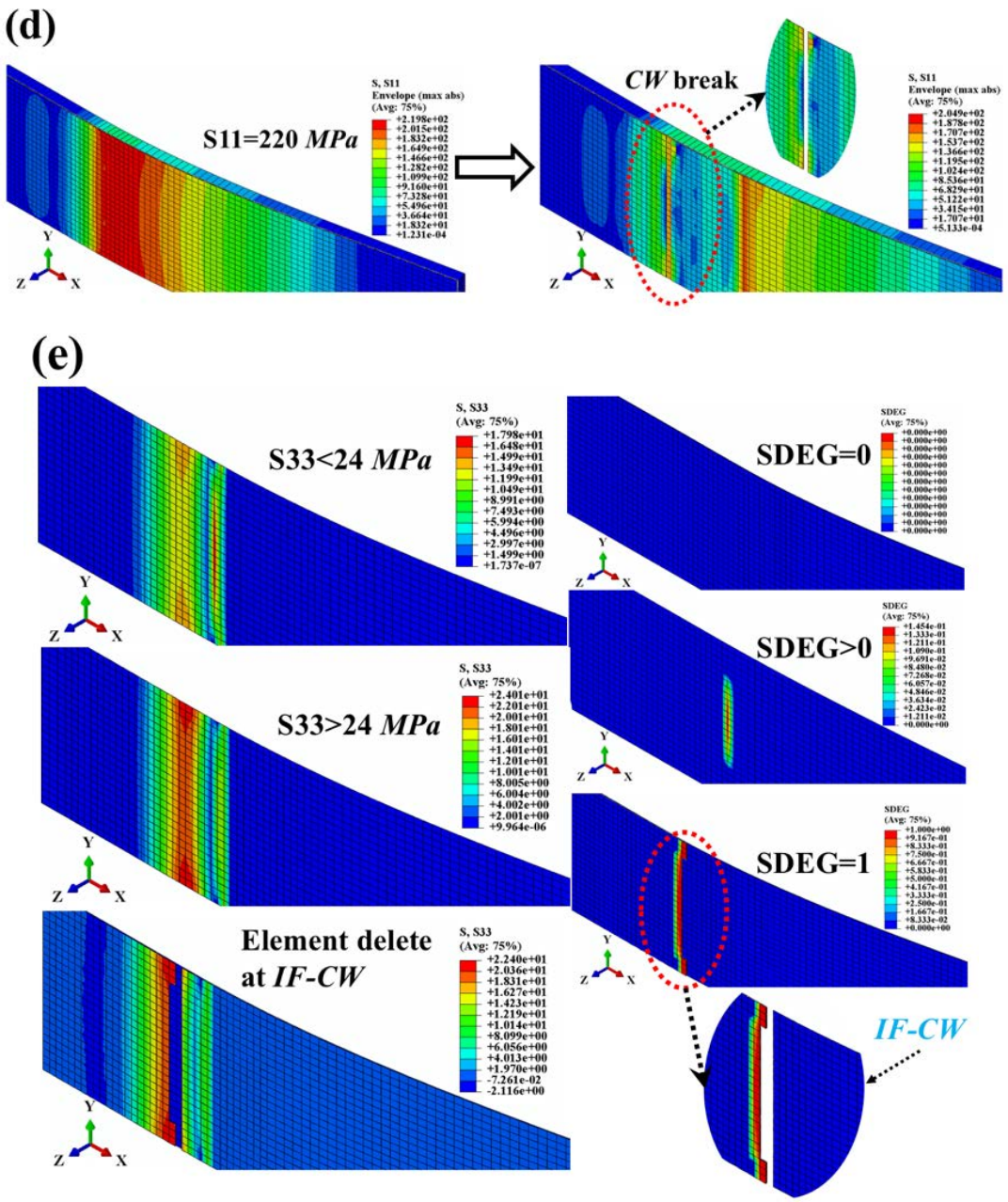

Figure 7.17 (continued).

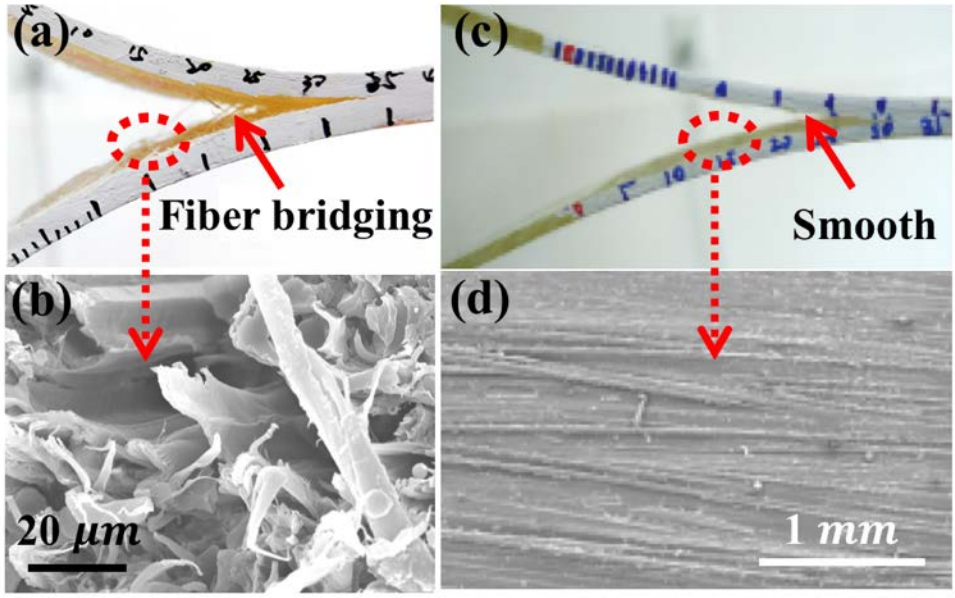

Figure 7.18 (a) and (c) Macroscopic and (b) and (d) *SEM* photographs of laminated *SFRCs* ((a) and (b)) and *GFRCs* ((c) and (d)).

Firstly, **Figure 7.17** (a) presents the distributions of the shear stress nephogram (S33) and damage factor (SDEG) on the *IF-IL* interface from non-cracking (SDEG=0), initial-cracking (SDEG>0) to partial-cracking (SDEG=1 for partial cohesive element) by simulating the triple-stage cracking process of laminated *SFRCs* in *FE* model. The cracking behavior of the *IF-IL* interface occurred first which was mainly due to the lower interfacial strength of the *IF-IL* interface ($\tau_{n1}^{c}/\tau_{s1}^{c}/\tau_{t1}^{c}$=15 MPa). It can be observed that the normal stress distribution around the delamination front in the *DCB* specimen started to propagate from the center of the specimen at first and then, spread toward both sides. Therefore, the maximum value of the normal stress was at the center of the specimen. The delamination growth behavior was characterized by the shape of an arc produced at the crack front, which was very well measured by the *DCB* experimental method. Then the maximum value moved from the center to the sides with an increase of the opening displacement, at final, the stress reached nearly

constant values. When the interfacial stress did not reach the interfacial strength of the composite laminate (t_{11}^{i}=60 s), the stress concentration at the crack tip was weaker. With the continuous increase of applied displacement, the stress concentration at the crack tip rose, then the interfacial cohesive element began to damage (SDEG>0) when the interfacial shear stress was equal to the interfacial strength (t_{12}^{i}=100 s). When the interfacial fracture energy exceeded the critical energy release rate (G_1^C=0.672 kJ/m^2), the damage factor SDEG of partial cohesive element reached to 1. The damage of the cohesive element slowly propagated, that is, the cracking behavior of the *IF-IL* interface occurred. The damage factor SDEG of a certain number of cohesive elements at the *IF-IL* interface was equal to 1 at t_{13}^{i} (386 s), indicating that these cohesive elements completely damaged and no longer have load-bearing capacity, that is, partial cracking happened on the *IF-IL* interface.

At this time (t_{11}^{f}=386 s), since the axial stress of the elementary fiber layer *ELE* reached its axial tensile strength (195 MPa), as shown in **Figure 7.17** (b), the elementary fiber layer broke. **Figure 7.17** (b) exhibits the distributions of stress nephogram on the elementary fiber layer *ELE* from non-fracture to complete-fracture by simulating the triple-stage fracture process of laminated *SFRCs* in *FE* model. It can be seen from the figure that the stress of the elementary fiber layer *ELE* at the crack front was the largest, while the stress away from the crack tip gradually decreased, which was the reason for the breakage of the elementary fiber layer occurred at the position of crack propagation front.

Secondly, with further increase of the applied displacement (t_{21}^{i} =392 s), the interfacial stress the *IF-ELE* interface increased and the cracking behavior of the *IF-ELE* interface started from the location of the breakage of the elementary fiber layer at t_{22}^{i} (395 s). **Figure 7.17** (c) illustrates the distributions of the shear stress nephogram (S33) and damage factor (SDEG) on the *IF-ELE* interface from non-cracking (SDEG=0), initial-cracking (SDEG>0) to partial-cracking (SDEG=1 for partial cohesive element) by simulating the triple-stage cracking process of laminated *SFRCs* in *FE* model. Similarly, when the interfacial fracture energy exceeded the critical energy release rate (G_2^C =1.070 kJ/m^2), the damage factor SDEG of partial cohesive element reached to 1. The cracking behavior of the *IF-ELE* interface occurred and the crack propagated. The damage factor SDEG of the *IF-ELE* interface for a certain number of cohesive elements had a value of 1 at t_{23}^{i} (426 s), indicating that partial cracking appeared on the *IF-ELE* interface.

Subsequently, as shown in **Figure 7.17** (d), the P/S1 layer of cell wall for the inner elementary fiber broke due to its axial stress reached its axial tensile strength (220 MPa) at t_{21}^{f} (426 s). **Figure 7.17** (d) displays the distributions of stress nephogram on the P/S1 layer of cell wall for the inner elementary fiber from non-fracture to complete-fracture by simulating the triple-stage fracture process of laminated *SFRCs* in *FE* model.

In general, the main compositions as the matrix of the plant fiber cell wall are hemicellulose and pectin. Finally, by continually applying the displacement (t_{31}^{i}=431 s), the interfacial stress of the *IF-CW* interface rose. Since, the matrix between the micro-fibrils was the weakest point and became the initiation point for cracks, the cracking behavior of the *IF-CW* interface could be seen from the breakage of P/S1 layer of cell wall for the inner elementary fiber at t_{32}^{i} (437 s). Different cell wall layers separated as the crack propagated. **Figure 7.17** (e) shows the distributions of the shear stress nephogram (S33) and damage factor (SDEG) on the *IF-CW* interface from non-cracking (SDEG=0), initial-cracking (SDEG>0) to partial-cracking (SDEG=1 for partial cohesive element) by simulating the triple-stage cracking process of laminated *SFRCs* in *FE* model. In the same way, when the interfacial fracture energy exceeded the critical energy release rate (G_3^C=1.299 kJ/m^2), the damage factor SDEG of partial cohesive element reached to 1. The cracking behavior of the *IF-CW* interface occurred. When the interfacial fracture energy reached the propagated fracture toughness (G_f^C=1.514 kJ/m^2), about at t_{33}^{i} (470 s), the stable propagation occurred at the pre-set cracking zone of the *IF-CW* interface and the cohesive elements continued to be damaged.

The results obtained from the previous section demonstrated that the Mode I *ILFT* of laminated *PFRCs* (i.e. *SFRCs*) was higher than that of laminated *AFRCs* (i.e., *GFRCs*). A completely different fracture surfaces for *SFRCs* specimens compared to *GFRCs* have been observed. More coarse and jagged delaminated surfaces can be seen from the macroscopic fracture morphologies (**Figure 7.18** (a)) of *SFRCs* during the *DCB*

test and the crack propagation in the laminate was accompanied by extensive remarkable fiber bridging. Meantime, it could be clearly observed with the aid of *SEM* (**Figure 7.18** (b)) that a large number of sisal technical fiber and micro-fibrils were pulled out and fractured and the cell wall of elementary fiber separated due to the fiber bridging effect, presenting a complex microscopic failure mode. Study on the *AFRCs* illustrated that very clean and relatively smooth delamination surfaces with almost no fiber bridging, pulling-out and fracture for the *GFRCs* specimens were observed due to the regular structure of glass fiber (**Figure 7.18** (c) and (d)). Consequently, this difference means that an easier path for crack propagation in the *GFRCs* was expected, while more tortuous path for that in *SFRCs*. Additionally, this phenomenon has been correlated with the structure of sisal fiber and the failure behavior of *SFRCs*. Unidirectional glass fiber fabrics are made of uniform and smooth glass fiber filaments that arranged in parallel, presenting a single layer fracture and few fibers bridging. Compared to glass fibers, sisal fibers possess a multi-layer and multi-scale structure. Sisal fibers are not uniform in diameter, and produce a multi-structure of single technical fiber, elementary fibers, cell walls and micro-fibrils, which is more likely to form fiber bridging effect. This structure allows the formation of good fiber bridging and fiber entanglement between the unidirectional sisal fiber fabrics. When the peel stress perpendicular to the in-plane direction was applied on the *SFRCs*, the fiber bridging and fiber entanglement between sisal technical fibers and the breakage of the cell wall and the pulling-out of micro-fibrils in sisal fiber all delayed the failure of the interface and enhanced the resistance ability of interfacial crack propagation, which could prolong the crack propagation path evidently, contributing to the improvement of the Mode I *ILFT* of the composite. The Mode I interlaminar cracks

tend to propagate along the interface within the pre-crack first. Therefore, the typical interlaminar cracking failure can be observed in *AFRCs*. The fiber surface was smooth and the surface structure of the fiber itself was not damaged. Whereas, during the process of crack propagation for *PFRCs*, the multi-layer interfaces in *PFRCs* made the crack not only propagate along the *IF-IL* interface but also along the *IF-ELE* and *IF-CW* interface. The structure of elementary fibers would be damaged and splitting failure along fibers in cell wall layer occurred. Thus, the occurrence of the failure in the *IF-ELE* and *IF-CW* interface resulted in the change of the failure mode from the interlaminar cracking to the damage of the fiber inherent structure and interface. The results on the interfacial failure modes in the *DCB* experiments are consistent with those obtained from single fiber pull-out tests, verifying the effect of the multi-layer interfaces on the failure behaviors of *PFRCs*.

Furthermore, although the basic mechanical properties (i.e., tensile properties) of *PFRCs* are lower than those of *AFRCs*, the interlaminar properties of *PFRCs* present distinct performance. A large amount of fiber bridging, pulling-out and fracture induced by the rough surface and multi-layer and multi-scale structural characteristics of plant fibers during the *DCB* test of *PFRCs* can effectively hinder and delay the growth of the crack and lead to more energy dissipation during delamination progress. The existence of the multi-layer interfaces played an important role in the way of delamination crack path and the interlaminar toughening effect. The multi-layer interfaces made in-plane crack propagation path more tortuous, which delayed the progress of crack growth and induced trans-layer phenomenon. Consequently, the

damage of the fiber structure itself and fiber bridging effect dissipated massive energy, which led to the increased Mode I *ILFT* of *PFRCs*.

Overall, it can be seen from the above studies that relying on illustrating the stress variations during the process of Mode I interlaminar cracking for laminated *PFRCs* and analyzing the mechanisms of multiple interfacial fracture behaviors, it was found that the existence of multi-layer interface made the failure mode of *PFRCs* different from that of *AFRCs* and increased the normal stress values of in-plane and interfacial cohesive regions of *PFRCs*. The higher interfacial normal stress of the internal interface of the *SFRCs* made the resistance ability of crack propagation improved, which was beneficial to improve the *ILFT* of the final composite laminate. The multi-layer damage in the meso- and micro-scale can effectively enhance the resistance ability of interlaminar crack propagation in *PFRCs* resulting in the improvement of the *ILFT* of laminated *PFRCs*.

7.7. Summary

The single fiber pull-out experimental measurement, theoretical calculation and numerical simulation performed in the previous chapters have characterized the multi-layer interface properties of *PFRCs* in the mesoscopic and microscopic scale. Finally, this chapter further explored the multiple-interface fracture behaviors of laminated *PFRCs* in the macroscopic scale using a virtual *DCB* experiment. The effect of multi-layer and multi-scale structure on their macroscopic interfacial properties (*ILFT*) and failure behaviors was determined and the delamination propagation of *PFRCs* was

analyzed. The unique interfacial failure modes caused by the presence of multiple interfaces and the change of the crack propagation path were discussed. Some accomplishments and issues investigated in this chapter are summarized in the following:

(1) The Mode I *ILFT* of composite laminates of continuous unidirectional sisal fiber and epoxy matrix was experimentally and numerically investigated. The Mode I interlaminar energy release rate of the *PFRCs* was experimentally determined through *DCB* test. Referring to the *DCB* experiment, a simulation procedure to predict the *ILFT* of *PFRCs* was proposed and a *3D FE* model of *DCB* specimen considering the multiple interface characteristics of *PFRC*s was established via *ABAQUS* software to construct the geometrical model with the multi-scale interfacial regions. Combination of the results obtained by nanoindentation techniques, single fiber pull-out experiments, tensile and *DCB* tests of the composites, as well as *CZM* interfacial parameters identified in the single fiber pull-out simulation, the *CZM* was inserted into the crack front of the *FE* model employing the concept of asymptotic homogenization and equivalent interface in the meso-mechanics of the composite material. The Mode I interlaminar fracture behavior of multi-interface *PFRCs* was described, and the *FE* model of the Mode I *ILFT* of *PFRCs* with multi-layer and multi-scale structure was proposed.

(2) The Mode I interlaminar cracking process of *PFRC* laminate was modelled and calculated with the proposed trilinear traction-separation cohesive law, using cohesive elements with a nonlinear softening law in order to model the large-scale fiber

bridging occurred during delamination. Through a series of parameter studies, the multi-interface toughness values of *PFRCs* were determined. Good consistency between the numerical simulation and the experiment results in the curves of force-crack opening displacement, strain energy release rate-crack length and crack length-opening displacement verified the efficiency of *CZM* in modelling the multi-layer failure behaviors of laminated *PFRCs*. The experimental findings and the results of this work suggest that the introduce of multi-layer interface for plant fiber was effective and can enhance the Mode I critical strain energy release rate (that is, *ILFT*) of their composite laminates. And comparing with the results of *FE* model with single interface established in the present chapter, it is crucial to consider the effects of in-plane fiber bridging to have an accurate prediction of the values of Mode I *ILFT* for the *PFRC* with hierarchical structure, showing consistent results with experiments.

(3) Furthermore, the stress variations during the process of Mode I interlaminar cracking for laminated *PFRCs* were illustrated to analyze the mechanisms of multiple interfacial fracture behaviors. It is found that the existence of multi-layer interface increases the normal stress values of in-plane and interfacial cohesive regions of *PFRCs*. The multi-layer damage in the meso- and micro-scale can enhance the resistance ability of interlaminar crack propagation in *PFRCs* resulting in the improvement of the *ILFT* of laminated *PFRCs*.

To sum up, the relationship between the microscopic structural characteristics of the *PFRCs* and the macroscopic interfacial mechanical properties (*ILFT*) were established relying on the combination of the *CZM* of composites in the meso-mechanics theory

and the interlaminar fracture *FE* numerical model at the macro-scale. The results of this chapter can help to deepen the understanding of the material behavior and interlaminar fracture mechanism of multi-layer and multi-scale *PFRCs*, which will assist in the development of larger practical engineering applications for the *PFRCs*.

.

CHAPTER 8

Conclusions and Recommendations for Future Research

8.1. Concluding remarks

To promote more widely practical engineering applications of *PFRCs*, researches on the structure design and optimization of plant fiber itself have been thrust into the attention of global scholars, to obtain the *PFRCs* with high performance by fully utilizing the designability of composite materials. Experience has verified that the interface is a key factor in controlling the mechanical properties of composite materials, including *PFRCs*. However, plant fibers with cellulose as the main chemical composition present strong hydrophilic properties, when manufacturing composites with hydrophobic matrix, weak interfacial bonding will be formed between the fiber and matrix. Thus, the limited benefits of the mechanical properties of *PFRCs* have become the bottleneck for their large-scale industrial applications,

which mainly caused by neglecting the existence of hierarchical structure of plant fibers. Compared with traditional synthetic fibers with the uniform structure, plant fibers possess the rough surface, non-uniform diameter, porous structure and complex multi-layer and multi-scale structure. In addition to possess the same mesoscopic interface as traditional *AFRCs*, *PFRCs* also possess the microscopic and nanoscopic interface, which leads to different interfacial bonding and fracture behavior, complex damage mechanisms and failure modes as well as the unique interfacial mechanical and physical performances relative to *AFRCs*. Moreover, existing theoretical researches on *PFRCs* still followed the similar modelling methods for *AFRCs* and concentrated on the analysis of the interfacial failure between fiber and matrix, ignoring the influence of the multi-layer structure of plant fibers on the interfacial failure behaviors of *PFRCs*.

This thesis emphasizes on the unique multi-stage failure behaviors of plant fibers and *PFRCs* and aims to gain insight into the failure mechanisms by combining the theoretical model with the experimental characterization. Specifically, to serve the task of interfacial design of *PFRCs*, this thesis systematically developed and proposed a series of experimental techniques (nanoindentation and *nano-DMA*, single fiber pull-out measurement and *AE* characterization) and analysis methods (double and triple interfaces model and *ABAQUS* simulation) for characterizing *PFRCs* with multi-layer and multi-scale structures. In this thesis, to address the problems of the effects of the multi-layer and multi-scale structure on the interfacial adhesion behaviors and the interfacial stress transfer mechanisms of *PFRCs*, the main

achievements and original contributions of this thesis can be briefly summarized as follows.

(1) The hierarchical organization of plant fibers leads to multi-interface regions in their reinforced composites. The multi-layer and multi-scale structure of the sisal fibers makes their reinforcing composites present the multi-stage interfacial failure behaviors. The nanoscopic mechanical properties, including elastic modulus and hardness of the epoxy matrix and cell wall layers of the sisal fibers and the interfacial mechanical properties of the three types of interfaces, were quantitatively measured by applying the nanoindentation technique. The transition zones, i.e., the multi-layer interfaces of *SFRCs*, were identified by a series of indents derived from matrix to each layer of sisal fiber cell walls. Their multi-layer structure can endow *PFRCs* with a superior ability, compared with *CFRCs* or *GFRCs*, for energy absorption and dissipation when subject to fatigue. The abilities of energy dissipation of the multi-layer interfaces and the multi-layer interfacial failure sequence and interfacial failure load were respectively illustrated and ascertained by combining the single-step and multi-step nanoindentation measurements at various indentation loads. Results from the single-step nanoindentation experiments indicated the distinct mechanical properties of the constituents of *SFRCs*, which featured a multi-layer and multi-scale structure with different modulus and hardness. The results also suggested the capacity of energy dissipation for the *IF-FM* was weaker than that for the *IF-ELE* and *IF-CW* due to the highest value regarding hardness to reduced elastic modulus of *IF-FM*. The results obtained from the multi-step nanoindentation experiments on the three interfaces showed a material hardening phenomenon, and the degrees of hardening

were different among the three interfaces. The results from the cyclic loading nanoindentation and further observations from *SEM* revealed a multi-stage failure behavior of *SFRCs*. The interface between the sisal fibers and epoxy matrix with a weaker bonding firstly underwent the crack initiation and propagation, then the cracks occurred at the *IF-ELE* with increasing cyclic loading, and finally the cracks presented on the *IF-CW*. The evaluation of nano-fatigue properties of the multiple interfaces within *SFRCs* and their differences in the nanofatigue behaviors are achieved by using the cyclic loading with varying applied indentation loads and oscillation frequencies. The change of the oscillation load and oscillation frequency can lead to the different time on occurring the nanofatigue failures. At the same oscillation load and oscillation frequency, the initiation and propagation of cracks at the three types of interface are also different. This phenomenon can be helpful to explain the fatigue damage accumulation rate and crack propagation mechanism of *PFRCs* in fatigue tests compared with traditional *AFRCs*. In summary, the existence of multiple interfaces of *SFRCs* makes them present unique multi-layer and multi-scale mechanical properties and failure behavior.

(2) The multiple interfacial debonding behaviors of *SFRCs* were experimentally investigated through single fiber pull-out test in conjunction with *AE* monitoring. Due to the multi-layer and multi-scale structure of sisal fibers, their reinforced composites have different interfacial failure mechanisms from those of *CFRCs* or *GFRCs*, presenting the complex interfacial failure mechanisms. The unique multi-stage interfacial failure behaviors of *SFRCs* were observed in the single fiber pull-out experiments. The residual pull-out strength of *SFRCs* was found to gradually decrease

when subject to tensile loading. The multi-interface debonding processes of *SFRCs*, including the debonding between the technical fiber and matrix, that between the elementary fibers and that between the cell walls, can be identified by *AE* signal characteristics. The measured *AE* features are coupled with supplementary information such as microstructural observations of the test specimen. Furthermore, *EMD* is in conjunction with usage of *HHT* spectrum of the signal to provide accurate time-frequency signal characteristics and make it possible to monitor the multi-interface debonding and multi-stage fiber components breakage behaviors using *AE* signals in real practice. Based on this, this paper proposed an effective method for accurately assessing the multi-layer and multi-scale pull-out behavior of *SFRCs* and determining the failure mode relying on the distribution of frequency and energy throughout the single sisal fiber pull-out process, which could be useful with the aim of failure mechanisms associated with multiple interface failure identification. The probability of technical fiber, elementary fiber and micro-fibrils pull-out was evaluated by employing statistical analysis, which showed the technical fiber and elementary fiber were more prone to be pulled out from the matrix while micro-fibrils can only occasionally be pulled-out from cell wall. An appropriate embedded fiber length for the *SFRCs* could not only result in the debond between technical fiber and matrix and pull-out behaviors of technical fiber, but also lead to the multi-stage debond and pull-out behaviors among technical fiber, elementary fibers and cell wall micro-fibrils.

(3) A double-interface model that incorporated the effects of interfacial roughness was developed to adequately describe the interfacial properties and failure modes of

PFRCs from the view of theoretical investigation. The calculated and measured maximum debond stresses increased with the increase of the embedded fiber length. Good agreement was achieved between the theoretical predictions of the proposed double-interface model and the experimental measurements. The double-interface model was found to produce more accurate results than the existing single-interface model, indicating that the former provided a better description of the multi-layer and multi-scale interfacial damage mechanisms of *PFRCs*. Using the proposed model, the failure mechanisms of *PFRCs* in the pull-out tests were analyzed in further detail. During the Process 1, the shear stress of the *IF-FM* was larger than that of the *IF-ELE*, so that debonding first occurred at the *IF-FM*. During the Process 2, the shear stresses in the debonded region of the *IF-ELE* became larger than that of the *IF-FM*, which resulted in the debonding of the *IF-ELE*.

(4) An appropriate three-interface *FE* model utilizing cohesive damage modelling is developed for the multi-layer interfacial behavior during the single sisal fiber pull-out test. The debonding process of sisal fiber with multi-layer interfaces was successfully simulated by using the cohesive force model and the deactivate and reactivate element technique in *ABAQUS*. The solving methods of *ABAQUS* standard and *ABAQUS* dynamic explicit were combined to simulate the process of multi-stage debonding and fracture of single sisal fiber. And a mixed ‘cohesive’ and ‘Coulomb-friction’ model was proposed to simulate the entire pull-out process. With the use of the proposed numerical model, a series of interfacial parameters were studied, analyzing the mechanism of the influence of the interface properties on the pull-out behavior. And then the multi-layer and multi-scale interfacial failure criteria of the *SFRCs* were

determined. Meantime, the applied stress-displacement curves have revealed that numerical analysis and experimental results can reach a good agreement, showing the validity of the developed triple-interface *FE* method. The interfacial strength varies with the embedded fiber length of sisal fiber, which is related to the multi-interface failure modes of *SFRCs*. Finally, the stress distributions of the components in *SFRCs* (i.e., sisal fibers, matrix and multi-layer interfaces) can be obtained via the numerical model calculation to present precise derivation of the interface stresses. The status of the interfacial failure during the pull-out process was obtained. The multi-interfacial failure process and mechanisms of *SFRCs* in the pull-out tests were further revealed and accounted for. Therefore, compared with the accuracy of the double-interface model built in the last chapter for predicting the multi-stage fracture behavior of *PFRCs*, the triple-interface *FE* model with one more hierarchical structure could more comprehensively and intuitively describe and analyze the complex multi-layer and multi-scale interfacial bonding conditions and interfacial failure behaviors of *PFRCs* for providing more accurate solutions and precise derivation of the interface stresses.

(5) Finally, the multiple-interface fracture behaviors of laminated *PFRCs* in the macroscopic scale was explored using a virtual *DCB* experiment. The effect of multi-layer and multi-scale structure on their macroscopic interfacial properties (*ILFT*) and failure behaviors was determined. The unique interfacial failure modes caused by the presence of multiple interfaces and the change of the crack propagation path were discussed. Referring to the *DCB* experiment, a *3D FE* model considering the multiple interface characteristics of *PFRC*s was established via *ABAQUS* software to construct the geometrical model with the multi-scale interfacial regions. Combination of the

results obtained by nanoindentation techniques, single fiber pull-out experiments, tensile and *DCB* tests of the composites, as well as *CZM* interfacial parameters identified in the single fiber pull-out simulation, the *CZM* was inserted into the crack front of the *FE* model employing the concept of asymptotic homogenization and equivalent interface in the meso-mechanics of the composite material. The Mode I interlaminar cracking process of *PFRCs* was calculated with the proposed trilinear traction-separation cohesive law. A series of parameter studies determined the multi-interface toughness values of *PFRCs*. Good consistency between the numerical simulation and the experiment results in the curves of force-crack opening displacement, strain energy release rate-crack length and crack length-opening displacement verified the efficiency of *CZM* in modelling the multi-layer failure behaviors of laminated *PFRCs*. The experimental findings and the results of this work suggest that the introduce of multi-layer interface for plant fiber was effective and can enhance the Mode I critical strain energy release rate (that is, *ILFT*) of their composite laminates. Furthermore, the stress variations during the process of Mode I interlaminar cracking for laminated *PFRCs* were illustrated to analyze the mechanisms of multiple interfacial fracture behaviors. It is found that the multi-layer damage in the meso- and micro-scale can effectively enhance the resistance ability of interlaminar crack propagation in *PFRCs* resulting in the improvement of the *ILFT* of laminated *PFRCs*.

In short, the present thesis investigated the multi-layer and multi-scale structure of plant fibers and the effects on the interfacial failure process and mechanisms of *PFRCs* by applying the mechanical characterization techniques from nano-scale to macro-scale. This research focused on the need for interfacial engineering and the efforts to

obtain enhanced mechanical properties at the interface of *PFRCs*. The combination of experimental measurements and theoretical calculations provided excellent evidence on the multi-layer interfacial failure behaviors and macro fracture evolutions of *PFRCs* and some guidance on the interfacial structural design of *PFRCs* in the future. The results of this paper can help to deepen the understanding of the material behavior and interfacial failure and interlaminar fracture mechanism of multi-layer and multi-scale *PFRCs*, which will assist in the development of practical engineering applications for the *PFRCs* in large industrial fields. To summarize, the existence of multiple interfaces of *PFRCs*, possessing different interfacial properties, results in the unique multi-layer and multi-scale failure modes of *PFRCs*.

8.2. Problematic issues and recommendations for future research

In this thesis, the research work on the multi-layer and multi-scale interfacial behaviors of *PFRCs* has been carried out from the perspective of composite material design. In spite of the promising results reported in this thesis, there are some problematic issues and challenges remaining and being worthy of future exploration and improvements. Therefore, several future works are as following.

First, although this thesis has investigated the multi-layer interfacial failure mechanisms of *SFRCs* by the nano-scale experimental characterizations, there are some restrictions in the nanoindentation experiments, such as the shape and the size of the tip, the qualities of the prepared specimen, etc. The nanoindentation test is a

complex process from the view of mechanics. Different locations of the materials present various responses under the indenter tip. The contact areas between the indenter tip and sample change when the indenter approaches different depth of the sample, which means the boundary conditions between the indenter tip and sample vary during one measurement. Therefore, the analytical method is not capable of solving the nanoindentation problem. Numerical simulation technique considering the unique multi-layer interface of plant fibers can be used to reproduce the whole indentation process and carry out some parameter study that cannot be achieved by the nanoindentation equipment. Nanoindentation technique is expected to gain broader applications on the evaluation of nano-scale mechanical properties of other materials and can be applied to a broad spectrum of engineering practice.

Second, this thesis has achieved a profound understanding of the multi-layer interfaces of *PFRCs* through qualitative and quantitative characterization with the use of nanoindentation technology and the establishment of multi-interface theoretical model in both meso- and macro-scale. Based on the research results obtained in current study, it is suggested that in-situ *SEM* can be used to visualize the process of multi-layer interface failure of *PFRCs* in future work. Meantime, it is necessary to consider how to design the interface of *PFRCs* and extend the design principle to the development of hierarchical biomimetic composites, so as to further demonstrate the effectiveness of the approach for use in real applications.

Third, the size and shape of the elementary fibers contained in a single plant technical fiber have certain dispersibility, which brings in both the uncertain mesoscopic and

macroscopic failure behaviors. In this thesis, only the interfacial failure occurring between *IF-FM* first and those between *IF-ELE* or *IF-CW* were analyzed. In fact, fiber treatments can improve the adhesion property in *IF-FM*, which may result in the internal structure failure of plant fibers. Thus, for the *PFRCs* with multi-layer interfaces, different fiber surface treatments not only affect the interfacial mechanical and fatigue properties and failure mechanisms between the plant fibers and the matrix, but also have an impact on the failure behavior of the internal interfaces of the plant fibers. Therefore, knowledge of the multi-layer interface failure mechanism of untreated *PFRCs* described in the present study is extremely important in understanding the static and dynamic mechanical behavior of the multi-layer interfaces of the *PFRCs* within various treatments based on the static and dynamic nanoindentation techniques, illustrating the effect of the fiber surface treatment on the improvement of the multiple interfaces of the *PFRCs*. Future study also could focus on establishing the corresponding theoretical model and developing interfacial failure criteria for this condition.

In addition, plant fibers possess the complex chemical composition. One interesting issue that this thesis does not address is the effect of various chemical bonds within the multi-layer interfaces of plant fibers on the interface failure behaviors of *PFRCs*, which cannot be well described by the proposed mechanical analysis. In fact, the best way to resolve this issue is molecular dynamics method, which can consider the distinct chemical bonding effect of plant fibers compared with that of synthetic fibers when revealing the multi-layer interfacial failure mechanisms of *PFRCs*. And the interfacial parameters obtained from the molecular dynamics calculation by

considering the chemical bonding force can facilitate the mechanical analysis of the multi-interfacial failure behaviors of *PFRCs* involving in synergistic effect of both physical and chemical bonding. Therefore, this aspect deserves more attention in the future theoretical studies.

Finally, more advanced algorithms or numerical tools, capable of considering practical working conditions is necessary to develop. More structural parameters, including the lumen size, fiber shape, fiber diameter, fiber component ratio, surface roughness, etc., need to be considered in the *FE* calculation. Other plant fibers also should be evaluated, so as to fulfil the large-scale real applications of *PFRCs* in the fields of aerospace, railway transportation, automotive engineering and civil infrastructures. Actually, so far most of the studies related to *PFRCs* are conducted in the laboratory-environment. Some efforts are required to transfer the results from the small-scale to medium or even large-scale production. To summarize, the interface regions in the real composites can be immensely complex and variable, thus, future study should focus on enhancing the adaptability of the developed experimental or theoretical technique to more complex structures to demonstrate the suitability of the proposed methods in the future applications with real engineering assets.

APPENDICES

Appendix A Stress transfer in the bonded regions of Processes 1 and 2

In order to satisfy the equilibrium conditions between the axial and shear stresses in the cylindrical shell of matrix and in that of technical fiber, respectively, the related equations could be derived as **[61]**:

$$\begin{aligned}&\partial\left(\sigma_m{}^{z}(z)\right)/\partial z+\partial\left(\tau_m{}^{rz}(r,z)\right)/\partial r+\tau_m{}^{rz}(r,z)/r=0\\&\partial\left(\sigma_{f1}{}^{z}(z)\right)/\partial z+\partial\left(\tau_{f1}{}^{rz}(r,z)\right)/\partial r+\tau_{f1}{}^{rz}(r,z)/r=0\end{aligned} \qquad \textbf{(A.1)}$$

Hence, the shear stresses in the matrix ($\tau_m{}^{rz}(r,z)$) and in the technical fiber ($\tau_{f1}{}^{rz}(r,z)$) can be respectively expressed as a function of the interfacial shear stresses, namely $\tau_{i1}{}^{rz}(z)$ and $\tau_{i2}{}^{rz}(z)$, with given boundary conditions ($\tau_m{}^{rz}(a_1,z)=\tau_{i1}{}^{rz}(z)$, $\tau_m{}^{rz}(b,z)=0$ and $\tau_{f1}{}^{rz}(a_2,z)=\tau_{i2}{}^{rz}(z)$, $\tau_{f1}{}^{rz}(a_1,z)=\tau_{i1}{}^{rz}(z)$).

$$\tau_m{}^{rz}(r,z)=\gamma\left(b^2-r^2\right)/(a_1 r)\tau_{i1}{}^{rz}(z) \qquad \textbf{(A.2)}$$

$$\tau_{f1}{}^{rz}(r,z)=-(1+\eta)\left(a_2{}^2-r^2\right)/(a_1 r)\tau_{i1}{}^{rz}(z)+\eta\left(a_1{}^2-r^2\right)/(a_2 r)\tau_{i2}{}^{rz}(z) \qquad \textbf{(A.3)}$$

Equation (A.4) is obtained after combining **Equations (5.3)** and **(A.2)** with the boundary condition of axial displacement continuity at the bonded interface ($u_m{}^z(a_1, z) = u_{f1}{}^z(a_1, z)$) and differentiation of shear stress with respect to z.

$$d\tau_{i1}{}^{rz}(z)/dz = E_m/\left((1+\nu_m)\left[2\gamma b^2/a_1\ln(b/a_1) - a_1\right]\right) \cdot\left[\varepsilon_m{}^z(b, z) - \varepsilon_{f1}{}^z(a_1, z)\right] \quad \textbf{(A.4)}$$

It is assumed that the technical fiber and matrix or the elementary fibers in between remain in contact during deformation, which should satisfy the continuity of radial displacement at the interface ($\varepsilon_{f1}{}^\theta(a_1, z) = \varepsilon_m{}^\theta(a_1, z)$ and $\varepsilon_{f2}{}^\theta(a_2, z) = \varepsilon_{f1}{}^\theta(a_2, z)$ according to **Equations (5.1)** and **(5.2)**). Then the radial stresses q_1^*, q_2^* and q_1^{**}, q_2^{**} for Processes 1 and 2 are subject to the stress boundary conditions ($\sigma_{f1}{}^r(a_1, z) = \sigma_m{}^r(a_1, z) = q^*$, $\sigma_{f1}{}^\theta(a_1, z) = -2\eta q^{**} + (1+2\eta)q^*$, $\sigma_m{}^r(b, z) = 0$, $\sigma_m{}^\theta(a_1, z) = -(1+2\gamma)q^*$, $\sigma_{f1}{}^r(a_2, z) = q^{**}$, $\sigma_{f2}{}^r(a_2, z) = \sigma_{f2}{}^\theta(a_2, z) = q^{**}$, $\sigma_{f1}{}^\theta(a_2, z) = -(1+2\eta)q^{**} + 2(1+\eta)q^*$, and $\sigma_m{}^\theta(b, z) = -2\gamma q^*$) and given in **Equation (A.5)**.

$$\begin{pmatrix} q_1^{*} \\ q_2^{*} \end{pmatrix} = \left(A_8 + A_9\right)/\left(1+\eta\right)\left[\sigma_{f1}{}^{z}(z) + \eta\sigma_{f2}{}^{z}(z)\right]$$
$$-A_4\left(\begin{pmatrix} 1 \\ \eta/(1+\eta) \end{pmatrix}\gamma_m\sigma - E_m\left(\alpha_m - \alpha_{f1}\right)\Delta T\right)$$
$$\begin{pmatrix} q_1^{**} \\ q_2^{**} \end{pmatrix} = A_8\sigma_{f1}{}^{z}(z) + A_9\sigma_{f2}{}^{z}(z) \qquad \textbf{(A.5)}$$
$$-A_4\left(\begin{pmatrix} 1 \\ \eta/(1+\eta) \end{pmatrix}\gamma_m\sigma - E_m\left(\alpha_m - \alpha_{f1}\right)\Delta T\right)$$

where the coefficients A_4, A_8 and A_9 are expressed in Appendix B and C. Finally, the differential equations for the axial technical fiber stress $\sigma_f{}^{z}(z)$ during Processes 1 and 2 are respectively obtained in **Equation (A.6)** by combining **Equations (5.3)-(5.5), (5.15)** and **(A.4)-(A.5)**.

$$d^2\sigma_f{}^{z}(z)/dz^2 = A_3\left(\sigma_f{}^{z}(z) + (1+\eta)A_1/\eta\sigma + A_2\right)$$
$$d^2\sigma_f{}^{z}(z)/dz^2 = A_3\left(\sigma_f{}^{z}(z) + A_1\sigma + A_2\right) \qquad \textbf{(A.6)}$$

The boundary conditions ($\sigma_f{}^{z}\left(l_{f1}\right) = \sigma_{lf1}$, $\sigma_f{}^{z}(L) = 0$ for Process 1 and $\sigma_f{}^{z}\left(l_{f2}\right) = \sigma_{lf2}$, $\sigma_f{}^{z}(L) = 0$ for Process 2) are used to solve **Equation (A.6)** and the stress distributions are expressed as **Equations (5.7)** and **(5.16)**.

Appendix B Stress transfer in the debonded regions of Processes 1 and 2

For the debonded region during Process 1, q_{01} can be derived as **Equation (B.1)** by considering the continuity of circumferential strains in **Equation (5.1)**.

$$q_{01} = A_4E_m\left(\alpha_m - \alpha_{f1}\right)\Delta T \qquad \textbf{(B.1)}$$

in which α_{f1} and α_m are the thermal expansion coefficients of the technical fiber and matrix, respectively. ΔT is the change of the temperature, and $\alpha = E_m / E_{f1}$ and $A_4 = 1/\left(\alpha - \alpha\nu_{f1} + 1 + 2\gamma + \nu_m\right)$.

$q_{a1}(z)$, $q_{R1}(z)$ for the debonded region during Process 1 and $q_{a2}(z)$, $q_{R2}(z)$ for Part 2 of the debonded region $0 < z < l_{f2}$ during Process 2 can be respectively described as

$$\begin{aligned} q_{a1}(z) &= A_4\left(\left(\alpha\nu_{f1} + \gamma\nu_m\right)\sigma_f{}^z(z) - \gamma\nu_m\sigma\right) \\ q_{R1}(z) &= -A_4 E_m / a_1\delta_1(z) = k_1\delta_1(z) \\ q_{a2}(z) &= A_8\sigma_{f1}{}^z(z) + A_9\sigma_{f2}{}^z(z) - \eta\gamma\nu_m A_4/(1+\eta)\sigma \\ q_{R2}(z) &= -A_4 E_m / a_2\delta_2(z) = k_2\delta_2(z) \end{aligned} \tag{B.2}$$

The Fourier series $d_{n_i}(i = 1,\ 2)$ and $B_{n_i}\left(= 2/L\int_0^L \delta_i(z)\cos\left(n_i\pi z / L\right)dz\right)$ are used to express the interfacial amplitude function $d_i(z)$ and the asperities mismatch function $\delta_i(z)$ in the two processes. The relative displacements $v_i(z)$ are computed by integrating $dv_1(z)/dz = -\left(\varepsilon_{f1}{}^z - \varepsilon_m{}^z\right)$ and $dv_2(z)/dz = -\left(\varepsilon_{f2}{}^z - \varepsilon_{f1}{}^z\right)$, respectively.

$$\begin{aligned} d_i(z) &= d_{0i}/2 + \sum_{n_i=1}^{\infty} d_{n_i}\cos\left(n_i\pi z / L\right) \\ \delta_i(z) &= d_i\left[z - v_i(z)\right] - d_i(z) = B_{0i}/2 + \sum_{n_i=1}^{\infty} B_{n_i}\cos\left(n_i\pi z / L\right) \end{aligned} \tag{B.3}$$

An iterative approach was employed for determining the Fourier series coefficient B_{n1} for Process 1 and B_{n2} for Process 2. The iterative process was stopped after fulfilling the condition $\left|\left({\sigma_f}^z(z)_{i,\,i+1}-{\sigma_f}^z(z)_{i,\,i}\right)/{\sigma_f}^z(z)_{i,\,i}\right|\le 10^{-6}$.

Appendix C Coefficients of Processes 1 and 2

$$A_1=-\gamma\eta\left(1-2\nu_m\left(A_8+A_9\right)\right)/\left(\left(1+\eta\right)A_0\right) \tag{C.1}$$

$$A_2=-\left(1+2\left(\alpha\nu_{f1}+\gamma\nu_m\right)A_4\right)/A_0E_m\left(\alpha_m-\alpha_{f1}\right)\Delta T \tag{C.2}$$

$$A_3=2A_0/\left(\left(1+\nu_m\right)\left(2\gamma b^2\ln\left(b/a_1\right)-{a_1}^2\right)\right) \tag{C.3}$$

$$A_5=2\mu_1\left(\alpha\nu_{f1}+\gamma\nu_m\right)A_4/a_1 \tag{C.4}$$

$$A_6=1-2\mu_1\alpha\nu_{f1}A_4/\left(a_1A_5\right)\left(1-e^{A_5l_{f1}}\right) \tag{C.5}$$

$$\begin{aligned}A_7=&\left(2q_{01}+k_1/a_1B_{01}\right)\left(A_6-1\right)/\left(2\alpha\nu_{f1}A_4\right)\\&-\sum_{n_1=1}^{\infty}\left(\begin{array}{l}B_{n_1}2\mu_1k_1A_5L^2/\left(a_1\left({A_5}^2L^2+{n_1}^2\pi^2\right)\right)\\\cdot\left(\cos\left(n_1\pi l_{f1}/L\right)-n_1\pi/\left(A_5L\right)\sin\left(n_1\pi l_{f1}/L\right)-e^{A_5l_{f1}}\right)\end{array}\right)\end{aligned} \tag{C.6}$$

$$A_8=\left(\alpha\nu_{f1}+\gamma\nu_m\right)A_4-A_9 \tag{C.7}$$

$$A_9=\left(\nu_{f1}+2\eta\left(\alpha\nu_{f1}+\gamma\nu_m\right)A_4\right)/\left(2\left(1+\eta\right)\right) \tag{C.8}$$

$$A_0=\alpha+\gamma-2\left(\alpha\nu_{f1}+\gamma\nu_m\right)^2A_4 \tag{C.9}$$

$$U_f=1/\left(2E_{f1}\right)\int_0^L\int_0^{a_1}\left[\begin{array}{l}\left({\sigma_f}^z\right)^2+\left({\sigma_f}^r\right)^2+\left({\sigma_f}^\theta\right)^2\\-2\nu_{f1}\left({\sigma_f}^z{\sigma_f}^r+{\sigma_f}^z{\sigma_f}^\theta+{\sigma_f}^\theta{\sigma_f}^r\right)\end{array}\right]\cdot 2\pi rdrdz \tag{C.10}$$

$$U_{f2}=1/\left(2E_{f1}\right)\int_0^L\int_0^{a_2}\begin{bmatrix}\left(\sigma_{f2}{}^{z}\right)^2+\left(\sigma_{f2}{}^{r}\right)^2+\left(\sigma_{f2}{}^{\theta}\right)^2\\-2\nu_{f1}\left(\sigma_{f2}{}^{z}\sigma_{f2}{}^{r}+\sigma_{f2}{}^{z}\sigma_{f2}{}^{\theta}+\sigma_{f2}{}^{\theta}\sigma_{f2}{}^{r}\right)\end{bmatrix}\cdot 2\pi rdrdz \quad \textbf{(C.11)}$$

$$U_m=1/\left(2E_m\right)\int_0^L\int_{a_1}^{b}\begin{bmatrix}\left(\sigma_m{}^{z}\right)^2+\left(\sigma_m{}^{r}\right)^2+\left(\sigma_m{}^{\theta}\right)^2\\+2\left(1+\nu_m\right)\left(\tau_m{}^{rz}\right)^2\\-2\nu_m\left(\sigma_m{}^{z}\sigma_m{}^{r}+\sigma_m{}^{z}\sigma_m{}^{\theta}+\sigma_m{}^{\theta}\sigma_m{}^{r}\right)\end{bmatrix}\cdot 2\pi rdrdz \quad \textbf{(C.12)}$$

$$U_{f1}=1/\left(2E_{f1}\right)\int_0^L\int_{a_2}^{a_1}\begin{bmatrix}\left(\sigma_{f1}{}^{z}\right)^2+\left(\sigma_{f1}{}^{r}\right)^2+\left(\sigma_{f1}{}^{\theta}\right)^2\\+2\left(1+\nu_{f1}\right)\left(\tau_{f1}{}^{rz}\right)^2\\-2\nu_{f1}\left(\sigma_{f1}{}^{z}\sigma_{f1}{}^{r}+\sigma_{f1}{}^{z}\sigma_{f1}{}^{\theta}+\sigma_{f1}{}^{\theta}\sigma_{f1}{}^{r}\right)\end{bmatrix}\cdot 2\pi rdrdz \quad \textbf{(C.13)}$$

$$\begin{aligned}p_1&=\partial\left(H_3H_6H_8+H_4\left(H_6{}^2+H_8{}^2\right)\right)/\partial l_{f1}+\pi a_1{}^2A_0/\left(2E_m\right)H_6{}^2\sinh^2\left(\phi_1\right)\\&+H_6H_8\phi_1\sinh\left(\phi_1\right)\left(\pi a_1{}^2A_0/\left(2E_m\right)-A_3H_5-1\right)+H_5\left(\partial A_6/\partial l_{f1}\right)^2\end{aligned} \quad \textbf{(C.14)}$$

$$\begin{aligned}p_2&=2H_4\left(\partial\left(H_6H_7+H_8H_9\right)/\partial l_{f1}\right)\\&+\left(\pi a_1{}^2A_0/E_m\sinh^2\left(\phi_1\right)-2A_3H_5\cosh^2\left(\phi_1\right)\right)\left(H_6H_7+H_8H_9\right)\\&+\pi a_1{}^2A_2A_0\left(1-\cosh\left(\phi_1\right)\right)/\left(E_m\sqrt{A_3}\right)\partial\left(H_6+H_8\right)/\partial l_{f1}\\&+\partial\left(H_3\left(H_7H_8+H_6H_9\right)\right)/\partial l_{f1}+2H_5\,\partial A_6/\partial l_{f1}\,\partial A_7/\partial l_{f1}\end{aligned} \quad \textbf{(C.15)}$$

$$\begin{aligned}p_3&=\partial\left(H_3H_7H_9+H_4\left(H_7{}^2+H_9{}^2\right)\right)/\partial l_{f1}\\&+\pi a_1k_1\delta_1\left(l_{f1}\right)\left(2a_1q_{01}/\left(A_4E_m\right)-\delta_1\left(l_{f1}\right)\right)+H_5\left(\partial A_7/\partial l_{f1}\right)^2\\&+\pi a_1{}^2A_0/E_m\begin{bmatrix}A_2A_0/\sqrt{A_3}\left(1-\cosh\left(\phi_1\right)\right)\partial\left(H_7+H_9\right)/\partial l_{f1}\\+\left(A_2\right)^2+\left(A_2+A_7\right)^2/2\end{bmatrix}\end{aligned} \quad \textbf{(C.16)}$$

$$\phi_1=\sqrt{A_3}\left(L-l_{f1}\right) \quad \textbf{(C.17)}$$

$$C_1 = \left(-D_3 C_4 \mathrm{e}^{r_2 l_{f2}} - D_4 C_5 \mathrm{e}^{r_3 l_{f2}} + D_1 - A_1 - C_8\right) / \left(C_3 e^{\eta l_{f2}} - C_4 D_5 e^{r_2 l_{f2}} + C_5 D_6 e^{r_3 l_{f2}}\right) \quad \textbf{(C.18)}$$

$$C_2 = \begin{pmatrix} -D_7 C_4 \mathrm{e}^{r_2 l_{f2}} - D_8 C_5 \mathrm{e}^{r_3 l_{f2}} + D_2 - A_2 - C_9 \\ -\sum_{n_2=1}^{\infty} B_{n_2}\left(C_6 \cos\left(n_2 \pi l_{f2} / L\right) - C_7 \sin\left(n_2 \pi l_{f2} / L\right)\right) \end{pmatrix} / \left(C_3 e^{\eta l_{f2}} - C_4 D_5 e^{r_2 l_{f2}} + C_5 D_6 e^{r_3 l_{f2}}\right) \quad \textbf{(C.19)}$$

$$C_{3,\,4,\,5} = a_2 / \left(2\mu_2 A_8\right) r_{1,\,2,\,3} - A_9 / A_8 \quad \textbf{(C.20)}$$

$$C_6 = \left(n_2 \pi a_2 / \left(2\mu_2 L\right) F_1 - D_9 A_9 - k_2\right) / A_8 \quad \textbf{(C.21)}$$

$$C_7 = \left(n_2 \pi a_2 / \left(2\mu_2 L\right) D_9 + A_9 F_1\right) / A_8 \quad \textbf{(C.22)}$$

$$\begin{pmatrix} C_8 & C_9 \end{pmatrix} = \begin{pmatrix} \eta\gamma\nu_m A_4 / (1+\eta) - A_9 F_2 & A_9 F_3 - q_{01} - k_2 B_{02} / 2 \end{pmatrix} / A_8 \quad \textbf{(C.23)}$$

$$\begin{pmatrix} D_3 \\ D_4 \end{pmatrix} = \begin{pmatrix} 1/\mathrm{e}^{r_2 l_{f1}} & 0 \\ 0 & -1/\mathrm{e}^{r_3 l_{f1}} \end{pmatrix} \left(\begin{pmatrix} C_5 \\ C_4 \end{pmatrix} \left(A_6 - F_2\right) + C_8 \right) / \left(C_5 - C_4\right) \quad \textbf{(C.24)}$$

$$D_{5,\,6} = \left(r_{3,\,2} - r_1\right) / \left(r_3 - r_2\right) \mathrm{e}^{\left(r_1 - r_{2,\,3}\right) l_{f1}} \quad \textbf{(C.25)}$$

$$\begin{pmatrix} D_7 \\ D_8 \end{pmatrix} = \begin{pmatrix} 1/\mathrm{e}^{r_2 l_{f1}} & 0 \\ 0 & -1/\mathrm{e}^{r_3 l_{f1}} \end{pmatrix} / \left(C_5 - C_4\right) \cdot \left[\begin{pmatrix} C_5 \\ C_4 \end{pmatrix} \left(F_3 + A_7\right) + C_9 - \sum_{n_2=1}^{\infty} B_{n_2} \left\{ \begin{pmatrix} \begin{pmatrix} C_5 \\ C_4 \end{pmatrix} D_9 - C_6 \end{pmatrix} \cos\left(n_2 \pi l_{f1} / L\right) + \begin{pmatrix} \begin{pmatrix} B_9 \\ B_8 \end{pmatrix} F_1 + C_7 \end{pmatrix} \sin\left(n_2 \pi l_{f1} / L\right) \right\} \right] \quad \textbf{(C.26)}$$

$$\begin{pmatrix} D_9 \\ F_1 \end{pmatrix} = \begin{pmatrix} F_8 {n_2}^2 \pi^2 - F_0 L^2 \\ n_2 \pi \left(F_9 L^2 - {n_2}^2 \pi^2 \right) / L \end{pmatrix} \cdot 2\mu_2 k_2$$
$$\cdot \left(F_9 L^4 - {n_2}^2 \pi^2 L^2 - 2\left(\alpha \nu_{f1} + \gamma \nu_m \right) A_8 F_9 L^4 / \left(E_m H_1 \right) \right) \quad \textbf{(C.27)}$$
$$/ \left(a_2 \left(\left(F_9 L^2 - {n_2}^2 \pi^2 \right)^2 {n_2}^2 \pi^2 + \left(F_8 {n_2}^2 \pi^2 - F_0 L^2 \right)^2 L^2 \right) \right)$$

$$F_2 = \eta\gamma \left(\nu_m \left(E_m A_4 H_1 - 2A_8 \left(A_8 + A_9 \right) \right) + A_8 \right) / \left(\left(1 + \eta \right) E_m \left(A_9 H_1 - A_8 H_2 \right) \right) \quad \textbf{(C.28)}$$

$$F_3 = \left(\left(E_m A_4 H_7 - 2A_8 \left(A_8 + A_9 \right) \right) \left(2q_{01} - k_2 B_{02} \right) - 2A_8 q_{01} \right)$$
$$/ \left(2E_m A_4 \left(A_9 H_1 - A_3 H_2 \right) \right) \quad \textbf{(C.29)}$$

$$r_1 = F_8 / 3 - 2^{1/3} \left(3F_9 - {F_8}^2 \right) / \left(3r_0 \right) + 2^{-1/3} r_0 / 3 \quad \textbf{(C.30)}$$

$$r_2 = \left(F_8 - r_1 \right) / 2 + \begin{pmatrix} 2^{-1/3} \sqrt{3} {r_0}^2 \\ +2^{1/3} \sqrt{3\left(6{F_8}^2 F_9 - 9{F_9}^2 - {F_8}^4 \right)} \end{pmatrix} / \left(6r_0 \right) \quad \textbf{(C.31)}$$

$$r_3 = F_8 - r_1 - r_2 \quad \textbf{(C.32)}$$

$$r_0 = \begin{pmatrix} 2{F_8}^3 - 9F_8 F_9 + 27F_0 \\ +3\sqrt{3} \sqrt{-{F_8}^2 {F_9}^2 + 4{F_9}^3 + 4{F_8}^3 F_0 - 18F_8 F_9 F_0 + 27{F_0}^2} \end{pmatrix}^{1/3} \quad \textbf{(C.33)}$$

BIBILIOGRAPHY

[1] DU S. Advanced composite materials and aerospace engineering. Acta Materiae Compositae Sinica. 2007; 24 (1): 12.

[2] Gibson RF. A review of recent research on mechanics of multifunctional composite materials and structures. Compos Struct. 2010; 92: 2793-2810.

[3] George M. Boeing's 787: trials, tribulations, and restoring the dream. Reinforced Plastics. 2009; 53 (8): 16-21.

[4] George M. Airbus A350 XWB update. Reinforced Plastics. 2010; 54 (6): 20-24.

[5] Wambua P, Ivens J, Verpoest I. Natural fibres: can they replace glass in fibre reinforced plastics? Compos Sci Technol. 2003; 63 (9): 1259-1264.

[6] Chand S. Carbon fibers for composites. J Mater Sci. 2000; 35 (6): 1303-1313.

[7] Dicker MPM, Duckworth PF, Baker AB, et al. Green composites: A review of material attributes and complementary applications. Compos Part A: Appl Sci and Manuf. 2014; 56: 280-289.

[8] Chand N, Tiwary RK, Rohatgi PK. Resource structure properties of natural cellulosic fibers - an annotated-bibliography. J Mater Sci. 1988; 23 (2): 381-387.

[9] Brief L. Opportunities in natural fiber composites. Lucintel LLC, Irving (TX). 2011: 16.

[10] Agarwal J, Sahoo S, Mohanty S, et al. Progress of novel techniques for lightweight automobile applications through innovative eco-friendly composite materials: A review. Journal of Thermoplastic Composite Materials. 2019; 0892705718815530: 1-36.

[11] Koronis G, Silva A, Fontul M. Green composites: A review of adequate materials for automotive applications. Compos Part B-Eng. 2013; 44: 120-127.

[12] Gurunathan T, Mohanty S, Nayak SK. A review of the recent developments in biocomposites based on natural fibres and their application perspectives. Compos Part A: Appl Sci and Manuf. 2015; 77: 1-25.

[13] Pickering KL, Efendy MGA, Le TM. A review of recent developments in natural fibre composites and their mechanical performance. Compos Part A: Appl Sci and Manuf. 2016; 83: 98-112.

[14] Bisanda ETN, Ansell MP. Properties of sisal-cnsl composites. J Mater Sci. 1992; 27 (6): 1690-1700.

[15] Joshi SV, Drzal LT, Mohanty AK, et al. Are natural fiber composites environmentally superior to glass fiber reinforced composites? Compos Part A: Appl Sci and Manuf. 2004; 35 (3): 371-376.

[16] Mishnaevsky L. Nanostructured interfaces for enhancing mechanical properties of composites: Computational micromechanical studies. Compos Part B-Eng. 2015; 68: 75-84.

[17] Chand N, Hashmi SAR. Mechanical-properties of sisal fiber at elevated-temperatures. J Mater Sci. 1993; 28 (24): 6724-6728.

[18] Joseph K, Thomas S, Pavithran C. Effect of chemical treatment on the tensile properties of short sisal fibre-reinforced polyethylene composites. Polymer. 1996; 37 (23): 5139-5149.

[19] Williams GI, Wool RP. Composites from natural fibers and soy oil resins. Appl Compos Mater. 2000; 7 (5-6): 421-432.

[20] Gassan J, Chate A, Bledzki AK. Calculation of elastic properties of natural fibers. J Mater Sci. 2001; 36 (15): 3715-3720.

[21] Bogoeva-Gaceva G, Avella M, Malinconico M, et al. Natural fiber eco - composites. Polymer Composites. 2007; 28 (1): 98-107.

[22] Li H, Zadorecki P, Flodin P. Cellulose fiber-polyester composites with reduced water sensitivity .1. Chemical treatment and mechanical-properties. Polymer Composites. 1987; 8 (3): 199-202.

[23] John MJ, Thomas S. Biofibres and biocomposites. Carbohyd Polym. 2008; 71 (3): 343-364.

[24] Charlet K, Jernot JP, Eve S, et al. Multi-scale morphological characterisation of flax: From the stem to the fibrils. Carbohyd Polym. 2010; 82 (1): 54-61.

[25] Singleton ACN, Baillie CA, Beaumont PWR, et al. On the mechanical properties, deformation and fracture of a natural fibre/recycled polymer composite. Compos Part B-Eng. 2003; 34 (6): 519-526.

[26] Towo AN, Ansell MP. Fatigue of sisal fibre reinforced composites: Constant-life diagrams and hysteresis loop capture. Compos Sci Technol. 2008; 68 (3-4): 915-924.

[27] Rong MZ, Zhang MQ, Liu Y, et al. The effect of fiber treatment on the mechanical properties of unidirectional sisal-reinforced epoxy composites. Compos Sci Technol. 2001; 61 (10): 1437-1447.

[28] Yu T, Wu CM, Wang CJ, et al. Effects of surface modifications on the interfacial bonding of flax/beta-polypropylene composites. Compos Interfaces. 2013; 20 (7): 483-496.

[29] Huo S, Thapa A, Ulven CA. Effect of surface treatments on interfacial properties of flax fiber-reinforced composites. Adv Compos Mater. 2013; 22 (2): 109-121.

[30] Gao YC, Mai YW, Cotterell B. Fracture of fiber-reinforced materials. Z Angew Math Phys. 1988; 39 (4): 550-572.

[31] Kim JK, Mai YW. Engineered interfaces in fiber reinforced composites: Elsevier; 1998.

[32] Li Y, Ma H, Shen YO, et al. Effects of resin inside fiber lumen on the mechanical properties of sisal fiber reinforced composites. Compos Sci Technol. 2015; 108: 32-40.

[33] Li Y, Li Q, Ma H. The voids formation mechanisms and their effects on the mechanical properties of flax fiber reinforced epoxy composites. Compos Part A: Appl Sci and Manuf. 2015; 72: 40-48.

[34] Chamis CC. Mechanics of load transfer at the interfaces. 1974.

[35] Fitzer E, Weiss R. Effect of surface-treatment and sizing of C-fibers on the mechanical-properties of Cfr thermosetting and thermoplastic polymers. Carbon. 1987; 25 (4): 455-467.

[36] Choi MH, Jeon BH, Chung IJ. The effect of coupling agent on electrical and mechanical properties of carbon fiber/phenolic resin composites. Polymer. 2000; 41 (9): 3243-3252.

[37] Mukherjee PS, Satyanarayana KG. Structure and properties of some vegetable fibers .1. Sisal fiber. J Mater Sci. 1984; 19 (12): 3925-3934.

[38] Li Y, Mai YW, Ye L. Sisal fibre and its composites: a review of recent developments. Compos Sci Technol. 2000; 60 (11): 2037-2055.

[39] Faruk O, Bledzki AK, Fink H-P, et al. Biocomposites reinforced with natural fibers: 2000–2010. Progress in Polymer Science. 2012; 37 (11): 1552-1596.

[40] Bisanda ETN, Ansell MP. The effect of silane treatment on the mechanical and physical-properties of sisal-epoxy composites. Compos Sci Technol. 1991; 41 (2): 165-178.

[41] MInus M, Kumar S. The processing, properties, and structure of carbon fibers. J Mater. 2005; 57 (2): 52-58.

[42] Huang XS. Fabrication and properties of carbon fibers. Materials. 2009; 2 (4): 2369-2403.

[43] Guo H, Zhong W, Zhang Z, et al. Characterization and analysis on several carbon fibers. Fuhe Cailiao Xuebao(Acta Materiae Compositae Sinica)(China)(China). 2001; 18: 38-42.

[44] Monteiro SN, Lopes FPD, Ferreira AS, et al. Natural-fiber polymer-matrix composites: cheaper, tougher, and environmentally friendly. Journal of the Minerals, Metals and Materials Society. 2009; 61 (1): 17-22.

[45] Charlet K, Jernot JP, Breard J, et al. Scattering of morphological and mechanical properties of flax fibres. Ind Crop Prod. 2010; 32 (3): 220-224.

[46] Beaugrand J, Nottez M, Konnerth J, et al. Multi-scale analysis of the structure and mechanical performance of woody hemp core and the dependence on the sampling location. Ind Crop Prod. 2014; 60: 193-204.

[47] Stamboulis A, Baillie C, Schulz E. Interfacial characterisation of flax fibre-thermoplastic polymer composites by the pull-out test. Angew Makromol Chem. 1999; 272: 117-120.

[48] Silva dAF, Chawla N, Filho RDdT. Tensile behavior of high performance natural (sisal) fibers. Compos Sci Technol. 2008; 68 (15-16): 3438-3443.

[49] Groom L, Shaler S, Mott L. Mechanical properties of individual southern pine fibers. Part III: Global relationships between fiber properties and fiber location within an individual tree. Wood and Fiber Science. 2007; 34 (2): 238-250.

[50] Charlet K, Jernot JP, Gomina M, et al. Influence of an Agatha flax fibre location in a stem on its mechanical, chemical and morphological properties. Compos Sci Technol. 2009; 69 (9): 1399-1403.

[51] Fidelis MEA, Pereira TVC, Gomes OdFM, et al. The effect of fiber morphology on the tensile strength of natural fibers. J Mater Res Technol. 2013; 2 (2): 149-157.

[52] Zhang YL, Li Y, Ma H, et al. Tensile and interfacial properties of unidirectional flax/glass fiber reinforced hybrid composites. Compos Sci Technol. 2013; 88: 172-177.

[53] Gundel DB, Majumdar BS, Miracle DB. Evaluation of the transverse response of fiber-reinforced composites using a cross-shaped sample geometry. Scripta Metall Mater. 1995; 33 (12): 2057-2065.

[54] Zhandarov S, Mader E. Characterization of fiber/matrix interface strength: applicability of different tests, approaches and parameters. Compos Sci Technol. 2005; 65 (1): 149-160.

[55] Romanowicz M. Progressive failure analysis of unidirectional fiber-reinforced polymers with inhomogeneous interphase and randomly distributed fibers under transverse tensile loading. Compos Part A: Appl Sci and Manuf. 2010; 41 (12): 1829-1838.

[56] Sela N, Ishai O. Interlaminar fracture-toughness and toughening of laminated composite-materials - a review. Compos. 1989; 20 (5): 423-435.

[57] Sham ML, Kim JK, Wu JS. Interlaminar properties of glass woven fabric composites: Mode I and mode II fracture. Key Eng Mat. 1998; 145-9: 799-804.

[58] Wong S, Shanks RA, Hodzic H. Mechanical behavior and fracture toughness of poly(L-lactic acid)-natural fiber composites modified with hyperbranched polymers. Macromol Mater Eng. 2004; 289 (5): 447-456.

[59] Li Y, Chen CZ, Xu J, et al. Improved mechanical properties of carbon nanotubes-coated flax fiber reinforced composites. J Mater Sci. 2015; 50 (3): 1117-1128.

[60] Ravandi M, Teo WS, Tran LQN, et al. The effects of through-the-thickness stitching on the Mode I interlaminar fracture toughness of flax/epoxy composite laminates. Mater Design. 2016; 109: 659-669.

[61] Zhou LM, Kim JK, Mai YW. Interfacial debonding and fiber pull-out stresses .2. A new model based on the fracture-mechanics approach. J Mater Sci. 1992; 27 (12): 3155-3166.

[62] Chai YS, Mai YW. New analysis on the fiber push-out problem with interface roughness and thermal residual stresses. J Mater Sci. 2001; 36 (8): 2095-2104.

[63] Zhou LM, Kim JK, Baillie C, et al. Fracture-mechanics analysis of the fiber fragmentation test. J Compos Mater. 1995; 29 (7): 881-902.

[64] Kang SK, Lee DB, Choi NS. Fiber/epoxy interfacial shear strength measured by the microdroplet test. Compos Sci Technol. 2009; 69 (2): 245-251.

[65] Herrerafranco PJ, Drzal LT. Comparison of methods for the measurement of fiber matrix adhesion in composites. Compos. 1992; 23 (1): 2-27.

[66] Broutman LJ, Sahu S. The effect of interfacial bonding on the toughness of glass filled polymers. Mater Sci Eng. 1971; 8 (2): 98-107.

[67] Broutman LJ, Agarwal BD. A theoretical study of the effect of an interfacial layer on the properties of composites. Polym Eng Sci. 1974; 14 (8): 581-588.

[68] George J, Sreekala MS, Thomas S. A review on interface modification and characterization of natural fiber reinforced plastic composites. Polym Eng Sci. 2001; 41 (9): 1471-1485.

[69] Khalil HPSA, Ismail H, Rozman HD, et al. The effect of acetylation on interfacial shear strength between plant fibres and various matrices. Eur Polym J. 2001; 37 (5): 1037-1045.

[70] Joseph S, Sreekala MS, Oommen Z, et al. A comparison of the mechanical properties of phenol formaldehyde composites reinforced with banana fibres and glass fibres. Compos Sci Technol. 2002; 62 (14): 1857-1868.

[71] Joffe R, Andersons J, Wallstrom L. Strength and adhesion characteristics of elementary flax fibres with different surface treatments. Compos Part A: Appl Sci and Manuf. 2003; 34 (7): 603-612.

[72] Karlsson JO, Blachot JF, Peguy A, et al. Improvement of adhesion between polyethylene and regenerated cellulose fibers by surface fibrillation. Polymer Composites. 1996; 17 (2): 300-304.

[73] Valadez-Gonzalez A, Cervantes-Uc JM, Olayo R, et al. Effect of fiber surface treatment on the fiber-matrix bond strength of natural fiber reinforced composites. Compos Part B-Eng. 1999; 30 (3): 309-320.

[74] Li Y, Hu C, Yu Y. Interfacial studies of sisal fiber reinforced high density polyethylene (HDPE) composites. Compos Part A: Appl Sci and Manuf. 2008; 39 (4): 570-578.

[75] Young TJ, Crocker LE, Broughton WR, et al. Observations on interphase characterisation in polymer composites by nano-scale indentation using AFM and FEA. Compos Part A: Appl Sci and Manuf. 2013; 50: 39-43.

[76] Bonilla MR, Stokes JR, Gidley MJ, et al. Interpreting atomic force microscopy nanoindentation of hierarchical biological materials using multi-regime analysis. Soft Matter. 2015; 11 (7): 1281-1292.

[77] Ternovskii AP, Alekhin VP, Shorshorov MK, et al. Micromechanical testing of materials by depression. Zavod Lab. 1974; 39 (10): 1242-1247.

[78] Oliver WC, Pharr GM. An improved technique for determining hardness and elastic-modulus using load and displacement sensing indentation experiments. J Mater Res. 1992; 7 (6): 1564-1583.

[79] Urena A, Rams J, Escalera MD, et al. Characterization of interfacial mechanical properties in carbon fiber/aluminium matrix composites by the nanoindentation technique. Compos Sci Technol. 2005; 65 (13): 2025-2038.

[80] Gao SL, Mader E. Characterisation of interphase nanoscale property variations in glass fibre reinforced polypropylene and epoxy resin composites. Compos Part A: Appl Sci and Manuf. 2002; 33 (4): 559-576.

[81] Kim JK, Sham ML, Wu JS. Nanoscale characterisation of interphase in silane treated glass fibre composites. Compos Part A: Appl Sci and Manuf. 2001; 32 (5): 607-618.

[82] Wimmer R, Lucas BN, Tsui TY, et al. Longitudinal hardness and Young's modulus of spruce tracheid secondary walls using nanoindentation technique. Wood Sci Technol. 1997; 31 (2): 131-141.

[83] Bourmaud A, Baley C. Nanoindentation contribution to mechanical characterization of vegetal fibers. Compos Part B-Eng. 2012; 43 (7): 2861-2866.

[84] Lee SH, Wang SQ, Pharr GM, et al. Evaluation of interphase properties in a cellulose fiber-reinforced polypropylene composite by nanoindentation and finite element analysis. Compos Part A: Appl Sci and Manuf. 2007; 38 (6): 1517-1524.

[85] Li XP, Wang SQ, Du GB, et al. Variation in physical and mechanical properties of hemp stalk fibers along height of stem. Ind Crop Prod. 2013; 42: 344-348.

[86] Pethica JB, Oliver WC. Tip surface interactions in STM and AFM. Phys Scripta. 1987; T19a: 61-66.

[87] Asif SAS, Wahl KJ, Colton RJ. Nanoindentation and contact stiffness measurement using force modulation with a capacitive load-displacement transducer. Rev Sci Instrum. 1999; 70 (5): 2408-2413.

[88] Odegard GM, Gates T, Herring HM. Characterization of viscoelastic properties of polymeric materials through nanoindentation. Exp Mech. 2005; 45 (2): 130-136.

[89] Hayot CM, Forouzesh E, Goel A, et al. Viscoelastic properties of cell walls of single living plant cells determined by dynamic nanoindentation. J Exp Bot. 2012; 63 (7): 2525-2540.

[90] Zhang YF, Bai SL, Li XK, et al. Viscoelastic properties of nanosilica‐filled epoxy composites investigated by dynamic nanoindentation. J Polym Sci Polym Phys. 2010; 47 (10): 1030-1038.

[91] Li X, Gao H, Scrivens WA, et al. Nanomechanical characterization of single-walled carbon nanotube reinforced epoxy composites. Nanotechnology. 2004; 15 (11): 1416.

[92] Sikdar D, Katti D, Katti K, et al. Effect of organic modifiers on dynamic and static nanomechanical properties and crystallinity of intercalated clay/polycaprolactam nanocomposites. J Appl Polym Sci. 2010; 105 (2): 790-802.

[93] Gu YZ, Li M, Wang J, et al. Characterization of the interphase in carbon fiber/polymer composites using a nanoscale dynamic mechanical imaging technique. Carbon. 2010; 48 (11): 3229-3235.

[94] Li XD, Bhushan B. Nanofatigue studies of ultrathin hard carbon overcoats used in magnetic storage devices. J Appl Phys. 2002; 91 (10): 8334-8336.

[95] Bourchak M, Farrow IR, Bond IP, et al. Acoustic emission energy as a fatigue damage parameter for CFRP composites. Int J Fatigue. 2007; 29 (3): 457-470.

[96] Nair A, Cai CS. Acoustic emission monitoring of bridges: Review and case studies. Eng Struct. 2010; 32 (6): 1704-1714.

[97] Ageorges C, Friedrich K, Ye L. Experiments to relate carbon-fibre surface treatments to composite mechanical properties. Compos Sci Technol. 1999; 59 (14): 2101-2113.

[98] Ageorges C, Friedrich K, Schuller T, et al. Single-fibre Broutman test: fibre-matrix interface transverse debonding. Compos Part A: Appl Sci and Manuf. 1999; 30 (12): 1423-1434.

[99] Park JM, Kim JW, Yoon DJ. Comparison of interfacial properties of electrodeposited single carbon fiber/epoxy composites using tensile and compressive fragmentation tests and acoustic emission. J Colloid Interf Sci. 2002; 247 (1): 231-245.

[100] Park JM, Kim JW, Yoon DJ. Interfacial evaluation and microfailure mechanisms of single carbon fiber/bismaleimide (BMI) composites by tensile and compressive fragmentation tests and acoustic emission. Compos Sci Technol. 2002; 62 (6): 743-756.

[101] Lee SI, Park JM, Shin DW, et al. Interfacial properties of glass fiber brittle-ductile dual-matrix composites using micromechanical techniques and acoustic emission. Polymer Composites. 1999; 20 (1): 19-28.

[102] Narisawa I, Oba T. An Evaluation of Acoustic-Emission from Fiber-Reinforced Composites .2. The Application of Acoustic-Emission Techniques to Aramid Fiber-Reinforced Model Composites. J Mater Sci. 1985; 20 (12): 4527-4531.

[103] Joung-ManPark, Quangson T, Jin-GyuJung, et al. Interfacial evaluation of single Ramie and Kenaf fiber/epoxy resin composites using micromechanical test and nondestructive acoustic emission. Compos Interfaces. 2006; 13 (2-3): 105-129.

[104] Park JM, Quang ST, Hwang BS, et al. Interfacial evaluation of modified Jute and Hemp fibers/polypropylene (PP)-maleic anhydride polypropylene copolymers (PP-MAPP) composites using micromechanical technique and

nondestructive acoustic emission. Compos Sci Technol. 2006; 66 (15): 2686-2699.

[105] Cox HL. The elasticity and strength of paper and other fibrous materials. Brit J Appl Phys. 1952; 3 (Mar): 72-79.

[106] Fukuda H, Kawata K. Stress and strain fields in short fibre-reinforced composites. Fibre Science and Technology. 1974; 7 (2): 129-156.

[107] Christoffersen J, Jensen HM. Kink band analysis accounting for the microstructure of fiber reinforced materials. Mech Mater. 1996; 24 (4): 305-315.

[108] Dinter J, Peters PWM, Hemptenmacher J. Finite element modelling of the push-out test for SiC fibre-reinforced titanium alloys. Compos Part A: Appl Sci and Manuf. 1996; 27 (9): 749-753.

[109] Ananth CR, Chandra N. Numerical modeling of fiber push-out test in metallic and intermetallic matrix composites - Mechanics of the failure process. J Compos Mater. 1995; 29 (11): 1488-1514.

[110] Honda K, Kagawa Y. Analysis of shear-stress distribution in pushout process of fiber-reinforced ceramics. Acta Metall Mater. 1995; 43 (4): 1477-1487.

[111] Hsueh CH. Strength versus energy debonding criteria at fiber matrix interfaces. Compos Eng. 1992; 2 (8): 665-675.

[112] Huang NC, Liu XY. Debonding and fiber pull-out in reinforced composites. Theor Appl Fract Mec. 1994; 21 (3): 157-176.

[113] Kim JK, Lu SV, Mai YW. Interfacial debonding and fiber pull-out stresses .4. Influence of interface layer on the stress transfer. J Mater Sci. 1994; 29 (2): 554-561.

[114] Zhou LM, Kim JK, Mai YW. On the single fiber pull-out problem - effect of loading method. Compos Sci Technol. 1992; 45 (2): 153-160.

[115] Kim JK, Baillie C, Mai YW. Interfacial debonding and fiber pull-out stresses .1. Critical comparison of existing theories with experiments. J Mater Sci. 1992; 27 (12): 3143-3154.

[116] Kim JK, Zhou LM, Mai YW. Interfacial debonding and fiber pull-out stresses .3. Interfacial properties of cement matrix composites. J Mater Sci. 1993; 28 (14): 3923-3930.

[117] Zhou LM, Mai YW, Baillie C. Interfacial debonding and fiber pull-out stresses .5. A methodology for evaluation of interfacial properties. J Mater Sci. 1994; 29 (21): 5541-5550.

[118] Liu HY, Zhou LM, Mai YW. On fiber pull-out with a rough interface. Philos Mag A. 1994; 70 (2): 359-372.

[119] Brandstetter J, Kromp K, Peterlik H, et al. Effect of surface roughness on friction in fibre-bundle pull-out tests. Compos Sci Technol. 2005; 65 (6): 981-988.

[120] Yao Y, Chen SH. Effects of the longitudinal surface roughness on fiber pull-out behavior in carbon fiber-reinforced epoxy resin composites. J Appl Mech-T Asme. 2013; 80 (2).

[121] Barenblatt GI. The formation of equilibrium cracks during brittle fracture. General ideas and hypotheses. Axially-symmetric cracks. J Appl Math Mech. 1959; 23 (3): 622-636.

[122] Needleman A. A continuum model for void nucleation by inclusion debonding. J Appl Mech. 1987; 54 (3): 525.

[123] Van der Giessen E, Needleman A. Discrete dislocation plasticity: a simple planar model. Modelling and Simulation in Materials Science and Engineering. 1999; 3 (3): 689.

[124] Ortiz M, Pandolfi A. Finite‐deformation irreversible cohesive elements for three‐dimensional crack‐propagation analysis. International Journal for Numerical Methods in Engineering. 2008; 44 (9): 1267-1282.

[125] Chen XY, Beyerlein IJ, Brinson LC. Curved-fiber pull-out model for nanocomposites. Part 1: Bonded stage formulation. Mech Mater. 2009; 41 (3): 279-292.

[126] Chen XY, Beyerlein IJ, Brinson LC. Curved-fiber pull-out model for nanocomposites. Part 2: Interfacial debonding and sliding. Mech Mater. 2009; 41 (3): 293-307.

[127] Zhao YM, Yang MJ. Pull-out behavior of an imperfectly bonded anchor system. Int J Rock Mech Min. 2011; 48 (3): 469-475.

[128] Jia YY, Yan WY, Liu HY. Carbon fibre pullout under the influence of residual thermal stresses in polymer matrix composites. Comp Mater Sci. 2012; 62: 79-86.

[129] Jia YY, Chen ZR, Yan WY. A numerical study on carbon nanotube-hybridized carbon fibre pullout. Compos Sci Technol. 2014; 91: 38-44.

[130] Koyanagi J, Nakatani H, Ogihara S. Comparison of glass-epoxy interface strengths examined by cruciform specimen and single-fiber pull-out tests under combined stress state. Compos Part A: Appl Sci and Manuf. 2012; 43 (11): 1819-1827.

[131] Kim SC, Kim JS, Yoon HJ. Experimental and numerical investigations of mode I delamination behaviors of woven fabric composites with carbon, Kevlar and their hybrid fibers. International Journal of Precision Engineering & Manufacturing. 2011; 12 (2): 321-329.

[132] Ravandi M, Teo WS, Yong MS, et al. Prediction of Mode I interlaminar fracture toughness of stitched flax fiber composites. J Mater Sci. 2018; 53: 1-16.

[133] Ishida H, Koenig JL. The reinforcement mechanism of fiber‐glass reinforced plastics under wet conditions: A review. Polym Eng Sci. 1978; 18 (2): 128-145.

[134] Narkis M, Chen EJH, Pipes RB. Review of methods for characterization of interfacial fiber-matrix interactions. Polymer Composites. 1988; 9 (4): 245-251.

[135] Tang LG, Kardos JL. A review of methods for improving the interfacial adhesion between carbon fiber and polymer matrix. Polymer Composites. 2010; 18 (1): 100-113.

[136] George G, Jose ET, Jayanarayanan K, et al. Novel bio-commingled composites based on jute/polypropylene yarns: Effect of chemical treatments on the mechanical properties. Compos Part A: Appl Sci and Manuf. 2012; 43 (1): 219-230.

[137] Bledzki AK, Gassan J. Composites reinforced with cellulose based fibres. Progress in Polymer Science. 1999; 24 (2): 221-274.

[138] Juntaro J, Pommet M, Mantalaris A, et al. Nanocellulose enhanced interfaces in truly green unidirectional fibre reinforced composites. Compos Interfaces. 2007; 14 (7-9): 753-762.

[139] Juntaro J, Pommet M, Kalinka G, et al. Creating hierarchical structures in renewable composites by attaching bacterial cellulose onto sisal fibers. Adv Mater. 2008; 20 (16): 3122-3126.

[140] Pommet M, Juntaro J, Heng JYY, et al. Surface modification of natural fibers using bacteria: Depositing bacterial cellulose onto natural fibers to create hierarchical fiber reinforced nanocomposites. Biomacromolecules. 2008; 9 (6): 1643-1651.

[141] Lee KY, Bharadia P, Blaker JJ, et al. Short sisal fibre reinforced bacterial cellulose polylactide nanocomposites using hairy sisal fibres as reinforcement. Compos Part A: Appl Sci and Manuf. 2012; 43 (11): 2065-2074.

[142] Sydenstricker THD, Mochnaz S, Amico SC. Pull-out and other evaluations in sisal-reinforced polyester biocomposites. Polym Test. 2003; 22 (4): 375-380.

[143] Hu R, Lim JK. Fabrication and mechanical properties of completely biodegradable hemp fiber reinforced polylactic acid composites. J Compos Mater. 2007; 41 (13): 1655-1669.

[144] Paul SA, Reussmann T, Mennig G, et al. The role of interface modification on the mechanical properties of injection-moulded composites from commingled polypropylene/banana granules. Compos Interfaces. 2007; 14 (7-9): 849-867.

[145] Chen CZ, Li Y, Yu T. Interlaminar toughening in flax fiber-reinforced composites interleaved with carbon nanotube buckypaper. J Reinf Plast Comp. 2014; 33 (20): 1859-1868.

[146] Wang D. Research on mechanical properties of plant fiber reinforced composites modified with nanocrystalline cellulose. Tongji University, School of aerospace engineering and applied mechanics, 2015.

[147] Zhang ZS, Li Y, Chen CZ. Synergic effects of cellulose nanocrystals and alkali on the mechanical properties of sisal fibers and their bonding properties with epoxy. Compos Part A: Appl Sci and Manuf. 2017; 101: 480-489.

[148] Jendli Z, Fitoussi J, Meraghni F, et al. Anisotropic strain rate effects on the fibre-matrix interface decohesion in sheet moulding compound composites. Compos Sci Technol. 2005; 65 (3-4): 387-393.

[149] Li Y, Mai YW, Ye L. Effects of fibre surface treatment on fracture-mechanical properties of sisal-fibre composites. Compos Interfaces. 2005; 12 (1-2): 141-163.

[150] Li Y, Wang D, Ma H. Improving interlaminar fracture toughness of flax fiber/epoxy composites with chopped flax yarn interleaving. Sci China Technol Sc. 2015; 58 (10): 1745-1752.

[151] Rong MZ, Zhang MQ, Liu Y, et al. Effect of stitching on in-plane and interlaminar properties of sisal/epoxy laminates. J Compos Mater. 2002; 36 (12): 1505-1526.

[152] Ma H, Li Y, Shen YO, et al. Effect of linear density and yarn structure on the mechanical properties of ramie fiber yarn reinforced composites. Compos Part A: Appl Sci and Manuf. 2016; 87: 98-108.

[153] Bos HL, Donald AM. In situ ESEM study of the deformation of elementary flax fibres. J Mater Sci. 1999; 34 (13): 3029-3034.

[154] Dai D, Fan M. Characteristic and performance of elementary hemp fibre. Materials Sciences and Applications. 2010; 1 (06): 336.

[155] Newman RH, Le Guen MJ, Battley MA, et al. Failure mechanisms in composites reinforced with unidirectional Phormium leaf fibre. Compos Part A: Appl Sci and Manuf. 2010; 41 (3): 353-359.

[156] Majumdar A, Bhushan B. Fractal model of elastic-plastic contact between rough surfaces. J Tribol-T Asme. 1991; 113 (1): 1-11.

[157] Baley C. Analysis of the flax fibres tensile behaviour and analysis of the tensile stiffness increase. Compos Part A: Appl Sci and Manuf. 2002; 33 (7): 939-948.

[158] Cheng Y-T, Cheng C-M. Relationships between hardness, elastic modulus, and the work of indentation. Appl Phys Letters. 1998; 73 (5): 614-616.

[159] Towo AN, Ansell MP. Fatigue evaluation and dynamic mechanical thermal analysis of sisal fibre-thermosetting resin composites. Compos Sci Technol. 2008; 68 (3-4): 925-932.

[160] Botelho EC, Silva RA, Pardini LC, et al. A review on the development and properties of continuous fiber/epoxy/aluminum hybrid composites for aircraft structures. Mater Res. 2006; 9 (3): 247-256.

[161] Czigany T. An acoustic emission study of flax fiber-reinforced polypropylene composites. J Compos Mater. 2004; 38 (9): 769-778.

[162] Kocsis Z, Czigány T. Investigation of the debonding process in wood fiber reinforced polymer composites by acoustic emission. Materials Science Forum. 2007; 537-538: 199-206.

[163] Li Q, Li Y, Zhou LM. Nanoscale evaluation of multi-layer interfacial mechanical properties of sisal fiber reinforced composites by nanoindentation technique. Compos Sci Technol. 2017; 152: 211-221.

[164] Pines D, Salvino L. Structural health monitoring using empirical mode decomposition and the Hilbert phase. J Sound Vib. 2006; 294 (1-2): 97-124.

[165] Baranov VM, Kudryavtsev EM, Sarychev GA. Modelling of the parameters of acoustic emission under sliding friction of solids. Wear. 1997; 202 (2): 125-133.

[166] Fan Y, Gu F, Ball A. Modelling acoustic emissions generated by sliding friction. Wear. 2010; 268 (5–6): 811-815.

[167] Li RY, He D. Rotational machine health monitoring and fault detection using EMD-based acoustic emission feature quantification. Ieee T Instrum Meas. 2012; 61 (4): 990-1001.

[168] Bos HL, Mussig J, van den Oever MJA. Mechanical properties of short-flax-fibre reinforced compounds. Compos Part A: Appl Sci and Manuf. 2006; 37 (10): 1591-1604.

[169] Hutchinson JW, Jensen HM. Models of fiber debonding and pullout in brittle composites with friction. Mech Mater. 1990; 9 (2): 139-163.

[170] Gao YC. Damage modeling of fiber reinforced composites. Theor Appl Fract Mec. 1989; 11 (3): 147-155.

[171] Genties F, Anderson J, LThomason J. Characterisation of the transverse thermoelastic properties of natural fibres used in composites. 14th Eur Conf Compos Mater ECCM14, 2010.

[172] Sun W, Lin F. Computer modeling and FEA simulation for composite single fiber pull-out. Journal of Thermoplastic Composite Materials. 2001; 14 (4): 327-343.

[173] Liu HY, Zhang X, Mai YW, et al. On steady-state fibre pull-outII Computer simulation. Compos Sci Technol. 1999; 59 (15): 2191-2199.

[174] Wei GF, Liu GY, Xu CH, et al. Finite element simulation of perfect bonding for single fiber pull-out test. Adv Mater Research. 2012; 418-420: 509-512.

[175] Beckert W, Lauke B. Critical discussion of the single-fibre pull-out test: does it measure adhesion? . Compos Sci Technol. 1998; 57 (12): 1689-1706.

[176] Chandra N, Li H, Shet C, et al. Some issues in the application of cohesive zone models for metal–ceramic interfaces. International Journal of Solids & Structures. 2002; 39 (10): 2827-2855.

[177] Wang JS. Random sequential adsorption, series expansion and Monte Carlo simulation. Physica A Statistical Mechanics & Its Applications. 1997; 254 (1-2): 179–184.

[178] Tvergaard V, Hutchinson JW. The relation between crack growth resistance and fracture process parameters in elastic-plastic solids. Journal of the Mechanics & Physics of Solids. 1992; 40 (6): 1377-1397.

[179] Song SH, Paulino GH, Buttlar WG. A bilinear cohesive zone model tailored for fracture of asphalt concrete considering viscoelastic bulk material. Eng Fract Mech. 2006; 73 (18): 2829-2848.

[180] Harper PW, Hallett SR. Cohesive zone length in numerical simulations of composite delamination. Eng Fract Mech. 2008; 75 (16): 4774-4792.

[181] Airoldi A, Dávila CG. Identification of material parameters for modelling delamination in the presence of fibre bridging. Compos Struct. 2012; 94 (11): 3240-3249.

[182] Dávila CG, Rose CA, Camanho PP. A procedure for superposing linear cohesive laws to represent multiple damage mechanisms in the fracture of composites. International Journal of Fracture. 2009; 158 (2): 211-223.